博士論文

Alternative State Representation for Orbit Uncertainty Propagation

(軌道不確定性伝播のための新規状態表現**)**

Javier Hernando Ayuso
ハビエル　エルナンド　アジュソ

This page intentionally left blank.

博士論文

Alternative State Representation for Orbit Uncertainty Propagation

(軌道不確定性伝播のための新規状態表現)

Javier Hernando Ayuso
ハビエル　エルナンド　アジュソ

Department of Aeronautics and Astronautics

The University of Tokyo

A thesis submitted for the degree of

Doctor of Philosophy
in the Field of Aeronautics and Astronautics

2018 June 01

Abstract

Orbit uncertainty propagation is a key aspect of Astrodynamics. In particular, in the context of planetary defense, reliable and efficient uncertainty propagation is crucial for the task of monitoring possible impacts of Near Earth Asteroids (NEAs) with our planet. Other important application is collision monitoring in Low Earth Orbit (LEO) and Geostationary Earth Orbit (GEO) for satellites and pieces of space debris.

The evolution of the orbit uncertainty can be in principle approximated by Monte Carlo simulations, but the computational cost can become too high if a good accuracy is required. A very simple approach for quick calculations is employing a fast linear propagation method. However, the accuracy of this approach depends on the set of variables used to represent the state vector. That is, the nonlinearity of the differential equations that govern the evolution of the uncertainty can be (partially) absorbed by a nonlinear transformation of the state, which is an algebraic equation and is easier to handle. To investigate which representations of the state are more interesting for orbital applications, an extensive campaign of numerical simulations employing different sets of orbital elements is performed in this research. Results show how the nonlinearity is mainly concentrated in the anomaly of the orbital motion. Mean anomaly is found to be more linear than the eccentric anomaly, which in turn shows a more linear behavior than true anomaly. Time elements are found to be the most linear, but they come at the cost of particularizing the formulation for elliptic, parabolic or hyperbolic orbits, and they require solving Kepler's Equation.

As a first example of how the representation of the state can be advantageous, curvilinear coordinates are used to improve the uncertainty propagation accuracy of space debris compared to a Cartesian method. First, a double-frequency quadratic-order solution of the Keplerian motion is presented. Using this solution, a state transition matrix is constructed to propagate the uncertainty of the orbital motion. This method is shown to be applicable for more than one week in the Geostationary region, and for a several orbital periods in LEO.

Next, linear propagation using the Dromo orbit formulation is presented. Dromo is a nonsingular set of orbital elements which has shown an excellent performance in terms of numerical orbit propagation. Using this formulation, the linear propagation of the uncertainty of NEAs subject to N-body perturbations is presented. The applicability of the method is characterized by two linearity indices, which allow to divide the NEAs into three categories: one in which the Cartesian and the Dromo propagation agrees, one in which the Dromo formulation outperforms a Cartesian linear method, and one in which the linearity is lost after a close approach with highly nonlinear dynamics.

To mitigate the third body gravitational perturbation linearization error, a primary body switch is proposed. This technique has been widely used for orbit propagation to reduce the numerical error in the integration, but its application to orbit uncertainty is a novel approach. The switch is found to be applicable to more of 90% of the close approaches, and the uncertainty propagation accuracy is improved up to a factor of 30.

Finally, the Dromo formulation is employed for orbit determination and navigation applications. A batch estimator based on least-squares and a sequantial estimator based on Kalman filter are presented using Dromo variables. The formulation is then applied to two different scenarios. The first one is orbit determination of an object in a LEO orbit, and the second is on the navigation of a spacecraft in a binary asteroid system using optical navigation techniques.

Acknowledgements

This dissertation is the result of the work of several years, and could not have been possible without the support and help of Claudio Bombardelli. Claudio was my supervisor during my bachelor and master's degree in the Technical University of Madrid, Spain. Thanks to Claudio I could work for the first time in a myriad of novel topics in Astrodynamics and learned how to become a researcher. Back in 2014 we started discussing about the topic of the present dissertation while we were working together in Spain, and after I came to Japan for my PhD and actually started to work on the research he always collaborated remotely, offering constructive and useful comments and ideas. The collaboration with Giulio Baù during the last year of my degree also contributed significantly to the methodologies and results presented in the main text. I have had the pleasure of working with different researchers in topics of space situational awareness that have not been included in the dissertation. I especially acknowledge here Ricardo Garcia-Pelayo and Davide Amato for our collaborations in collision probability and asteroid impact monitoring.

I also want to thank my multiple colleagues and friends that supported me at some point during my pursue of the degree in Tokyo. First, I am especially thankful to my colleague Ralf Boden, with whom I had the pleasure of sharing the pains and difficulties of the doctoral course, both inside and outside our laboratory. Nicola Baresi offered me his invaluable help in multiple topics, and more concretely regarding orbit determination techniques. I also shared valuable experiences and learned to overcome insurmountable challenges while working in the OMOTENASHI project with Stefano Campagnola, Yusuke Ozawa, Shota Takahashi and Toshinori Ikenaga among others, and I am deeply grateful to them. I want to express gratitude to all the colleagues that offered me their moral support at lunch time, coffee breaks and outside the laboratory, especially Stefania Soldini, Chit Hong Yam *Hippo*, Daniel García Yárnoz, Onur Celik, Colleen Madlinger, Roger Gutiérrez Ramon, Tommaso Pino, Mattia Pugliatti, Ferran Gonzalez Franquesa, Naoya Ozaki and Stefaan van Wal. Outside the university, I espe-

cially thank Iñigo de Arcos Villa for being always there when one needs a friend and never letting me down.

I also want to thank my supervisor Prof. Junich'iro Kawaguchi for accepting me in his laboratory at the Institute of Space and Astronautical Science (ISAS) of the Japan Aerospace Exploration Agency (JAXA). During my stay in ISAS/JAXA, I could connect with different scientists and engineers working in multiple space projects, and I had the opportunity to collaborate in different proposals and missions, like a Japanese secondary payload proposal in the American Asteroid Redirect Robotic Mission (ARRM), a novel shape estimation algorithm for the Japanese next generation solar sail OKEANOS, orbit design for a spacecraft with transformable structure for last-minute detection of Earth-impacting asteroids, and trajectory design of the Japanese cubesat OMOTENASHI which aims to be the first spacecraft to perform a semi-hard landing on the Moon surface.

The committee members of my dissertation also played a key role in the completion of this thesis, as they offered very interesting and useful ideas to improve the final version of this work. For this, I am thankful to Prof. Akira Iwasaki and Prof. Ryu Funase from The University of Tokyo, Prof. Toshio Fukushima from the National Astronomical Observatory of Japan, Prof. Daniel J. Scheeres from The University of Colorado Boulder, and Prof. Brandon A. Jones from The University of Texas at Austin. I am also indebted to my labmate Yuki Takao for his support with all the necessary paperwork at the university.

The Ministry of Education, Culture, Sports, Science and Technology (MEXT) supported my doctoral studies with one of their scholarships for graduate students (文部科学省奨学金). Additional economic support was provided by ISAS/JAXA via its Research Assistant program.

Last, but not least, I am deeply grateful to my parents for supporting me all the way to the completion of the PhD program.

Contents

List of Figures viii

List of Tables xii

1 Introduction 1

1.1 Motivation . . . 1
1.2 Contributions and Research Goal . . . 5
1.3 Thesis Overview . . . 6
1.4 Publications . . . 7

I Nonlinearities in Orbit Uncertainty Propagation 11

2 Nonlinearities in Orbit Uncertainty Propagation 13

2.1 Introduction . . . 13
2.2 Uncertainty propagation . . . 13
2.2.1 Linear system . . . 14
2.2.2 Nonlinear system . . . 15
2.3 Influence of the State Representation . . . 16
2.4 Numerical Comparison of Different State Representations . . . 17
2.4.1 Benchmark Set of Variables . . . 18
2.4.1.1 Cartesian coordinates . . . 18
2.4.1.2 Equinoctial elements . . . 18
2.4.1.3 Alternate Equinoctial elements . . . 19
2.4.1.4 Dromo . . . 19
2.4.1.5 EDromo . . . 20
2.4.2 Results . . . 21

2.5 Conclusions 32

II Curvilinear Coordinates **33**

3 Curvilinear Coordinates **35**

3.1 Introduction 35
3.2 Curvilinear coordinates 36
3.2.1 Equations of Motion in Curvilinear Coordinates 38
3.3 Curvilinear Clohessy-Wiltshire 39
3.4 Quadratic solution 39
3.5 Linearization around the quadratic solution (QuadLin) 42
3.6 Results 46
3.6.1 Application to the GEO region 47
3.6.2 Application to the LEO region 56
3.7 Conclusions 60

III Dromo Formulation and Applications **63**

4 Relative Motion and Uncertainty Propagation with Dromo **65**

4.1 Introduction 65
4.2 Overview of the Dromo Formulation 67
4.2.1 Dromo variables 67
4.2.2 Dromo Hodograph plane 69
4.2.3 Equations of Motion in Dromo Elements 70
4.3 Probability Distribution Function of the Dromo Variables 71
4.4 Linear propagation with Dromo 73
4.4.1 Gradient Matrices 74
4.4.2 N-body term 75
4.5 Linearity indices 77
4.5.1 Orbit Condition Code 77
4.5.2 Close approach linearization error 80
4.6 Real case application 81
4.6.1 2000SG344 83

4.6.2 2011AM37 . . . 85
4.6.3 2013HO . . . 87
4.6.4 2016DJ . . . 88
4.7 Discussion on the linear indices . . . 91
4.8 Anomaly Transition Tensor . . . 92
4.8.1 Formulae for the quadratic terms . . . 93
4.8.2 Formulae for the cubic terms . . . 93
4.9 Conclusions . . . 95

5 Primary Body Switch **97**
5.1 Introduction . . . 97
5.2 Primary body switch . . . 98
5.3 Results . . . 100
5.3.1 2011AG5 . . . 101
5.3.2 2012AP10 . . . 101
5.3.3 2004RQ252 . . . 102
5.3.4 2001AV43 . . . 103
5.3.5 99942 Apophis . . . 104
5.4 Discussion . . . 106
5.5 Conclusion . . . 110

6 Orbit Determination using Dromo **111**
6.1 Introduction . . . 111
6.2 Observations . . . 112
6.2.1 Range . . . 112
6.2.2 Range-Rate . . . 113
6.2.3 Optical navigation . . . 114
6.3 Batch Estimation based on Least-Squares . . . 115
6.3.1 A priori information . . . 116
6.3.2 Least-Squares Estimation in Dromo . . . 117
6.4 Sequential Estimation. Conventional Kalman Filter . . . 119
6.5 Applications . . . 121
6.5.1 Example in LEO . . . 121

6.5.2 Application to Navigation of a Spacecraft in the Binary Asteroid System Didymos 128
6.6 Conclusions 137

7 Conclusions **139**
7.1 Concluding Remarks 139
7.2 Future Work 140

A Probability Distribution Function and Moments **143**
A.1 One–Dimensional Random Variable 143
A.1.1 Parent Distribution 143
A.1.2 Sampling Distribution 145
A.2 Multi–Dimensional Random Variable 146

B Orbital Elements as a Function of the Curvilinear Coordinates **149**

C Melton´s Method **153**

D Relations of Dromo with Other Sets of Variables **157**
D.1 Relations with Classical Orbital Elements 157
D.1.1 Dromo to Classical Orbital Elements Transformation 157
D.1.2 Dromo to Classical Orbital Elements Jacobian 158
D.1.3 Classical Orbital Elements to Dromo Transformation 158
D.1.4 Classical Orbital Elements to Dromo Jacobian 159
D.2 Relations with Cartesian Coordinates 159
D.2.1 Dromo to Cartesian Coordinates Transformation 159
D.2.2 Dromo to Cartesian Coordinates Jacobian 159
D.2.3 Cartesian Coordinates to Dromo Transformation 161
D.2.4 Cartesian Coordinates to Dromo Jacobian 162
D.3 Relations with Equinoctial Elements 163
D.3.1 Dromo to Equinoctial Elements Transformation 164
D.3.2 Dromo to Equinoctial Elements Jacobian 165
D.3.3 Equinoctial Elements to Dromo Transformation 166

E NEODyS data **169**

E.1 2000SG344 170
E.2 2011AM37 171
E.3 2013HO 172
E.4 2016DJ 173
E.5 (367789) 2011AG5 174
E.6 2012AP10 175
E.7 2004RQ252 176
E.8 2001AV43 177
E.9 (99942) Apophis 178

References **179**

List of Figures

1.1 Space debris population that come into LEO region 3
1.2 Space debris population that come into GEO region 3
1.3 Prediction of the evolution of space debris population in LEO region . . 4
1.4 Thesis structure. The numbers correspond to the chapter numbers. . . . 8

2.1 Root Mean Square error for the LEO ($e = 0.01$) orbit. 24
2.2 Root Mean Square error for the LEO ($e = 0.1$) orbit. 25
2.3 Root Mean Square error for the LEO ($e = 0.2$) orbit. 26
2.4 Root Mean Square error for IBEX orbit. 27
2.5 Root Mean Square error for Simbol-X orbit. 28
2.6 Comparison of RMS of the angular variables for the LEO ($e = 0.01$) orbit. 29
2.7 Comparison of RMS of the angular variables for the LEO ($e = 0.1$) orbit. 29
2.8 Comparison of RMS of the angular variables for the LEO ($e = 0.2$) orbit. 30
2.9 Comparison of RMS of the angular variables for IBEX. 30
2.10 Comparison of RMS of the angular variables for Simbol-X. 31

3.1 Relative motion geometry and curvilinear coordinates. 37
3.2 Relative motion in the $\mathcal{C}$ frame: Full view (left) and zoom (right). 48
3.3 ρ standard deviation error (GEO). 49
3.4 $\dot{\rho}$ standard deviation error (GEO). 50
3.5 θ standard deviation error (GEO). 50
3.6 $\dot{\theta}$ standard deviation error (GEO). 51
3.7 z standard deviation error (GEO). 51
3.8 $\dot{z}$ standard deviation error (GEO). 52
3.9 Uncertainty dispersion in the $\Delta\theta$–$\Delta\rho$ plane at an intermediate epoch (GEO, $\tau = 2.81$ days). 52

3.10 Uncertainty dispersion in the $\Delta\theta$–$\Delta\rho$ plane at an intermediate epoch (GEO, $\tau = 8.00$ days). 53
3.11 Angular-radial uncertainty clouds including Melton's method at an early epoch (GEO, $\tau = 0.80$ days). 54
3.12 Angular-radial uncertainty clouds including Melton's method at an intermediate epoch (GEO, $\tau = 2.81$ days). 54
3.13 Average position error including comparison with Melton's method (GEO). 55
3.14 Maximum value over time of the average position error in the GEO scenario for different values of the eccentricity of the Follower. 55
3.15 ρ standard deviation error (LEO, $i = 98$ deg). 57
3.16 ρ standard deviation error (LEO, $i = 45$ deg). 58
3.17 θ standard deviation error (LEO, $i = 98$ deg). 58
3.18 θ standard deviation error (LEO, $i = 45$ deg). 59
3.19 z standard deviation (LEO, $i = 98$ deg). 59
3.20 z standard deviation (LEO, $i = 45$ deg). 60

4.1 Inertial ($\mathcal{I} = \langle x_\mathcal{I}, y_\mathcal{I}, z_\mathcal{I} \rangle$) and intermediate ($\mathcal{P} = \langle x_\mathcal{P}, y_\mathcal{P}, z_\mathcal{P} \rangle$) frames. . . 69
4.2 Intermediate ($\mathcal{P} = \langle x_\mathcal{P}, y_\mathcal{P}, z_\mathcal{P} \rangle$) and LVLH ($\mathcal{R} = \langle x_\mathcal{R}, y_\mathcal{R}, z_\mathcal{R} \rangle$) frames. . 69
4.3 Dromo Hodograph plane 70
4.4 Geometry of close approach with uncertainty 81
4.5 2000SG344 Uncertainty cloud. 84
4.6 Non-linearity indices for 2000SG344 84
4.7 Skewness and excess kurtosis for 2000SG344 85
4.8 2011AM37 Uncertainty cloud. 86
4.9 Non-linearity indices for 2011AM37 86
4.10 Skewness and excess kurtosis for 2011AM37 87
4.11 2013HO Uncertainty cloud. 88
4.12 Non-linearity indices for 2013HO 89
4.13 Skewness and excess kurtosis for 2013HO 89
4.14 2016DJ Uncertainty cloud. 90
4.15 Non-linearity indices for 2016DJ 90
4.16 Skewness and excess kurtosis for 2016DJ 91

5.1 Primary body switch flow chart. 99
5.2 Average position error for 2011AG5 at year 2050 as a function of the switch distance 102
5.3 Average position error for 2012AP10 at year 2050 as a function of the switch distance 103
5.4 Average position error for 2004RQ252 at year 2050 as a function of the switch distance 104
5.5 Average position error for 2004RQ252 as a function of time. 105
5.6 Average position error for 2001AV43 at year 2040 as a function of the switch distance 105
5.7 Average position error for 99942 Apophis at year 2040 as a function of the switch distance. 106
5.8 Optimum switch distance. 107
5.9 Switch error-reduction factor 108

6.1 Elevation as seen from ground stations and observations. 123
6.2 Ground track and observations 124
6.3 Range and range-rate residuals after each pass of the Dromo least-squares estimation algorithm. 125
6.4 Distribution of range and range-rate residuals after the last pass of the Dromo least-squares estimation algorithm. 125
6.5 3–σ Dromo covariance envelopes and error of the reference trajectory after the last pass of the Dromo least-squares estimation algorithm. . . . 126
6.6 Range and range-rate residuals after each pass of the Cartesian least-squares estimation algorithm. 127
6.7 Distribution of range and range-rate residuals after the last pass of the Cartesian least-squares estimation algorithm. 127
6.8 3–σ Cartesian covariance envelopes and error of the reference trajectory after the last pass of the Cartesian least-squares estimation algorithm. . . 128
6.9 Didymos system 130
6.10 Seven days backwards propagation of the nominal trajectory 132
6.11 Seven days backwards propagation of the nominal trajectory 134

6.12 Maximum position standard deviation when changing the observations interval from 0.1 to 84 hours, with a step of 0.05. Values for the maximum value over time and for the final epoch. 135
6.13 Maximum position standard deviation with observations taken at intervals of 0.5, 1, 3 and 6 hours. 135
6.14 Dromo Covariance envelopes for with observations taken at intervals of 0.5, 1, 3 and 6 hours. 136

List of Tables

2.1 Initial conditions for the LEO orbits. 23
2.2 Initial conditions for IBEX. 23
2.3 Initial conditions for Simbol-X. 23

4.1 Selected Asteroids 83
4.2 Close approaches for 2000SG344 84
4.3 Close approaches for 2011AM37 86
4.4 Close approaches for 2013HO 88
4.5 Close approaches for 2016DJ 90

5.1 Significant data of the asteroids considered in the analysis. 100
5.2 Summary of the results 108
5.3 Summary of closest approaches. 109
5.4 Statistics of Earth encounters after a search in the NEODyS database. . . 109

6.1 Initial conditions expressed expressed in the Earth-centered J2000 Equatorial frame. 122
6.2 Ground stations 123
6.3 RMS error of the range and range-rate residuals after each pass of the Dromo least-squares algorithm. 124
6.4 RMS error of the range and range-rate residuals after each pass of the Cartesian least-squares algorithm. 126
6.5 Characteristics of the Didymos system 129
6.6 Final and initial values of the backwards propagation 131

Chapter 1

Introduction

1.1 Motivation

Orbit uncertainty propagation is a key aspect of Astrodynamics that has been receiving increasing attention in the last years. For some applications, it is not enough to just analyze the nominal orbit of an object, and it becomes paramount to carefully consider the deviation between the real and the predicted orbit.

In particular, in the context of planetary defense, reliable and efficient uncertainty propagation is crucial for the task of monitoring possible impacts of Near Earth Asteroids (NEAs) with our planet. These asteroids have sizes that range from the 16.8 km of 433 Eros to a few meters as in the case of small bodies like 2015 TC25. The NEAs on the small size of this spectrum are very faint and especially hard to detect and observe, and many of them can be observed only when they fly-by the Earth. This poses challenges for object-orbit linkage and precise orbit determination, which further complicates the task of Earth-impact monitoring. Orbit uncertainty is also key in missions that include a rendezvous with small NEAs, as the small size is associated with a low magnitude, and several months must be allocated for a search phase once the spacecraft has reached the expected position of the target asteroid [42]. In this scenario, a mismodeled uncertainty region may make its duration unnecessarily long. For these applications, efficient orbit uncertainty propagation and orbit determination techniques are important to reduce the required resources allocated to these tasks.

Other important application is collision monitoring in Low Earth Orbit (LEO) and Geostationary Earth Orbit (GEO) for satellites and pieces of space debris. As a collateral

damage of the use of space by military, scientific and commercial spacecraft missions, tens of thousands of derelict objects have been left in orbit around our planet. They are usually referred to as space debris, and their number is growing year by year [54, 66]. The population of space debris is diverse in size, orbit an origin. The number of objects in orbit around Earth has been steadily growing since the beginning of the space era that begun with the launch of Sputnik in 1957. In fact, the number of objects in LEO and GEO shows no signs of deceleration as can be seen in Figs.1.1 and 1.2 taken from a report of the European Space Agency [85]. Several authors predict that this trend will continue, as Krag et al. reported (see Fig. 1.3 taken from [67]). Additionally, plans for mega constellations of small satellites in the near future may magnify the problems caused by the large number of Earth-orbiting objects [74].

Even if the nominal trajectories of two orbiting objects do not lead to an impact, uncertainty in their orbit may mask a collision. The probability of collision for a pair of objects is low, but since the population of satellites and space debris is large and growing every year, the total risk cannot be neglected. In November 2010, the U.S. military reported an average of 190 conjunctions per week [54]. These conjunctions may lead to a collision between the bodies, causing minor damages, major damages or even mission termination or body fragmentation. Collision avoidance maneuvers are performed several times during the lifetime of a satellite: as an example Envisat executed 4 maneuvers in 2011 [67]. There are several examples of collisions in the past, like the 2009 Iridium-Cosmos collision [84] or the non-catastrophic damage sustained by the solar panels of the European satellite Copernicus Sentinel-1A in August 2016 [68]. The assessment of the risk of collision between two orbiting objects in low Earth orbit (LEO) requires the knowledge of the covariance matrices of both objects propagated up to the collision epoch (see [36] and references therein). In geostationary orbits (GEO), where conjunctions occur throughout a much larger time scale, these matrices may even need to be propagated throughout the conjunction duration to properly evaluate collision probabilities [23, pp. 153-171]. An example of potential collision in GEO was presented by [71].

The problem of space debris can be partially mitigated by Post Mission Disposal [33] or Active Debris Removal [75]. In any case, the increasing number of objects must be constantly monitored for collisions between them and with other active spacecraft. This is done nowadays by ground-based telescopes and radars [33], but their coverage

is limited and the time between observations can become large in the near future. This calls for advance and efficient methods of uncertainty propagation and conjunction monitoring.

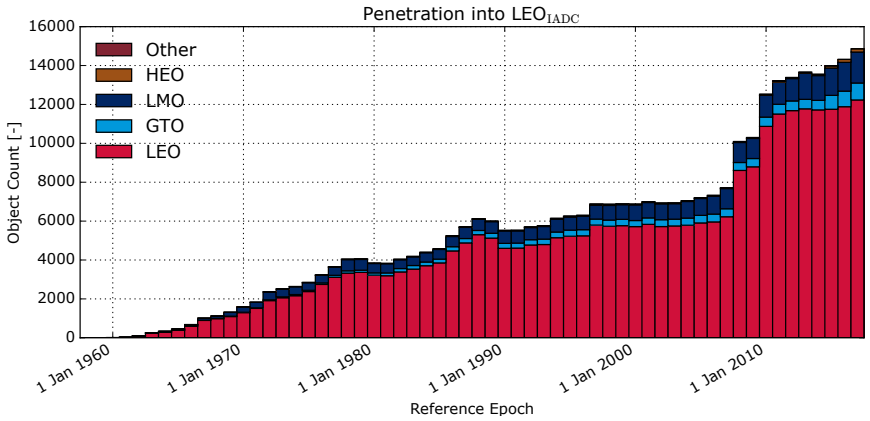

Figure 1.1: Space debris population that come into LEO region (taken from [85]).

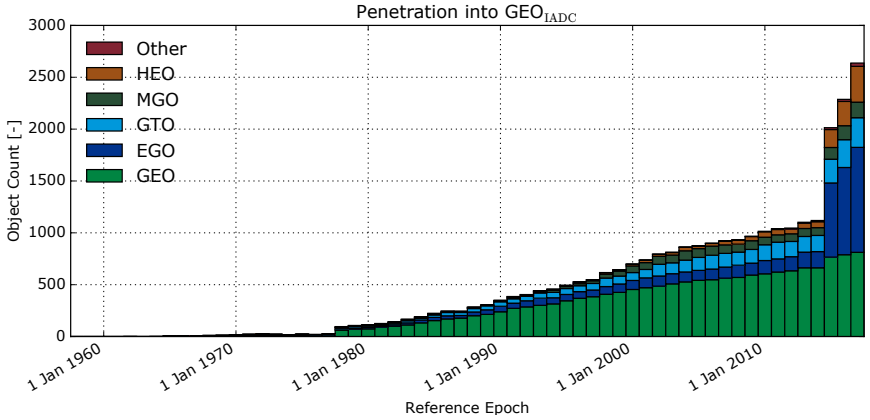

Figure 1.2: Space debris population that come into GEO region (taken from [85]).

Last but not least, orbit uncertainty is the foundation of spacecraft navigation [100, 110].

When the uncertainty is small, the probability distribution function (pdf) is usually modeled as Gaussian because of the central limit theorem and because its analytical properties, mainly preservation of Gaussianity under linear transformations. Unfortunately, the orbital motion is strongly nonlinear and the assumption of a Gaussian distribution propagated linearly eventually loses validity. When this happens, in general one must obtain the pdf by solving complicated partial differential equations, like the

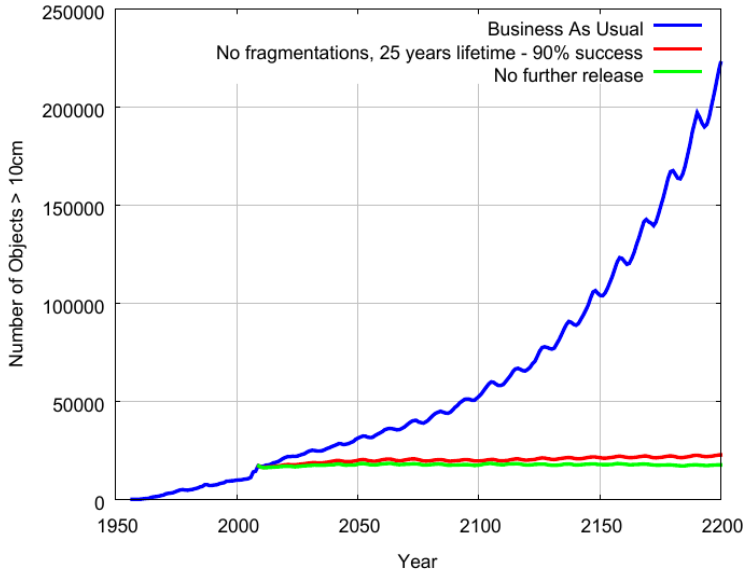

Figure 1.3: Prediction of the evolution of space debris population in LEO region (taken from [67]).

Fokker-Plank Equation [78, pp. 192-202], or use another method to accurately calculate the evolution of the orbit pdf. For instance, Park et al. [88] proposed generalizing the state transition matrix (STM) to higher orders by constructing state transition tensors. The use of Differential Algebra (DA) has also been considered for orbit uncertainty nonlinear propagation [105], orbit determination [6], and for real cases like the 2029 close approach of the asteroid Apophis [5]. Another possibility is to model the orbit uncertainty as a sum of Gaussian kernels in the Gaussian Mixture Model (GMM) [38].

There is a whole family of non-intrusive methods that exploit already existing orbit propagation tools. The most elementary method one could think of is a simple Monte Carlo (MC) method, which propagates random samples of the initial distribution. If the samples are not random but correspond to carefully chosen points, computational time can be greatly reduced by the use of the Unscented Kalman Filter [58]. The solution can be conveniently projected in an orthonormal basis using Polynomial Chaos Expansions (PCE), and the components in the new basis can be calculated from propagation of a reduced number of samples [56]. Vittaldev and Russell proposed a combination of GMM and PCE [107]. Kriging, a method for interpolation from discrete data, has also been applied for orbit uncertainty propagation [101]. When studying the orbit uncertainty of NEAs, Milani et al introduced the concept of Line Of Variations (LOV), a

one-dimensional sampling along a carefully chosen direction that accounts for most of the orbit uncertainty [81].

Some techniques are possible to extend the validity of linear methods, which are usually faster than the algorithms mentioned above. Junkins et al. [59] pointed out that the accuracy of the predicted covariance depends on the set of variables that constitute the state vector. They proposed the use of orbital elements substituting the classical Cartesian representation, Other authors have also explored the use of equinoctial orbital elements to improve the propagation of the uncertainty [34, 96], and Kechichian provided the required partial derivatives of the equations of motion in equinoctial elements including the effect of non-Keplerian perturbations while considering linearization techniques for low-thrust trajectory optimization [60, 61, 62, 63, 64]. Roa et al. studied the applicability of different advanced sets of orbital elements for orbit uncertainty propagation [95]. Following a similar approach, Weis proposed studying orbit uncertainty in Kustaanheimo-Stiefel space [108]. Conversely, curvilinear coordinates have also been proven to ameliorate the problem (see [27, 46, 52, 69, 79] for instance). These techniques also have applications in orbit determination, as Weisman et al. showed while studying the nonlinear mapping of the uncertainty between Cartesian coordinates and orbital elements and comparing to Monte Carlo simulations [109] .

1.2 Contributions and Research Goal

In this thesis, the importance of the representation of the state vector for orbit uncertainty propagation is explored. A numerical survey to analyze the linearization error for different representations of the state is presented. Then, two different formulations are proposed for space situational awareness and spacecraft navigation applications.

The first formulation is based in an analytical solution of the equations of motion in curvilinear coordinates. It is very efficient in orbits in which the gradient of the perturbation is not dominant, and allow for quick computations of evolution of the uncertainty of space debris in LEO and GEO.

The second formulation is Dromo, a relatively recent orbital motion formulation that was proposed by Peláez et al. in 2007 [89] and considerably improved in subsequent works by Urrutxua et al. [103], Roa et al. [93] and Baù et al. in 2013 [8], 2014 [9], and 2015 [10]. It employs seven non-singular orbital elements and a fictitious time de-

rived from a second order Sundman transformation. It has been shown that Dromo exhibits an excellent performance in terms of numerical propagation of orbits. Using this formulation, the linear propagation of the uncertainty of NEAs subject to N-body perturbation has been developed by the author of the present dissertation, drastically improving its Cartesian counterpart [44]. The method has been applied to Earth-bounded orbits as well, obtaining satisfactory results [47]. While linearization with the original Dromo formulation is possible [95], it leads to problems of time synchrony in the propagated pdf [94]. The first step in order to make the formulation applicable to covariance propagation in time was to choose time as the independent variable. This is crucial when the covariance propagation process involves time-dependent perturbations whose time-derivative needs to be evaluated. The propagation of asteroid orbits, for instance, requires the computation of N-bodies gravitational perturbations obtained from time-dependent ephemerides. Next, one has to construct a state transition matrix (STM) in Dromo elements and obtain the fundamental (linear) differential equation that governs its time evolution by computing the partial derivatives of the perturbing accelerations with respect to the Dromo state variables. Once the time evolution of the state transition matrix is obtained, the covariance matrix propagation can be carried out analytically, effectively propagating the initial orbit uncertainty into the future. For the case of close encounters of Near Earth Asteroids with the Earth, a primary body switch is proposed to overcome the limitations of a purely linear propagation. Finally, the Dromo formulation is also employed for orbit determination and navigation applications.

1.3 Thesis Overview

Chapter 2 introduces the problem of orbit uncertainty propagation and the advantages and disadvantages of employing a linear method. Furthermore, the possibility of partially absorbing the nonlinearity of the equations of motion with an appropriate choice of the state representation is presented, and a numerical comparison of different formulations is included.

An interesting choice of state representation for weakly-perturbed orbits with small eccentricity is the use of curvilinear coordinates. It is possible to obtain an analytical solution for the relative motion expressed in curvilinear coordinates [17]. This solution can be truncated to a quadratic-order, double frequency, which provides a state

transition matrix for the relative motion [46]. This approach is presented in Chapter 3.

Chapter 4 is devoted to the relative motion and uncertainty propagation using Dromo. The Dromo state transition matrix is proposed and the necessary gradient matrices are provided for numerical efficiency. Then, the linear propagation of the orbit uncertainties of Near Earth Asteroids is presented, improving the results of a linear method based on Cartesian coordinates [44]. The applicability of this algorithm is found to be limited only by the gravitational force linearization error during close approaches with the Earth.

To mitigate the linearization error of the third-body perturbation acceleration during close approaches, a primary body switch is introduced in Chapter 5. The primary body switch consists in replacing the body used as reference to construct the Dromo elements. The primary body switch is found to reduce the average error up to a factor of 30 [50].

Finally, in Chapter 6, the applicability of the Dromo formulation to orbit determination is studied. A least-squares and a Kalman filter in Dromo variables are proposed and applied first to an object in LEO, and then to a spacecraft in the vicinity of a binary asteroid system.

The thesis structure is shown in Fig. 1.4.

1.4 Publications

The following papers have been published while pursuing the doctoral degree:

Journal papers

- Javier Hernando-Ayuso, Claudio Bombardelli, and Giulio Baù. *"Uncertainty propagation in the N-body problem using dromo elements"*. Acta Astronautica, 2017. In press (December 2017). [50]

- Javier Hernando-Ayuso and Claudio Bombardelli. *"Covariance propagation via quadratic-order state transition matrix in curvilinear coordinates"*. Celestial Mechanics and Dynamical Astronomy, 129(1):215–234, Sep 2017. [46]

Conference papers

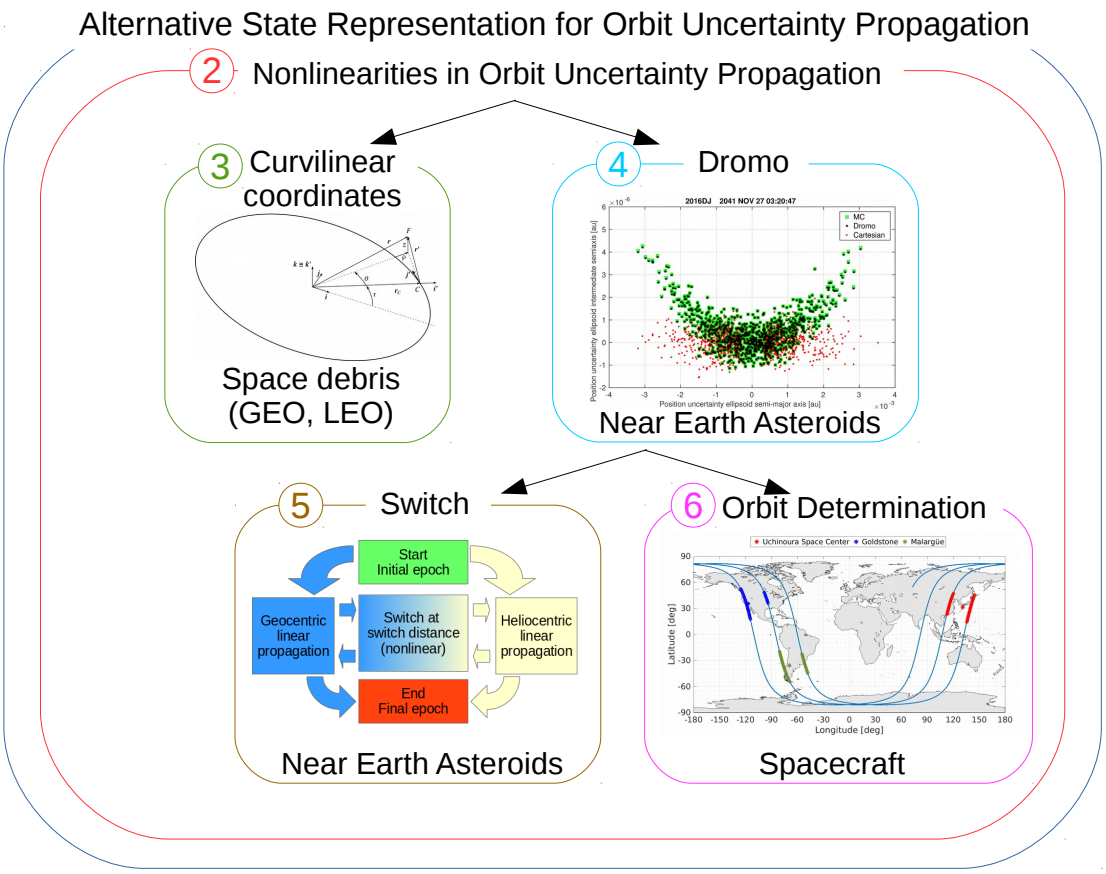

Figure 1.4: Thesis structure. The numbers correspond to the chapter numbers.

- Javier Hernando-Ayuso, Claudio Bombardelli, Giulio Baù and Kawaguchi Junichiro. *"Nongaussianities in orbit uncertainty representation"*. In 27th Workshop on JAXA Astrodynamics and Flight Mechanics, Sagamihara, Japan, 25 July 2017. [49]

- Javier Hernando-Ayuso and Claudio Bombardelli. *"Orbit uncertainty propagation around nonspherical bodies using the Dromo formulation"*. In 26th International symposium on Space Flight Dynamics, held together the 31st International Symposium on Space Technology and Science, number 2017-d-071, Matsuyama, Japan, 3-9 June 2017. [47]

- Javier Hernando-Ayuso, Claudio Bombardelli, and Giulio Baù. *"Uncertainty propagation in the N-body problem using Dromo elements"*. In 2017 IAA Planetary Defense Conference, number IAA-PDC-17-03-P21, Tokyo, Japan, 15-19 May 2017. [48]

- Javier Hernando-Ayuso and Claudio Bombardelli. *"Orbit uncertainty propagation using Dromo"*. In AIAA/AAS Astrodynamics Specialist Conference, number AIAA 2016-5632, Long Beach, CA, 2016. [44]
- Javier Hernando-Ayuso and Claudio Bombardelli. *"Advances in uncertainty propagation using curvilinear coordinates"*. In 26th Workshop on JAXA Astrodynamics and Flight Mechanics, Sagamihara, Japan, 25 July 2016. [45]

This page intentionally left blank.

Part I

Nonlinearities in Orbit Uncertainty Propagation

This page intentionally left blank.

Chapter 2

Nonlinearities in Orbit Uncertainty Propagation

2.1 Introduction

The orbit of an object is determined from observations which have limited accuracy. Combined with the uncertainties in the dynamical model, this causes that the orbit cannot be perfectly known, and our best guess will have a confidence region associated to it. When propagating the orbit uncertainty, the case of a Gaussian distribution linearly propagated is especially efficient, while the general scenario is harder to solve. The important question we seek answer for is the following: *can we convert a hard problem into the easy problem of a linearly propagated Gaussian?*

In this chapter, we review key concepts for orbit uncertainty propagation in Section 2.2. In Section 2.3, we highlight the possibility of answering the question that was posed above, proposing a general way to propagate in a more efficient way the uncertainty. Finally, we perform a numerical study of different state representations and their linearity in Section 2.4.

2.2 Uncertainty propagation

Let $\boldsymbol{X} = (X_1, \ldots, X_N) \in \mathbb{R}^N$ be a N-dimensional random variable that represents the state of the orbiting particle. Its cumulative distribution function $g(\boldsymbol{x})$ is defined as

$$g(\boldsymbol{x}) = P(\boldsymbol{X} \leqslant \boldsymbol{x}) = \int_{-\infty}^{x_1} \ldots \int_{-\infty}^{x_N} p(\boldsymbol{x}) \mathrm{d}\boldsymbol{x}, \tag{2.1}$$

where $p(\boldsymbol{x})$ is the probability distribution function (pdf) associated to $\boldsymbol{X}$. For the particular case of a multidimensional Gaussian distribution, its pdf is

$$p(\boldsymbol{x}) = \frac{1}{\sqrt{(2\pi)^N |\boldsymbol{C}|}} \exp\left\{-\frac{1}{2}\left(\boldsymbol{x} - \langle \boldsymbol{x} \rangle\right)^\top \boldsymbol{C}^{-1}\left(\boldsymbol{x} - \langle \boldsymbol{x} \rangle\right)\right\}, \tag{2.2}$$

where $\langle \boldsymbol{x} \rangle$ is the mean value of $\boldsymbol{X}$ and $\boldsymbol{C}$ is its covariance matrix.

More details about the probability distribution function and its moments are included in Appendix A.

2.2.1 Linear system

The evolution on time of a linear dynamical system with white Gaussian noise is governed by the stochastic differential equation [77, pp. 133–174]

$$\mathrm{d}\boldsymbol{x}(\tau) = \boldsymbol{F}(\tau)\boldsymbol{x}(t)\mathrm{d}\tau + \boldsymbol{G}(\tau)\mathrm{d}\boldsymbol{\beta}(\tau), \tag{2.3}$$

where $\boldsymbol{\beta}$ corresponds to a Brownian motion process of zero mean and diffusion $\boldsymbol{Q}(\tau)$. For practical applications, the following model is used instead [77, p. 163]

$$\mathrm{d}\boldsymbol{x}(\tau) = \boldsymbol{F}(\tau)\boldsymbol{x}(t)\mathrm{d}\tau + \boldsymbol{G}(\tau)\boldsymbol{\omega}(\tau)\mathrm{d}\tau. \tag{2.4}$$

where $\boldsymbol{G}(\tau)$ is a known matrix of piecewise continuous functions, and $\boldsymbol{Q}(\tau)$ becomes the strength of the Gaussian process $\boldsymbol{\omega}(\tau)$. Equation (2.3) can be easily solved using the state transition matrix $\boldsymbol{\Phi}$:

$$\boldsymbol{x}(\tau) = \boldsymbol{\Phi}\left(\tau, \tau_0\right)\boldsymbol{x}(\tau_0) + \int_{\tau_0}^{\tau} \boldsymbol{\Phi}\left(t, t_0\right)\boldsymbol{G}(t)\boldsymbol{w}(t)\mathrm{d}t. \tag{2.5}$$

The state transition matrix satisfies

$$\frac{\mathrm{d}\boldsymbol{\Phi}\left(\tau, \tau_0\right)}{\mathrm{d}\tau} = \boldsymbol{F}\left(\tau\right)\boldsymbol{\Phi}\left(\tau, \tau_0\right), \qquad \Phi\left(\tau_0, \tau_0\right) = \boldsymbol{I}, \tag{2.6}$$

and is a measure of the sensitivity to the initial conditions:

$$\boldsymbol{\Phi}\left(\tau, \tau_0\right) = \frac{\partial \boldsymbol{x}(\tau)}{\partial \boldsymbol{x}\left(\tau_0\right)}. \tag{2.7}$$

A very important property of linear systems is that Gaussianity is preserved [77, pp. 111-113], and the propagated distribution is uniquely determined by its mean and covariance:

$$\langle \boldsymbol{x} \rangle(\tau) = \boldsymbol{\Phi}\left(\tau, \tau_0\right)\langle \boldsymbol{x} \rangle(\tau_0), \tag{2.8}$$

$$\boldsymbol{C}(\tau) = \boldsymbol{\Phi}\left(\tau, \tau_0\right) \boldsymbol{C}_0 \boldsymbol{\Phi}^{\top}\left(\tau, \tau_0\right) + \int_{\tau_0}^{\tau} \boldsymbol{\Phi}\left(\tau, t\right) \boldsymbol{G}(t) \boldsymbol{Q}(t) \boldsymbol{G}^{\top}(t) \boldsymbol{\Phi}^{\top}\left(\tau, t\right) \mathrm{d}t. \tag{2.9}$$

That is, the solution of the dynamical linear system, including deterministic and stochastic effects, is obtained with little computational effort. The solution is further simplified when the system can be considered as deterministic, as the integral in Eq. (2.9) vanishes in that case.

2.2.2 Nonlinear system

When dealing with nonlinear systems, Gaussianity is no longer preserved in the general case. The evolution of a nonlinear system with white Gaussian noise can be described by the differential stochastic equation [78, pp. 192-202]

$$\mathrm{d}\boldsymbol{x} = \boldsymbol{f}(\boldsymbol{x}, \tau)\mathrm{d}\tau + \boldsymbol{G}(\boldsymbol{x}, \tau)\mathrm{d}\boldsymbol{\beta}(\tau). \tag{2.10}$$

As the pdf does not remain Gaussian, it is necessary to propagate it on time to know its evolution with time. To this end, we introduce the Forward Kolmogorov Equation, also called Fokker-Planck Equation:

$$\frac{\partial p(\boldsymbol{x}, \tau)}{\partial \tau} = -\sum_{i=1}^{N} \frac{\partial}{\partial x_i} \left\{ p(\boldsymbol{x}, \tau) f_i(\boldsymbol{x}, \tau) \right\} + \frac{1}{2} \sum_{i=1}^{N} \sum_{j=1}^{N} \frac{\partial^2 \boldsymbol{f}}{\partial x_i \partial x_j} \left\{ \boldsymbol{G}(\boldsymbol{x}, \tau) \boldsymbol{Q}(\tau) \boldsymbol{G}^{\top}(\boldsymbol{x}, \tau) \right\}_{ij}. \tag{2.11}$$

Unfortunately, solving the Forward Kolmogorov Equation is *hard*. First of all, it is a partial differential equation instead of an ordinary differential equation as usually encountered in astrodynamics. Second, it is defined on an infinite domain and must satisfy boundary conditions at infinity:

$$p(\boldsymbol{x} \to \pm\infty, t) \to 0. \tag{2.12}$$

Moreover, the pdf must satisfy the normalization constraint over the domain

$$\int \cdots \int p(\boldsymbol{x}, t)\mathrm{d}\boldsymbol{x} = 1. \tag{2.13}$$

Finally, it suffers the so-called *curse of dimensionality*. Augmenting the dimension of the state vector increases the difficulty of the problem exponentially and the problem quickly becomes intractable. To solve the Forward Kolmogorov Equation, many authors have proposed different methods as like GMM, PCE, DA, LOV or Kriging (see section 1.1).

2.3 Influence of the State Representation

Hereon, and unless otherwise specified, we assume that the dynamical model is purely deterministic, and that all the uncertainty lays in the state for simplicity. Then, Eq. (2.10) reduces to

$$\mathrm{d}\boldsymbol{x} = \boldsymbol{f}(\boldsymbol{x}, \tau)\mathrm{d}\tau, \tag{2.14}$$

and by expanding in Taylor series we obtain

$$\mathrm{d}\boldsymbol{x}(\tau) = \left(\boldsymbol{f}(\boldsymbol{0}, \tau) + \boldsymbol{F}(\tau)\boldsymbol{x}(t) + \mathcal{O}\left(\boldsymbol{x}^2\right)\right)\mathrm{d}\tau, \tag{2.15}$$

where the term $\boldsymbol{f}(\boldsymbol{0}, \tau)$ can be eliminated with an appropriate change of variables. To the first approximation, Eq. (2.15) is equivalent to the deterministic version of Eq. (2.3). However, if the nonlinear terms in the *differential equation* given by Eq. (2.14) have an important contribution, one must solve the Fokker-Planck equation (see Eq. (2.11)). The uncertainty in the variable $\boldsymbol{x}$ will significantly become *non-Gaussian* in general, and its propagation will be a *hard problem*.

Suppose a new state representation $\boldsymbol{y}$, related to $\boldsymbol{x}$ by a invertible nonlinear transformation of the state vector of the form

$$\boldsymbol{y} = \boldsymbol{y}\left(\boldsymbol{x}\right), \tag{2.16}$$

and whose evolution with time is given by

$$\mathrm{d}\boldsymbol{y} = \boldsymbol{g}(\boldsymbol{y}, \tau)\mathrm{d}\tau. \tag{2.17}$$

First, note that if the distribution in $\boldsymbol{x}$ is Gaussian and its main-axes standard deviations are small, the distribution in $\boldsymbol{y}$ will be reasonably Gaussian. Here *small* is determined from the transformation between the variables, as it must behave linearly across the characteristic length of the distribution. This is specially useful to transform the pdf at the initial epoch.

More importantly, if we can find a transformation $\boldsymbol{y}\left(\boldsymbol{x}\right)$ that has associated a time-derivative function $\boldsymbol{g}$ with greatly reduced or negligible nonlinear terms, the propagation of the uncertainty in the variable $\boldsymbol{y}$ will be easy, because Gaussianity will be preserved. That is, $\boldsymbol{y}$ will more closely follow a Gaussian distribution which can be linearly propagated. Once the Gaussian in the variable $\boldsymbol{y}$ has been obtained, one can use

the inverse of the nonlinear mapping given by Eq. (2.16) to recover the non-Gaussian distribution in the variable $\boldsymbol{x}$. This can be achieved using methods like sampling and estimation of moments, Taylor expansions or other techniques as shown in [109].

In this process, we have exchanged the nonlinearity of the problem from a complicated *differential equation* to an *algebraic equation*, greatly reducing the complexity of the propagation. In the cases where this is possible, we say that *the representation of the state (partially) absorbs the nonlinearities of the motion*.

The question that remains to be answered is what representation of the state is more advantageous for orbit determination applications. This question will be answered in the following section.

2.4 Numerical Comparison of Different State Representations

To determine which representations of the state vector behaves in a more linear fashion, a numerical study is performed in this section. For several states representations and different orbits, the linearization error is quantified. To measure it, we consider N random samples from the initial distribution and compare the linear propagation with the propagation using the equations of motion. The linear propagation is approximated using finite differences by scaling the initial uncertainty by a factor $\alpha \ll 1$:

$$\boldsymbol{x}_{i,\text{lin}}\left(\tau\right) = \frac{1}{\alpha}\boldsymbol{X}\left(\alpha\boldsymbol{x}_{i,0}, \tau\right), \tag{2.18}$$

where $\boldsymbol{X}$ is the result of integrating Eq. (2.14) from τ_0 to τ, and the coordinates of each sample $\boldsymbol{x}_i$ are defined with respect to the center of the distribution.

The dynamical model is considered as deterministic. We employ a 2×2 spherical harmonics model for the Earth, and include the gravitational perturbations of the Moon and the Sun.

In all cases, the initial uncertainty distribution is assumed to be Gaussian in Cartesian coordinates. The sampling is performed in the Cartesian state, and each sample is then transformed to the corresponding set of variables. The scaling performed for the linear propagation is performed directly on the set of elements whose linearity is being analyzed. To measure the linearization error, the root mean square error (RMS) of the

marginal distributions is employed

$$RMS(\tau) = \sqrt{\sum_{j}^{N} \frac{\left(x_j(\tau) - x_{j,\text{lin}}(\tau)\right)^2}{N}}. \tag{2.19}$$

2.4.1 Benchmark Set of Variables

In this section, we present different sets of variables we use to express the uncertainty of the orbital state. In all cases, the initial semi-major axis is chosen as unit of length, and the unit of time is defined so that the gravitational parameter of Earth becomes unity. This canonical system of units is adopted in order to facilitate the interpretation of the results for the different orbits that will be tested, as position, velocity, semi-major axis and mean motion become quantities of order unity, making possible a direct comparison.

2.4.1.1 Cartesian coordinates

Cartesian coordinates are the most natural choice of variables to study the motion of a celestial body because they have a direct interpretation. For conjunction assessment, it is also the most preferable form because distances are easily represented. However, the equations of orbital motion are highly nonlinear because of the $1/r^2$ term associated to the gravitational acceleration of the primary body.

2.4.1.2 Equinoctial elements

Equinoctial elements provide a representation of the orbital motion which is singular only for a purely retrograde orbit ($i = 180\,\text{deg}$) or for vanishing angular momentum ($h = 0$) (see [21] or [7, pp. 490–494]).

The first element is typically chosen the semi-major axis a. Two more elements, P_1 and P_2, are defined as the projections of the eccentricity vector $\boldsymbol{e}$ onto an intermediate frame

$$P_1 = e \sin(\Omega + \omega), \tag{2.20}$$

$$P_2 = e \cos(\Omega + \omega), \tag{2.21}$$

where Ω is the right ascension of the ascending node, and ω is the argument of periapsis.

By introducing two more elements Q_1 and Q_2, the orbital plane becomes completely defined

$$Q_1 = \sin\Omega \tan\frac{i}{2}, \tag{2.22}$$

$$Q_2 = \cos\Omega \tan\frac{i}{2}. \tag{2.23}$$

Finally, the sixth variable is the mean longitude l, which gives the angular position along the orbit:

$$l = \Omega + \omega + M, \tag{2.24}$$

where M is the mean anomaly. It evolves linearly with time τ (as $M = n\tau$ in the Keplerian case, being n the mean motion) and is expected to behave smoother than the true or eccentric anomalies. However, it requires solving Kepler's Equation to recover the Cartesian state.

2.4.1.3 Alternate Equinoctial elements

Horwood et al. proposed an alternate set of equinoctial elements [53], in which they replaced the semi-major axis a by the mean motion n. This is motivated because the evolution mean longitude in the unperturbed motion is given by $n\Delta\tau$, a linear function of the mean motion. Then, initial errors in the mean motion will result in a linear growth with time of the mean longitude, preserving Gaussianity.

The alternate equinoctial elements are then n, P_1, P_2, Q_1, Q_2 and l.

2.4.1.4 Dromo

Dromo is a special perturbation method developed by Peláez et al. at the Space Dynamics Group of the Technical University of Madrid [8, 89, 92, 103]. Section 4.2 contains detailed explanation about the Dromo formulation, including its seven elements $q_1, \ldots, q_7$ and a fictitious time σ that follows from a second order Sundman Transformation.

In addition, we consider a time element for the Dromo Formulation. A time element is, as defined by Stiefel et al. [99, p. 83], *"a quantity which during a pure Kepler motion is a linear function of the independent variable"*. Following Baù et al. [9], two time elements can be obtained for the Dromo formulation when considering the fictitious time as independent variable. Starting starting from Kepler's Equation, Baù et al. derived

a *"linear"* time element that is proportional to the fictitious time, and a *"constant"* time element in which the fictitious time does not appear explicitly. Here we employ the latter because it can be regarded as a orbital element since it remains constant for the Keplerian motion. The constant time element q_0 can be calculated as

$$q_0 = \tau_p - a^{3/2}\beta, \tag{2.25}$$

where τ_p is the time of periapsis passage, and β is the drift of the fictitious time defined in section 4.2. The constant time element q_0 is also a time element when employing the real time as independent variable.

Note that when introducing a time element, one must solve Kepler's Equation, and consequently particularize the formulation for elliptic, parabolic or hyperbolic motion.

2.4.1.5 EDromo

The classical Dromo formulation is derived following a second order Sundman transformation. By using a first order Sundman transformation, an analogous formulation called EDromo was obtained by Baù et. al [10]. In this way, a fictitious time ϕ is defined as the sum of the osculating *eccentric* anomaly plus an angular drift γ caused by the perturbations

$$\phi = E + \gamma. \tag{2.26}$$

The use of the eccentric anomaly in EDromo improves the performance of the numerical propagation for very high eccentric orbits. The seven Edromo elements are constructed as follows [10]

$$\lambda_1 = e\cos\gamma, \qquad \lambda_2 = e\sin\gamma, \qquad \lambda_3 = a, \tag{2.27}$$

$$\begin{aligned} \lambda_4 &= \sin\frac{i}{2}\cos\frac{\Omega-\omega+\gamma}{2}, \qquad \lambda_5 = \sin\frac{i}{2}\sin\frac{\Omega-\omega+\gamma}{2}, \\ \lambda_6 &= \cos\frac{i}{2}\sin\frac{\Omega+\omega-\gamma}{2}, \qquad \lambda_7 = \cos\frac{i}{2}\cos\frac{\Omega+\omega-\gamma}{2}. \end{aligned} \tag{2.28}$$

Finally, the fictitious time is introduced as the eight state variable of the EDromo state vector:

$$\lambda_8 = \phi. \tag{2.29}$$

2.4.2 Results

We study five different orbits in the comparison of state representations. In the first place, we consider a set of LEO orbits with different values of the eccentricity. The initial conditions and the initial standard deviations for the LEO orbits are listed in Table 2.1. Then, we select the orbit of the IBEX satellite, an American astronomy mission placed in a highly elliptical orbit which is strongly perturbed by Earth's spherical harmonics close to perigee, and by the Moon in apogee. Its initial conditions are shown in Table 2.2. The final orbit corresponds to the French-Italian canceled project Simbol-X, an X-ray telescope that was to be placed in a highly elliptical orbit. Table 2.3 shows the initial conditions for Simbol-X

In all cases, the comparison is performed for ten periods of the initial osculating orbit. For the scaling factor, we chose $\alpha = 10^{-3}$. The sampling is used employing the same random seed for all the variable sets. The sampling size was selected as 100 points, since no significant difference was appreciated when selecting 500 samples.

The results are shown in Figs. 2.1, 2.2 and 2.3 for the LEO orbits with increasing eccentricity, Fig. 2.4 for IBEX and Fig. 2.5 for Simbol-X. In these figures, the Cartesian RMS is shown in the upper left subfigure. The results for equinoctial and alternate equinoctial elements are shown under the previous one. On the right and in descending order, the results for Dromo, Dromo with Constant Time Element (CTE) and EDromo are presented. A comparison between the anomalies of the different sets of orbital elements is shown in Figs. 2.6, 2.7, 2.8 2.9 and 2.10.

For all the orbits, the Cartesian state shows a high RMS in all components. For orbits of larger eccentricity, the RMS increases near perigee and decreases near apogee, but the value is larger than the rest set of variables in any case.

Next, for the equinoctial, Dromo and EDromo formulations, the anomaly has a RMS several orders of magnitude larger than the rest variables. The along-track angular variable is related to the mean anomaly in equinoctial elements, to the eccentric anomaly in EDromo and to the true anomaly in Dromo. This follows from a zeroth-order, first order and second order Sundman transformation, respectively. In general, the mean anomaly presents a smoother behavior, the true anomaly presents oscillations with peaks of RMS higher than the mean anomaly and valleys under it. The eccentric anomaly is an intermediate case; it also presents oscillations but their amplitude is smaller. Note that while the value of the anomaly of equinoctial elements presents a more regular value of the

RMS, it requires solving Kepler's equation, with the increased computational burden it carries. The quaternion components of Dromo and EDromo show RMS values constant with time and large in some of the situations. This is probably caused by numerical problems of the approximation to the linearized solution, but neither increasing the number of samples nor changing the value of the scaling factor α modifies the result.

For every considered orbit, two formulations stand out, as the RMS remains small for longer periods of time: Dromo with a Constant Time Element and alternative equinoctial elements. The anomaly of both formulation is a time variable that has the peculiarity of being a linear function of the other state variables, preserving Gaussianity of the pdf of the Keplerian motion. These two sets of variables have advantages and drawbacks. On one hand, Dromo employs a state vector with dimension 8 instead of 6, the minimum required to completely characterize the orbital motion. This introduces constraints that cause rank deficiency in the covariance and observation matrices (Sections 4.1 and 6.3.2), and may complicate solving Fokker-Planck Equation or applying higher order methods based on sampling like PCE. On the other hand, the use of alternate equinoctial elements further complicates obtaining the gradient matrices that govern the evolution of the state transition matrix [60, 61, 62, 63, 64].

However, one must remember that time elements come associated with Kepler's equation. On top of the increased computational cost, one must particularize the employed formulation according to the value of the eccentricity. Thus, to obtain a formulation applicable to all values of eccentricity and with reduced computational burden, in Part III we will employ the Dromo formulation. This especially interesting for application of Near Earth Asteroids and Space Debris with small eccentricity, as it will be proven that the linearization error becomes small in those cases.

Table 2.1: Initial conditions for the LEO orbits.

Component	Value
Epoch	2012 Jul 04 23:58:53
a [km]	8500
e [-]	$\{0.01,\ 0.1,\ 0.2\}$
i [deg]	80
Ω [deg]	30
ω [deg]	-20
ν [deg]	0
Position standard deviation [km]	0.1
Velocity standard deviation [km/s]	10^{-6}

Table 2.2: Initial conditions for IBEX.

Component	Value
Epoch	2012 Jul 04 23:58:53
a [km]	185039.850185
e [-]	0.69258199579
i [deg]	30.7632425335
Ω [deg]	320.362493377
ω [deg]	183.325596694
ν [deg]	297.113056627
Position standard deviation [km]	0.1
Velocity standard deviation [km/s]	10^{-6}

Table 2.3: Initial conditions for Simbol-X.

Component	Value
Epoch	2018 Dec 22 17:49:12
a [km]	106247.136454
e [-]	0.75173
i [deg]	5.2789
Ω [deg]	49.351
ω [deg]	180.008
ν [deg]	0
Position standard deviation [km]	0.1
Velocity standard deviation [km/s]	10^{-6}

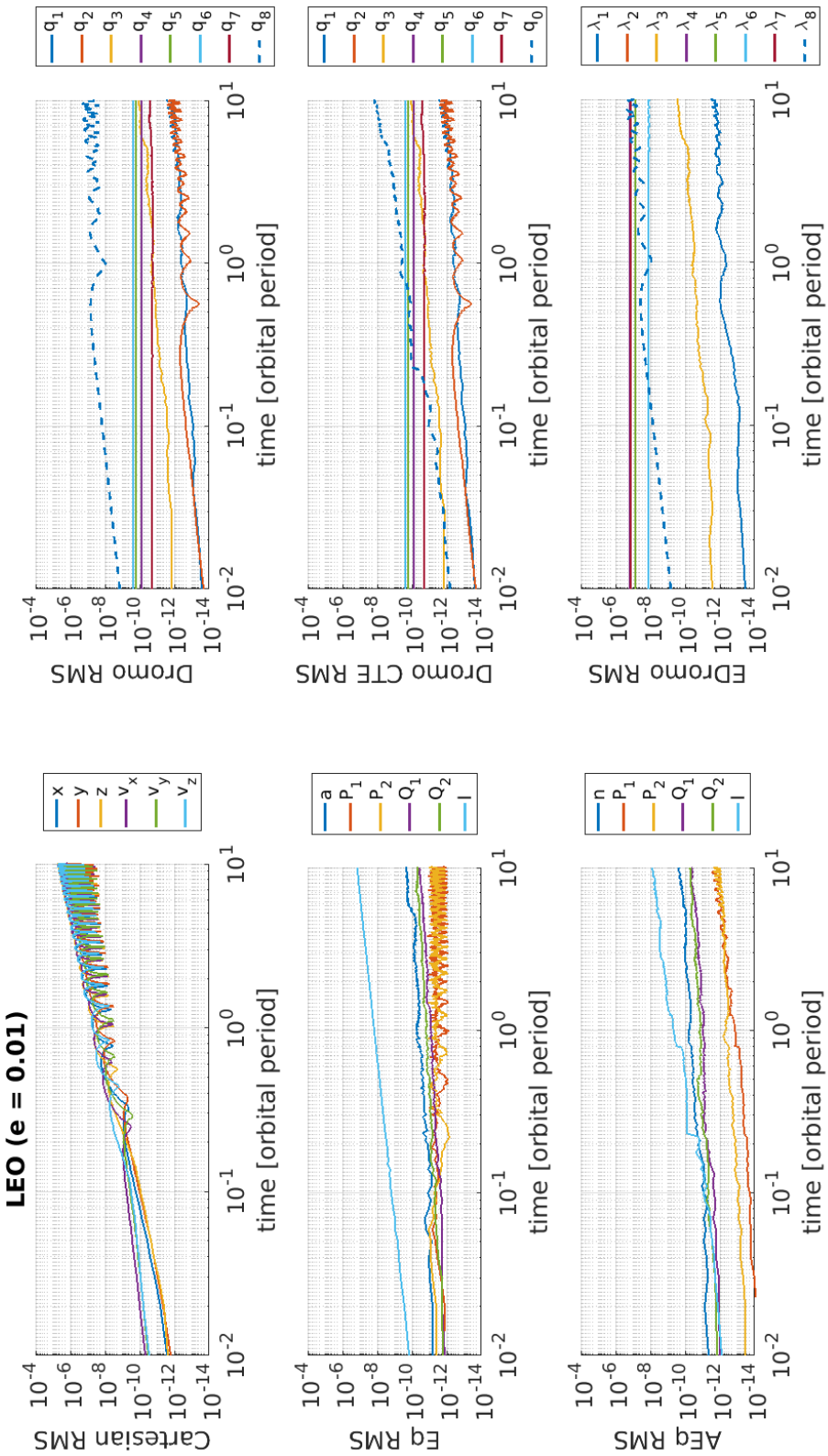

Figure 2.1: Root Mean Square error for the LEO ($e = 0.01$) orbit.

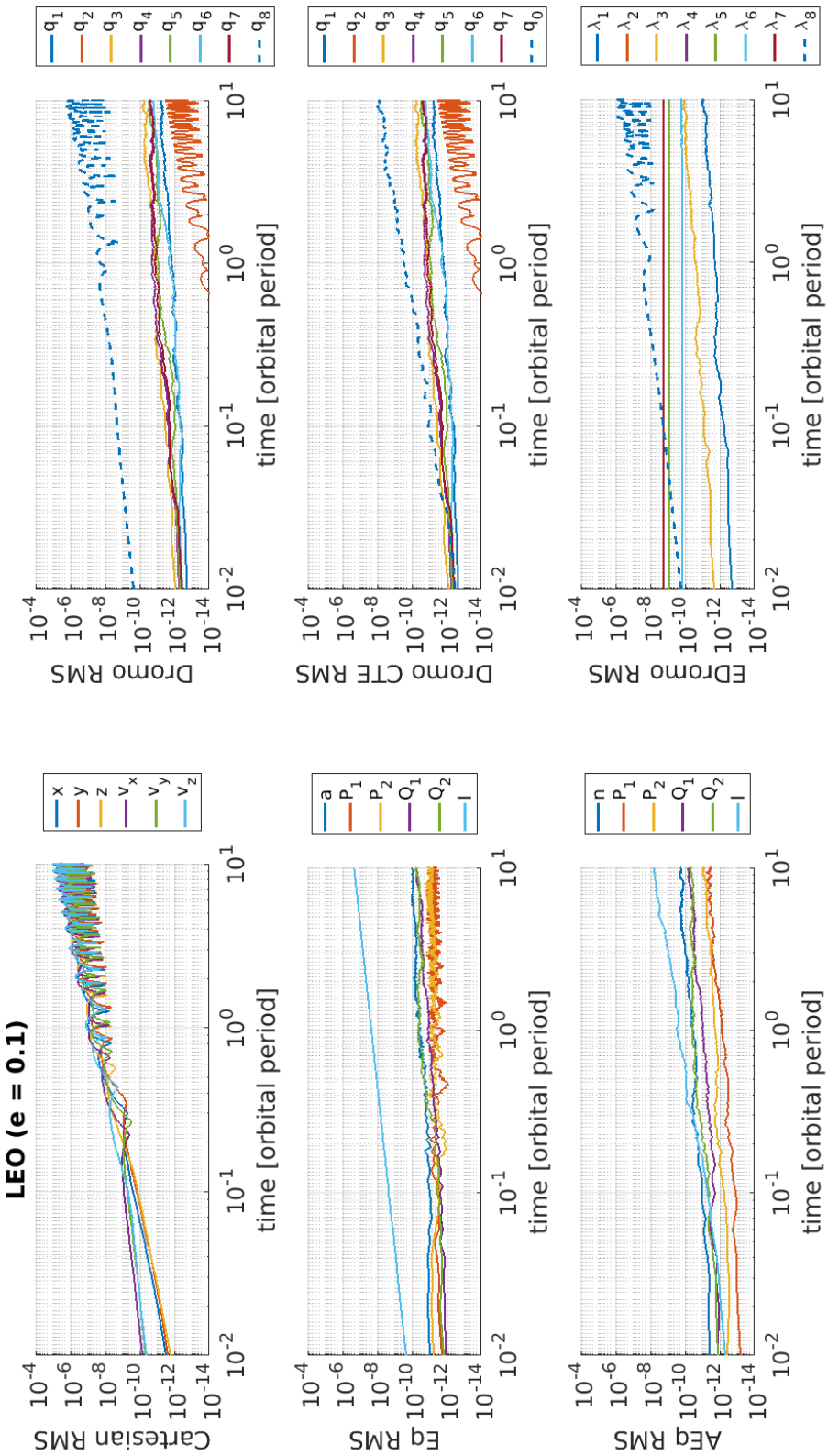

Figure 2.2: Root Mean Square error for the LEO ($e = 0.1$) orbit.

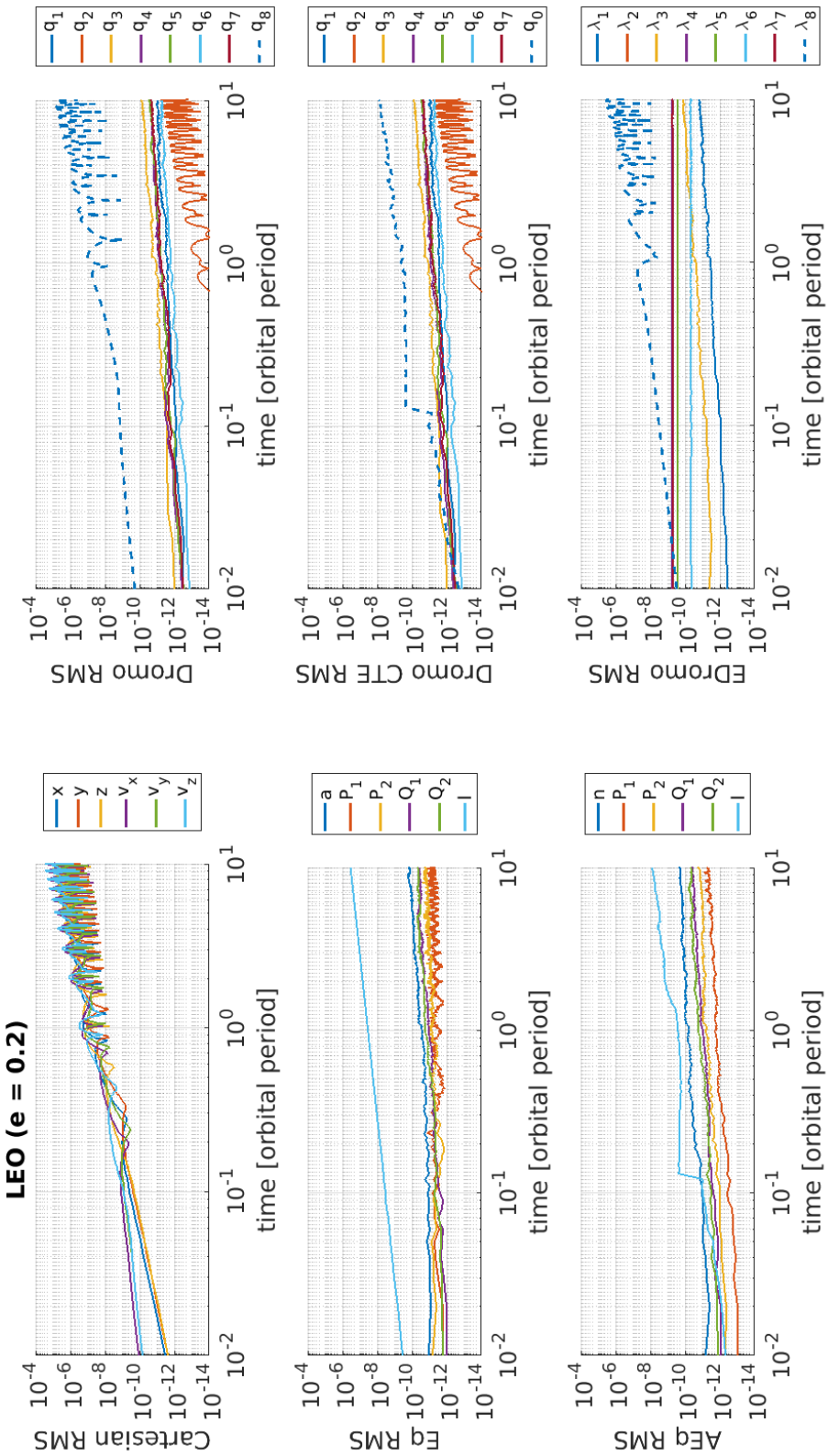

Figure 2.3: Root Mean Square error for the LEO ($e = 0.2$) orbit.

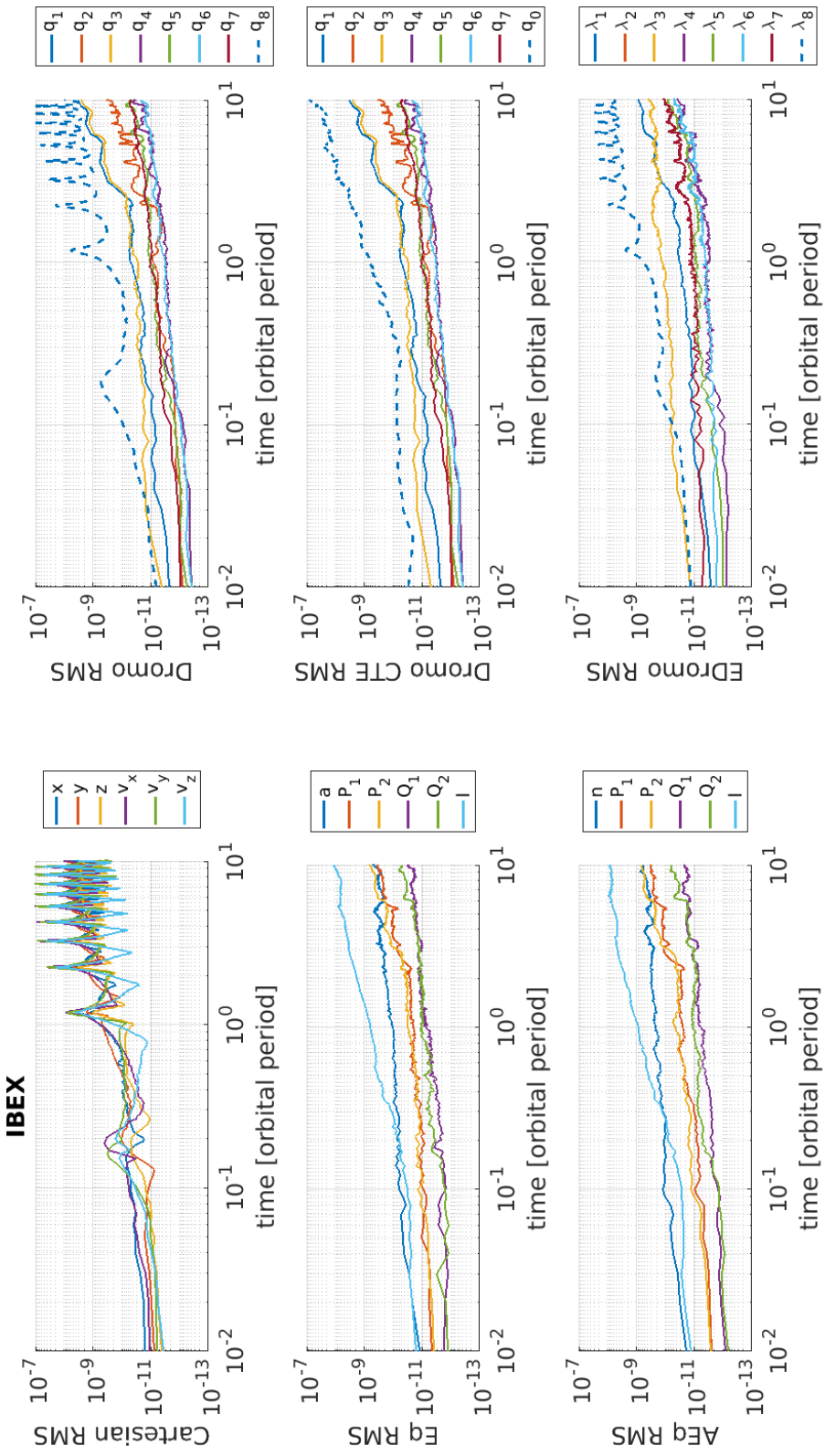

Figure 2.4: Root Mean Square error for IBEX orbit.

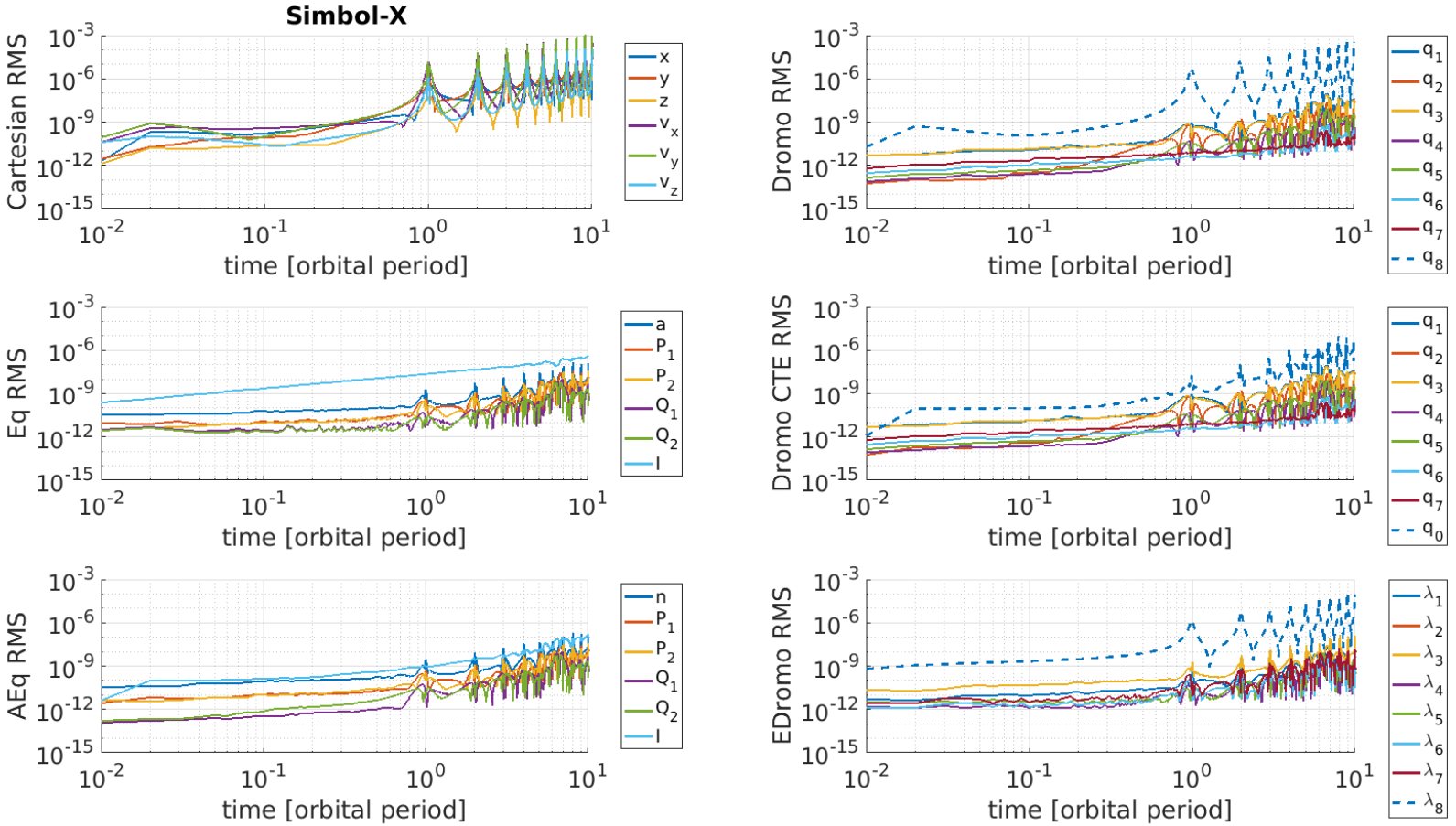

Figure 2.5: Root Mean Square error for Simbol-X orbit.

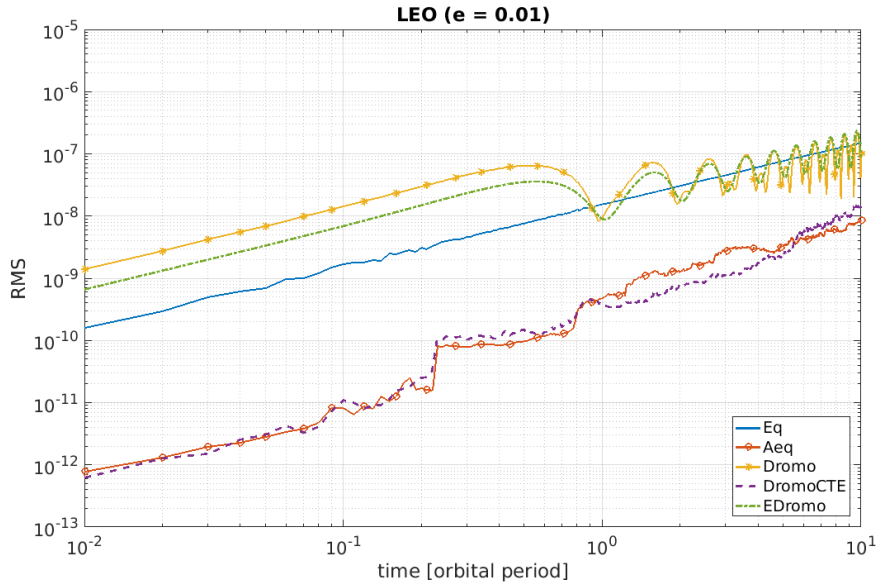

Figure 2.6: Comparison of RMS of the angular variables for the LEO ($e = 0.01$) orbit.

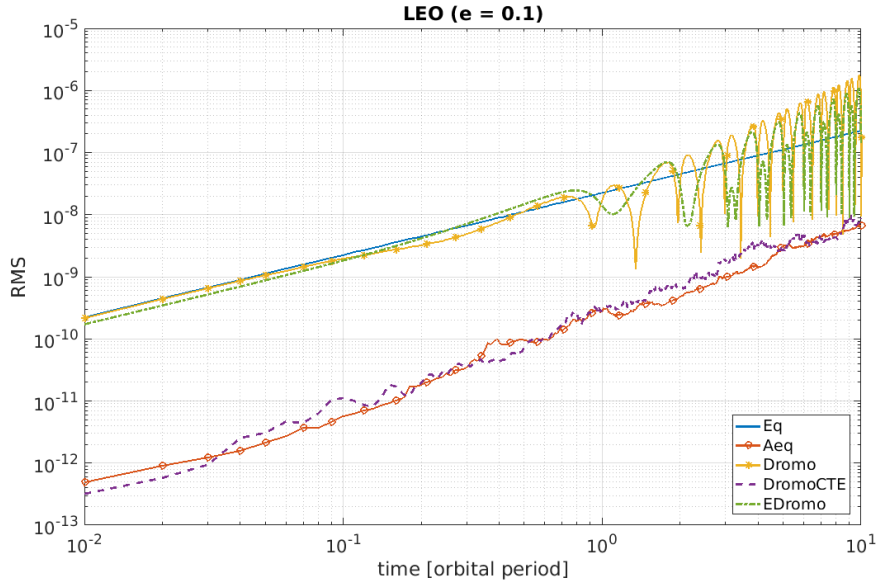

Figure 2.7: Comparison of RMS of the angular variables for the LEO ($e = 0.1$) orbit.

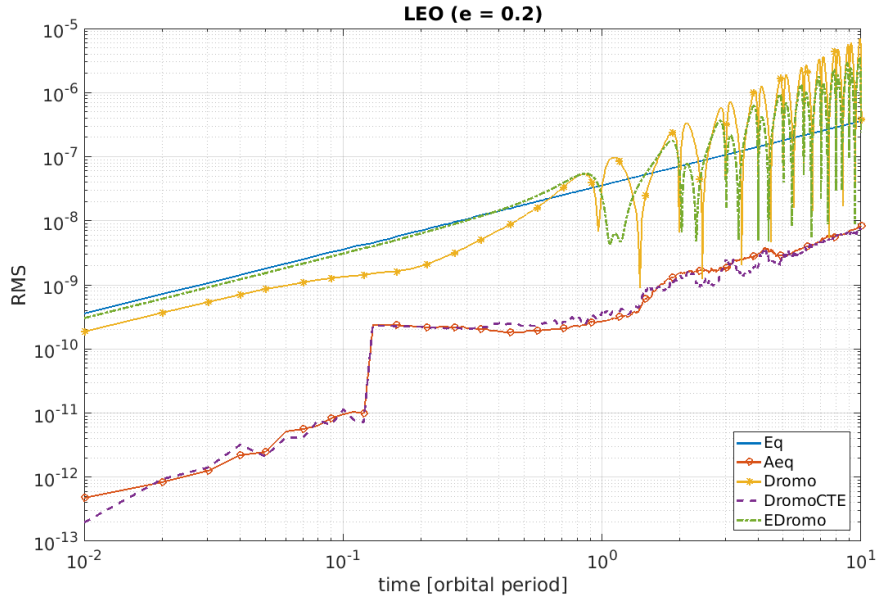

Figure 2.8: Comparison of RMS of the angular variables for the LEO ($e = 0.2$) orbit.

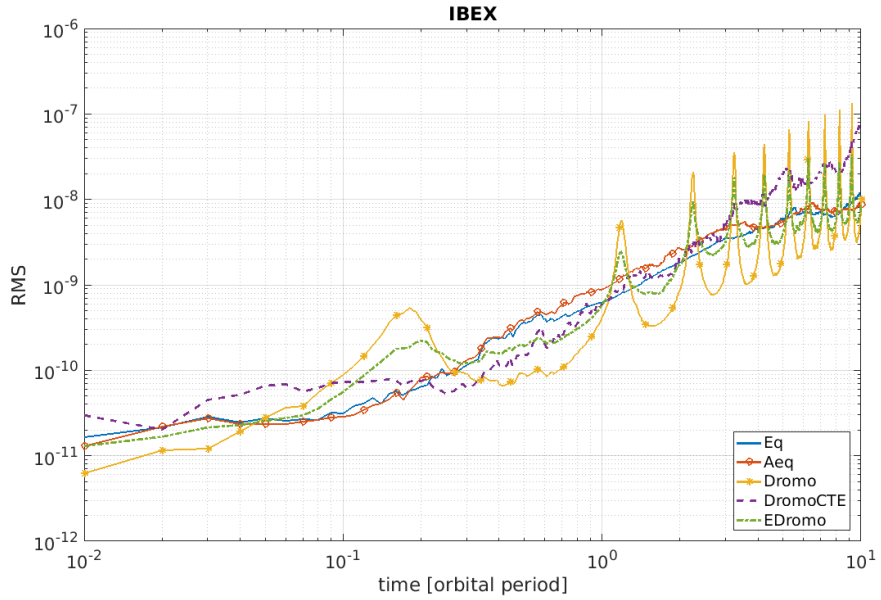

Figure 2.9: Comparison of RMS of the angular variables for IBEX.

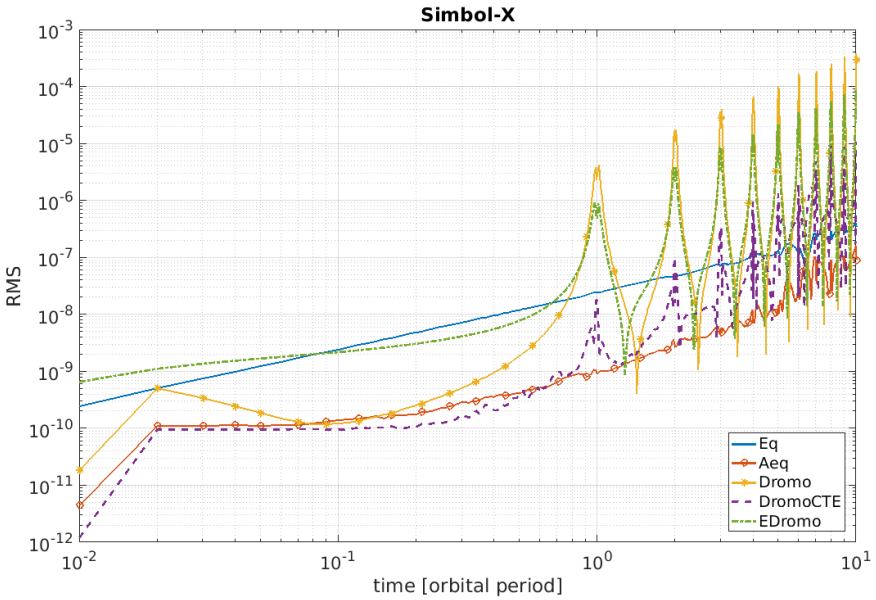

Figure 2.10: Comparison of RMS of the angular variables for Simbol-X.

2.5 Conclusions

In this chapter, the foundations of the probability distribution function of the orbital state and its linear and nonlinear propagation were laid. We revisited the known fact that Gaussian distributions are easily propagated using linear theory, while nonlinear propagation results in general in a non-Gaussian distribution whose pdf in the future is hard to calculate.

It was also pointed out that the nonlinearity of the physical processes that govern the propagation of the uncertainty can be partially absorbed by a convenient choice of the state. That is, the nonlinearity in the equations of motion may be transformed into a more linear form of the equations of motion and a nonlinear algebraic equation, being this algebraic equation easier to handle mathematically.

Additionally, a numerical comparison of different state representations for the orbital motion was performed. The benchmark variables were Cartesian coordinates, equinoctial elements and a variation of it, and three alternate forms of the Dromo formulation. Results confirm the well known fact that Cartesian coordinates are highly nonlinear. Formulations with the most linear behavior are those that employ a time element as state variable in substitution of the orbital anomaly, as long as this anomaly is a linear function of the other state variables. Eccentric and true anomaly show larger errors, but employing them allows one to avoid Kepler's equation and its associated increased computational time of the calculations.

Part II

Curvilinear Coordinates

This page intentionally left blank.

Chapter 3

Curvilinear Coordinates

3.1 Introduction

As stated in the introduction, the use of *curvilinear* coordinates and orbital elements is known to be advantageous with respect to an approach based on Cartesian coordinates [59], as the along-track error is effectively projected onto the orbit, instead of being tangent to it. Here, *curvilinear* means that the coordinate lines of the coordinate system may be curved. The simplest examples of curvilinear coordinates are polar coordinates in $\mathbb{R}^2$ and cylindrical and spherical coordinates in $\mathbb{R}^3$.

However, in spite of their limitations Cartesian coordinates have been widely used for uncertainty propagation. In fact, one of the most elementary techniques is to employ the Clohessy-Wiltshire (C-W) linear solution. In [79], Melton improved the C-W solution considering reference elliptical orbits using a series expansion on the eccentricity. Melton also proposed using an angular variable to increase accuracy. However, in his method the relation between the angular variable and the Cartesian coordinates was linearized; thus variations of the angular variable are no longer contained inside the orbit. More recently, Lee at al. [72] presented a semi-analytical method (it requires solving Kepler's Equation) for propagating the covariance matrix expressed in Cartesian coordinates, which is based on the Yamanaka-Ankersen state transition matrix [111] and consequently valid for elliptical orbits. Again, the method does not allow one to project the along-track error along the curved orbital path.

The use of curvilinear coordinates is especially interesting for propagating the orbit uncertainty because variations in the angular variable lead to a time delay, preserving

the orbit shape. This fact allows one to accurately propagate uncertainties over a much larger time span when compared to Cartesian methods. Alfriend et al. [1] and Geller et al. [37] presented the equations of motion using cylindrical coordinates in linear and full form, respectively. Bombardelli et al. [17] presented the solution for the Keplerian relative motion expressed in curvilinear coordinates. In their work, they provided the exact solution as an infinite convergent series, a linear solution which can be regarded as an improved version of the C-W solution and a single-frequency quadratic solution among others. Other authors have employed spherical coordinates (see [69] for example) or elliptical curvilinear coordinates ([27, 52] among others).

In this chapter, the results of [17] are revisited in sections 3.2 and 3.3, and then extended to a double-frequency quadratic solution in section 3.4. A linearization technique around such solution is then applied to obtain a new analytical state transition matrix, valid for orbits with small eccentricity ($e < 0.1$ approximately). However, this limitation does not hinder the applicability of the method, as 54.5% of the trackable orbits around Earth describe near-circular orbits ($e \leqslant 0.01$), and another 32.0% of the objects have a moderate eccentricity ($0.01 < e \leqslant 0.1$) [66, p. 17]. The STM is then employed as a straightforward mean to propagate the state uncertainty along the orbit. The domain of validity of the proposed method is investigated by comparing the analytically propagated uncertainty with numerical results obtained using a Monte Carlo method and accounting for all relevant environmental perturbations. Test cases in LEO and GEO are considered.

3.2 Curvilinear coordinates

The relative motion of a Follower object (F) with respect to a Chief (C) spacecraft which moves in a circular orbit can be conveniently described using curvilinear coordinates. This motivated the works of [1], [37] and [17] among others. In the following we employ a similar approach to [17], and reproduce the key equations for completeness.

We will employ the Chief orbital radius and the inverse of the mean motion as unit of length and time respectively. Let $\mathcal{I}\ \langle \boldsymbol{i}, \boldsymbol{j}, \boldsymbol{k} \rangle$ be the Earth-centered reference frame where we set $\boldsymbol{k}$ perpendicular to the Chief orbital plane and $\boldsymbol{i}$ pointing to the Chief at the initial epoch $\tau = 0$. A non-inertial reference system $\mathcal{C}\ \langle \boldsymbol{i}', \boldsymbol{j}', \boldsymbol{k}' \rangle$ is defined as the Chief Local Vertical Local Horizontal reference frame. The axes of this Chief-centered

system are oriented such that $\boldsymbol{k}'$ is parallel to $\boldsymbol{k}$ and $\boldsymbol{j}'$ is parallel to the Chief orbital velocity vector. The reference systems $\mathcal{I}$ and $\mathcal{C}$ are shown in Fig. 3.1.

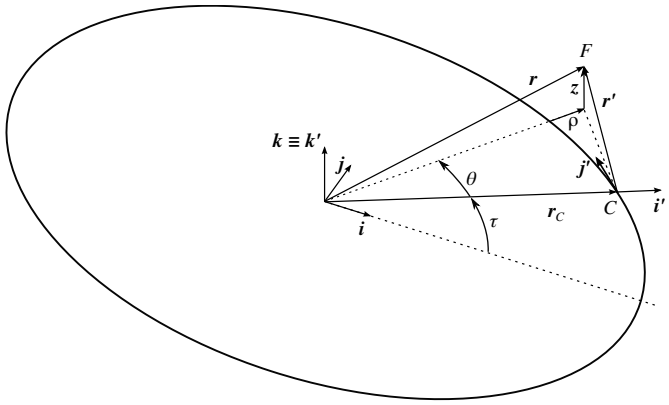

Figure 3.1: Relative motion geometry and curvilinear coordinates.

The relative position and velocity between the Follower and the Chaser can be written in $\mathcal{C}$ as

$$\boldsymbol{r}' = x\boldsymbol{i}' + y\boldsymbol{j}' + z\boldsymbol{k}', \tag{3.1}$$

$$\boldsymbol{v}' = \dot{x}\boldsymbol{i}' + \dot{y}\boldsymbol{j}' + \dot{z}\boldsymbol{k}'. \tag{3.2}$$

After introducing the curvilinear coordinates of the follower, ρ and $\theta \in (-\pi, \pi]$

$$\rho = -1 + \sqrt{(x+1)^2 + y^2}, \tag{3.3}$$

$$\theta = \operatorname{atan2}(y, 1+x), \tag{3.4}$$

the relative position and velocity components can be expressed as a function of the curvilinear coordinates and its time-derivatives as

$$x = -1 + (1+\rho)\cos\theta, \tag{3.5}$$

$$y = (1+\rho)\sin\theta, \tag{3.6}$$

$$\dot{x} = \dot{\rho}\cos\theta - \dot{\theta}(1+\rho)\sin\theta, \tag{3.7}$$

$$\dot{y} = \dot{\rho}\sin\theta + \dot{\theta}(1+\rho)\cos\theta. \tag{3.8}$$

We note that the presented curvilinear coordinates can also describe the absolute position of the Follower in cylindrical coordinates $(1+\rho, \theta+\tau, z)$.

We introduce for later use the curvilinear state vector

$$\boldsymbol{c} = \left(\rho, \theta, z, \dot{\rho}, \dot{\theta}, \dot{z}\right)^{\top}. \tag{3.9}$$

Finally, orbital elements of the Follower in the rotating frame can be constructed from the curvilinear state vector (see Appendix B for details).

3.2.1 Equations of Motion in Curvilinear Coordinates

The absolute position, velocity and acceleration of the Follower in the non-inertial reference system $\mathcal{C}$ can be written as

$$\boldsymbol{r} = \boldsymbol{r}_C + \boldsymbol{r}', \tag{3.10}$$

$$\boldsymbol{v} = \boldsymbol{v}_C + \boldsymbol{v}' + \boldsymbol{\omega}_C \times \boldsymbol{r}', \tag{3.11}$$

$$\boldsymbol{a} = \boldsymbol{\omega}_{\mathcal{C}} \times \left(\boldsymbol{\omega}_{\mathcal{C}} \times \boldsymbol{r}'\right) + 2\boldsymbol{\omega}_{\mathcal{C}} \times \boldsymbol{v}' + \boldsymbol{a}_C + \boldsymbol{a}' = -\frac{\boldsymbol{r}}{r^3}, \tag{3.12}$$

where $\boldsymbol{r}_C$, $\boldsymbol{v}_C$ and $\boldsymbol{a_C}$ are the known position, velocity and acceleration vectors of the Chief, $\boldsymbol{\omega}_{\mathcal{C}}$ is the angular velocity vector of the reference system $\mathcal{C}$, and $\boldsymbol{v}'$ and $\boldsymbol{a}'$ are the time-derivatives of Eq. (3.1) and Eq. (3.2) respectively. Note that in the right hand side of Eq. (3.12), the gravitational parameter becomes unity in the system of units defined above and therefore is omitted. After some manipulations of the equations we obtain:

$$\ddot{\rho} - 2\dot{\theta} - 3\rho = a_{i\rho} + a_{g\rho} \tag{3.13a}$$

$$\ddot{\theta} + 2\dot{\rho} = a_{i\theta} \tag{3.13b}$$

$$\ddot{z} + z = a_{gz} \tag{3.13c}$$

where the non-linear terms, which do not depend on θ, can be divided into inertial accelerations ($a_{i\rho}$ and $a_{i\theta}$) and gravitational accelerations ($a_{g\rho}$ and a_{gz}). The non-linear accelerations obey:

$$a_{i\rho} = \dot{\theta}^2\left(1+\rho\right) + 2\dot{\theta}\rho, \tag{3.14a}$$

$$a_{g\rho} = -2\rho + 1 - \frac{1+\rho}{\left[\left(1+\rho\right)^2 + z^2\right]^{3/2}}, \tag{3.14b}$$

$$a_{i\theta} = \frac{2\dot{\rho}\left(\rho - \dot{\theta}\right)}{1+\rho}, \tag{3.14c}$$

$$a_{gz} = z - \frac{z}{\left[\left(1+\rho\right)^2 + z^2\right]^{3/2}}. \tag{3.14d}$$

3.3 Curvilinear Clohessy-Wiltshire

The homogeneous solution to the system of differential equations of Eq. (3.13) corresponds to the case in which the non-linear accelerations are negligible. Analyzing the non-linear accelerations reveals that this will happen when

$$\left(|\rho_0|, |z_0|, |\dot{\rho}_0|, |\dot{\theta}_0|, |\dot{z}_0|\right) \ll 1.$$

Eq. (3.13) reduces then to:

$$\ddot{\rho} - 2\dot{\theta} - 3\rho = 0 \tag{3.15a}$$

$$\ddot{\theta} + 2\dot{\rho} = 0 \tag{3.15b}$$

$$\ddot{z} + z = 0 \tag{3.15c}$$

The homogeneous equations have the same structure of the Cartesian Clohessy-Wiltshire (C-W) equations after replacing the Cartesian y coordinate with θ. However, Eqs. (3.15) have a larger domain of validity compared to the Cartesian C-W due to the fact that θ, unlike y, does not play any role in the non-linear terms (see Eq. (3.14)) and need not to be small for the preceding linearization to be valid. The homogeneous solution with initial conditions $\boldsymbol{c}_0$ at epoch $\tau = 0$ reads:

$$\boldsymbol{c} = \boldsymbol{\Phi}_{CW}\boldsymbol{c}_0 \tag{3.16}$$

with

$$\boldsymbol{\Phi}_{CW} = \begin{bmatrix} 4-3\cos\tau & 0 & 0 & \sin\tau & 2(1-\cos\tau) & 0 \\ 6(-\tau+\sin\tau) & 1 & 0 & 2(-1+\cos\tau) & -3\tau+4\sin\tau & 0 \\ 0 & 0 & \cos\tau & 0 & 0 & \sin\tau \\ 3\sin\tau & 0 & 0 & \cos\tau & 2\sin\tau & 0 \\ 6(-1+\cos\tau) & 0 & 0 & -2\sin\tau & -3+4\cos\tau & 0 \\ 0 & 0 & -\sin\tau & 0 & 0 & \cos\tau \end{bmatrix} \tag{3.17}$$

3.4 Quadratic solution

In [17], Bombardelli et al. presented a single-frequency, quadratic solution to the relative motion using curvilinear coordinates. Bombardelli et al. neglected the double-frequency terms, but a careful inspection of the general solution reveals that the double-frequency terms are also of quadratic order. In this section, we prove this fact and complete the quadratic solution with the double-frequency correction.

First, we report the exact solution in curvilinear coordinates as a function of the orbital elements of the follower (normalized semi-major axis a, eccentricity e, inclination i, right ascension of the ascending node Ω, argument of periapsis ω, and true anomaly ν):

$$\rho = -1 + \frac{a(1-e^2)}{1+e\cos\nu}\sqrt{1-\sin^2 i\ \sin^2(\omega+\nu)}\,, \tag{3.18a}$$

$$\theta = -\tau + \Omega + \operatorname{atan2}\Big(\cos i\ \sin(\omega+\nu),\ \cos(\omega+\nu)\Big), \tag{3.18b}$$

$$z = \frac{a(1-e^2)}{1+e\cos\nu}\sin i\ \sin(\omega+\nu). \tag{3.18c}$$

In this equation, ν is related to the eccentric anomaly E by

$$\cos\nu = \frac{\cos E - e}{1-e\cos E}, \tag{3.19a}$$

$$\sin\nu = \frac{\sqrt{1-e^2}\sin E}{1-e\cos E}, \tag{3.19b}$$

which in turn is related to the normalized time τ by Kepler's Equation:

$$M = M_0 + n\tau = E - e\sin E, \tag{3.20}$$

where M is the mean anomaly and n is the normalized mean motion. Even if a close-form solution to the relative motion is available, Eq. (3.18a) requires solving Kepler's equation for each epoch so it cannot be considered completely analytical. However, it is possible to expand $\cos\nu$ and $\sin\nu$ in series as a function of the eccentricity using J_j, the Bessel function of the first kind and order j. Following [7, p. 210], Eq. (3.19) can be expanded as

$$\cos\nu = -e + \frac{2\left(1-e^2\right)}{e}\sum_{j=1}^{\infty} J_j(je)\cos jM, \tag{3.21a}$$

$$\sin\nu = 2\sqrt{1-e^2}\sum_{j=1}^{\infty}\frac{1}{j}\frac{\mathrm{d}J_j(je)}{\mathrm{d}e}\sin jM. \tag{3.21b}$$

Equation (3.21a) can be substituted into Eq. (3.18a) after applying the angle sum trigonometric identities. We can express a, e, i, Ω, ω, M_0 and n in Eqs. (3.18a–3.21a) as a function of the initial curvilinear coordinates $\boldsymbol{c}_0$ (see Appendix B).

The obtained equations provide the exact solution to the relative motion as a function of $\boldsymbol{c}_0$ and τ, but involve convoluted expressions and infinite summations. With

the help of a symbolic manipulator, we expand them in series of the initial curvilinear coordinates. After neglecting terms of order $\mathcal{O}(\boldsymbol{c}_0^3)$ and higher, the double-frequency quadratic solution is obtained as

$$\rho(\tau) \simeq \rho_{\text{const}} + \rho_{C\tau}\cos n\tau + \rho_{S\tau}\sin n\tau + \rho_{C2\tau}\cos 2n\tau + \rho_{S2\tau}\sin 2n\tau, \tag{3.22a}$$

$$\theta(\tau) \simeq \theta_{\text{const}} + \theta_{C\tau}\cos n\tau + \theta_{S\tau}\sin n\tau + \theta_{C2\tau}\cos 2n\tau + \theta_{S2\tau}\sin 2n\tau + \theta_{\text{sec}}\tau, \tag{3.22b}$$

$$z(\tau) \simeq z_{\text{const}} + z_{C\tau}\cos n\tau + z_{S\tau}\sin n\tau + z_{C2\tau}\cos 2n\tau + z_{S2\tau}\sin 2n\tau. \tag{3.22c}$$

where the coefficients and the normalized mean motion n are quadratic functions of $\boldsymbol{c}_0$. The triple-frequency terms were found to be at least of cubic order and thus are not included.

The normalized mean motion can be approximated by a quadratic function as

$$n \simeq 1 - 6\rho_0 - 3\dot{\theta}_0 - \frac{3}{2}\left(z_0^2 + \dot{z}_0^2 + \dot{\rho}_0^2 - 5\rho_0^2\right). \tag{3.23}$$

The coefficients for ρ in Eq. (3.22a) are given by

$$\rho_{\text{const}} = 4\rho_0 + 2\dot{\theta}_0 + \frac{39}{2}\rho_0^2 + 26\rho_0\dot{\theta}_0 + \frac{3}{4}z_0^2 + \frac{3}{2}\dot{\rho}_0^2 + 7\dot{\theta}_0^2 + \frac{3}{4}\dot{z}_0^2, \tag{3.24a}$$

$$\rho_{C\tau} = -3\rho_0 - 2\dot{\theta}_0 - 15\rho_0^2 - 20\rho_0\dot{\theta}_0 - \frac{1}{2}z_0^2 - 2\dot{\rho}_0^2 - 5\dot{\theta}_0^2 - \dot{z}_0^2, \tag{3.24b}$$

$$\rho_{S\tau} = \dot{\rho}_0 - \dot{\rho}_0\dot{\theta}_0 + z_0\dot{z}_0, \tag{3.24c}$$

$$\rho_{C2\tau} = -\frac{9}{2}\rho_0^2 - 6\rho_0\dot{\theta}_0 - \frac{1}{4}z_0^2 + \frac{1}{2}\dot{\rho}_0^2 - 2\dot{\theta}_0^2 + \frac{1}{4}\dot{z}_0^2, \tag{3.24d}$$

$$\rho_{S2\tau} = 3\rho_0\dot{\rho}_0 - \frac{1}{2}z_0\dot{z}_0 + 2\dot{\theta}_0\dot{\rho}_0. \tag{3.24e}$$

For the angular variable, the corresponding expressions are:

$$\theta_{\text{const}} = \theta_0 - 2\dot{\rho}_0 + \frac{1}{2}\dot{\rho}_0\rho_0 + \dot{\rho}_0\dot{\theta}_0 - 2z_0\dot{z}_0, \tag{3.25a}$$

$$\theta_{\text{sec}} = (n-1), \tag{3.25b}$$

$$\theta_{C\tau} = 2\dot{\rho}_0 - 8\dot{\theta}_0\dot{\rho}_0 - 6\dot{\rho}_0\dot{\theta}_0 + 2z_0\dot{z}_0, \tag{3.25c}$$

$$\theta_{S\tau} = 4\dot{\theta}_0 + 6\rho_0 + 6\rho_0^2 + 12\rho_0\dot{\theta}_0 + 4\dot{\rho}_0^2 + 2\dot{\theta}_0^2 + 2\dot{z}_0^2 + z_0^2, \tag{3.25d}$$

$$\theta_{C2\tau} = \frac{15}{2}\rho_0\dot{\rho}_0 - \frac{1}{2}z_0\dot{z}_0 + 5\dot{\theta}_0\dot{\rho}_0, \tag{3.25e}$$

$$\theta_{S2\tau} = \frac{45}{4}\rho_0^2 + 15\rho_0\dot{\theta}_0 + \frac{1}{4}z_0^2 - \frac{5}{4}\dot{\rho}_0^2 + 5\dot{\theta}_0^2 - \frac{1}{4}\dot{z}_0^2. \tag{3.25f}$$

The coefficients of the quadratic formula for the out-of-plane motion read:

$$z_{\text{const}} = \frac{3}{2}\dot{\rho}_0\dot{z}_0 - 3z_0\dot{\theta}_0 - \frac{9}{2}\rho_0 z_0, \tag{3.26a}$$

$$z_{C\tau} = z_0 + 3\rho_0 z_0 - 2\dot{\rho}_0\dot{z}_0 + 2\dot{\theta}_0 z_0, \tag{3.26b}$$

$$z_{S\tau} = \dot{z}_0 + 3\rho_0\dot{z}_0 + \dot{\rho}_0 z_0 + \dot{\theta}_0\dot{z}_0, \tag{3.26c}$$

$$z_{C2\tau} = \frac{3}{2}\rho_0 z_0 + z_0\dot{\theta}_0 + \frac{1}{2}\dot{\rho}_0\dot{z}_0, \tag{3.26d}$$

$$z_{S2\tau} = \frac{3}{2}\dot{z}_0\rho_0 - \frac{1}{2}z_0\dot{\rho}_0 + \dot{\theta}_0\dot{z}_0. \tag{3.26e}$$

The following expressions provide the time-derivative of the curvilinear coordinates

$$\dot{\rho}(\tau) \simeq n\left(\rho_{S\tau}\cos n\tau - \rho_{C\tau}\sin n\tau\right) + 2n\left(\rho_{S2\tau}\cos 2n\tau - \rho_{C2\tau}\sin 2n\tau\right), \tag{3.27a}$$

$$\dot{\theta}(\tau) \simeq n\left(\theta_{S\tau}\cos n\tau - \theta_{C\tau}\sin n\tau\right) + 2n\left(\theta_{S2\tau}\cos 2n\tau - \theta_{C2\tau}\sin 2n\tau\right) + \theta_{\text{sec}}, \tag{3.27b}$$

$$\dot{z}(\tau) \simeq n\left(z_{S\tau}\cos n\tau - z_{C\tau}\sin n\tau\right) + 2n\left(z_{S2\tau}\cos n2\tau - z_{C2\tau}\sin 2n\tau\right). \tag{3.27c}$$

3.5 Linearization around the quadratic solution (QuadLin)

Let $\boldsymbol{c}_{\text{nom}}$ be the nominal orbit with initial conditions $\boldsymbol{c}_0 = \left(\rho_0, \theta_0, z_0, \dot{\rho}_0, \dot{\theta}_0, \dot{z}_0\right)^\top$. The nominal orbit can be calculated using the quadratic solution $\boldsymbol{q}$:

$$\boldsymbol{c}_{\text{nom}} = \boldsymbol{q}\left(\boldsymbol{c}_0\right). \tag{3.28}$$

Another orbit $\boldsymbol{c}$ very close to the previous one will have as initial conditions

$$\boldsymbol{c}_0 + \delta\boldsymbol{c}_0 = \left(\rho_0 + \delta\rho_0, \theta_0 + \delta\theta_0, z_0 + \delta z_0, \dot{\rho}_0 + \delta\dot{\rho}_0, \dot{\theta}_0 + \delta\dot{\theta}_0, \dot{z}_0 + \delta\dot{z}_0\right)^\top, \tag{3.29}$$

and the quadratic formula will yield

$$\boldsymbol{c} = \boldsymbol{q}\left(\boldsymbol{c}_0 + \delta\boldsymbol{c}_0\right). \tag{3.30}$$

It is possible to expand $\boldsymbol{q}$ in Taylor series around $\boldsymbol{c}_0$. The zeroth-order term is simply $\boldsymbol{c}_{\text{nom}}$, which corresponds to the evolution of the nominal orbit and can be calculated with a more accurate method if necessary. If the difference between the orbits is very small, the linear terms will provide a sufficiently accurate approximation

$$\boldsymbol{c} = \boldsymbol{c}_{\text{nom}} + \left.\frac{\partial\boldsymbol{q}}{\partial\boldsymbol{c}_0}\right|_{\boldsymbol{c}_0}\delta\boldsymbol{c}_0 + \ldots, \tag{3.31a}$$

$$\delta\boldsymbol{c} = \boldsymbol{c} - \boldsymbol{c}_{\text{nom}} \simeq \boldsymbol{\Phi}(\tau, \tau_0)\delta\boldsymbol{c}_0. \tag{3.31b}$$

The matrix $\left.\frac{\partial \boldsymbol{q}}{\partial \boldsymbol{c}_0}\right|_{\boldsymbol{c}_0}$ constitutes a state transition matrix (STM) $\boldsymbol{\Phi}(\tau, \tau_0)$ for the Keplerian relative motion. $\boldsymbol{\Phi}(\tau, \tau_0)$ corresponds to an approximate solution, since it was developed from the truncated quadratic solution, and as a consequence it deviates from the real solution by cubic and higher order terms.

The first row of $\boldsymbol{\Phi}(\tau, \tau_0)$ reads

$$\begin{aligned}\left.\frac{\partial \rho}{\partial \boldsymbol{c}_0}\right|_{\boldsymbol{c}_0} &= \begin{bmatrix}\Phi_{\rho\rho}, & \Phi_{\rho\theta}, & \Phi_{\rho z}, & \Phi_{\rho\dot{\rho}}, & \Phi_{\rho\dot{\theta}}, & \Phi_{\rho\dot{z}}\end{bmatrix} = \\ &= \left\{ \frac{\partial \rho_{\text{const}}}{\partial \boldsymbol{c}_0} + \left(\frac{\partial \rho_{C\tau}}{\partial \boldsymbol{c}_0} + \rho_{S\tau}\frac{\partial n}{\partial \boldsymbol{c}_0}\tau\right)\cos(n\tau) + \left(\frac{\partial \rho_{S\tau}}{\partial \boldsymbol{c}_0} - \rho_{C\tau}\frac{\partial n}{\partial \boldsymbol{c}_0}\tau\right)\sin(n\tau) + \right. \\ &\quad \left. \left(\frac{\partial \rho_{C2\tau}}{\partial \boldsymbol{c}_0} + 2\rho_{S2\tau}\frac{\partial n}{\partial \boldsymbol{c}_0}\tau\right)\cos(2n\tau) + \left(\frac{\partial \rho_{S2\tau}}{\partial \boldsymbol{c}_0} - 2\rho_{C2\tau}\frac{\partial n}{\partial \boldsymbol{c}_0}\tau\right)\sin(2n\tau) \right\}_{\boldsymbol{c}_0}\end{aligned} \tag{3.32}$$

where the partial derivatives are given by the row vectors

$$\left.\frac{\partial \rho_{\text{const}}}{\partial \boldsymbol{c}_0}\right|_{\boldsymbol{c}_0} = \begin{bmatrix} 4+39\rho_0+26\dot{\theta}_0 \;,\; 0, & \frac{3}{2}z_0 \;, & 3\dot{\rho}_0 \;, & 2+26\rho_0+14\dot{\theta}_0 \;, & \frac{3}{2}\dot{z}_0 \end{bmatrix} \tag{3.33a}$$

$$\left.\frac{\partial \rho_{C\tau}}{\partial \boldsymbol{c}_0}\right|_{\boldsymbol{c}_0} = \begin{bmatrix} -3-30\rho_0-20\dot{\theta}_0,\; 0, & -z_0 \;, & -4\dot{\rho}_0 \;, & -2-29\rho_0-10\dot{\theta}_0, & -\dot{z}_0 \end{bmatrix} \tag{3.33b}$$

$$\left.\frac{\partial \rho_{C2\tau}}{\partial \boldsymbol{c}_0}\right|_{\boldsymbol{c}_0} = \begin{bmatrix} -9\rho_0-6\dot{\theta}_0 \;,\; 0,\; -\frac{1}{2}z_0, & \dot{\rho}_0 \;, & -6\rho_0-4\dot{\theta}_0 \;, & \frac{1}{2}\dot{z}_0 \end{bmatrix} \tag{3.33c}$$

$$\left.\frac{\partial \rho_{S\tau}}{\partial \boldsymbol{c}_0}\right|_{\boldsymbol{c}_0} = \begin{bmatrix} 0 \;,\; 0, & \dot{z}_0 \;, & 1-\dot{\theta}_0 \;, & \dot{\rho}_0 \;, & z_0 \end{bmatrix} \tag{3.33d}$$

$$\left.\frac{\partial \rho_{S2\tau}}{\partial \boldsymbol{c}_0}\right|_{\boldsymbol{c}_0} = \begin{bmatrix} 3\dot{\theta}_0 \;,\; 0,\; -\frac{1}{2}\dot{z}_0, & 3\rho_0+2\dot{\theta}_0, & 2\dot{\rho}_0 \;, & -\frac{1}{2}z_0 \end{bmatrix} \tag{3.33e}$$

and

$$\left.\frac{\partial n}{\partial \boldsymbol{c}_0}\right|_{\boldsymbol{c}_0} = \begin{bmatrix} -6+15\rho_0,\; 0,\; -3z_0,\; -3\dot{\rho}_0,\; -3\dot{\theta}_0,\; -3\dot{z}_0 \end{bmatrix} \tag{3.34}$$

The row corresponding to the angular variable θ can be calculated as

$$\begin{aligned}\left.\frac{\partial\theta}{\partial\boldsymbol{c}_0}\right|_{\boldsymbol{c}_0} &= \left[\Phi_{\theta\rho},\quad \Phi_{\theta\theta},\quad \Phi_{\theta z},\quad \Phi_{\theta\dot{\rho}},\quad \Phi_{\theta\dot{\theta}},\quad \Phi_{\theta\dot{z}}\right] = \\ &= \left\{ \frac{\partial\theta_{\text{const}}}{\partial\boldsymbol{c}_0} + \frac{\partial n}{\partial\boldsymbol{c}_0}\tau + \right. \\ &\quad \left(\frac{\partial\theta_{C\tau}}{\partial\boldsymbol{c}_0} + \theta_{S\tau}\frac{\partial n}{\partial\boldsymbol{c}_0}\tau\right)\cos(n\tau) + \left(\frac{\partial\theta_{S\tau}}{\partial\boldsymbol{c}_0} - \theta_{C\tau}\frac{\partial n}{\partial\boldsymbol{c}_0}\tau\right)\sin(n\tau) + \\ &\quad \left.\left(\frac{\partial\theta_{C2\tau}}{\partial\boldsymbol{c}_0} + 2\theta_{S2\tau}\frac{\partial n}{\partial\boldsymbol{c}_0}\tau\right)\cos(2n\tau) + \left(\frac{\partial\theta_{S2\tau}}{\partial\boldsymbol{c}_0} - 2\theta_{C2\tau}\frac{\partial n}{\partial\boldsymbol{c}_0}\tau\right)\sin(2n\tau)\right\}_{\boldsymbol{c}_0}\end{aligned} \tag{3.35}$$

together with

$$\left.\frac{\partial\theta_{\text{const}}}{\partial\boldsymbol{c}_0}\right|_{\boldsymbol{c}_0} = \left[\begin{array}{ccccc} \frac{1}{2}\dot{\rho}_0 & ,\ 1, & -\frac{3}{2}\dot{z}_0, & \frac{1}{2}\rho_0 + \dot{\theta}_0 - 2\,, & \dot{\rho}_0 \quad , \quad -\frac{3}{2}z_0 \end{array}\right] \tag{3.36a}$$

$$\left.\frac{\partial\theta_{C\tau}}{\partial\boldsymbol{c}_0}\right|_{\boldsymbol{c}_0} = \left[\begin{array}{ccccc} -8\dot{\rho}_0 & ,\ 0, & 2\dot{z}_0\ , & 2 - 8\rho_0 - 6\dot{\rho}_0, & -6\dot{\rho}_0 \quad , \quad 2z_0 \end{array}\right] \tag{3.36b}$$

$$\left.\frac{\partial\theta_{C2\tau}}{\partial\boldsymbol{c}_0}\right|_{\boldsymbol{c}_0} = \left[\begin{array}{ccccc} \frac{15}{2}\dot{\rho}_0 & ,\ 0, & -\frac{1}{2}\dot{z}_0, & \frac{15}{2}\rho_0 + 5\dot{\theta}_0\ , & 5\dot{\rho}_0 \quad , \quad -\frac{1}{2}z_0 \end{array}\right] \tag{3.36c}$$

$$\left.\frac{\partial\theta_{S\tau}}{\partial\boldsymbol{c}_0}\right|_{\boldsymbol{c}_0} = \left[\begin{array}{ccccc} 8\rho_0 + 12\dot{\theta}_0 + 6\,, & 0, & 2z_0\ , & 8\dot{\rho}_0 \quad , & 12\rho_0 + 4\dot{\theta}_0 + 4, \quad 4\dot{z}_0 \end{array}\right] \tag{3.36d}$$

$$\left.\frac{\partial\theta_{S2\tau}}{\partial\boldsymbol{c}_0}\right|_{\boldsymbol{c}_0} = \left[\begin{array}{ccccc} \frac{45}{2}\rho_0 + 12\dot{\theta}_0 + 6, & 0, & 2z_0\ , & 8\dot{\rho}_0 \quad , & 12\rho_0 + 4\dot{\theta}_0 + 4, \quad 4\dot{z}_0 \end{array}\right] \tag{3.36e}$$

The out-of-plane row of the STM is governed by

$$\begin{aligned}\left.\frac{\partial z}{\partial\boldsymbol{c}_0}\right|_{\boldsymbol{c}_0} &= \left[\Phi_{z\rho},\quad \Phi_{z\theta},\quad \Phi_{zz},\quad \Phi_{z\dot{\rho}},\quad \Phi_{z\dot{\theta}},\quad \Phi_{z\dot{z}}\right] = \\ &= \left\{ \frac{\partial z_{\text{const}}}{\partial\boldsymbol{c}_0} + \left(\frac{\partial z_{C\tau}}{\partial\boldsymbol{c}_0} + z_{S\tau}\frac{\partial n}{\partial\boldsymbol{c}_0}\tau\right)\cos(n\tau) + \left(\frac{\partial z_{S\tau}}{\partial\boldsymbol{c}_0} - z_{C\tau}\frac{\partial n}{\partial\boldsymbol{c}_0}\tau\right)\sin(n\tau)\right. \\ &\quad \left. + \left(\frac{\partial z_{C2\tau}}{\partial\boldsymbol{c}_0} + 2z_{S2\tau}\frac{\partial n}{\partial\boldsymbol{c}_0}\tau\right)\cos(2n\tau) + \left(\frac{\partial z_{S2\tau}}{\partial\boldsymbol{c}_0} - 2z_{C2\tau}\frac{\partial n}{\partial\boldsymbol{c}_0}\tau\right)\sin(2n\tau)\right\}_{\boldsymbol{c}_0}\end{aligned} \tag{3.37}$$

where we set

$$\left.\frac{\partial z_{\text{const}}}{\partial \boldsymbol{c}_0}\right|_{\boldsymbol{c}_0} = \left[\begin{array}{cccccc} -\frac{9}{2}z_0, & 0, & -\frac{9}{2}\rho_0 - 3\dot{\theta}_0\ , & \frac{3}{2}\dot{z}_0\ , & -3z_0, & \frac{3}{2}\dot{\rho}_0 \end{array}\right] \tag{3.38a}$$

$$\left.\frac{\partial z_{C\tau}}{\partial \boldsymbol{c}_0}\right|_{\boldsymbol{c}_0} = \left[\begin{array}{cccccc} 3z_0\ , & 0, & 1 + 3\rho_0 + 2\dot{\theta}_0, & -2\dot{z}_0, & 2z_0\ , & -2\dot{\rho}_0 \end{array}\right] \tag{3.38b}$$

$$\left.\frac{\partial z_{C2\tau}}{\partial \boldsymbol{c}_0}\right|_{\boldsymbol{c}_0} = \left[\begin{array}{cccccc} \frac{3}{2}z_0\ , & 0, & \frac{3}{2}\rho_0 + \dot{\theta}_0\ , & \frac{1}{2}\dot{z}_0\ , & z_0\ , & \frac{1}{2}\dot{\rho}_0 \end{array}\right] \tag{3.38c}$$

$$\left.\frac{\partial z_{S\tau}}{\partial \boldsymbol{c}_0}\right|_{\boldsymbol{c}_0} = \left[\begin{array}{cccccc} 3\dot{z}_0\ , & 0, & \dot{\rho}_0\ , & z_0\ , & \dot{z}_0\ , & 1 + 3\rho_0 + \dot{\theta}_0 \end{array}\right] \tag{3.38d}$$

$$\left.\frac{\partial z_{S2\tau}}{\partial \boldsymbol{c}_0}\right|_{\boldsymbol{c}_0} = \left[\begin{array}{cccccc} \frac{3}{2}\dot{z}_0\ , & 0, & -\frac{1}{2}\dot{\rho}_0\ , & -\frac{1}{2}z_0, & \dot{z}_0\ , & \frac{3}{2}\rho_0 + \dot{\theta}_0 \end{array}\right] \tag{3.38e}$$

Finally, the last three rows of $\boldsymbol{\Phi}(\tau, \tau_0)$ can be obtained as the τ–derivative of the first three rows

$$\begin{aligned} \left.\frac{\partial \dot{\rho}}{\partial \boldsymbol{c}_0}\right|_{\boldsymbol{c}_0} =& \frac{\mathrm{d}}{\mathrm{d}\tau}\left(\left.\frac{\partial \rho}{\partial \boldsymbol{c}_0}\right|_{\boldsymbol{c}_0}\right) = \left[\Phi_{\dot{\rho}\rho},\quad \Phi_{\dot{\rho}\theta},\quad \Phi_{\dot{\rho}z},\quad \Phi_{\dot{\rho}\dot{\rho}},\quad \Phi_{\dot{\rho}\dot{\theta}},\quad \Phi_{\dot{\rho}\dot{z}}\right] = \\ =& \left\{ \begin{array}{l} n\left(\frac{\partial \rho_{S\tau}}{\partial \boldsymbol{c}_0} - \rho_{C\tau}\frac{\partial n}{\partial \boldsymbol{c}_0}\tau\right)\cos(n\tau) - \rho_{C\tau}\frac{\partial n}{\partial \boldsymbol{c}_0}\sin(n\tau) \\ \quad - n\left(\frac{\partial \rho_{C\tau}}{\partial \boldsymbol{c}_0} + \rho_{S\tau}\frac{\partial n}{\partial \boldsymbol{c}_0}\tau\right)\sin(n\tau) + \rho_{S\tau}\frac{\partial n}{\partial \boldsymbol{c}_0}\cos(n\tau) \\ \quad + 2n\left(\frac{\partial \rho_{S2\tau}}{\partial \boldsymbol{c}_0} - 2\rho_{C2\tau}\frac{\partial n}{\partial \boldsymbol{c}_0}\tau\right)\cos(2n\tau) - 2\rho_{C2\tau}\frac{\partial n}{\partial \boldsymbol{c}_0}\sin(2n\tau) \\ \quad - 2n\left(\frac{\partial \rho_{C2\tau}}{\partial \boldsymbol{c}_0} + 2\rho_{2S\tau}\frac{\partial n}{\partial \boldsymbol{c}_0}\tau\right)\sin(2n\tau) + 2\rho_{S\tau}\frac{\partial n}{\partial \boldsymbol{c}_0}\cos(2n\tau) \end{array} \right\}_{\boldsymbol{c}_0} \end{aligned} \tag{3.39}$$

$$\begin{aligned}\left.\frac{\partial\dot{\theta}}{\partial\boldsymbol{c}_0}\right|_{\boldsymbol{c}_0} =& \frac{\mathrm{d}}{\mathrm{d}\tau}\left(\left.\frac{\partial\theta}{\partial\boldsymbol{c}_0}\right|_{\boldsymbol{c}_0}\right) = \left[\Phi_{\dot{\theta}\rho},\quad \Phi_{\dot{\theta}\theta},\quad \Phi_{\dot{\theta}z},\quad \Phi_{\dot{\theta}\dot{\rho}},\quad \Phi_{\dot{\theta}\dot{\theta}},\quad \Phi_{\dot{\theta}\dot{z}}\right] = \\ =& \left\{ \frac{\partial n}{\partial\boldsymbol{c}_0} + n\left(\frac{\partial\theta_{S\tau}}{\partial\boldsymbol{c}_0} - \theta_{C\tau}\frac{\partial n}{\partial\boldsymbol{c}_0}\tau\right)\cos(n\tau) - \theta_{C_\tau}\frac{\partial n}{\partial\boldsymbol{c}_0}\sin(n\tau)\right. \\ & - n\left(\frac{\partial\theta_{C\tau}}{\partial\boldsymbol{c}_0} + \theta_{S\tau}\frac{\partial n}{\partial\boldsymbol{c}_0}\tau\right)\sin(n\tau) + \theta_{S\tau}\frac{\partial n}{\partial\boldsymbol{c}_0}\cos(n\tau) \\ & + 2n\left(\frac{\partial\theta_{S2\tau}}{\partial\boldsymbol{c}_0} - 2\theta_{C2\tau}\frac{\partial n}{\partial\boldsymbol{c}_0}\tau\right)\cos(2n\tau) - 2\theta_{C2\tau}\frac{\partial n}{\partial\boldsymbol{c}_0}\sin(2n\tau) \\ & \left. - 2n\left(\frac{\partial\theta_{C2\tau}}{\partial\boldsymbol{c}_0} + 2\theta_{S2\tau}\frac{\partial n}{\partial\boldsymbol{c}_0}\tau\right)\sin(2n\tau) + 2\theta_{S\tau}\frac{\partial n}{\partial\boldsymbol{c}_0}\cos(2n\tau)\right\}_{\boldsymbol{c}_0}\end{aligned} \tag{3.40}$$

$$\begin{aligned}\left.\frac{\partial\dot{z}}{\partial\boldsymbol{c}_0}\right|_{\boldsymbol{c}_0} =& \frac{\mathrm{d}}{\mathrm{d}\tau}\left(\left.\frac{\partial z}{\partial\boldsymbol{c}_0}\right|_{\boldsymbol{c}_0}\right) = \left[\Phi_{\dot{z}\rho},\quad \Phi_{\dot{z}\theta},\quad \Phi_{\dot{z}z},\quad \Phi_{\dot{z}\dot{\rho}},\quad \Phi_{\dot{z}\dot{\theta}},\quad \Phi_{\dot{z}\dot{z}}\right] \\ =& \left\{ n\left(\frac{\partial z_{S\tau}}{\partial\boldsymbol{c}_0} - z_{C\tau}\frac{\partial n}{\partial\boldsymbol{c}_0}\tau\right)\cos(n\tau) - z_{C\tau}\frac{\partial n}{\partial\boldsymbol{c}_0}\sin(n\tau)\right. \\ & - n\left(\frac{\partial z_{C\tau}}{\partial\boldsymbol{c}_0} + z_{S\tau}\frac{\partial n}{\partial\boldsymbol{c}_0}\tau\right)\sin(n\tau) + z_{S\tau}\frac{\partial n}{\partial\boldsymbol{c}_0}\cos(n\tau) \\ & + 2n\left(\frac{\partial z_{S2\tau}}{\partial\boldsymbol{c}_0} - 2z_{C2\tau}\frac{\partial n}{\partial\boldsymbol{c}_0}\tau\right)\cos(2n\tau) - 2z_{C2\tau}\frac{\partial n}{\partial\boldsymbol{c}_0}\sin(2n\tau) \\ & \left. - 2n\left(\frac{\partial z_{C2\tau}}{\partial\boldsymbol{c}_0} + 2z_{2S\tau}\frac{\partial n}{\partial\boldsymbol{c}_0}\tau\right)\sin(2n\tau) + 2z_{S\tau}\frac{\partial n}{\partial\boldsymbol{c}_0}\cos(2n\tau)\right\}_{\boldsymbol{c}_0}\end{aligned} \tag{3.41}$$

Finally, the covariance matrix expressed in curvilinear coordinates can be propagated on time as

$$\boldsymbol{C}(\tau) = \boldsymbol{\Phi}(\tau,\tau_0)\,\boldsymbol{C}_0\,\boldsymbol{\Phi}^\top(\tau,\tau_0)\,. \tag{3.42}$$

3.6 Results

In this section, we first apply the proposed STM to the uncertainty propagation problem of a piece of space debris orbiting in the GEO region with respect to an active satellite. We propagate the covariance matrix of the relative state using the curvilinear C-W and the QuadLin STM's. To assess whether the Gaussian distributions associated to these

matrices are representative of the dynamics of the problem, we compare them to high-fidelity numerical simulations considering Luni-Solar, J_2 and $C_{2,2}$ perturbations. To this end, the initial uncertainty distribution is sampled and propagated via direct integration of the equations of motion. The covariance matrix is then estimated at every epoch from the samples. The evolution of the samples is also compared to the result of applying the STM's to the relative initial states. Additionally, a comparison with the work of Melton [79] is included. The equations employed for Melton's Method are provided in Appendix C for completeness.

An example in LEO using a fictitious reference orbit is also presented following the same procedure as in the GEO example.

3.6.1 Application to the GEO region

An active GEO satellite whose orbit is known with arbitrary accuracy is considered as the Chief. The unit of length is set as its orbital radius, approximately equal to $42164\,\text{km}$. The unit of time is equal to $86400/(2\pi)\,\text{s}$, which is approximately $13751\,\text{s}$. In these units, Earth's gravitational parameter becomes unity and the GEO orbital period is simply 2π. The ratio of the unit of distance to the unit of length is equal to the velocity of a satellite in GEO orbit, around $3.066\,\text{km/s}$.

The motion of a nearby piece of space debris or a non-maneuverable, non-cooperative object is studied using the linearization method presented in the previous section. The initial relative state is fixed by imposing $\rho_0 = -0.0003$, $\dot{\rho}_0 = 0.001$, $\theta_0 = 10.55\,\text{deg}$, $e = 0.01$ and $i = 0\,\text{deg}$. Fig. 3.2 shows the nominal relative motion between both bodies in the $\mathcal{C}$ reference frame. The relative orbit is propagated for $8\,\text{days}$. The nominal orbits do not intersect, but the orbit uncertainty could lead to a collision.

The relative position and velocity uncertainty at the initial epoch are assumed to follow independent isotropic Gaussian distributions expressed in Cartesian coordinates, with $\sigma_{\text{pos}} = 10^{-4}$ and $\sigma_{\text{vel}} = 10^{-5}$. In non-normalized units, these values correspond to $4.2\,\text{km}$ and $3\,\text{cm/s}$ approximately. As the uncertainty is small, an initial Gaussian distribution in curvilinear coordinates can be generated from the initial distribution in Cartesian coordinates using a linear mapping based on the Jacobian of Eqs. (3.3, 3.4) and its time-derivatives. Here we exploit the fact that linear transformations preserve Gaussianity, and because the uncertainty distribution is small, higher order terms can

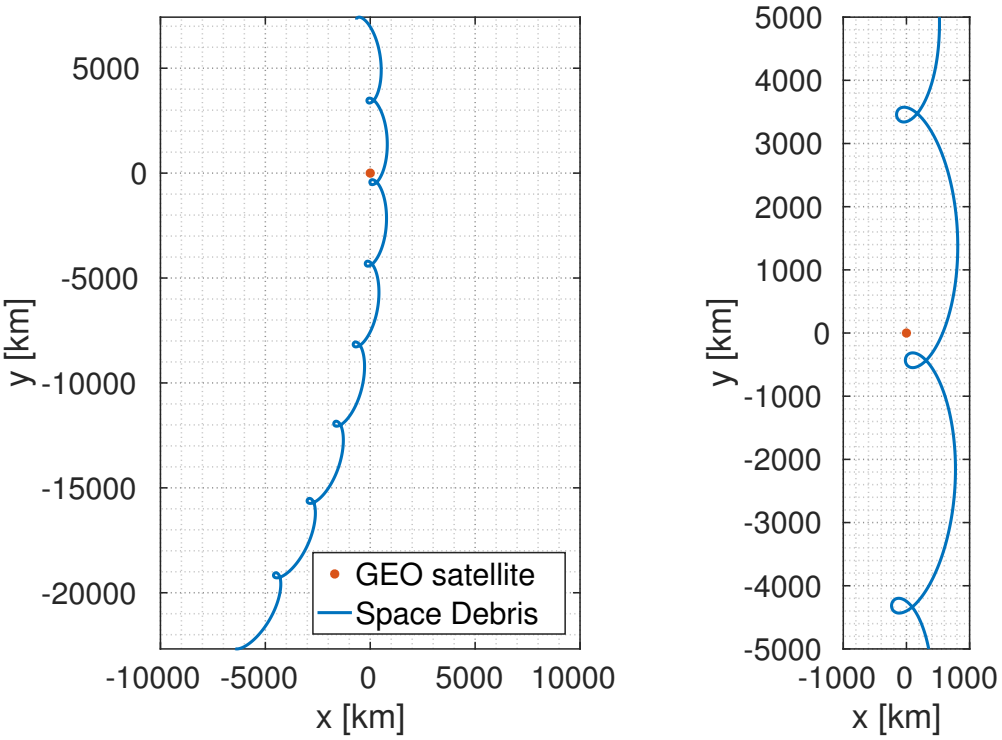

Figure 3.2: Relative motion in the $\mathcal{C}$ frame: Full view (left) and zoom (right).

be neglected. From this point onwards, we refer to the uncertainty distribution in curvilinear coordinates.

The covariance matrix is propagated employing the curvilinear C-W solution and the linearization around the quadratic solution (QuadLin). To assess the validity of the method, a validation against a Monte Carlo simulation (M-C) is performed. For each of N samples in the initial distribution, the orbit is propagated using the curvilinear C-W solution, the QuadLin solution and a high-fidelity numerical solution including Luni-Solar, J_2 and $C_{2,2}$ perturbations. Finally, for each time step the mean orbit is estimated as

$$\langle \boldsymbol{c}(\tau) \rangle = \frac{1}{N} \sum_{i=1}^{N} \boldsymbol{c}_i(\tau), \tag{3.43}$$

and the covariance matrix is estimated as

$$\boldsymbol{C}(\tau) = \frac{1}{N-1} \sum_{i=1}^{N} \Big(\boldsymbol{c}_i(\tau) - \langle \boldsymbol{c}(\tau) \rangle \Big) \Big(\boldsymbol{c}_i(\tau) - \langle \boldsymbol{c}(\tau) \rangle \Big)^{\top}. \tag{3.44}$$

Figures 3.3–3.8 show the standard deviation absolute errors with respect to the high-fidelity numerical M-C simulations. The blue lines correspond to the curvilinear C-W solution, and the green dashed lines represent the QuadLin method. When considering second-order terms in the covariance propagation, the absolute error is reduced by one to two orders of magnitude.

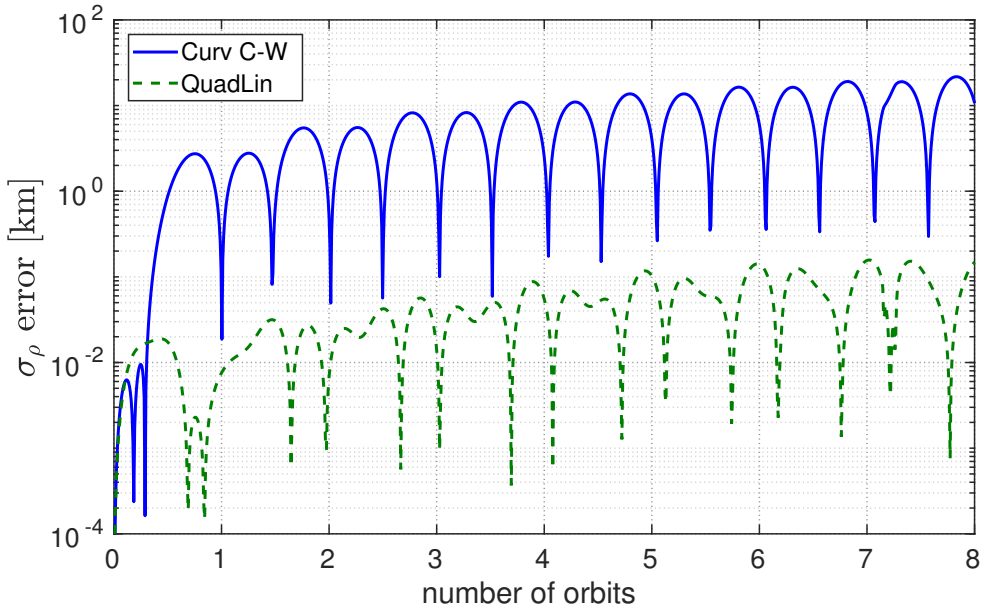

Figure 3.3: ρ standard deviation error (GEO).

One can gain more insight into the performance of the methods by looking at the samples of the M-C simulations. The uncertainty point-clouds are identical at the initial epoch for the three compared methods. However, at an intermediate epoch (Fig. 3.9) the C-W solution shows a considerable deviation on the $(\Delta\theta, \Delta\rho)$ plane. This effect is multiplied for later epochs as can be seen in Fig. 3.10. In both figures, the QuadLin method is able reproduce the covariance evolution with a higher fidelity. The M-C points show a slight "banana" shape, which suggests that the real uncertainty distribution starts to depart from Gaussianity owing to nonlinear effects. The result in all cases show improvement compared to the curvilinear C-W method.

Additionally, a comparison against Melton's method [79] is performed. Numerical simulations reveal that out-of-plane motion accuracy is similar between the proposed and Melton's method. The θ error remains smaller for Melton's method as it considers the high-fidelity nonlinear expression for the normalized mean motion n, instead of

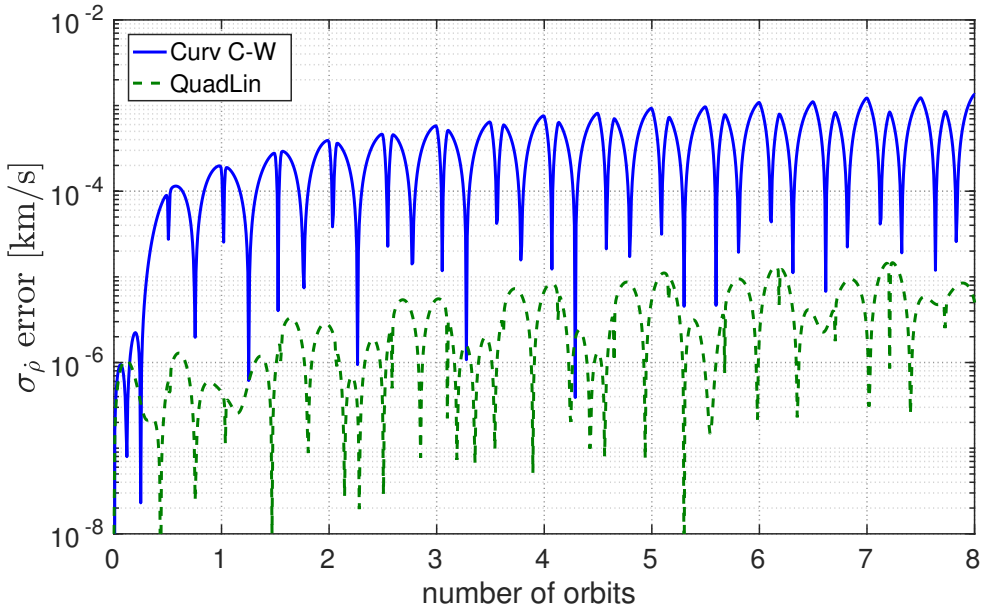

Figure 3.4: $\dot{\rho}$ standard deviation error (GEO).

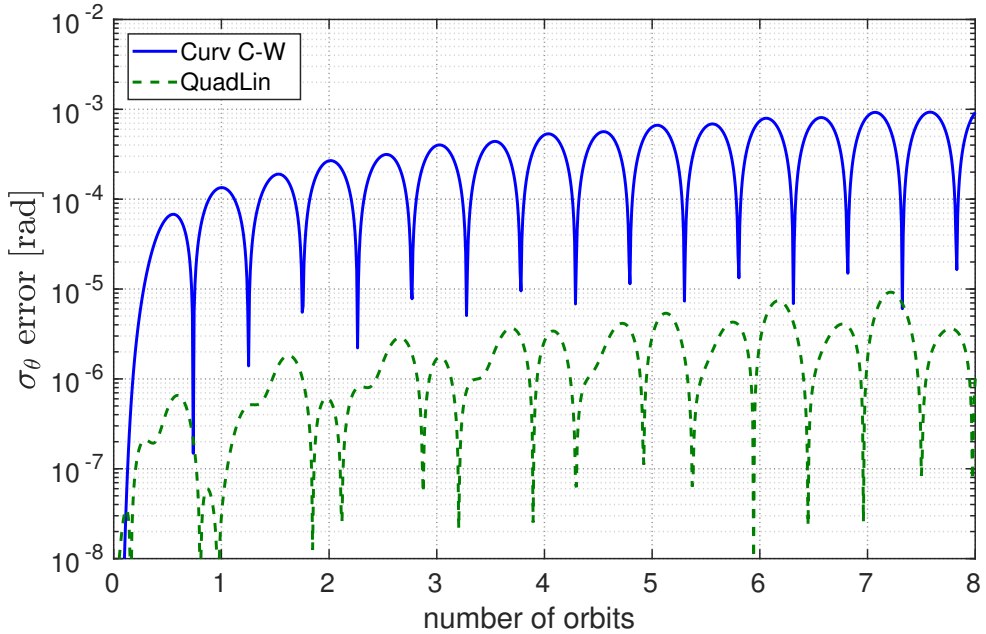

Figure 3.5: θ standard deviation error (GEO).

its second order expansion. However, Melton's method is not able to reproduce with high fidelity the nonlinear motion in the radial direction. Figures 3.11 and 3.12 show

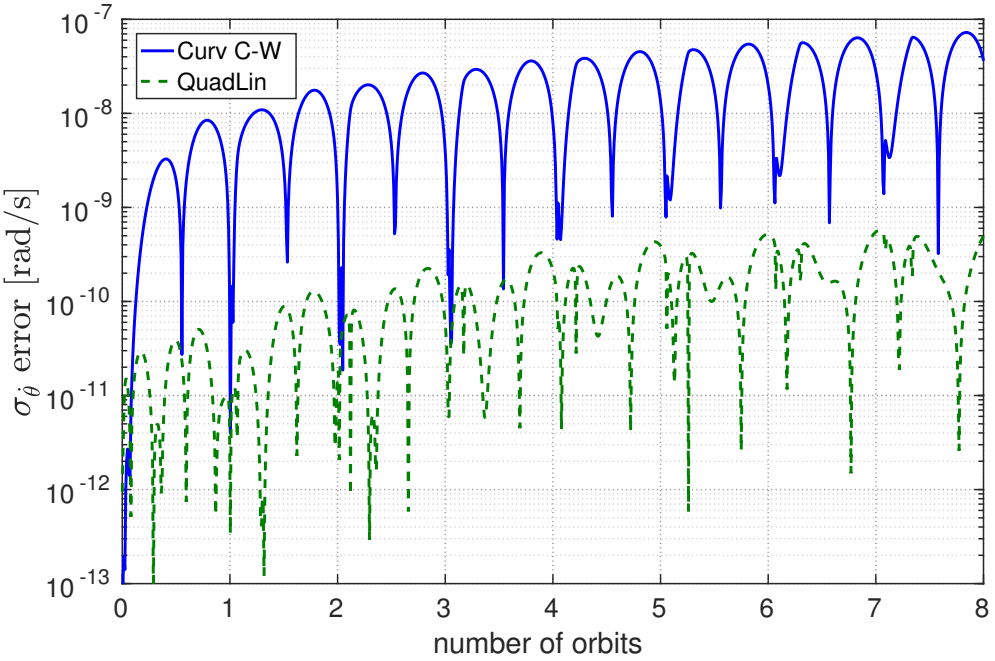

Figure 3.6: $\dot{\theta}$ standard deviation error (GEO).

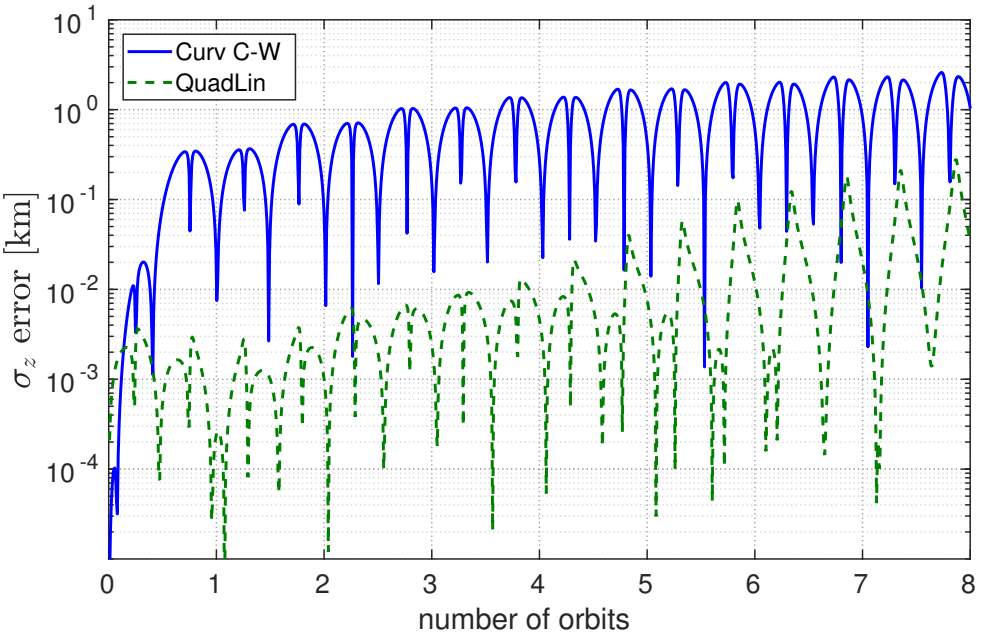

Figure 3.7: z standard deviation error (GEO).

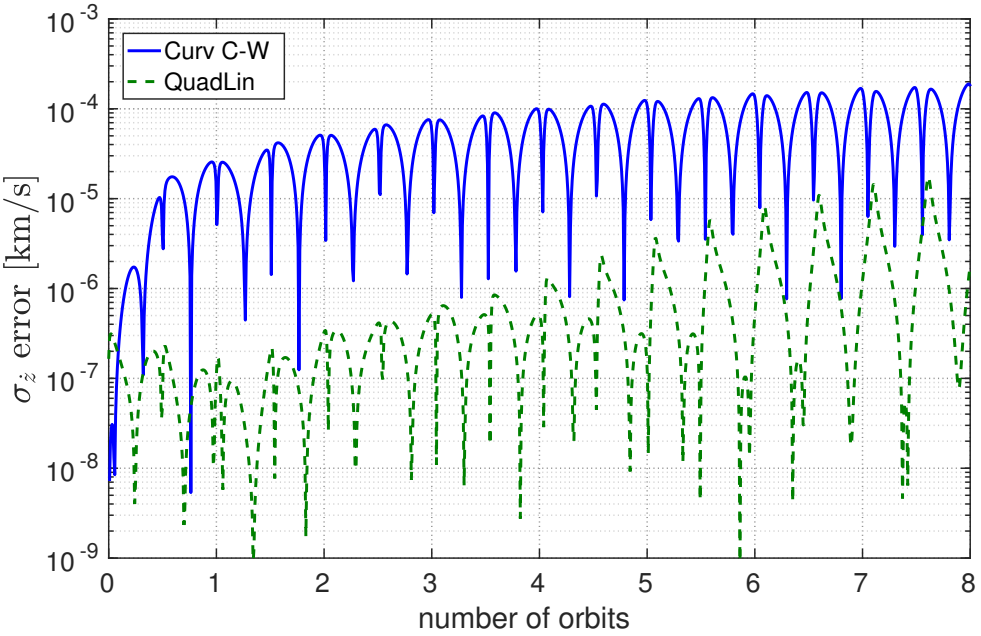

Figure 3.8: $\dot{z}$ standard deviation error (GEO).

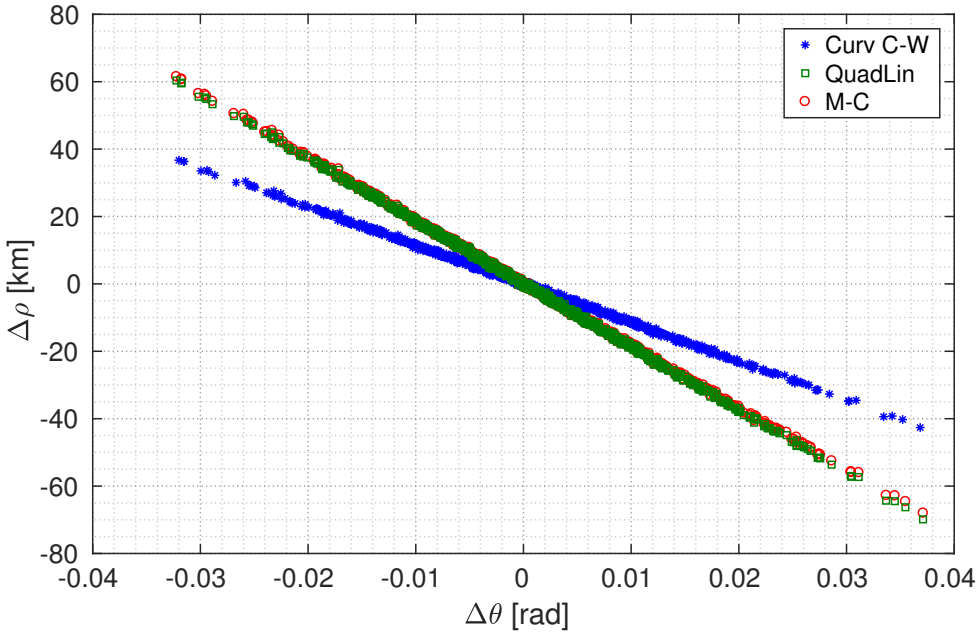

Figure 3.9: Uncertainty dispersion in the $\Delta\theta$–$\Delta\rho$ plane at an intermediate epoch (GEO, $\tau = 2.81$ days).

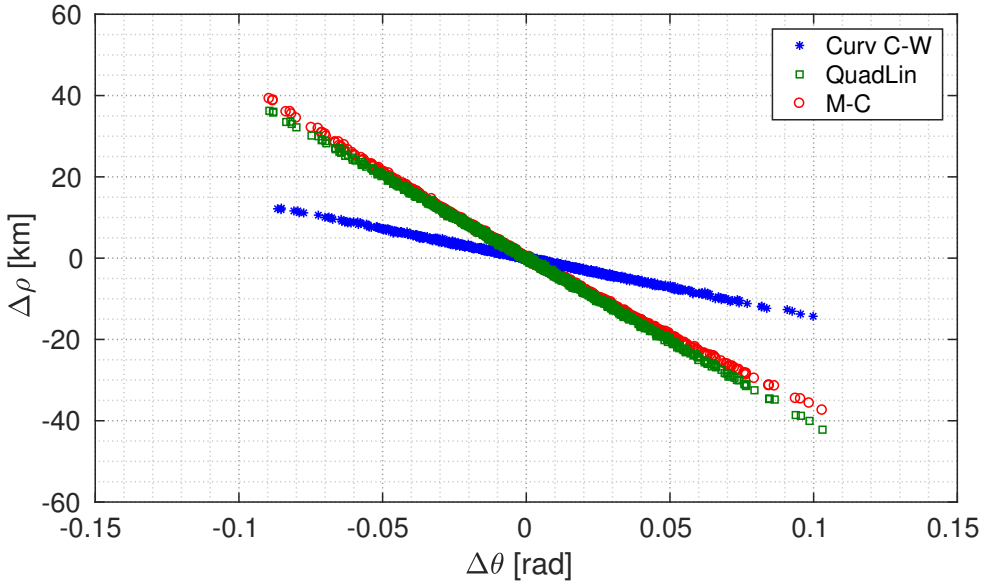

Figure 3.10: Uncertainty dispersion in the $\Delta\theta$–$\Delta\rho$ plane at an intermediate epoch (GEO, $\tau = 8.00$ days).

this effect: for early epochs Melton's method presents a small error, but the accuracy degrades as the covariance grows larger. This could be caused by the definition of Melton's angular variable as a linear function of the transversal distance, which makes the orbit error to be tangent to the orbit instead of curved along the orbit. We note however that Melton's method was probably not developed with long-term propagation in mind, and his approximation yields high accuracy for small errors and short propagation times.

Finally we consider the position error with respect to the Monte Carlo result, averaged over the samples for each epoch (see Fig. 3.13). The QuadLin method shows the best accuracy for almost every epoch. The only exception is for very short propagation arcs (smaller than 0.1 days), when the three compared methods provides results with error of the same order of magnitude. For the proposed method, the maximum average error around 5 km. This is about one order of magnitude smaller when compared to the Curvilinear C-W solution and Melton's method. Figure 3.13 also includes the average error for the single-frequency quadratic-order method. For propagation times close to integer numbers of the orbital period, the error is comparable to the double frequency algorithm, but the double frequency terms improve the accuracy of the solution

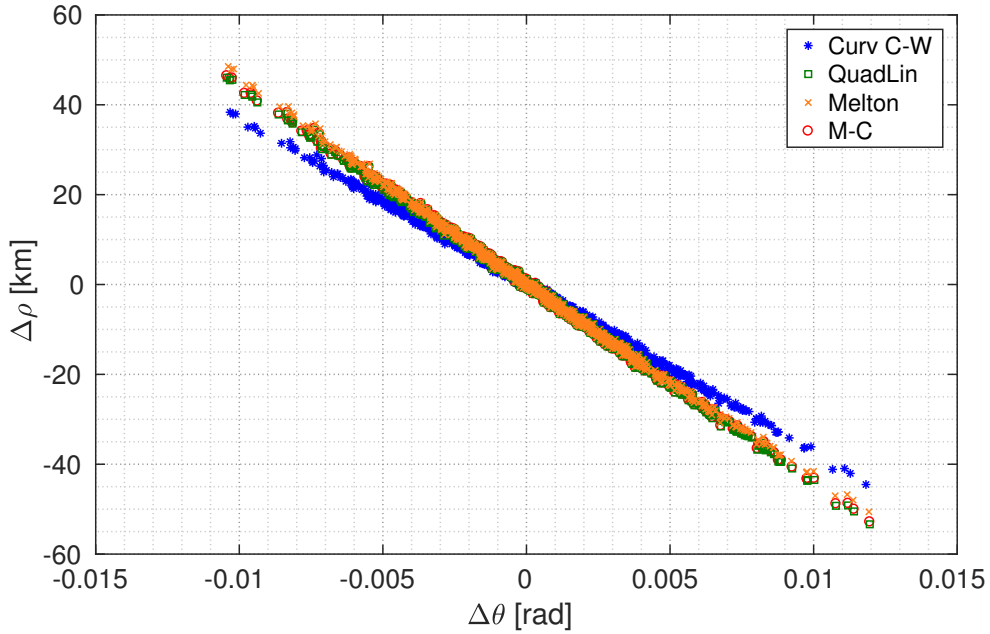

Figure 3.11: Angular-radial uncertainty clouds including Melton's method at an early epoch (GEO, $\tau = 0.80$ days).

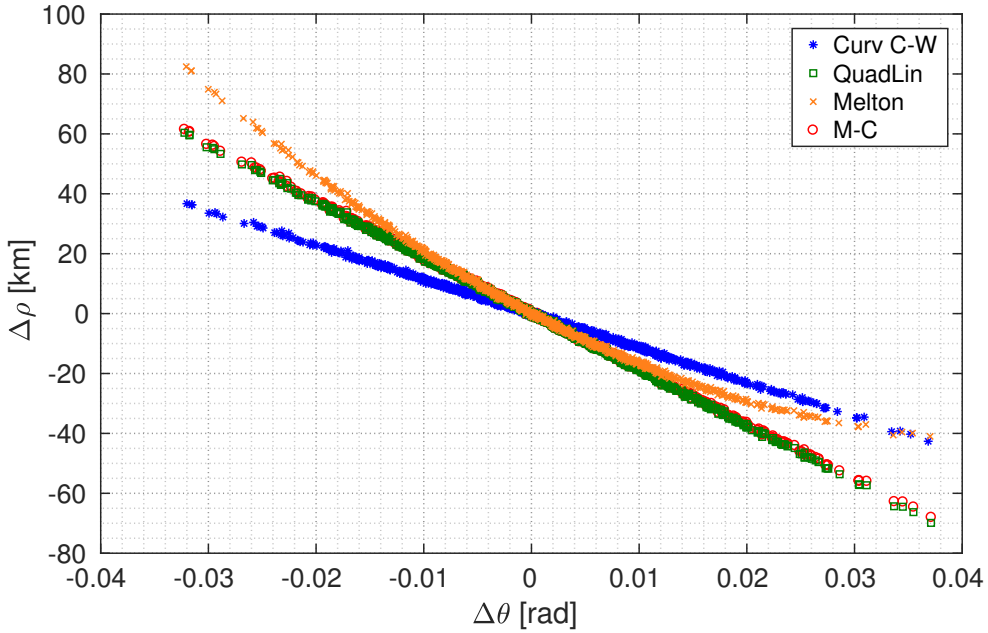

Figure 3.12: Angular-radial uncertainty clouds including Melton's method at an intermediate epoch (GEO, $\tau = 2.81$ days).

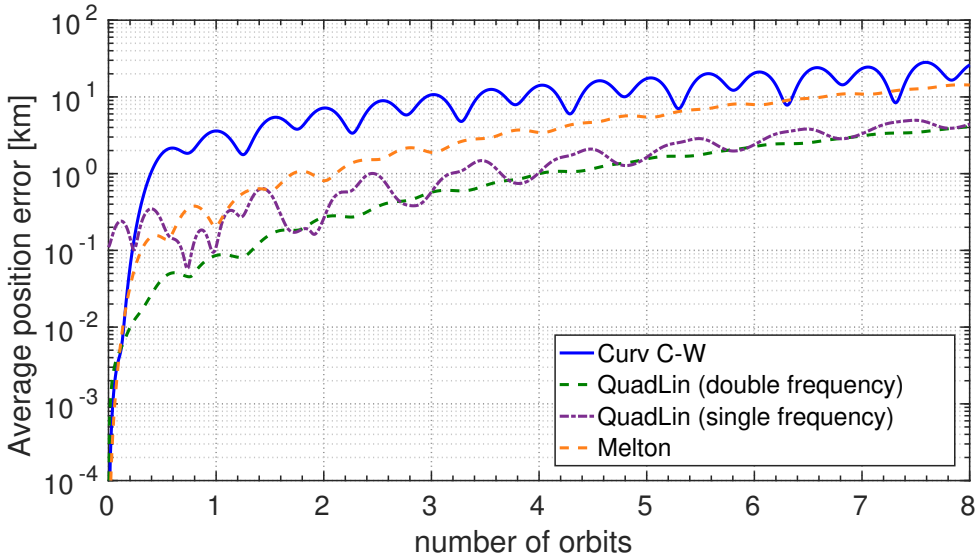

Figure 3.13: Average position error including comparison with Melton's method (GEO).

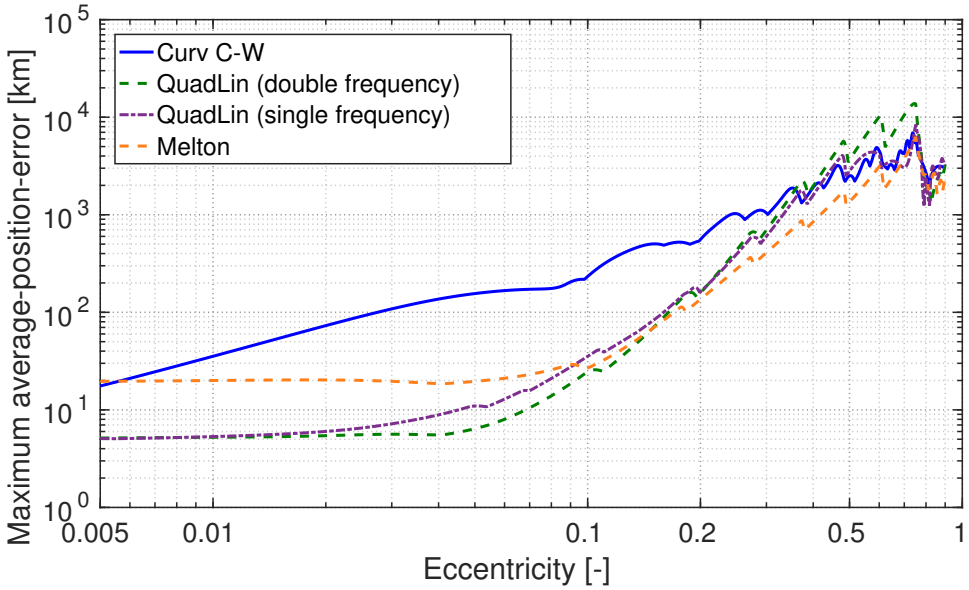

Figure 3.14: Maximum value over time of the average position error in the GEO scenario for different values of the eccentricity of the Follower.

for other epochs. Furthermore, inspection of Fig. 3.13 reveals that in order to correctly represent the initial relative state using the quadratic solution, it is necessary to include the novel double-frequency terms.

Figure 3.14 shows the maximum value over time of the average position error when

propagating during 8 days for different values of the eccentricity of the Follower in the GEO example. For eccentricity up to about 0.1, the QuadLin method offers an average error smaller than the other methods, and for values up to about 0.2 the average error is of the same order of magnitude than Melton's method. Finally, for very high values of the eccentricity the quadratic expansion convergence degrades progressively as the eccentricity increases.

3.6.2 Application to the LEO region

We consider an uncontrolled object following an elliptical orbit in the LEO region with $a = 7000\,\text{km}$ and $e = 0.01$. We set for simplicity $\Omega = \omega = \nu_0 = 0\,\text{deg}$. We study two cases with different inclination: 98 and $45\,\text{deg}$. The former is commonly used for sun-synchronous orbits, while the latter is characterized by a stronger perturbation that induces a higher precession of the orbital plane. The position standard deviations are taken as $10\,\text{m}$, $362\,\text{m}$ and $12\,\text{m}$ in the cross-track, along-track and out-of-plane directions respectively, following the values reported in [16]. The velocity covariance is set as isotropic with standard deviation of $10^{-3}\,\text{m/s}$. The orbit and the covariance matrix are propagated for 20 orbits. We employ here a fictitious circular reference orbit with the same energy, and whose orbital plane and in-plane angular position coincide with that of the initial osculating orbit. The numerical Monte Carlo solution is referred to the orbital plane of the nominal orbit. In general, this orbital plane will be different than the one used to construct the analytical solutions, but the numerical solution of the reference orbit can be employed as an improved reference. In this way, the uncertainty distribution will follow the motion of the nominal, and the deformation of the distribution will be governed by the gradient of the perturbing force, which is smaller than the perturbation itself.

The in-plane covariance propagation for both inclinations provides good accuracy using the QuadLin method: the second-order terms correspond to a correction to the curvilinear C-W solution. In Figs. 3.15 and 3.16, the standard deviation in the radial direction is reproduced with a higher accuracy using the QuadLin solution than with the curvilinear Clohessy-Wiltshire approach. This is the case as well for the circumferential direction (see Figs. 3.17 and 3.18). The out-of-plane covariance in Figs. 3.19 and 3.20 shows smaller improvements with the quadratic and double-frequency terms, as the out-of-plane motion can be conveniently approximated by a harmonic oscillator for the

Keplerian case. Moreover, the effect of the perturbations starts to degrade the accuracy of the QuadLin solution in the case of $i = 45\,\text{deg}$ after several revolutions, as can be seen in the plots for ρ and z (Figures 3.16 and 3.20, respectively).

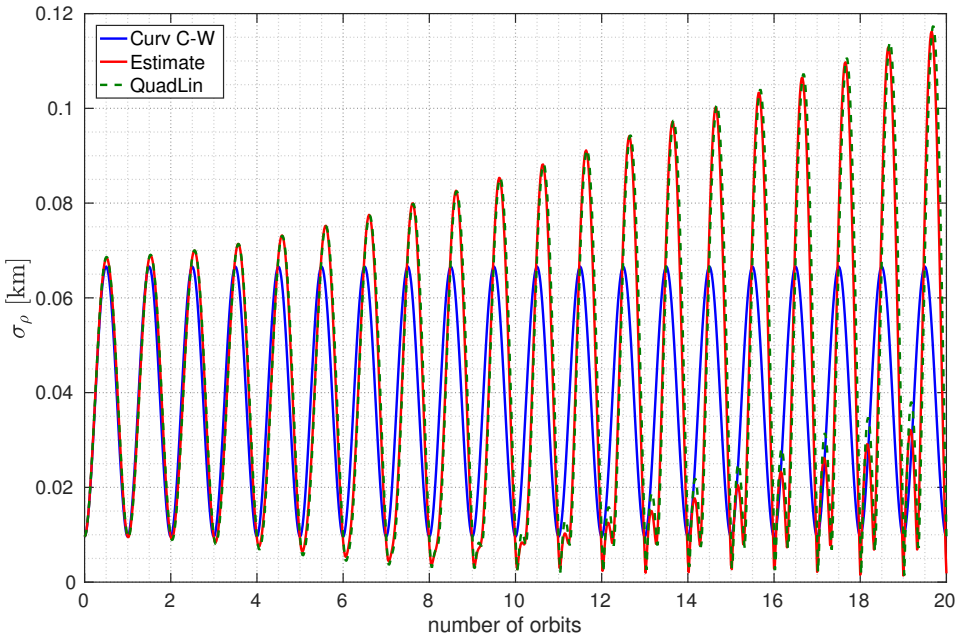

Figure 3.15: ρ standard deviation error (LEO, $i = 98\,\text{deg}$).

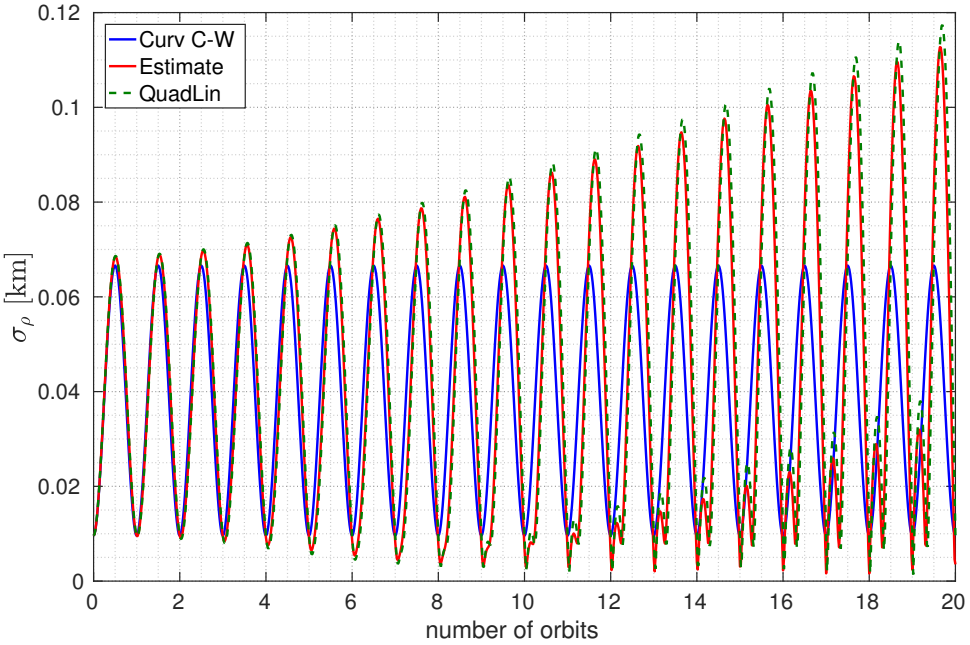

Figure 3.16: ρ standard deviation error (LEO, $i = 45$ deg).

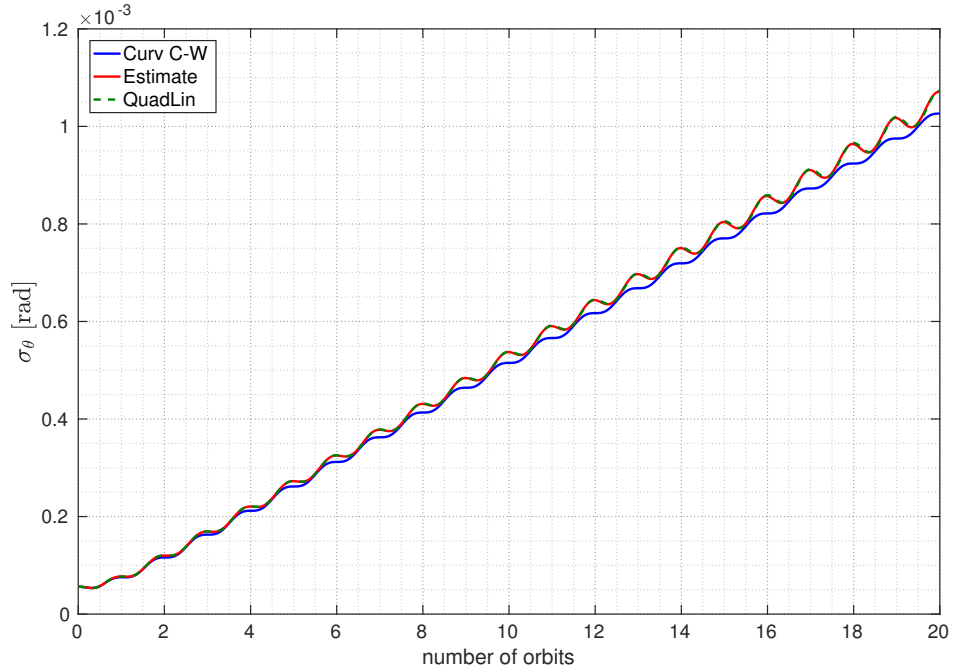

Figure 3.17: θ standard deviation error (LEO, $i = 98$ deg).

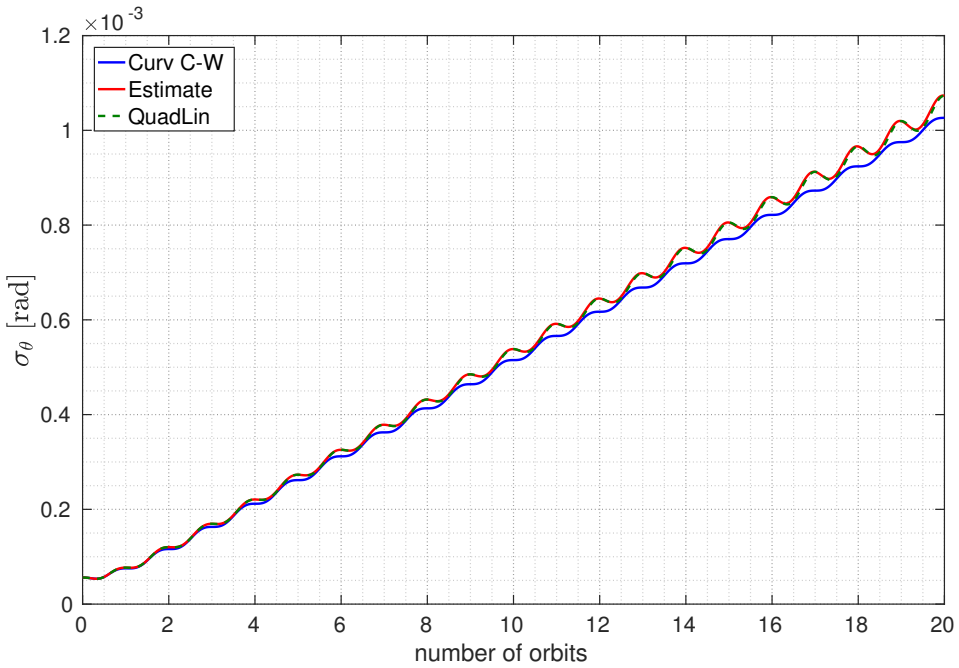

Figure 3.18: θ standard deviation error (LEO, $i = 45\,\text{deg}$).

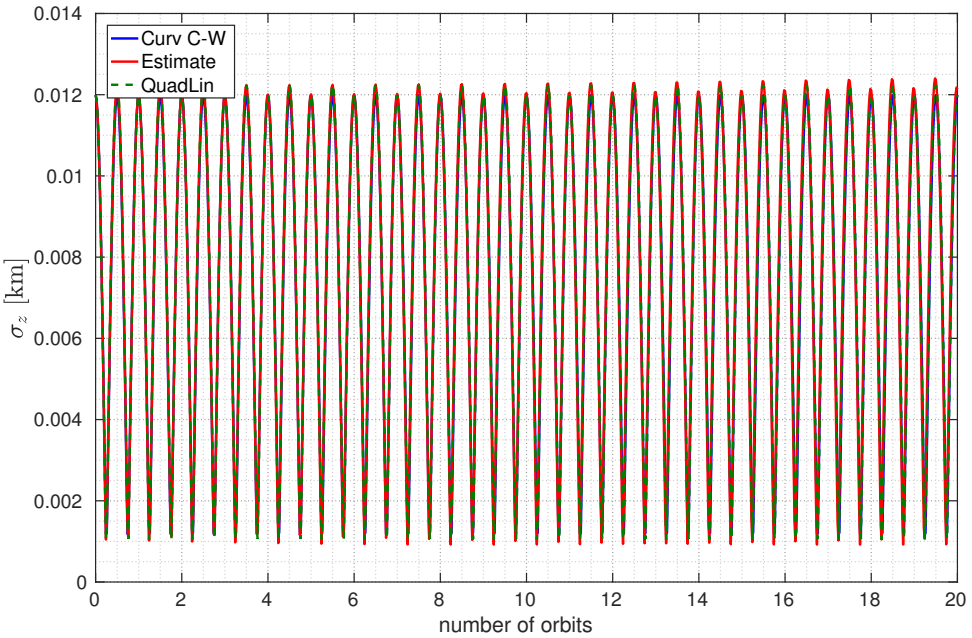

Figure 3.19: z standard deviation (LEO, $i = 98\,\text{deg}$).

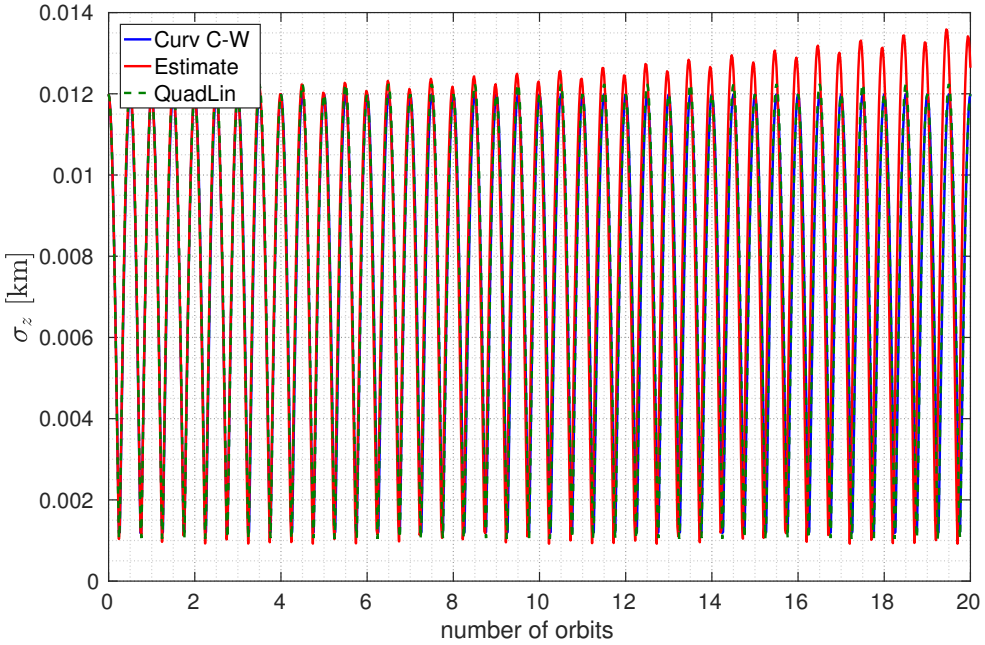

Figure 3.20: z standard deviation (LEO, $i = 45\,\text{deg}$).

3.7 Conclusions

A double-frequency, quadratic-order analytical solution to the relative motion with respect to a a reference circular orbit, expressed in curvilinear coordinates, was presented and employed as a fast and efficient tool for covariance propagation. The covariance propagation can be analytically performed with a new analytical state transition matrix constructed from the proposed quadratic solution.

The proposed covariance propagation method was compared with other linear covariance propagation methods using GEO and LEO orbits and accounting for all main perturbations. An improvement of between one and two orders of magnitude was observed when comparing the accuracy of the proposed method with a curvilinear Clohessy-Wiltshire model and a previous model proposed by Melton.

As for the range of validity of the method two main limitations appear. The first is related to the eccentricity of the nominal orbit, which should be low enough ($e < 0.1$) in order not to exceed the range of validity of the quadratic solution. However, this limitation does not hinder the applicability of the proposed approach, as in LEO all objects have low eccentricity because the perigee distance must be greater than the Earth Ra-

dius, and among all objects orbiting the Earth, more than 86% satisfy the eccentricity criteria. The second limitation concerns the effect of environmental perturbations, which is only negligible as long as secular effects do not accumulate beyond a limit threshold. For near geostationary orbits, no appreciable degradation was observed after propagation time span of around 8 orbits assuming position and velocity uncertainties of the order of km and cm/s, respectively. On the other hand, the linear uncertainty propagation in LEO was found to be limited to about 10 orbits owing mainly to the J_2-induced orbital plane precession, which directly affects the covariance propagation error in the direction orthogonal to the initial reference plane. Ways to mitigate these effects will be explored in the future.

This page intentionally left blank.

Part III

Dromo Formulation and Applications

This page intentionally left blank.

Chapter 4

Relative Motion and Uncertainty Propagation with Dromo

4.1 Introduction

Dromo is a special perturbation method developed by Peláez et al. [89] of the Space Dynamics Group (SDG) of the Technical University of Madrid, Spain. Its initial purpose was the analysis of the orbital motion of space tethers, but its outstanding performance lead the researchers of the SDG to generalize it to arbitrary orbiting objects. Dromo is a regularized theory, and a fictitious time σ derived from a second order Sundman transformation is considered as independent variable. Dromo employs seven non-singular orbital elements q_i and an intermediate frame which is *Hansel ideal*[1], allowing to decouple the in-plane dynamics from the motion of the orbital plane. It has been shown that Dromo exhibits an excellent performance in terms of numerical propagation of orbits, as well as interesting analytical properties.

Further improvements have been made to Dromo by members of the SDG and external collaborators. Urrutxua et al. remarked the importance of Hansel's concept of ideal frame [103], particularized the formulation for the planar case and applied it to the Tsien problem [104]. Baù et al. in 2013 [8] adapted the Dromo formulation for forces that can be derived from a potential, improved the formulation by introducing time elements in 2014 [9], and proposed replacing the second order Sundman transformation

[1] A Hansen ideal frame satisfies that its angular velocity is parallel to the orbiting particle position vector, then the velocity in the inertial and in the inertial frame coincides (see [43, p. 66], [55]).

by a first order one in 2015 [10]. Roa et al. also proposed several improvements of the formulation, including propagation in Minkowskian geometry [93], analyzed singularities in the formulation [91], and studied the applicability of Dromo to relative motion [92, 94, 95]. In [70], Lara proposed to combine the quaternion elements that give the orientation of the intermediate plane with the magnitude of the angular momentum, effectively reducing by one the dimension of the state vector. Herrera-Montojo et al. used Dromo to obtain an analytical solution of Keplerian orbits perturbed by the J_2 effect of the primary [51]. Additionally, The Dromo formulation has also been applied to trajectory and maneuver optimization problems, obtaining interesting analytical and numerical results by Gonzalo et al. (see [41], [40] and [39, pp. 187–203]) and Bombardelli et al. [13, 14, 15, 16, 18]. Finally, Amato et al. [4] applied the Dromo formulation to planetary close encounters and proposed a primary body switch to further improve the numerical performance.

There is a family of methods that share similarities with the Dromo formulation. Deprit [30] was one of the first authors to exploit the concept of *ideal coordinates*, employing an intermediate *ideal* frame. Palacios et al. proposed a formulation that resembles Dromo, employing a quaternion to define the orientation of an intermediate frame which is Hansel ideal and a second order Sundman transformation, but he did not exploit the Variation of Parameters technique for the in-plane motion, obtaining variables that are not constant for a pure Kepler motion[87]. Another formulation with some similarities with Dromo is the Unified State Model by Altman [2, 106] for orbit propagation, and also proposed for orbit determination application [3, 90]. Recently it has been employed for trajectory optimization [82]. Altman approach was to employ three variables that describe the Hodograph and four variables corresponding to the components of a quaternion. While the variables that correspond to the hodograph are integration constants in the Keplerian motion, Altman chose his quaternion to characterize the orientation of the local horizontal local vertical frame, which are not orbital elements and evolve with the fast frequency of the orbit on top of the slow frequency of the orbit perturbations.

In this chapter, the linear propagation using Dromo is presented, and all the gradient matrices needed to account for non-Keplerian perturbations are obtained. Applications to propagation of orbits of Near Earth Asteroids are also presented. Finally, it is noted that most of the propagation error lays on the fictitious time σ. Thus, the

possibility of expanding σ to higher orders is proposed.

4.2 Overview of the Dromo Formulation

4.2.1 Dromo variables

Let us consider a particle of negligible mass orbiting around a primary of gravitational parameter μ. Let us employ, from now on and unless specified, $\tilde{r} = 1$ au as unit of distance and $1/\tilde{n}$ as the inverse of unit of time (τ), where $\tilde{n}$ is the angular rate of a *circular* orbit with radius equal to the reference radius $\tilde{r}$:

$$\tilde{n} = \sqrt{\frac{\mu}{\tilde{r}^3}}. \tag{4.1}$$

In this canonical system of units, the gravitational parameter of the primary becomes unity.

The Dromo formulation is characterized by the use of a fictitious time σ as given by the second-order Sundman transformation

$$\frac{\mathrm{d}\tau}{\mathrm{d}\sigma} = \frac{r^2}{h}, \tag{4.2}$$

where h is the angular momentum and r corresponds to the orbital radius. The fictitious time σ is related to the osculating true anomaly ν by

$$\sigma = \nu + \beta. \tag{4.3}$$

That is, the fictitious time evolves as the osculating true anomaly plus a drift β caused by orbital perturbations. Without any loss of generality, we can set the value of β for the initial epoch equal to zero. In contrast with the classical Dromo formulation, we use real time τ as independent variable instead of the fictitious time σ. This yields an easier treatment of time-dependent forces, as in the case of N-bodies gravitational perturbation deriving from time-dependent ephemerides, and makes it straightforward to track the evolution of the state uncertainties in time because we can avoid cumbersome transformations to assure the τ–σ synchrony of the propagated pdf [92, 94]. Therefore, we will consider σ as a variable that depends on time, and propagate it together with the rest of the Dromo elements.

To avoid singularities in the description of the orbital motion, seven generalized

orbital elements are employed. The first three Dromo elements are defined as

$$q_1 = \frac{e}{h}\cos\beta, \tag{4.4a}$$
$$q_2 = \frac{e}{h}\sin\beta, \tag{4.4b}$$
$$q_3 = \frac{1}{h}, \tag{4.4c}$$

where e corresponds to the magnitude of the eccentricity vector $\boldsymbol{e}$.

The four remaining generalized orbital elements are the Euler-Rodrigues parameters characterizing the rotation associated to the matrix $\boldsymbol{P}$. This rotation brings an *intermediate frame* $\mathcal{P}$ (having two axes constantly lying in the instantaneous orbital plane of the particle) to overlap with a reference inertial frame ($\mathcal{I}$). In the classical Dromo formulation [89], the intermediate frame was chosen to coincide with the local-vertical local-horizontal (LVLH) orbital frame $\mathcal{R}$ at $\tau = 0$. Here we choose $\mathcal{P}$ in such a way that it coincides with the perifocal frame at $\tau = 0$, as done in Ref. [103]. The matrix $\boldsymbol{P}$ reads

$$\boldsymbol{P} = \begin{bmatrix} q_4^2 - q_5^2 - q_6^2 + q_7^2 & 2\left(q_4 q_5 - q_6 q_7\right) & 2\left(q_4 q_6 + q_5 q_7\right) \\ 2\left(q_4 q_5 + q_6 q_7\right) & -q_4^2 + q_5^2 - q_6^2 + q_7^2 & 2\left(q_5 q_6 - q_4 q_7\right) \\ 2\left(q_4 q_6 - q_5 q_7\right) & 2\left(q_5 q_6 + q_4 q_7\right) & -q_4^2 - q_5^2 + q_6^2 + q_7^2 \end{bmatrix}. \tag{4.5}$$

An additional rotation matrix $\boldsymbol{Q}$ brings the orbital frame $\mathcal{R}$ to overlap with the intermediate frame $\mathcal{P}$ through a rotation of $-\sigma$ around the common z-axis, which is oriented towards the angular momentum vector:

$$\boldsymbol{Q} = \begin{bmatrix} \cos\sigma & -\sin\sigma & 0 \\ \sin\sigma & \cos\sigma & 0 \\ 0 & 0 & 1 \end{bmatrix}. \tag{4.6}$$

Finally, the rotation from the $\mathcal{I}$ to the $\mathcal{R}$ frame can be built as the composition of the rotations previously introduced, and is characterized by the matrix $\boldsymbol{R}$ given by

$$\boldsymbol{R} = \boldsymbol{P}\,\boldsymbol{Q}. \tag{4.7}$$

The Euler-Rodrigues parameters can be related to the classical orbital elements (inclination i, right ascension of the ascending node Ω, and argument of periapsis ω) as follows:

$$q_4 = \sin\frac{i}{2}\cos\frac{\Omega-\omega+\beta}{2}, \tag{4.8a}$$

$$q_5 = \sin\frac{i}{2}\sin\frac{\Omega-\omega+\beta}{2}, \tag{4.8b}$$

$$q_6 = \cos\frac{i}{2}\sin\frac{\Omega+\omega-\beta}{2}, \tag{4.8c}$$

$$q_7 = \cos\frac{i}{2}\cos\frac{\Omega+\omega-\beta}{2}, \tag{4.8d}$$

where β was introduced in Eq. (4.3).

The inertial reference frame $\mathcal{I}$, the intermediate frame $\mathcal{P}$ and the LVLH frame $\mathcal{R}$, as well as the rotations that relate them, are shown in figures 4.1 and 4.2.

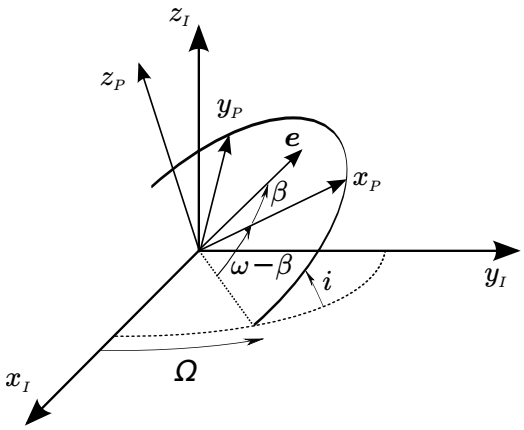

Figure 4.1: Inertial ($\mathcal{I} = \langle x_\mathcal{I}, y_\mathcal{I}, z_\mathcal{I}\rangle$) and intermediate ($\mathcal{P} = \langle x_\mathcal{P}, y_\mathcal{P}, z_\mathcal{P}\rangle$) frames.

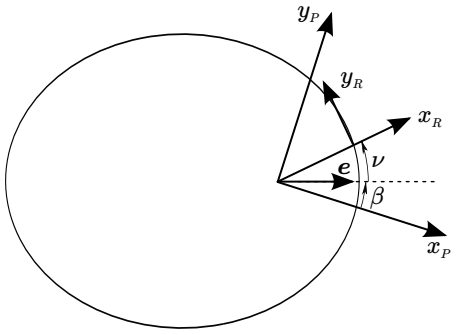

Figure 4.2: Intermediate ($\mathcal{P} = \langle x_\mathcal{P}, y_\mathcal{P}, z_\mathcal{P}\rangle$) and LVLH ($\mathcal{R} = \langle x_\mathcal{R}, y_\mathcal{R}, z_\mathcal{R}\rangle$) frames. Note that $z_\mathcal{R} \equiv z_\mathcal{P}$.

Other relations between Dromo elements and Cartesian coordinates, classical orbital elements and equinoctial elements, as well as the corresponding Jacobian matrices, are provided in Appendix D.

4.2.2 Dromo Hodograph plane

The Hodograph is a useful tool to analyze the motion by considering only the velocity components [7, pp. 126–127]. It has been employed in multiple applications, including orbit transfers (see [7, pp. 531 – 536] and [3] for reference). The Hodograph in Dromo variables takes a especially simple expression, because the coordinates q_1, q_2, q_3 are

selected as the components of the Hodograph equation.

In fact, the transversal and radial components of the velocity, s and u respectively, are given by

$$s = q_1 \cos\sigma + q_2 \sin\sigma + q_3, \tag{4.9}$$

$$u = q_1 \sin\sigma - q_2 \cos\sigma. \tag{4.10}$$

The Dromo Hodograph plane is shown in Fig. 4.3. On the left, the terms that form s and u are decomposed in different colors, while on the right they are combined into the classical Hodograph plane. Note that the classical Hodograph plane for the transversal and radial components of the velocity measures the true anomaly from the horizontal axis [7, pp. 126–127], while in the Dromo formulation the angle employed is σ, and thus the reference is rotated by an angle of $-\beta$.

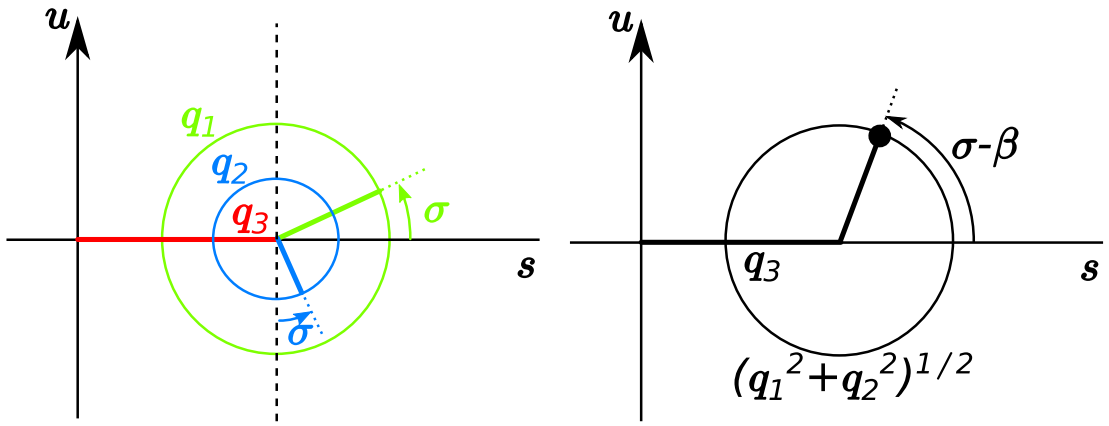

(a) Hodograph components. (b) Combined Hodograph.

Figure 4.3: Dromo Hodograph plane

4.2.3 Equations of Motion in Dromo Elements

The evolution in time of the generalized orbital elements under the effect of the radial (f_r), transversal (f_θ) and out-of-plane (f_h) components of the dimensionless perturbing acceleration is governed by the differential equations (see [103] for a detailed deriva-

tion):

$$\frac{\mathrm{d}}{\mathrm{d}\sigma}\begin{pmatrix} q_1 \\ q_2 \\ q_3 \end{pmatrix} = \frac{1}{q_3 s^3}\begin{bmatrix} s\sin\sigma & (s+q_3)\cos\sigma \\ -s\cos\sigma & (s+q_3)\sin\sigma \\ 0 & -q_3 \end{bmatrix}\begin{pmatrix} f_r \\ f_\theta \end{pmatrix}, \tag{4.11}$$

$$\frac{\mathrm{d}}{\mathrm{d}\sigma}\begin{pmatrix} q_4 \\ q_5 \\ q_6 \\ q_7 \end{pmatrix} = \frac{f_h}{2q_3 s^3}\begin{bmatrix} 0 & 0 & -\sin\sigma & \cos\sigma \\ 0 & 0 & \cos\sigma & \sin\sigma \\ \sin\sigma & -\cos\sigma & 0 & 0 \\ -\cos\sigma & -\sin\sigma & 0 & 0 \end{bmatrix}\begin{pmatrix} q_4 \\ q_5 \\ q_6 \\ q_7 \end{pmatrix}, \tag{4.12}$$

to be accompanied by the equation governing the evolution of the fictitious time, rewritten as a function of the Dromo variables as

$$\frac{\mathrm{d}\tau}{\mathrm{d}\sigma} = \frac{1}{q_3 s^2}. \tag{4.13}$$

After introducing the Dromo state vector $\boldsymbol{q} = (q_1, \ldots, q_7, \sigma)^\top$, the equations of motion in the presence of a perturbing acceleration $\boldsymbol{f}(\boldsymbol{q}, \tau) = (f_r, f_\theta, f_h)^\top$ expressed in the $\mathcal{R}$ frame can be written as (see [47])

$$\frac{\mathrm{d}\boldsymbol{q}}{\mathrm{d}\tau} = \boldsymbol{g}(\boldsymbol{q}, \boldsymbol{f}(\boldsymbol{q}, \tau)) \tag{4.14}$$

where

$$g_1 = \frac{\mathrm{d}q_1}{\mathrm{d}\tau} = \frac{f_\theta}{s}(s+q_3)\cos\sigma + f_r\sin\sigma, \tag{4.15a}$$

$$g_2 = \frac{\mathrm{d}q_2}{\mathrm{d}\tau} = \frac{f_\theta}{s}(s+q_3)\sin\sigma - f_r\cos\sigma, \tag{4.15b}$$

$$g_3 = \frac{\mathrm{d}q_3}{\mathrm{d}\tau} = -f_\theta\frac{q_3}{s}, \tag{4.15c}$$

$$g_4 = \frac{\mathrm{d}q_4}{\mathrm{d}\tau} = \frac{f_h}{2s}(q_7\cos\sigma - q_6\sin\sigma), \tag{4.15d}$$

$$g_5 = \frac{\mathrm{d}q_5}{\mathrm{d}\tau} = \frac{f_h}{2s}(q_6\cos\sigma + q_7\sin\sigma), \tag{4.15e}$$

$$g_6 = \frac{\mathrm{d}q_6}{\mathrm{d}\tau} = -\frac{f_h}{2s}(q_5\cos\sigma - q_4\sin\sigma), \tag{4.15f}$$

$$g_7 = \frac{\mathrm{d}q_7}{\mathrm{d}\tau} = -\frac{f_h}{2s}(q_4\cos\sigma + q_5\sin\sigma), \tag{4.15g}$$

$$g_8 = \frac{\mathrm{d}\sigma}{\mathrm{d}\tau} = q_3 s^2. \tag{4.15h}$$

4.3 Probability Distribution Function of the Dromo Variables

The good results obtained in orbit propagation with the Dromo formulation motivate to apply it to the relative motion and uncertainty propagation problems. For example,

starting from an initial Gaussian distribution one could linearly propagate the orbit uncertainty. However, one must be careful when following this approach. Rigorously, a Gaussian distribution is defined on the real numbers, but this is not the case for the all the Dromo elements. First, the variables corresponding to quaternion components $q_4, \ldots, q_7$ must satisfy the unit-norm constraint, and their distributions are not defined in $\mathbb{R}^4$ but in the hypersphere $\mathbb{S}^3$, associated to the group $SO(3)$ of rotations in the three-dimensional space.

$$q_4^2 + q_5^2 + q_6^2 + q_7^2 = 1 \tag{4.16}$$

An additional implicit constraint naturally arises by the definition of the Dromo variables, and corresponds to rotations of angle β the intermediate ideal frame over an axis perpendicular to it.

$$\beta = \operatorname{atan2}(q_2, q_1). \tag{4.17}$$

Another minor limitation is that the third element must be strictly positive

$$q_3 > 0. \tag{4.18}$$

Additionally, the fictitious time σ is an angle which is naturally defined on a circle, and satisfies

$$\sigma = \sigma + 2\pi. \tag{4.19}$$

The branch of statistics that studies distribution of variables defined in circles, spheres or hyperspheres is called *directional statistics*, and the main concepts are covered in [76]. A useful distribution for variables defined on a circle is the Von Mises distribution, which can be approximated by a wrapped normal distribution, and generated by a two-dimensional Gaussian distribution constrained to the unit circle [76, pp. 36 – 45]. The equivalent for variables defined over the 4-dimensional unit-hypersphere is the Bingham distribution (see [76, pp. 159–244] or [83, p. 89]). Some other applications of directional statistics in astrodynamics include nonlinear filtering for orbital tracking problems [65].

When the uncertainty is small, one can approximate the distributions mentioned above by Gaussian distributions. For the fictitious time, the error will be important only

if the tails of the distribution start to wrap around a whole revolution. For the components of the quaternion, we employ an approach commonly used in filtering with a nonlinear constraint, which consists on relaxing the constraint and then projecting the result onto the surface defined by it [57]. Relaxing the unit-norm constraint, yields a Gaussian contained in the hyper-plane tangent to the unit hypersphere at the mean values of the quaternion, but is quaternion norm becomes a non-observable quantity. This translates into a rank deficiency in the direction of the mean values of the quaternion, as was reported for spacecraft attitude applications by Lefferts et al. [73]. Another way of interpreting this rank deficiency emerges from the procedure of Section D.2.4, which highlights that variations of the quaternion components are not linearly independent. These variations can still be projected onto the unit hypersphere to generate a valid quaternion with unit norm, following the projection approach. In the same Section D.2.4, it is proven that assigning the value of β for the initial time induces a linear dependence between variations of two of the Dromo variables, and consequently the rank of the covariance matrix further decreases by one. Combining both results, the covariance matrix in Dromo will have dimension 8 but a maximum rank of 6. This rank deficiency is a mathematical artifact and not a physical singularity, as converting back to the Cartesian space yields a full rank covariance matrix.

4.4 Linear propagation with Dromo

An orbit $\boldsymbol{q}$ close to a reference orbit $\boldsymbol{q}_{\text{ref}}$ can be linearly propagated via the state transition matrix (STM) as

$$\boldsymbol{q}\left(\tau\right) = \boldsymbol{q}_{\text{ref}}\left(\tau\right) + \boldsymbol{\Phi}\left(\tau, \tau_0\right)\left(\boldsymbol{q}\left(\tau_0\right) - \boldsymbol{q}_{\text{ref}}\left(\tau_0\right)\right). \tag{4.20}$$

The evolution of the STM is given by

$$\frac{\mathrm{d}\boldsymbol{\Phi}(\tau,\tau_0)}{\mathrm{d}\tau} = \boldsymbol{G}\left(\boldsymbol{q}_{\text{ref}}\left(\tau\right), \tau\right)\boldsymbol{\Phi}(\tau,\tau_0), \tag{4.21a}$$

$$\boldsymbol{\Phi}(\tau_0,\tau_0) = \boldsymbol{I}_8, \tag{4.21b}$$

which must be integrated together with Eq. (4.14), and where $\boldsymbol{I}_8$ is the eight-dimensional identity matrix. The gradient matrix $\boldsymbol{G}$ corresponds to the following total derivative evaluated on the reference orbit

$$\boldsymbol{G} = \frac{\mathrm{d}\boldsymbol{g}}{\mathrm{d}\boldsymbol{q}} = \frac{\partial \boldsymbol{g}}{\partial \boldsymbol{q}} + \frac{\partial \boldsymbol{g}}{\partial \boldsymbol{f}}\frac{\partial \boldsymbol{f}}{\partial \boldsymbol{q}} \tag{4.22}$$

where $\boldsymbol{f}$ must be expressed in the $\mathcal{R}$ reference system.

The derivative $\frac{\partial \boldsymbol{g}}{\partial \boldsymbol{q}}$ must be calculated for constant $\boldsymbol{f}$:

$$\frac{\partial \boldsymbol{g}}{\partial \boldsymbol{q}} = \begin{bmatrix} -\frac{f_\theta q_3 \cos^2\sigma}{s^2} & -\frac{f_\theta q_3 \cos\sigma \sin\sigma}{s^2} & f_\theta \frac{s-q_3}{s^2}\cos\sigma & 0 & 0 & 0 & 0 & \frac{\partial g_1}{\partial \sigma} \\ -\frac{f_\theta q_3 \cos\sigma \sin\sigma}{s^2} & -\frac{f_\theta q_3 \sin^2\sigma}{s^2} & f_\theta \frac{s-q_3}{s^2}\sin\sigma & 0 & 0 & 0 & 0 & \frac{\partial g_2}{\partial \sigma} \\ \frac{f_\theta q_3 \cos\sigma}{s^2} & \frac{f_\theta q_3 \sin\sigma}{s^2} & -f_\theta \frac{s-q_3}{s^2} & 0 & 0 & 0 & 0 & -f_\theta \frac{u}{s}\frac{q_3}{s} \\ -\frac{g_4 \cos\sigma}{s} & -\frac{g_4 \sin\sigma}{s} & -\frac{g_4}{s} & 0 & 0 & -\frac{f_h \sin\sigma}{2s} & \frac{f_h \cos\sigma}{2s} & \frac{g_4 u - g_5 s}{s} \\ -\frac{g_5 \cos\sigma}{s} & -\frac{g_5 \sin\sigma}{s} & -\frac{g_5}{s} & 0 & 0 & \frac{f_h \cos\sigma}{2s} & \frac{f_h \sin\sigma}{2s} & \frac{g_5 u + g_4 s}{s} \\ -\frac{g_6 \cos\sigma}{s} & -\frac{g_6 \sin\sigma}{s} & -\frac{g_6}{s} & \frac{f_h \sin\sigma}{2s} & -\frac{f_h \cos\sigma}{2s} & 0 & 0 & \frac{g_6 u - g_7 s}{s} \\ -\frac{g_7 \cos\sigma}{s} & -\frac{g_7 \sin\sigma}{s} & -\frac{g_7}{s} & -\frac{f_h \cos\sigma}{2s} & -\frac{f_h \sin\sigma}{2s} & 0 & 0 & \frac{g_7 u + g_6 s}{s} \\ 2q_3 s\cos\sigma & 2q_3 s\sin\sigma & s^2 + 2q_3 s & 0 & 0 & 0 & 0 & -2q_3 s\, u \end{bmatrix}, \tag{4.23}$$

with

$$\frac{\partial g_1}{\partial \sigma} = f_r \cos\sigma + f_\theta \left(\frac{u}{s}\frac{q_3}{s}\cos\sigma - \left(1 + \frac{q_3}{s}\right)\sin\sigma \right), \tag{4.24}$$

$$\frac{\partial g_2}{\partial \sigma} = f_r \sin\sigma + f_\theta \left(\frac{u}{s}\frac{q_3}{s}\sin\sigma + \left(1 + \frac{q_3}{s}\right)\cos\sigma \right). \tag{4.25}$$

The second derivative, $\frac{\partial \boldsymbol{g}}{\partial \boldsymbol{f}}$, is calculated considering a constant Dromo state vector:

$$\frac{\partial \boldsymbol{g}}{\partial \boldsymbol{f}} = \begin{bmatrix} \sin\sigma & \left(1 + \frac{q_3}{s}\right)\cos\sigma & 0 \\ -\cos\sigma & \left(1 + \frac{q_3}{s}\right)\sin\sigma & 0 \\ 0 & -\frac{q_3}{s} & 0 \\ 0 & 0 & \frac{1}{2s}\left(q_7\cos\sigma - q_6\sin\sigma\right) \\ 0 & 0 & \frac{1}{2s}\left(q_6\cos\sigma + q_7\sin\sigma\right) \\ 0 & 0 & -\frac{1}{2s}\left(q_5\cos\sigma - q_4\sin\sigma\right) \\ 0 & 0 & -\frac{1}{2s}\left(q_4\cos\sigma + q_5\sin\sigma\right) \\ 0 & 0 & 0 \end{bmatrix}. \tag{4.26}$$

Finally, the last derivative $\frac{\partial \boldsymbol{f}}{\partial \boldsymbol{q}}$ depends on the nature of the perturbing accelerations and must be calculated for each of them. A general formulation is given in section 4.4.1, and expressions particularized for for third-body perturbing accelerations, key for uncertainty propagation of NEAs, are given in section 4.4.2.

4.4.1 Gradient Matrices

Let M perturbations act on the mass particle whose motion is under study. The total perturbing acceleration is

$$\boldsymbol{f} = \sum_{k=1}^{M} \boldsymbol{f}_k. \tag{4.27}$$

Then, the last term in Eq. (4.22) becomes

$$\frac{\partial \boldsymbol{f}}{\partial \boldsymbol{q}} = \sum_{k=1}^{M} \frac{\partial \boldsymbol{f}_k}{\partial \boldsymbol{q}}. \tag{4.28}$$

That is, linearity allows one to simply add the gradient of each perturbation.

One example of a perturbation with multiple terms is the gravitational perturbation of the nonspherical primary body. The point-mass term is already contained in the Dromo formulation, but considering a spherical harmonics expansion of the potential up to some degree and order introduces further perturbations. The perturbing potential, the acceleration in the *inertial frame* $\mathcal{I}$ and its gradient can be calculated via iterative methods [31].

The question is, how to relate $\frac{\partial \boldsymbol{f}^{\mathcal{I}}}{\partial \boldsymbol{r}^{\mathcal{I}}}$ to $\frac{\partial \boldsymbol{f}^{\mathcal{R}}}{\partial \boldsymbol{q}}$? To answer it, first note that

$$\boldsymbol{f}^{\mathcal{R}} = \boldsymbol{R}^{\top} \boldsymbol{f}^{\mathcal{I}}. \tag{4.29}$$

Then,

$$\frac{\partial \boldsymbol{f}^{\mathcal{R}}}{\partial \boldsymbol{q}} = \frac{\partial \boldsymbol{R}^{\top}}{\partial \boldsymbol{q}} \boldsymbol{f}^{\mathcal{I}} + \boldsymbol{R}^{\top} \frac{\partial \boldsymbol{f}^{\mathcal{I}}}{\partial \boldsymbol{q}}. \tag{4.30}$$

The term $\frac{\partial \boldsymbol{R}}{\partial \boldsymbol{q}}$ can be easily calculated using Eq. (4.7). The last term in the right hand side can be calculated using the chain rule as

$$\frac{\partial \boldsymbol{f}^{\mathcal{I}}}{\partial \boldsymbol{q}} = \frac{\partial \boldsymbol{f}^{\mathcal{I}}}{\partial \boldsymbol{r}^{\mathcal{I}}} \frac{\partial \boldsymbol{r}^{\mathcal{I}}}{\partial \boldsymbol{q}} \tag{4.31}$$

which is easily calculated since the first factor is assumed to be known, and the second is given by the upper half of Eq. (D.7).

4.4.2 N-body term

The N-body perturbing acceleration can be written as

$$\boldsymbol{f} = -\sum_{j=2}^{N-1} \mu_j \frac{\boldsymbol{r} - \boldsymbol{r}_j}{\|\boldsymbol{r} - \boldsymbol{r}_j\|^3} - \sum_{j=2}^{N-1} \mu_j \frac{\boldsymbol{r}_j}{\|\boldsymbol{r}_j\|^3} \tag{4.32}$$

where $j = 1$ is the primary body already considered in the Dromo formulation and $j = N$ is the propagated object, whose mass is considered negligible with respect to the perturbing bodies. The quantities $\boldsymbol{r}_j$ and μ_j are the position vector and the gravitational parameter of the j^{th} body respectively.

It is important to underline that in order to derive analytical expressions for the 3×8 Jacobian matrix $\frac{\partial \boldsymbol{f}}{\partial \boldsymbol{q}}$, the perturbing acceleration $\boldsymbol{f}$ has to be projected onto the $\mathcal{R}$ reference frame. The representation of the particle position vector with respect to such frame is straightforward:

$$\boldsymbol{r}^{\mathcal{R}} = \left(\frac{1}{q_3 s}, 0, 0 \right)^{\top}. \tag{4.33}$$

The position of the j^{th} body only depends on time and can be obtained using JPL's DE ephemeris [35] or VSOP [98] (*Variations Séculaires des Orbites Planétaires*), for example. This position is usually expressed as a vector $\boldsymbol{r}_j^{\mathcal{I}}$ with respect to the inertial frame and can be projected onto $\mathcal{R}$ as follows

$$\boldsymbol{r}_j^{\mathcal{R}} = \boldsymbol{R}^{\top} \boldsymbol{r}_j^{\mathcal{I}}. \tag{4.34}$$

The derivative of the force components in $\mathcal{R}$ can be obtained by applying the chain rule, if we consider that $\boldsymbol{f}$ depends on $\boldsymbol{q}$ through $\boldsymbol{r}$ and $\boldsymbol{r}_j$:

$$\frac{\partial \boldsymbol{f}}{\partial \boldsymbol{q}} = \frac{\partial \boldsymbol{f}}{\partial \boldsymbol{r}^{\mathcal{R}}} \frac{\partial \boldsymbol{r}^{\mathcal{R}}}{\partial \boldsymbol{q}} + \sum_{j=2}^{N-1} \frac{\partial \boldsymbol{f}}{\partial \boldsymbol{r}_j^{\mathcal{R}}} \frac{\partial \boldsymbol{r}_j^{\mathcal{R}}}{\partial \boldsymbol{q}} \tag{4.35}$$

Reordering the terms in the summation, we obtain

$$\begin{aligned} \frac{\partial \boldsymbol{f}}{\partial \boldsymbol{q}} = -\sum_{j=2}^{N-1} \mu_j \Bigg\{ & \left(\frac{\boldsymbol{I}_3}{\left\| \boldsymbol{r}^{\mathcal{R}} - \boldsymbol{r}_j^{\mathcal{R}} \right\|^3} - 3 \frac{\left(\boldsymbol{r}^{\mathcal{R}} - \boldsymbol{r}_j^{\mathcal{R}} \right) \left(\boldsymbol{r}^{\mathcal{R}} - \boldsymbol{r}_j^{\mathcal{R}} \right)^{\top}}{\left\| \boldsymbol{r}^{\mathcal{R}} - \boldsymbol{r}_j^{\mathcal{R}} \right\|^5} \right) \left(\frac{\partial \boldsymbol{r}^{\mathcal{R}}}{\partial \boldsymbol{q}} - \frac{\partial \boldsymbol{r}_j^{\mathcal{R}}}{\partial \boldsymbol{q}} \right) \\ & + \left(\frac{\boldsymbol{I}_3}{\left\| \boldsymbol{r}_j^{\mathcal{R}} \right\|^3} - 3 \frac{\boldsymbol{r}_j^{\mathcal{R}} \boldsymbol{r}_j^{\mathcal{R}\top}}{\left\| \boldsymbol{r}_j^{\mathcal{R}} \right\|^5} \right) \frac{\partial \boldsymbol{r}_j^{\mathcal{R}}}{\partial \boldsymbol{q}} \Bigg\} \end{aligned} \tag{4.36}$$

where $\boldsymbol{I}_3$ is the 3-dimensional identity matrix, $\boldsymbol{y}\, \boldsymbol{y}^{\top}$ represents the outer product of the vector $\boldsymbol{y} \in \mathbb{R}^3$ with itself, which results in a 3-dimensional matrix, and

$$\frac{\partial \boldsymbol{r}^{\mathcal{R}}}{\partial \boldsymbol{q}} = \begin{bmatrix} -\frac{\cos\sigma}{q_3 s^2} & -\frac{\sin\sigma}{q_3 s^2} & -\frac{s+q_3}{q_3^2 s^2} & 0 & 0 & 0 & 0 & \frac{u}{q_3 s^2} \\ 0 & 0 & 0 & 0 & 0 & 0 & 0 & 0 \\ 0 & 0 & 0 & 0 & 0 & 0 & 0 & 0 \end{bmatrix}, \tag{4.37}$$

$$\frac{\partial \boldsymbol{r}_j^{\mathcal{R}}}{\partial \boldsymbol{q}} = \begin{bmatrix} 0 & 0 & 0 & | & & \cdots & | & & | \\ 0 & 0 & 0 & \boldsymbol{Q}^\top \frac{\partial \boldsymbol{P}^\top}{\partial q_4} \boldsymbol{R} \boldsymbol{r}_j^{\mathcal{R}} & \cdots & \boldsymbol{Q}^\top \frac{\partial \boldsymbol{P}^\top}{\partial q_7} \boldsymbol{R} \boldsymbol{r}_j^{\mathcal{R}} & \frac{\partial \boldsymbol{Q}^\top}{\partial \sigma} \boldsymbol{Q} \boldsymbol{r}_j^{\mathcal{R}} \\ 0 & 0 & 0 & | & & \cdots & | & & | \end{bmatrix}, \tag{4.38}$$

where the derivatives of the $\boldsymbol{P}$ matrix are given by Eq. (D.10), and

$$\frac{\partial \boldsymbol{Q}^\top}{\partial \sigma} = \begin{bmatrix} -\sin\sigma & -\cos\sigma & 0 \\ \cos\sigma & -\sin\sigma & 0 \\ 0 & 0 & 0 \end{bmatrix}. \tag{4.39}$$

4.5 Linearity indices

In this section we introduce two indices that allow one to estimate when the uncertainty distribution can be propagated using linear theory.

4.5.1 Orbit Condition Code

The Orbit Condition Code (OCC), also referred to as *Uncertainty Parameter*[1] U, provides an estimate of the rate of change of the longitude in a logarithmic scale, and takes integer values from 0 to 9. A value of 0 is assigned to very well determined orbits and 9 implies a very imprecise orbit. A simple algorithm to calculate the OCC is as follows. First, we calculate the longitude runoff $\dot{\lambda}$, measured in seconds of arc per decade as

$$\dot{\lambda} = \left(e\, \sigma_{T_p}\big|_{\mathrm{d}} + 10\, \sigma_P|_{\mathrm{d}}\, \frac{1}{P|_{\mathrm{y}}} \right) k \frac{1}{P|_{\mathrm{y}}} \times 3600 \times 3 \tag{4.40}$$

where $\sigma_{T_p}\big|_{\mathrm{d}}$ is the uncertainty in the time of perihelion passage in days, $P|_{\mathrm{y}}$ is the orbital period in years, $\sigma_P|_{\mathrm{d}}$ is the uncertainty in the orbital period in days and $k = \frac{180}{\pi} \times 0.01720209895\,\mathrm{deg}$ is the Gaussian constant in degrees. Then, one can calculate the OCC as

$$OCC = \left\lfloor \ln \frac{\dot{\lambda}}{\dot{\lambda}_0} + 1 \right\rfloor, \tag{4.41}$$

where $\lfloor y \rfloor$ is the floor function, and $\dot{\lambda}_0$ is a constant such that

$$\dot{\lambda}_0 = \frac{\ln 648000}{9} \simeq 1.49. \tag{4.42}$$

[1] `http://www.minorplanetcenter.net/iau/info/UValue.html`, accessed on 2018 May 21

To obtain a better understanding of the evolution of the longitude runoff, we will also consider the OCC without applying the floor function.

Larger values of OCC cause a uncertainty distribution to grow in shorter times, even if the initial uncertainty distribution is small. A method based on Cartesian coordinates will have its performance degraded as the uncertainty growth will not be contained on the orbit.

By writing Eq. (4.40) as a function of the Dromo variables $\boldsymbol{q}$, we can calculate the OCC in the Dromo formulation. First note that the orbital period P can be written as

$$P = 2\pi a^{3/2} = \frac{2\pi}{\left(q_3^2 - q_1^2 - q_2^2\right)^{3/2}}. \tag{4.43}$$

The time of periapsis passage T_p can be calculated starting from Kepler's Equation

$$M = n\left(\tau - T_p\right) = E - e\sin E. \tag{4.44}$$

The above equation can be rearranged to yield

$$T_p = \tau - \frac{E - e\sin E}{n}. \tag{4.45}$$

We can easily obtain $\sin E$ by using the classical equations that relate trigonometric functions of the eccentric and true anomalies [7, pp. 158 – 159]. In particular, starting from

$$\sin E = \frac{\sqrt{1-e^2}\sin\nu}{1 + e\cos\nu}, \tag{4.46}$$

it is straightforward to obtain

$$\sin E = \frac{\sqrt{q_3^2 - q_1^2 - q_2^2}\left(q_1\sin\sigma - q_2\cos\sigma\right)}{\sqrt{q_1^2 + q_2^2}\left(q_3 + q_1\cos\sigma + q_2\sin\sigma\right)} = \frac{u}{s}\frac{\sqrt{q_3^2 - q_1^2 - q_2^2}}{\sqrt{q_1^2 + q_2^2}}, \tag{4.47}$$

where s and u are the transversal and radial velocity and are given be Eqs. (4.9) and (4.10), respectively. By multiplying by the orbital eccentricity, one of the terms in Kepler's equation is obtained as

$$e\sin E = \frac{u}{s}\frac{\sqrt{q_3^2 - q_1^2 - q_2^2}}{q_3}. \tag{4.48}$$

To express the eccentric anomaly E, it is possible to write a similar expression for $\cos E$ and use the $\mathrm{atan2}$ function. However, a simplified formula can be obtained by the use of the elegant relation given by Broucke et al [20]

$$E = \nu - 2\,\mathrm{atan}\left(\frac{e\sin\nu}{1 + \sqrt{1-e^2}\cos\nu}\right) \tag{4.49}$$

yielding the simple result

$$E = \sigma - \beta - 2\,\mathrm{atan}\left(\frac{u}{s + \sqrt{q_3^2 - q_1^2 - q_2^2}}\right) \tag{4.50}$$

Finally, The mean motion reads

$$n = \frac{1}{a^{3/2}} = (q_3^2 - q_1^2 - q_2^2)^{3/2}, \tag{4.51}$$

and combining all the previous results

$$T_p = \tau - \frac{\sigma - \beta - 2\,\mathrm{atan}\left(\frac{u}{s+\sqrt{q_3^2-q_1^2-q_2^2}}\right)}{(q_3^2 - q_1^2 - q_2^2)^{3/2}} + \frac{u}{s}\frac{1}{q_3\left(q_3^2 - q_1^2 - q_2^2\right)}. \tag{4.52}$$

Note that neither P nor T_p depend on the Dromo elements corresponding to quaternion components $q_4, \ldots q_7$. The standard deviations of P and T_p can be calculated using their gradient with respect to the Dromo state vector for frozen time and the Dromo covariance matrix $\boldsymbol{P}$

$$\sigma_P^2 = \frac{\partial P}{\partial \boldsymbol{q}} \boldsymbol{C} \frac{\partial P}{\partial \boldsymbol{q}}^\top \tag{4.53}$$

$$\sigma_{T_p}^2 = \frac{\partial T_p}{\partial \boldsymbol{q}} \boldsymbol{C} \frac{\partial T_p}{\partial \boldsymbol{q}}^\top \tag{4.54}$$

The gradient of the orbital period $\frac{\partial P}{\partial \boldsymbol{q}}$ reads

$$\frac{\partial P}{\partial \boldsymbol{q}} = \begin{bmatrix} \frac{6\pi q_1}{q_3^2\left(1-q_1^2-q_2^2\right)^{5/2}} & \frac{6\pi q_2}{q_3^2\left(1-q_1^2-q_2^2\right)^{5/2}} & \frac{-6\pi}{q_3^4\left(1-q_1^2-q_2^2\right)^{3/2}} & 0 & 0 & 0 & 0 & 0 \end{bmatrix} \tag{4.55}$$

The gradient of the time of periapsis passage $\frac{\partial T_p}{\partial \boldsymbol{q}}$ takes a more complex expression. To give compact formulae, we will use auxiliary variables to get the following results:

$$\begin{aligned} \frac{\partial T_p}{\partial q_1} = &- a\cos E \frac{a\,u q_1 - \sin\sigma}{e q_3 s} - a\,u \frac{2q_1 + q_3\cos\sigma}{e^2 q_3^2 s^2} + 3E q_1 a^{5/2} + \\ &\frac{a\,u\cos\sigma}{q_3 s^2} - a\frac{2a\,u q_1 + \sin\sigma}{q_3 s}, \end{aligned} \tag{4.56}$$

$$\begin{aligned} \frac{\partial T_p}{\partial q_2} = &- a\cos E \frac{a\,u q_2 + \cos\sigma}{e q_3 s} - a\,u \frac{2q_2 + q_3\sin\sigma}{e^2 q_3^2 s^2} + 3E q_2 a^{5/2} + \\ &\frac{a\,u\sin\sigma}{q_3 s^2} - a\frac{2a\,u q_2 - \cos\sigma}{q_3 s}, \end{aligned} \tag{4.57}$$

$$\frac{\partial T_p}{\partial q_3} = \frac{a^2 u \cos E}{e\, s} - a\, u \frac{q_1 \cos\sigma + q_2 \sin\sigma}{e^2 q_3^2 s^2} - 3E q_3 a^{5/2} + a\, u \frac{s + q_3 + 2a q_3^2 s}{(q_3 s)^2}, \tag{4.58}$$

$$\frac{\partial T_p}{\partial q_j} = 0, \qquad j = 4, \dots 7, \tag{4.59}$$

$$\frac{\partial T_p}{\partial \sigma} = \frac{1}{q_3^3 \left(1 + e\cos\nu\right)^2}, \tag{4.60}$$

where a and e are given by Eqs. (D.1a) and (D.1b), respectively, and with

$$\cos E = \frac{q_1^2 + q_2^2 + q_1 q_3 \cos\sigma + q_2 q_3 \sin\sigma}{s\sqrt{q_1^2 + q_2^2}}. \tag{4.61}$$

4.5.2 Close approach linearization error

The second index Γ is a measure of the error induced by the linearization of the third-body perturbing acceleration, especially important during close approaches with a large uncertainty distribution. Γ is inspired by a simple 1-dimensional model in which for any point in the uncertainty distribution close to the perturbing third body, the perturbing acceleration can be expanded in power series as

$$f_j \simeq \mu_j \frac{1}{\left(\rho_{\text{nom}} + \delta\rho\right)^2} = \mu_j \frac{1}{\rho_{\text{nom}}^2} \left(1 - 2\frac{\delta\rho}{\rho_{\text{nom}}} + 3\left(\frac{\delta\rho}{\rho_{\text{nom}}}\right)^2 + \dots\right), \tag{4.62}$$

where $\rho = r - r_j$ and the subindex nom refers to the nominal orbit and $\delta\rho = \rho - \rho_{\text{nom}}$. We define Γ as the first term neglected in the linearization of the above expression:

$$\Gamma = 3\mu_j \frac{\delta\rho^2}{\rho_{\text{nom}}^4}, \tag{4.63}$$

which has units of $\tilde{r}\tilde{n}^2$.

In orbits in three dimensions and as a first approximation, the uncertainty distribution is expected to be elongated along the velocity vector direction as sketched in Fig. 4.4, and the position of the extrema of the uncertainty distribution $\boldsymbol{\rho}$ reads

$$\boldsymbol{\rho} = \boldsymbol{\rho}_{\text{nom}} \pm \delta\boldsymbol{\varrho} \tag{4.64}$$

where $\delta\boldsymbol{\varrho}$, the relative position vector of the tail of the distribution with respect to its center, can be written as

$$\delta\boldsymbol{\varrho} = \boldsymbol{v}\sigma_\tau \simeq \boldsymbol{v}\frac{\mathrm{d}\tau}{\mathrm{d}\sigma}\sigma_\sigma = \boldsymbol{v}\frac{1}{\eta_3 s^2}\sigma_\sigma \tag{4.65}$$

with σ_τ and σ_σ being the standard deviation of the real and the fictitious time respectively. The norm of this vector is the along-orbit drift:

$$\delta\varrho = v\frac{1}{\eta_3 s^2}\sigma_\sigma = \sqrt{u^2+s^2}\frac{1}{q_3 s^2}\sigma_\sigma. \tag{4.66}$$

Finally, $\delta\rho$ can be approximated by the difference between ρ_{nom} and the projection of $\boldsymbol{\rho}$ on the $\boldsymbol{\rho}_{\mathrm{nom}}$ direction

$$\delta\rho \simeq \left|\rho_{\mathrm{nom}} - \boldsymbol{\rho}\cdot\frac{\boldsymbol{\rho}_{\mathrm{nom}}}{\rho_{\mathrm{nom}}}\right| = \left|\delta\boldsymbol{\varrho}\cdot\frac{\boldsymbol{\rho}_{\mathrm{nom}}}{\rho_{\mathrm{nom}}}\right| \tag{4.67}$$

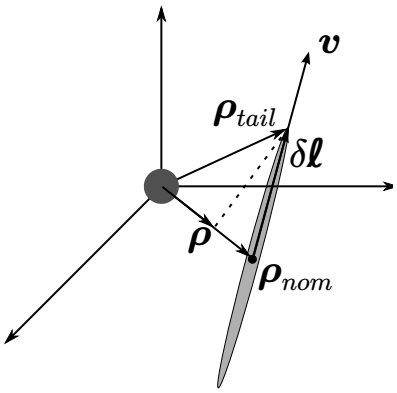

Figure 4.4: Geometry of close approach with uncertainty. $\boldsymbol{\rho}_{\mathrm{nom}}$ is in general located at an arbitrary point of the space.

During a close approach, a high value of Γ indicates that the linearization of the gravitational force may induce large errors in the results. An empiric threshold will be suggested on section 4.7.

4.6 Real case application

In order to assess the accuracy of the proposed method, we calculated the Dromo STM for an extensive list of asteroids and compared the results with a Monte Carlo method

which was performed for samples randomly drawn from the initial uncertainty distribution, propagating the orbit of each of the points individually. Additionally, the STM employing a Cartesian linear method was also included in the comparisons of our study. The number of MC samples was chosen as $N_{MC} = 10^3$, and the execution time of the linear methods was about 5 times smaller than the sample-wise numerical propagation.

The orbital elements and the 1-σ covariance matrices were obtained from the NEODyS database[1]. NEODyS, maintained by the University of Pisa and the SpaceDyS company, offers this information for two different epochs: *Near middle of observational arc* and *Near present day*. We chose the former, aiming to minimize the deviations from Gaussianity caused by the orbital motion. The data used in the simulations is presented in Appendix E. To construct the dimensionless variables, we chose $\tilde{r} = 1$ au, leading to $\tilde{n} = 2\pi$ y^{-1}.

The analyzed asteroids can be divided into three categories:

1. Those whose uncertainty distribution is small, and thus both the Dromo STM and the Cartesian STM can reproduce the results of the MC method. Examples of these asteroids are 2002AA29 and 469219 (2016HO3).

2. Those which have a moderate-size uncertainty distribution but have not been strongly perturbed by a close approach. In these cases, even if the Cartesian STM based method fails to reproduce the non-linear orbital motion, the Dromo method follows the MC results with a reasonable accuracy until a catastrophic close approach occurs. Examples of these asteroids will be given below.

3. Those which are strongly affected by the non-linear perturbation induced by the Earth gravitational force during close approaches, like 2016CA138. In some cases, they are discovered in the vicinity of the Earth and the orbit fitting process yields an initial Gaussian distribution that rapidly becomes non-Gaussian because of the Earth influence.

The asteroids in the first category are usually characterized by a small OCC and close approaches with small Γ, so their uncertainty distribution can be considered to evolve linearly with very high accuracy.

[1] `http://newton.dm.unipi.it/neodys/`, accessed on 2018 May 22

The third category is comprised of asteroids that usually have faced a close approach with a large value of Γ. After this encounter, the linearity of the motion of the uncertainty cloud is lost.

The second category consists of intermediate cases between the two others. They are characterized by a small to moderate OCC, and the range of time validity of the proposed method is governed by Γ at the incoming close approaches. During a future close approach, if the distance between the asteroid and the encountering body is small and the along-orbit drift is large, they may transit into the third category.

Table 4.1 shows some selected examples of the second category of asteroids, as well as the initial and final propagation time and the initial OCC. The NEODyS raw data employed is listed in Appendix E.

Table 4.1: Selected Asteroids

Name	Initial propagation time	Final propagation time	Initial OCC
2000SG344	1999 Nov 08 12:10:56	2050 Jun 30 00:00:00	4
2011AM37	2011 Jan 14 01:29:15	2050 Jun 30 00:00:00	7
2013HO	2013 Apr 18 21:59:11	2050 Jun 30 00:00:00	6
2016DJ	2016 Mar 05 02:31:27	2050 Jun 30 00:00:00	4

4.6.1 2000SG344

The first selected asteroid, 2000SG344, is a small body with absolute magnitude $H = 24.7$. It was discovered in 2000 right before a close approach with the Earth, and has multiple predictions for very deep close approaches in the future (see Table 4.2 for a list until 2050).

The propagation for the orbit uncertainty distribution of this asteroid begins some months before a close approach in which distance between the nominal orbit and the asteroid is 0.04 au or $3.98\, r_{\text{SoI}}$[1]. During this first close approach the uncertainty is small enough for the linearity of the motion to be preserved both using Cartesian and Dromo elements. As time evolves, the Cartesian linear method starts to show errors while the proposed method is more accurate, as can be seen in Fig. 4.5(a).

Figure 4.5(b) shows the effect of the 2028 and the first 2029 close approach in the

[1] r_{SoI} stands for radius of the Sphere of Influence of the Earth.

Table 4.2: Close approaches for 2000SG344

Epoch	Minimum distance [r_{SoI}]	Minimum distance [au]	Γ [$\tilde{r}\tilde{n}^2$]
2000 Sep 12	3.98	0.04	7.40×10^{-10}
2028 May 07	1.96	0.02	4.99×10^{-06}
2029 Feb 16	5.27	0.05	7.99×10^{-07}
2029 Jul 28	3.43	0.03	1.03×10^{-08}
2029 Nov 21	4.53	0.05	2.00×10^{-07}
2030 Sep 22	3.42	0.03	4.12×10^{-05}

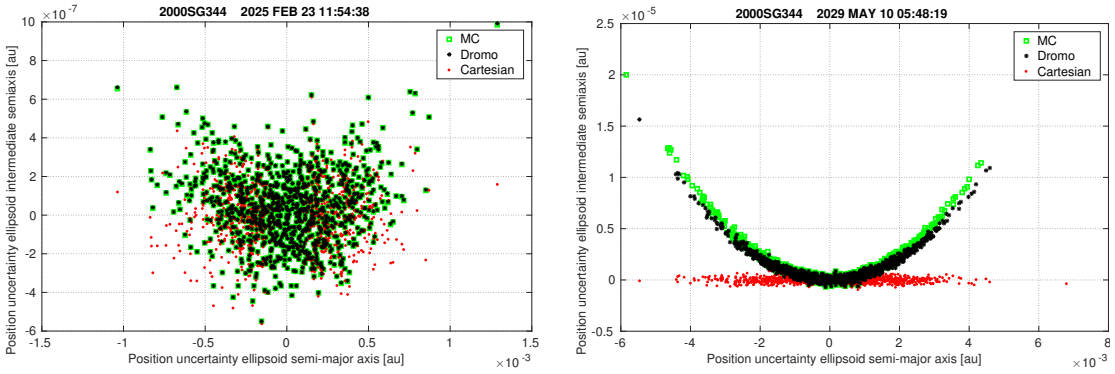

(a) Before the close approach. (b) After the close approach.

Figure 4.5: 2000SG344 Uncertainty cloud.

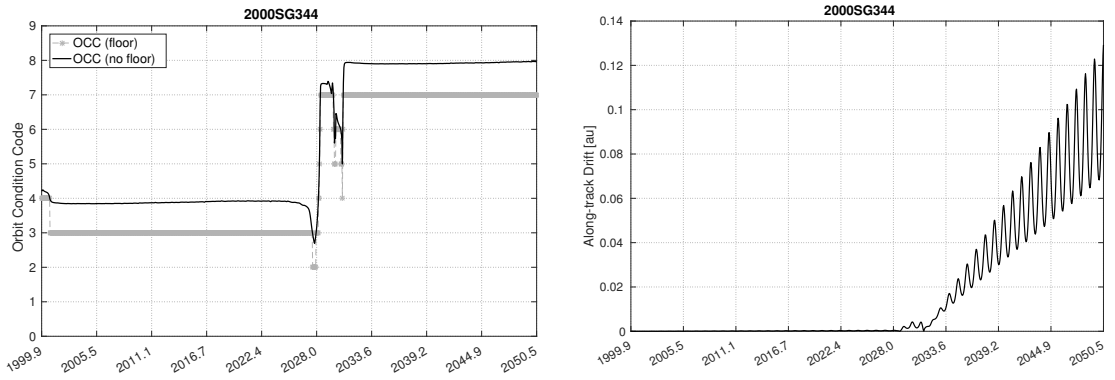

(a) OCC as a function of time (b) Along-track drift as a function of time

Figure 4.6: Non-linearity indices for 2000SG344

uncertainty distribution, where the Dromo linear method suffers only minor errors as the relatively low value of Γ suggests. As the OCC and the along-track drift grows

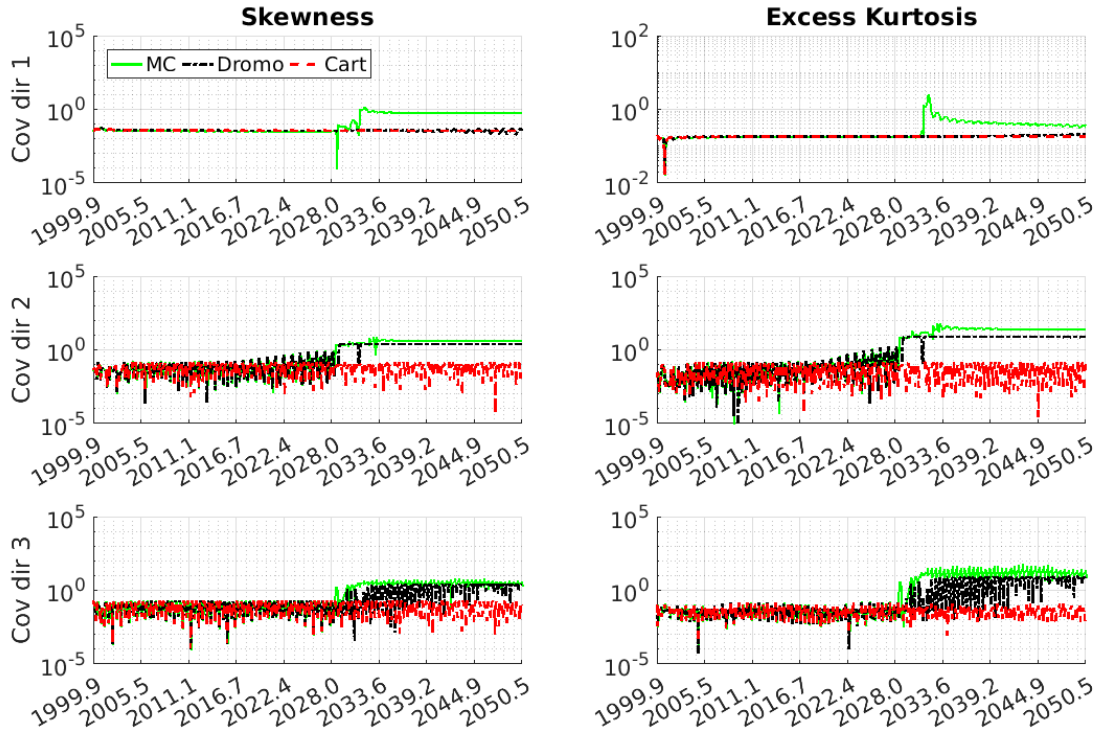

Figure 4.7: Skewness and excess kurtosis for 2000SG344 as a function of time in the position uncertainty ellipsoid main directions.

(see Fig. 4.6), the Cartesian method predicts an erroneous elliptical region, expressed in Cartesian coordinates, while the Dromo method can retain some of the non-linearities of the full model. As the along-orbit drift increases, the Dromo method performance degrades in these series of close approaches as large enough values of the index Γ are achieved.

Finally, Fig. 4.7 shows the skewness and excess kurtosis as a function of time, for the marginal distributions corresponding to the main directions of the position covariance ellipsoid, and reflects the effect of the close approaches in the distribution. These quantities are calculated via Eqs. (A.15, A.16) of Appendix A.

4.6.2 2011AM37

We start the propagation for 2011AM37 short after a close approach with nominal distance 0.0009 au on 2011 January 14. The orbit fit is poor, consequence of a reduced number of only 17 observations during a timespan of less than 2 hours. This has a

direct impact in the OCC, which starts at a high value of 7, and accordingly the along-track drift will grow at a fast pace as can be seen in Fig. 4.9.

Table 4.3: Close approaches for 2011AM37

Epoch	Minimum distance [r_{SoI}]	Minimum distance [au]	Γ [$\tilde{r}\tilde{n}^2$]
2025 Jul 22	17.57	0.18	1.21×10^{-06}
2026 Jan 13	1.30	0.01	1.79×10^{-01}
2033 Jan 22	11.58	0.12	2.18×10^{-01}

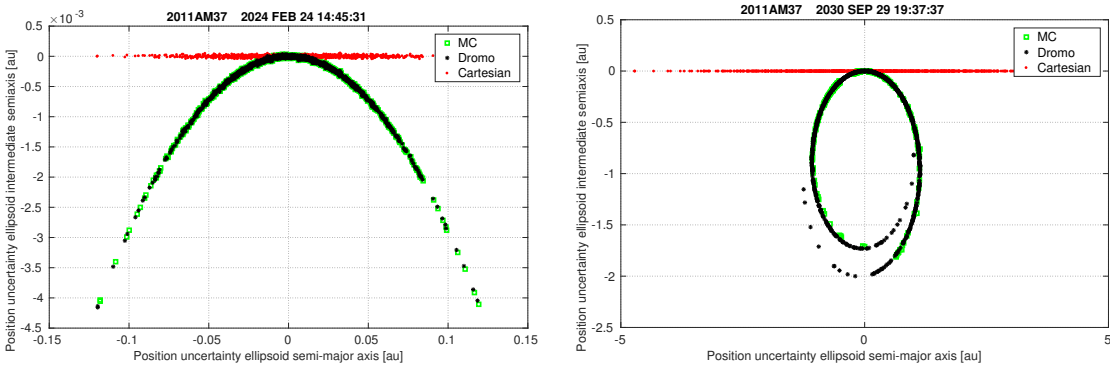

(a) Before the close approach. (b) After the close approach.

Figure 4.8: 2011AM37 Uncertainty cloud.

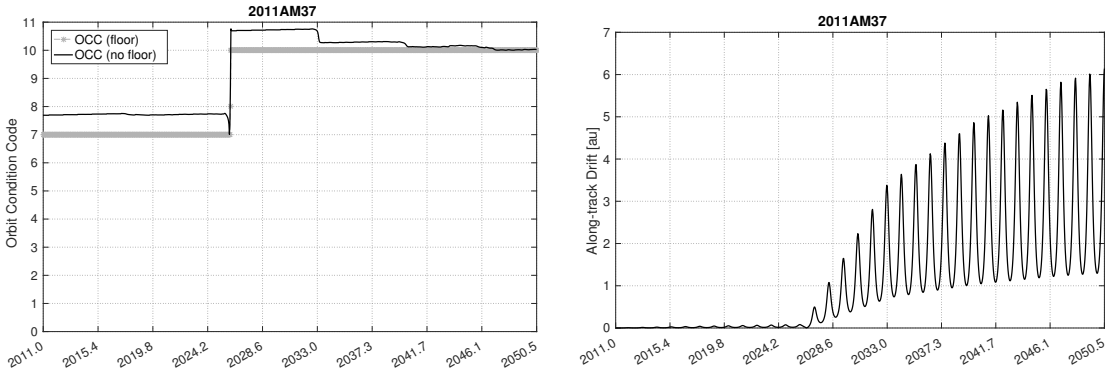

(a) OCC as a function of time (b) Along-track drift as a function of time

Figure 4.9: Non-linearity indices for 2011AM37

Such an initial orbit uncertainty leads to a quick growth of the covariance matrix, which the Cartesian method cannot reproduce. The Dromo method shows an accept-

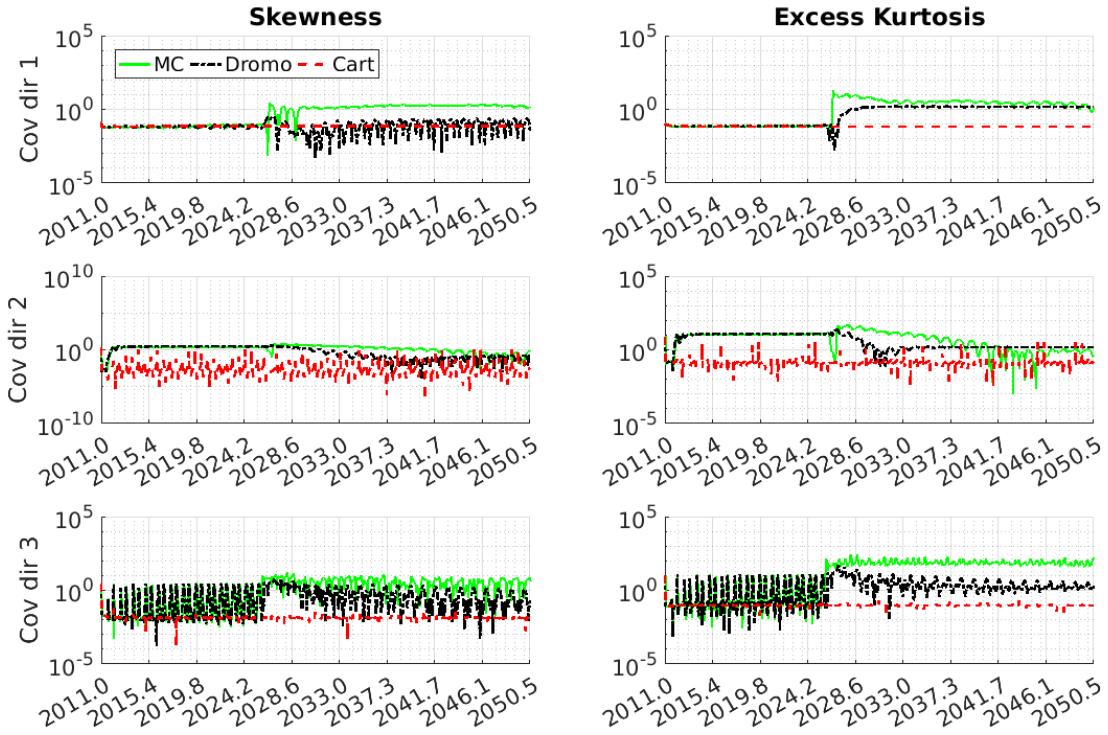

Figure 4.10: Skewness and excess kurtosis for 2011AM37 as a function of time in the position uncertainty ellipsoid main directions.

able performance, showing only minor errors in the tails of the distribution until the 2025 and 2026 close approaches. During them, the strongly non-linear perturbation of the Earth over the very large uncertainty distribution makes the motion of the MC samples to depart from Gaussianity. After these close approaches, it becomes unfeasible to apply the linear methods considered here.

4.6.3 2013HO

In the case of 2013HO, the orbit propagation starts a week after a close approach of nominal distance 0.02 au. The two close approaches of 2013 don't have a large impact on the accuracy of the Dromo based method as a small value of Γ would suggest, but the Cartesian coordinates based one starts accumulating small errors (Figure 4.11(a)) as a consequence of the large along-track drift. As Fig. 4.12 reflects, the large OCC of this asteroid makes the along-orbit uncertainty grow quickly, which causes the Cartesian method to show major errors compared to the MC solution (Figure 4.11(b)). Finally,

during the close approaches of 2040-2042, large enough values of the index Γ induces errors in the proposed method as the MC method shows a highly non-linear behavior. The skewness and excess kurtosis for the orbit uncertainty of 2013HO are shown in Fig. 4.13.

Table 4.4: Close approaches for 2013HO

Epoch	Minimum distance [r_{SoI}]	Minimum distance [au]	Γ [$\tilde{r}\tilde{n}^2$]
2013 Apr 11	1.90	0.02	1.57×10^{-08}
2013 Oct 04	17.03	0.17	5.12×10^{-09}
2040 Oct 21	13.97	0.14	1.30×10^{-06}
2041 Apr 14	9.54	0.10	5.28×10^{-06}
2041 Oct 12	7.77	0.08	1.09×10^{-05}
2042 Apr 10	12.09	0.12	1.89×10^{-06}

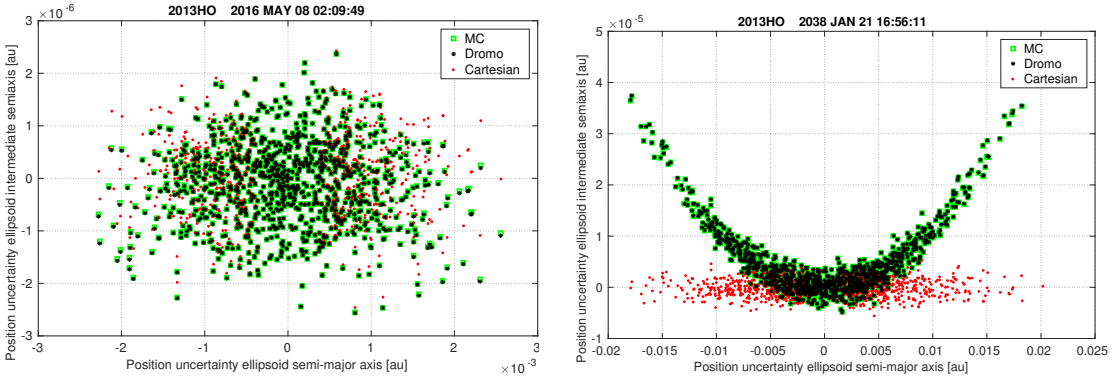

(a) After the first close approaches. (b) Before the final close approaches.

Figure 4.11: 2013HO Uncertainty cloud.

4.6.4 2016DJ

As the previously analyzed asteroids, the initial epoch is after a close approach with the Earth, around one month before in this case, and with minimum distance 0.04 au. A very shallow close-approach on 2017 with a small value of Γ does not have a large effect on the validity of the linear methods , but the high value of OCC leads to a growing along-orbit drift (see Fig. 4.15). This makes the Cartesian coordinates based method to lose accuracy even in the absence of intermediate close approaches, as can be seen

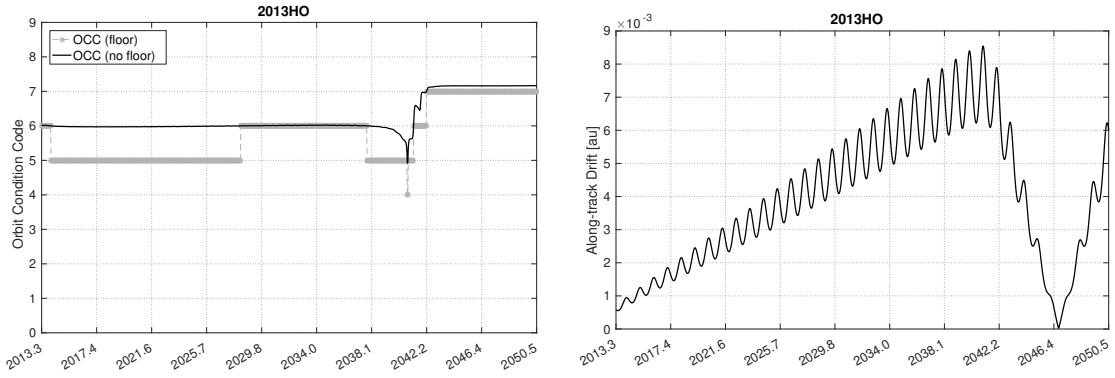

(a) OCC as a function of time (b) Along-track drift as a function of time

Figure 4.12: Non-linearity indices for 2013HO

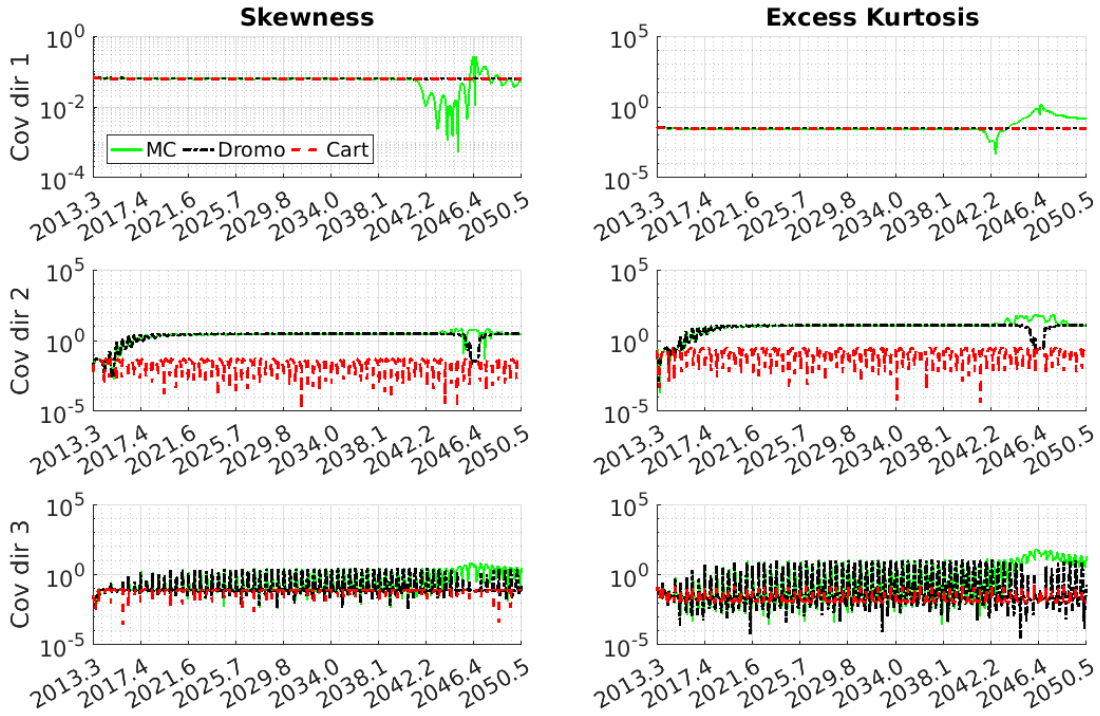

Figure 4.13: Skewness and excess kurtosis for 2013HO as a function of time in the position uncertainty ellipsoid main directions.

in Fig. 4.14(a). The proposed method shows a good performance, only limited by by the close approaches of 2042-2046 (Figure 4.14(b)). This is reflected in the higher order moments shown in Fig. 4.16.

Table 4.5: Close approaches for 2016DJ

Epoch	Minimum distance [r_{SoI}]	Minimum distance [au]	$\Gamma\ [\tilde{r}\tilde{n}^2]$
2017 Feb 13	19.39	0.19	9.81×10^{-12}
2042 Aug 08	3.01	0.03	1.13×10^{-07}
2043 Jun 11	17.32	0.17	3.37×10^{-09}
2043 Oct 15	13.87	0.14	1.66×10^{-09}
2044 Apr 21	18.84	0.19	2.87×10^{-10}
2045 Feb 23	10.12	0.10	3.88×10^{-07}
2046 Feb 10	10.90	0.11	5.61×10^{-07}

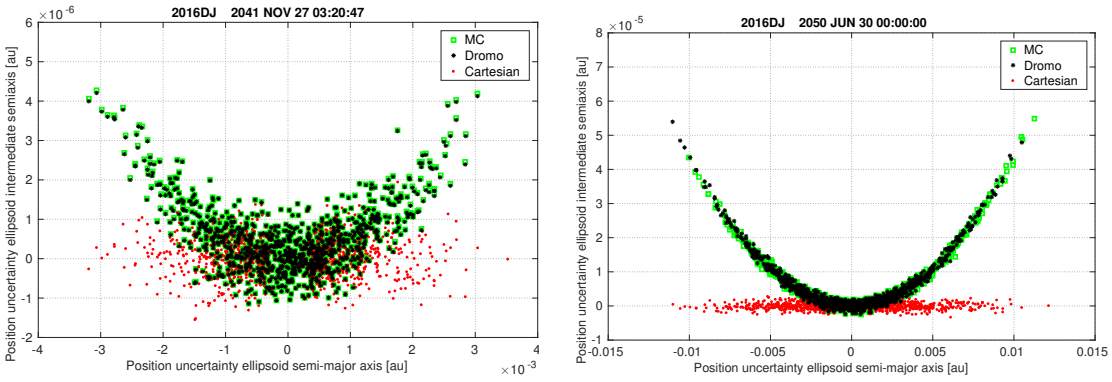

(a) Before the close approach. (b) After the close approach.

Figure 4.14: 2016DJ Uncertainty cloud.

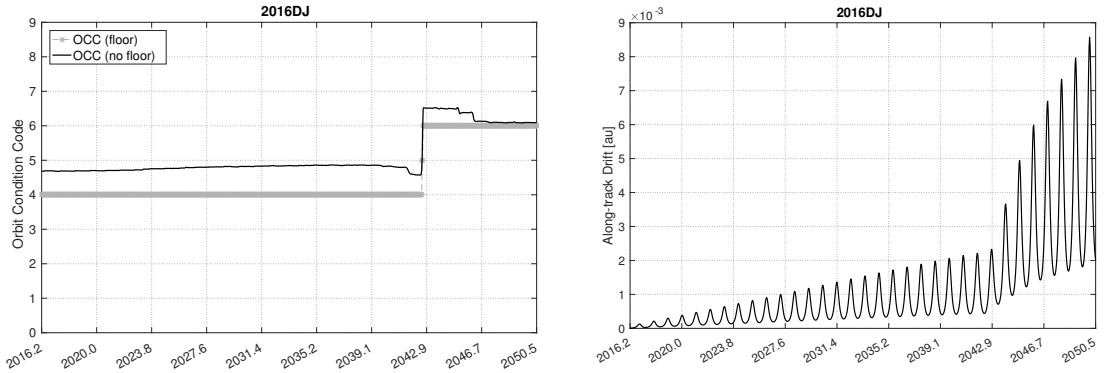

(a) OCC as a function of time (b) Along-track drift as a function of time

Figure 4.15: Non-linearity indices for 2016DJ

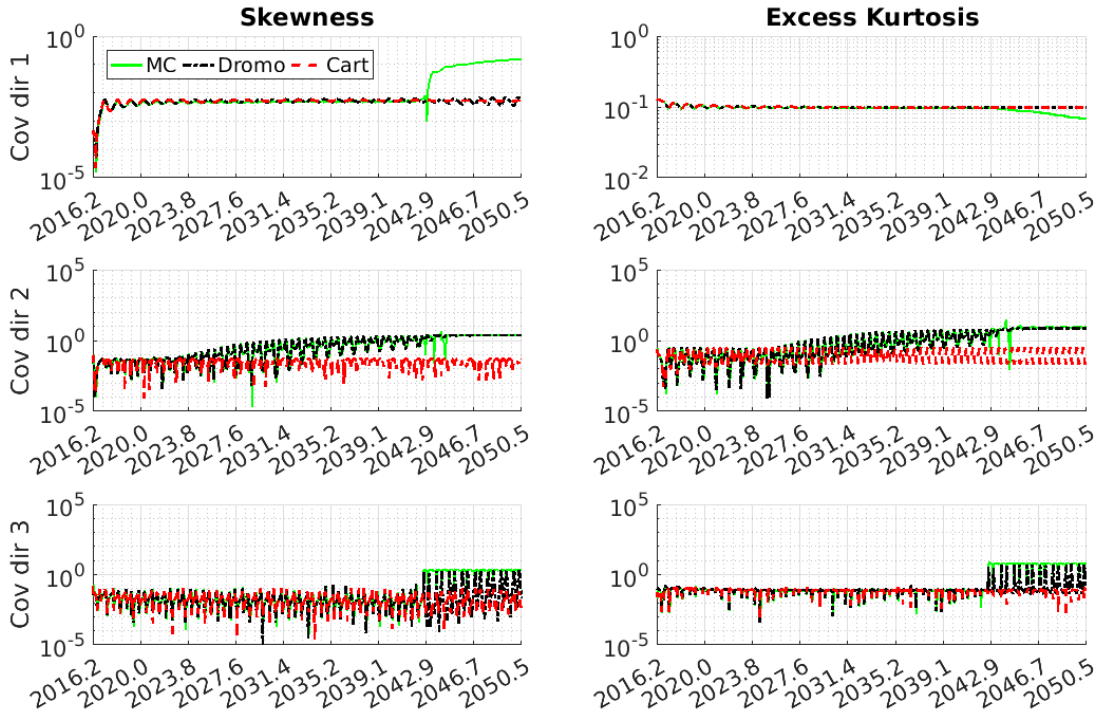

Figure 4.16: Skewness and excess kurtosis for 2016DJ as a function of time in the position uncertainty ellipsoid main directions.

4.7 Discussion on the linear indices

The two indices introduced in section 4.5 have different impact on the presented technique and on the Cartesian linear method.

The OCC is more important for the Cartesian linear method, as a large value will cause considerable errors since the growing along-orbit drift cannot follow the curvature of the orbit when employing this approach. The Dromo method is not strongly affected by the OCC, as the along-orbit drift is taken into account with the fictitious time uncertainty. However, minor effects may still arise as the perturbations are linearized around the nominal orbit, and variations of σ outside of the linearity may introduce errors in our formulation.

The close-approach linearization error index Γ affects both methods as the Dromo linear method employs a Cartesian gravity gradient matrix, later transformed into Dromo elements. Thus, non-linearities appearing during close approaches will degrade the solution provided by both methods, which according to the simulation

results seems to happen for $\Gamma > 10^{-6}$.

4.8 Anomaly Transition Tensor

In chapter 2, it was determined that most nonlinear variable in the weakly-perturbed orbital motion is usually the anomaly. This is especially the case for orbits of high eccentricity, as the neglected terms by approximating Eq. (4.15h) by the last row of the STM given by Eq. (4.20) are all multiplied by powers of u, which is proportional to the eccentricity.

Thus, in the Dromo formulation it is convenient to expand the fictitious time σ to higher orders:

$$\begin{aligned}\delta\sigma = &\sum_{i=1,2,3,8} \Phi_{8,i}\,\delta q_{0,i} \\ &+ \frac{1}{2}\sum_{(i,j)=1,2,3,8}\sum \Phi_{8,ij}\,\delta q_{0,i}\delta q_{0,j} \\ &+ \frac{1}{3!}\sum_{(i,j,k)=1,2,3,8}\sum\sum \Phi_{8,ijk}\,\delta q_{0,i}\delta q_{0,j}\delta q_{0,k} + \dots\end{aligned} \tag{4.68}$$

where we exploited that g_8 does not depend on $q_4, \dots q_7$ to reduce the summation indices domain. Note that $\Phi_{8,i}$ correspond to the terms already present in the STM. To solve for the coefficients, we must use substitute Eq. (4.68) into Eq. (4.15h)

$$\frac{\mathrm{d}\Phi_{8,i}}{\mathrm{d}\tau} = \frac{\partial g_8}{\partial q_i} \tag{4.69a}$$

$$\frac{\mathrm{d}\Phi_{8,ij}}{\mathrm{d}\tau} = \frac{\partial^2 g_8}{\partial q_i \partial q_j} \tag{4.69b}$$

$$\frac{\mathrm{d}\Phi_{8,ijk}}{\mathrm{d}\tau} = \frac{\partial^3 g_8}{\partial q_i \partial q_j \partial q_k} \tag{4.69c}$$

For $(i,j,k) = 1,2,3,8$. The right hand sides take simple values because g_8 does not depend explicitly on the non-Keplerian perturbation, so closed-form formulae can be obtained for any scenario. The initial conditions for the equations above are all identically equal to zero, except for the term $\Phi_{8,8} = 1$.

The number of necessary terms grow exponentially with the order of the expansion. However, symmetries allow to reduce the number of terms that must be calculated

$$\Phi_{8,ij} = \Phi_{8,ji} \tag{4.70a}$$

$$\Phi_{8,ijk} = \Phi_{8,ijk} = \Phi_{8,jik} = \Phi_{8,jki} = \Phi_{8,kij} = \Phi_{8,kji} \tag{4.70b}$$

It is a a known result that the number of independent components of a symmetric tensor of rank r in d dimensions is[1]

$$\binom{d+r-1}{r} = \frac{(d+r-1)\,(d+r)\ldots(d+1)\,d}{r!} \tag{4.71}$$

Then, to include quadratic terms, 10 terms are needed in the integration, retaining cubic terms requires additional 20 coefficients, the quadratic terms would require another 35 coefficients and so on.

4.8.1 Formulae for the quadratic terms

In this section, we give expressions for Eq. (4.69b)

$$\frac{\mathrm{d}\Phi_{8,1,1}}{\mathrm{d}\tau} = 2q_3\cos^2\sigma, \tag{4.72a}$$
$$\frac{\mathrm{d}\Phi_{8,1,2}}{\mathrm{d}\tau} = 2q_3\cos\sigma\sin\sigma, \tag{4.72b}$$
$$\frac{\mathrm{d}\Phi_{8,1,3}}{\mathrm{d}\tau} = 2\,(q_3+s)\cos\sigma, \tag{4.72c}$$
$$\frac{\mathrm{d}\Phi_{8,1,4}}{\mathrm{d}\tau} = -2q_3\,(u\cos\sigma + s\sin\sigma)\,, \tag{4.72d}$$
$$\frac{\mathrm{d}\Phi_{8,2,2}}{\mathrm{d}\tau} = 2q_3\sin^2\sigma, \tag{4.72e}$$
$$\frac{\mathrm{d}\Phi_{8,2,3}}{\mathrm{d}\tau} = 2q_3\sin\sigma + 2s\sin\sigma, \tag{4.72f}$$
$$\frac{\mathrm{d}\Phi_{8,2,4}}{\mathrm{d}\tau} = 2q_3\,(s\cos\sigma - u\sin\sigma)\,, \tag{4.72g}$$
$$\frac{\mathrm{d}\Phi_{8,3,3}}{\mathrm{d}\tau} = 2q_3 + 4s, \tag{4.72h}$$
$$\frac{\mathrm{d}\Phi_{8,3,4}}{\mathrm{d}\tau} = -2q_3u - 2s\,u, \tag{4.72i}$$
$$\frac{\mathrm{d}\Phi_{8,4,4}}{\mathrm{d}\tau} = 2q_3\left(u^2 + s\,(q_3 - s)\right) \tag{4.72j}$$

4.8.2 Formulae for the cubic terms

In this section, we give expressions for Eq. (4.69c)

$$\frac{\mathrm{d}\Phi_{8,1,1,1}}{\mathrm{d}\tau} = 0, \tag{4.73a}$$

[1] `http://www.physics.mcgill.ca/~yangob/symmetric%20tensor.pdf` Accessed on 2018 May 21

$$\frac{\mathrm{d}\Phi_{8,1,1,2}}{\mathrm{d}\tau} = 0, \tag{4.73b}$$
$$\frac{\mathrm{d}\Phi_{8,1,1,3}}{\mathrm{d}\tau} = 2\cos^2\sigma, \tag{4.73c}$$
$$\frac{\mathrm{d}\Phi_{8,1,1,4}}{\mathrm{d}\tau} = -4q_3\cos\sigma\sin\sigma, \tag{4.73d}$$
$$\frac{\mathrm{d}\Phi_{8,1,2,2}}{\mathrm{d}\tau} = 0, \tag{4.73e}$$
$$\frac{\mathrm{d}\Phi_{8,1,2,3}}{\mathrm{d}\tau} = 2\cos\sigma\sin\sigma, \tag{4.73f}$$
$$\frac{\mathrm{d}\Phi_{8,1,2,4}}{\mathrm{d}\tau} = 2q_3\left(\cos^2\sigma - \sin^2\sigma\right), \tag{4.73g}$$
$$\frac{\mathrm{d}\Phi_{8,1,3,3}}{\mathrm{d}\tau} = 4\cos\sigma, \tag{4.73h}$$
$$\frac{\mathrm{d}\Phi_{8,1,3,4}}{\mathrm{d}\tau} = -2\left(u\cos\sigma + (s+q_3)\sin\sigma\right), \tag{4.73i}$$
$$\frac{\mathrm{d}\Phi_{8,1,4,4}}{\mathrm{d}\tau} = 2q_3\left(2u\sin\sigma + (q_3-2s)\cos\sigma\right), \tag{4.73j}$$
$$\frac{\mathrm{d}\Phi_{8,2,2,2}}{\mathrm{d}\tau} = 0, \tag{4.73k}$$
$$\frac{\mathrm{d}\Phi_{8,2,2,3}}{\mathrm{d}\tau} = 2\sin^2\sigma, \tag{4.73l}$$
$$\frac{\mathrm{d}\Phi_{8,2,2,4}}{\mathrm{d}\tau} = 4q_3\cos\sigma\sin\sigma, \tag{4.73m}$$
$$\frac{\mathrm{d}\Phi_{8,2,3,3}}{\mathrm{d}\tau} = 4\sin\sigma, \tag{4.73n}$$
$$\frac{\mathrm{d}\Phi_{8,2,3,4}}{\mathrm{d}\tau} = 2\left(q_3+s\right)\cos\sigma - 2u\sin\sigma, \tag{4.73o}$$
$$\frac{\mathrm{d}\Phi_{8,2,4,4}}{\mathrm{d}\tau} = 2q_3\sin\sigma\left(q_3-2s\right) - 4q_3u\cos\sigma, \tag{4.73p}$$
$$\frac{\mathrm{d}\Phi_{8,3,3,3}}{\mathrm{d}\tau} = 6, \tag{4.73q}$$
$$\frac{\mathrm{d}\Phi_{8,3,3,4}}{\mathrm{d}\tau} = -4u, \tag{4.73r}$$
$$\frac{\mathrm{d}\Phi_{8,3,4,4}}{\mathrm{d}\tau} = 2q_3^2 - 2s^2 + 2u^2, \tag{4.73s}$$
$$\frac{\mathrm{d}\Phi_{8,4,4,4}}{\mathrm{d}\tau} = -2q_3u\left(3q_3-4s\right). \tag{4.73t}$$

4.9 Conclusions

In this section, a novel method for linear orbit uncertainty propagation was developed. The proposed algorithm is based on the special perturbation method Dromo, which offers key advantages for obtaining analytical expressions of the necessary Jacobian matrices.

The method was applied to study the evolution of the uncertainty distribution of several Near Earth Asteroids and the results were compared to Monte Carlo simulations and Cartesian coordinates based linear methods.

For well-determined orbits, the proposed method shows equal or better performance than linear methods based on Cartesian coordinates. When the uncertainty distribution grows to middle or large size, the new algorithm is found to be more accurate, and its performance deteriorates only in the presence of close-encounters characterized by a strongly non-linear gravitational perturbation across the size of the uncertainty distribution.

The applicability of the linear methods in Cartesian and Dromo coordinates depends on the quality of the initial orbit and the presence of close-approaches, can be qualitatively predicted by referring to two non-linearity indexes. The first is the Orbit Condition Code (OCC) proposed by the Minor Planet Center, whose evolution in time is here investigated. The second, proposed here for the first time, is an estimate of the linearization error over the uncertainty distribution in the presence of close encounters. The OCC gives an estimate of when applying the Dromo formulation has advantages over the Cartesian method, and the second index predicts when linearity will be lost for both formulations. Future work will be focused on a more precise determination of the domain of applicability of the method and ways to improve its performance

Finally, a higher order expansion of the angular variable was proposed. The higher order expansion seeks mitigating the error on this variable, which is dominant. In Dromo, the evolution of the fictitious time does not depend explicitly on the orbital perturbations, hence the coefficients of the expansion are relatively easy to calculate.

This page intentionally left blank.

Chapter 5

Primary Body Switch

5.1 Introduction

A *primary body switch* consists on replacing the central body used as a reference in the integration of the equations of motion by another massive body. It is well known that a primary body switch can greatly reduce the numerical truncation error in the cases of planets flybys. Recently, Amato et al. [4] showed that the distance at which the primary body switch is performed when using a Dromo formulation strongly affects the accuracy of the calculations. The existence of a non-trivial optimum switch distance was also reported. This distance does not coincide with the size of the Sphere of Influence of the approached planet, but is actually greater.

In the present chapter, the advantages of a primary body switch on the propagation of orbit uncertainty are explored, under the assumption of a deterministic dynamical system. When propagating the uncertainty of the orbital motion, a primary body switch seeks reducing the third-body gravity linearization error. This is especially the case for formulations that absorb the nonlinearity associated to the $1/r^2$ term of the equations of motion.

To highlight the benefit of the switch, we employ a Monte Carlo method with random sampling of the initial pdf. Each sample is propagated linearly around the mean orbit, and the nonlinear function that describes the primary body switch in Dromo elements allows reducing the uncertainty propagation error. Without loss of generality, this strategy can be combined with other methods mentioned in the introduction (LOV, GMM, STT, PCE, DA, etc) reducing the number of terms or samples needed for a given

accuracy, or decreasing the error for an equivalent computational time.

5.2 Primary body switch

To overcome the limitations of a purely heliocentric linear propagation in the presence of close approaches with planets, we introduce a primary body switch at a threshold distance from the encountering planet. Without loss of generality, we assume that the encountering planet is the Earth.

When employing the primary body switch strategy, the linear propagation is substituted with a hybrid Monte Carlo (MC) method. At the initial epoch, we sample $M = 1000$ random points from the Gaussian distribution described by the nominal orbit and the covariance matrix. For each asteroid, the nominal orbit and covariance matrix are obtained from the NEODyS database. We employ the uncertainty data provided in equinoctial elements, and the covariance matrix accounts for the uncertainty in the six equinoctial elements.

We propagate each sample using the STM of the nominal orbit of the object of study (Eq. (4.20)). If the nominal orbit intrudes the sphere of a given radius centered at the Earth, the heliocentric propagation is interrupted and all the MC samples ($i = 1, \dots, M$) are transformed from the heliocentric to the geocentric reference frame. In the geocentric phase, we consider a reference frame with origin in the Earth center and having the same orientation of the heliocentric inertial frame. We compute the relative positions and velocities with respect to the Earth by

$$\hat{\boldsymbol{r}}_i = \boldsymbol{r}_i - \boldsymbol{r}_\oplus \tag{5.1}$$

$$\hat{\boldsymbol{v}}_i = \boldsymbol{v}_i - \boldsymbol{v}_\oplus \tag{5.2}$$

where we denote the geocentric variables with a hat ($\hat{}$), and employ $\oplus$ as the Earth symbol. From $\hat{\boldsymbol{r}}_i$, $\hat{\boldsymbol{v}}_i$ we obtain the geocentric Dromo representation of the MC samples, which are propagated again using linear theory until the distance between the nominal orbit and the Earth is greater than the employed threshold. At that point, another primary body switch is performed to return to the heliocentric frame. The switch is repeated if needed in case the nominal orbit comes again close to the Earth. A scheme of this process is shown in Fig. 5.1.

The switch is calculated using Eqs. (D.4, D.5, 5.1, 5.2) and the formulae in Section D.2.1 that provide the Dromo elements as a function of the inertial Cartesian state vector and vice versa. This set of equations is constituted by fully analytical expressions involving the position and velocities of the asteroid and the Earth, and in general is nonlinear. When performing a switch, a Gaussian distribution will remain Gaussian if the eigenvalues of its covariance matrix are sufficiently small, because in that case the equations that define the switch can then be linearized around the reference orbit with negligible error. A second switch under similar conditions will yield a final distribution that will also be approximately Gaussian. Moreover, for primary body switches that are well approximated by a linear mapping, a combination of switches with heliocentric and geocentric STMs will result in a STM which is mathematically equivalent to the purely heliocentric STM. On the other hand, if the equations that govern the primary body switch cannot be replaced by their linearized form, Gaussianity will not be conserved in general. We note that close orbits can still be propagated using a STM even if they follow a non-Gaussian distribution. That is, we can combine linear propagation arcs with primary body switches, retaining with a higher degree of fidelity the nonlinearities of the orbital motion. The uncertainty distribution at a generic epoch is characterized by the dispersed MC states, and if necessary, the covariance matrix and other higher order moments can be estimated [28, pp. 341-363].

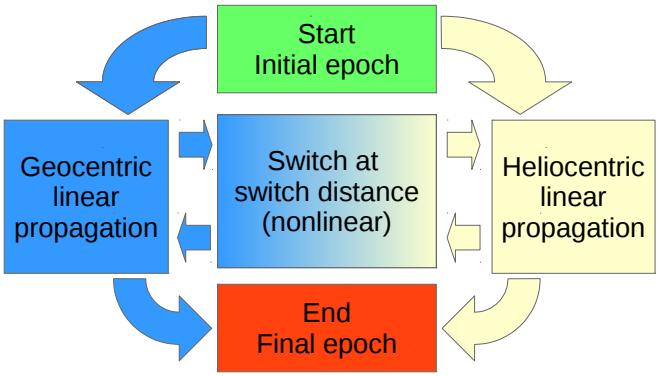

Figure 5.1: Primary body switch flow chart.

We highlight that the primary body switch, when applied to the orbit uncertainty propagation problem, is a technique that seeks reducing the third-body gravitational perturbation *linearization error* of the orbital uncertainty dispersion. This is different

from the classical application of the primary body switch, which aims to reduce the *numerical error* of a single orbit [4].

5.3 Results

In this section we present examples of orbit uncertainty propagation for some selected asteroids employing the primary body switch strategy.

These asteroids were chosen as good candidates to perform the primary body switch based on two criteria. First, all of them have their closest approach before the year 2050 at a distance no much greater than 1 radius of the Sphere of Influence of the Earth $R_{\text{SoI}} \simeq 0.0062\,\text{au} \simeq 9.25 \times 10^5\,\text{km}$. For reference, 1 lunar distance corresponds to $384400\,\text{km} \simeq 0.42\,R_{\text{SoI}}$. Second, they have a well determined orbit. Here, we employ the Orbit Condition Code (OCC), introduced in section 4.5.1, to decide whether to apply the switch or not to a particular asteroid. We only selected asteroids with initial OCC equal to 0 or 1.

The selected asteroids are shown in Table 5.1. For all these asteroids, we performed a parametric search on the switch distance to analyze its effect on the propagation accuracy. We took as lower bound the minimum close approach distance, and consider performing a switch as far as 3 radii of the Sphere of Influence of the Earth.

Table 5.1: Significant data of the asteroids considered in the analysis.

Asteroid	OCC	Closest approach distance [R_{SoI}]	Closest approach epoch	Final propagation epoch
2011AG5	1	1.17	2040-02-04	2050-01-01
2012AP10	1	0.51	2042-12-29	2050-01-01
2004RQ252	1	0.57	2043-04-01	2050-01-01
2001AV43	0	0.34	2029-11-11	2040-01-01
99942 Apophis	0	0.04	2029-04-13	2040-01-01

To better understand the effect of the primary body switch, we also considered cases where the initial standard deviations, expressed in equinoctial elements, were scaled up or down by a factor of 10.

We used as a measure of the linearization error the position error averaged over all

the MC samples:

$$\epsilon = \frac{1}{M}\sum_{i=1}^{M}\sqrt{(x_i - x_i^*)^2 + (y_i - y_i^*)^2 + (z_i - z_i^*)^2} \tag{5.3}$$

where the true solution $(x_i^*, y_i^*, z_i^*)^\top$ was calculated by integrating the equations of motion for each individual sample. Furthermore, for each asteroid and initial uncertainty scaling factor, we normalized the average error with the maximum position standard deviation estimated from the true solution at the final epoch.

5.3.1 2011AG5

The orbit uncertainty propagation of 2011AG5, a Potential Hazardous Asteroid (PHA), was carried out using the primary body switch. 2011AG5 will experience a close approach with the Earth in 2040 February 4 with a minimum distance of about 0.007 au, which is slightly larger than the radius of the Sphere of Influence. The propagation was performed from 2011 November 29, and the average error was evaluated on 2050 January 1.

Figure 5.2 shows the average error as a function of the switch distance for this asteroid at the end of the propagation. If the switch distance is smaller than the closest approach distance, the switch cannot be performed. However, for distances of about 1.05 times the Earth closest approach distance, the average error drops between one and two orders of magnitude. This behavior persists even when scaling up or down the initial uncertainty, which suggests that for 2011AG5, performing a switch may help to greatly reduce the uncertainty propagation error. The gray region in Fig. 5.2 corresponds to a switch distance between 1.05 and 1.15 times the closest approach distance of the nominal orbit.

5.3.2 2012AP10

2012AP10 is a 20 m asteroid that will flyby the Earth in 2042 December 29 at a nominal distance of about 1.4 lunar distances, but its minimum distance with the Earth could be as low as 0.4 lunar distances. This is reflected in its condition code of 1. We propagate from 2013 April 5 to 2050 January 1, and evaluate the average error at the end of the propagation. As it can be seen in Fig. 5.3, the average error is effectively reduced for the

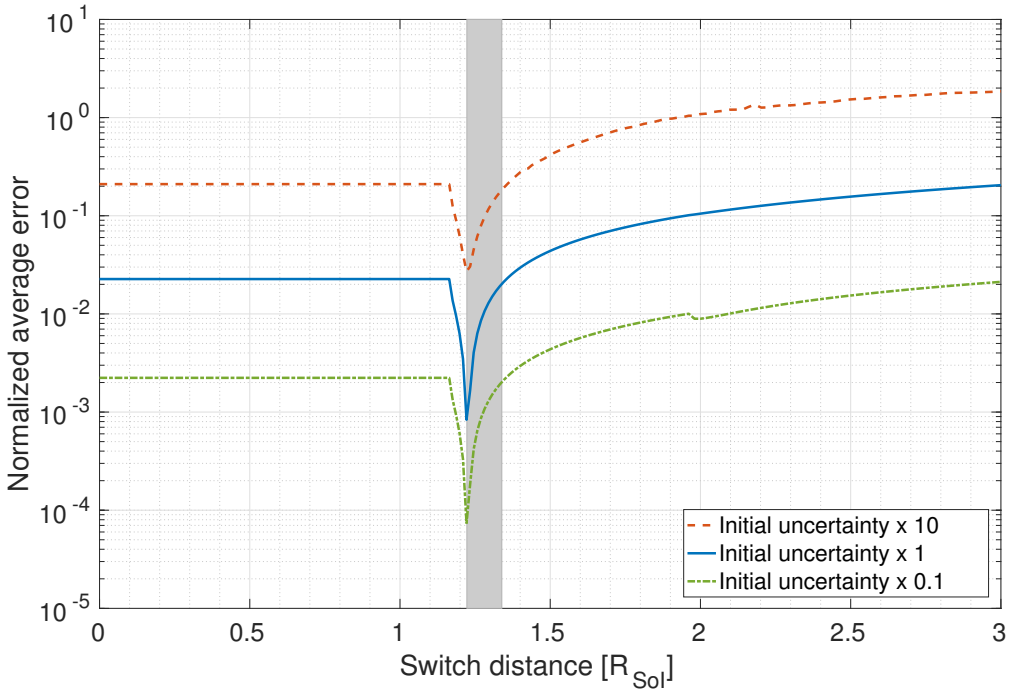

Figure 5.2: Average position error for 2011AG5 at year 2050 as a function of the switch distance. For the real initial covariance, the normalization factor is about 1.8×10^6 km. The gray region corresponds to a switch distance between 1.05 and 1.15 times the closest approach distance of the nominal orbit.

actual initial uncertainty, as well as for its scaled-up initial covariance matrix. However, by lowering the initial uncertainty the switch becomes less effective in this case.

5.3.3 2004RQ252

2004RQ252 will flyby the Earth at a distance of about 8×10^5 km in 2043 April 1. Our integration starts in 2006 March 5, and is performed until 2050 January 1. Figure 5.4 shows the average position error at the final epoch. The effectiveness of the switch with this asteroid resembles that of 2011AG5, with a very high efficiency for a switch performed at a distance of about 1.05 times the Earth closest approach distance.

For 2004RQ252, we also provide a comparison between the Dromo linear propagation without performing any switch, and a linear propagation in Cartesian coordinates. Figure 5.5 shows how the Dromo linear method outperforms its Cartesian counterpart until the 2043 flyby. After this close encounter, the error of the two methods is compa-

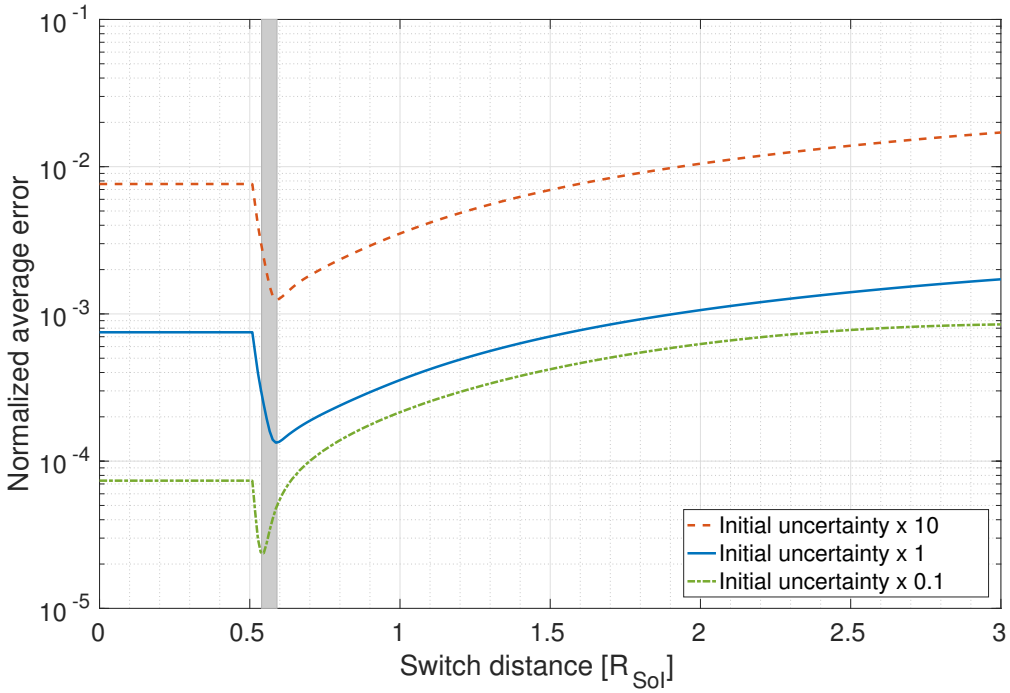

Figure 5.3: Average position error for 2012AP10 at year 2050 as a function of the switch distance. For the real initial covariance, the normalization factor is about 1.3×10^5 km. The gray region corresponds to a switch distance between 1.05 and 1.15 times the closest approach distance of the nominal orbit.

rable. By employing the primary body switch strategy, the final error can be reduced by a factor of 17.75.

5.3.4 2001AV43

The propagation of the orbit uncertainty of 2001AV43 was performed starting from 2012 October 14, and was carried out until 2040 January 1. In this interval, 2001AV43 has an Earth flyby on 2029 November 11, approaching as close as $0.34\ R_{\mathrm{SoI}}$.

Figure 5.6 shows the results of the primary body switch evaluated at the final epoch. For the actual or the scaled-down initial orbit uncertainty, the advantages of performing a primary body switch are not clear. This could be explained by its well-determined orbit, which has an OCC of 0. When considering larger initial uncertainty, a switch at distances of about three times the closest approach distance reduces the final error in more than half. We note that for 2001AV43, the closest approach occurs at a distance

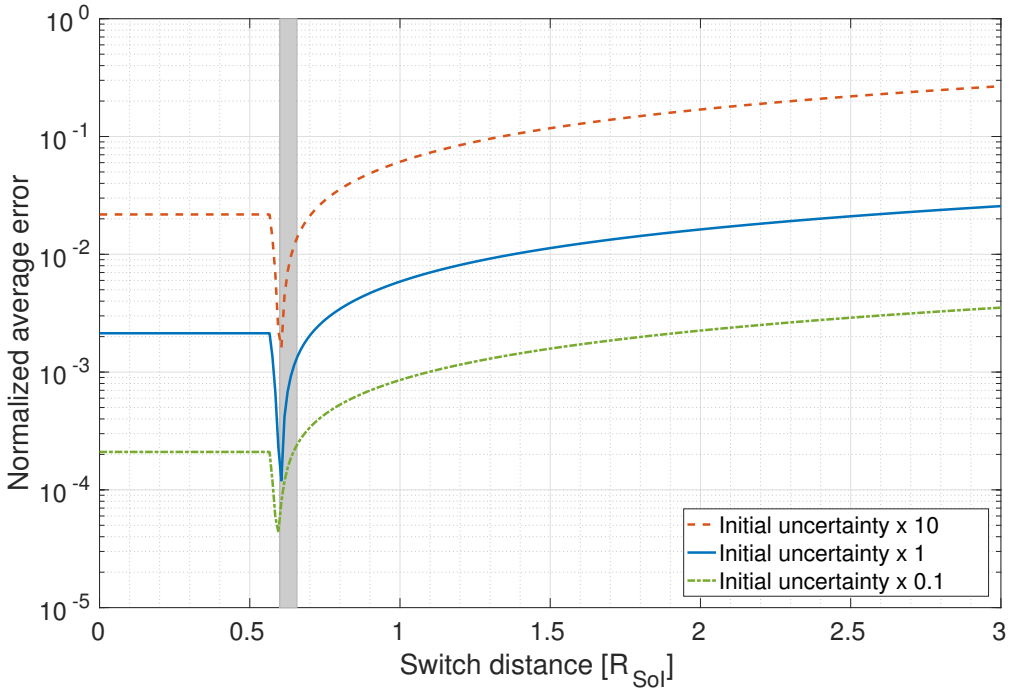

Figure 5.4: Average position error for 2004RQ252 at year 2050 as a function of the switch distance. For the real initial covariance, the normalization factor is about 1.6×10^5 km. The gray region corresponds to a switch distance between 1.05 and 1.15 times the closest approach distance of the nominal orbit.

of the same order of magnitude as the Moon distance, whose gravity at close distances may affect the accuracy of the linear propagation. Finally, the change of behavior at approximately $1.2\ R_{\text{SoI}}$ in Fig. 5.6 is caused by a second close approach that complicated the propagation of the uncertainty.

5.3.5 99942 Apophis

We applied the proposed primary body switch to the PHA Apophis. The propagation starts on 2009 May 6 and is performed until 2040 January 1, when we evaluate the average position error. In 2029, Apophis will fly by the Earth at a nominal closest-approach distance of about 38000 km. During this close flyby, the nonlinear nature of the Earth's gravitational force across the uncertainty region may strongly affect the evolution of the orbit uncertainty of this asteroid.

Figure 5.7 shows the results of performing the primary body switch at different

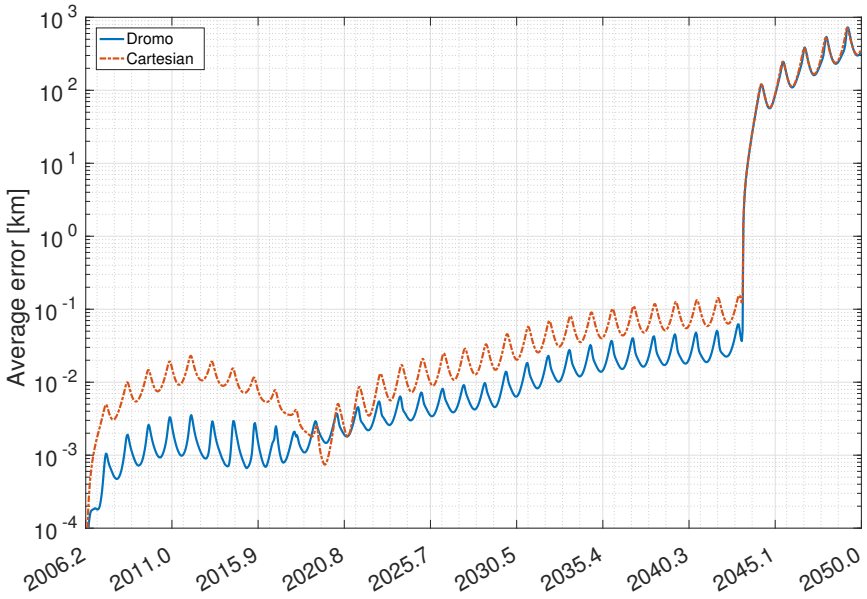

Figure 5.5: Average position error for 2004RQ252 as a function of time.

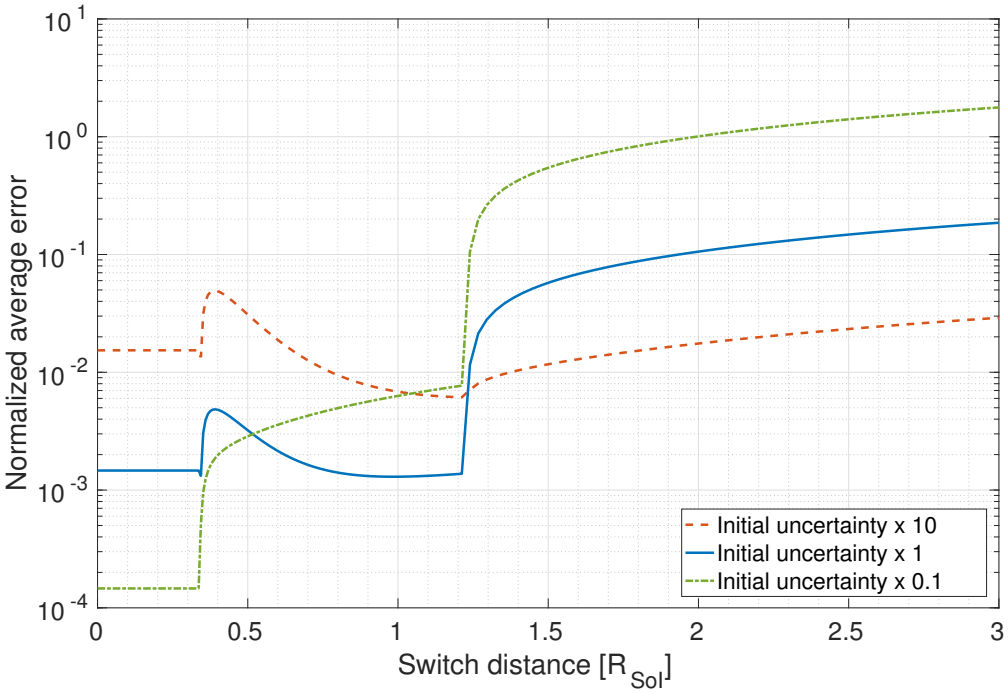

Figure 5.6: Average position error for 2001AV43 at year 2040 as a function of the switch distance. For the real initial covariance, the normalization factor is about 2.9×10^5 km.

distances from the Earth and for different scalings of the initial uncertainty. For the actual initial uncertainty, the error can be reduced by 40% if a switch is performed at about $0.6\,R_{\text{SoI}}$. Similar results are obtained when considering larger initial uncertainties, where the reduction increases to almost 70%. However, a scaled-down initial uncertainty does not seem to benefit from the primary body switch.

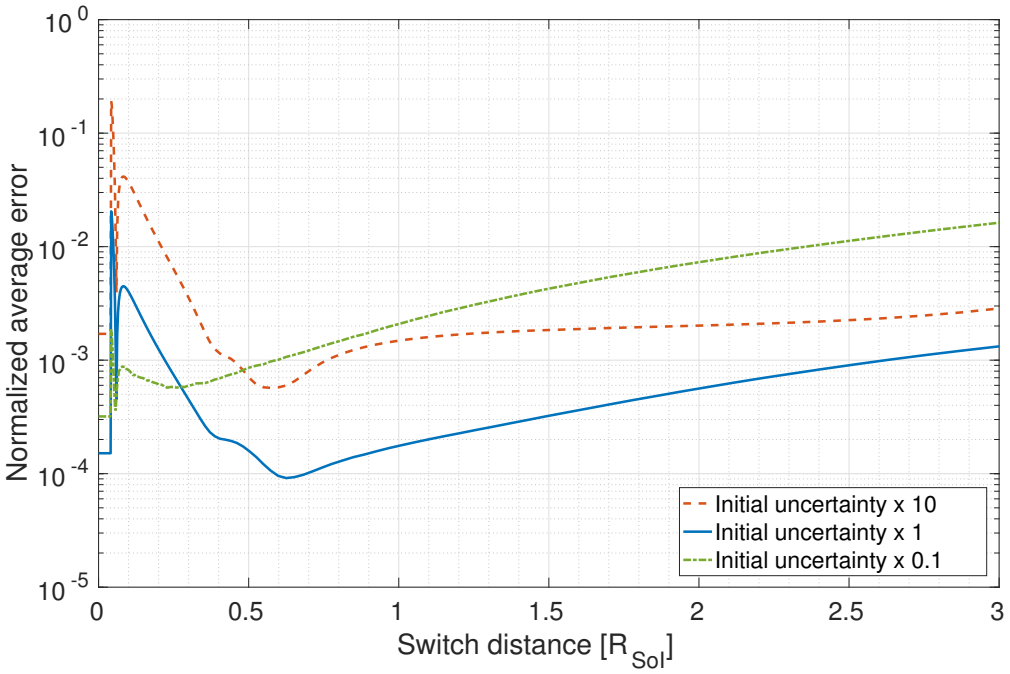

Figure 5.7: Average position error for 99942 Apophis at year 2040 as a function of the switch distance. For the real initial covariance, the normalization factor is about 2.9×10^5 km.

5.4 Discussion

Figure 5.8 shows the optimum distance that minimizes the final average error. Figure 5.9 shows the switch error-reduction factor, which is defined as the ratio of the error that we have without performing the switch to the minimum error that we obtain among all the possible switch distances. That is, a higher value of the error-reduction factor means that the switch is a more effective way of decreasing the error for that particular case. The results are summarized in Table 5.2. In Table 5.3, we provide the closest approach distance with respect to the Earth and the Moon for each asteroid. For 2001AV43 and Apophis, the switch did not reduce the error for a scaling factor of 0.1.

We indicated this in Table 5.2 as N/A (not applicable).

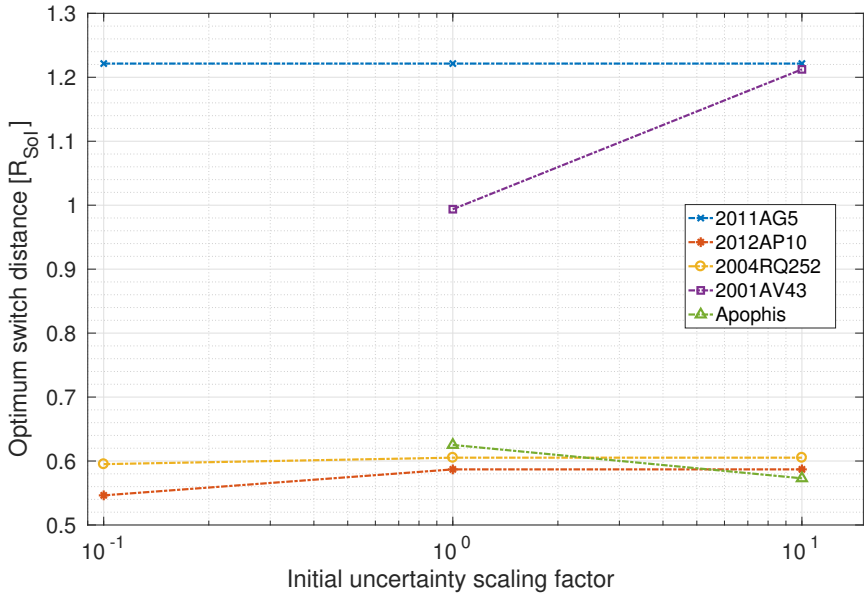

Figure 5.8: Optimum switch distance. For 2001AV43 and Apophis, the switch did not reduce the error for a scaling factor of 0.1.

2011AG5, 2012AP10 and 2004RQ252 are characterized by having an optimum switch distance that does not vary significantly with the initial uncertainty scaling factor, and corresponds to a switch distance slightly larger than the closest approach distance. The optimum switch distance lays between a 5% and a 15% larger than the minimum close approach distance with respect to the Earth. For these asteroids, performing the switch over very short propagation arcs improves drastically the result of the uncertainty propagation. This is justified because near the close approach is where the linearization error of Earth's gravity becomes critical [44]. However, longer geocentric propagation arcs are not beneficial in these cases because the Sun gravity linearization error would become dominant.

On the other hand, a less clear behavior is observed for Apophis and 2001AV43. In the case of Apophis, the nonlinearity of its very close flyby causes multiple local minima in the curve of average error for some of the initial uncertainty scaling factors. Additionally, during the 2029 close encounter, Apophis comes as close to the Moon as 6.5×10^{-4} au, which further complicates the propagation of the uncertainty. For

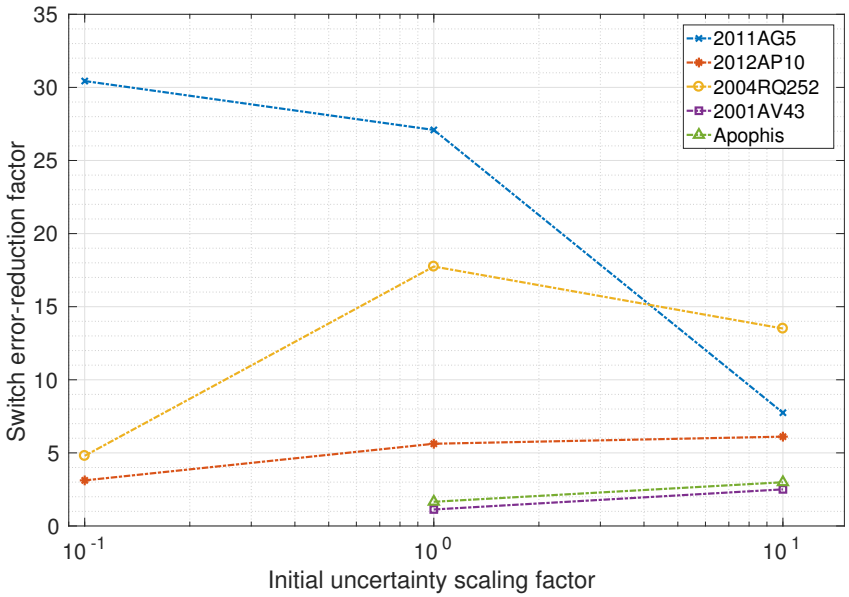

Figure 5.9: Switch error-reduction factor. For 2001AV43 and Apophis, the switch did not reduce the error for a scaling factor of 0.1.

Table 5.2: Summary of the results. For 2001AV43 and Apophis, the switch did not reduce the error for a scaling factor of 0.1.

Asteroid	Scaling factor	Optimum switch distance [R_{SoI}]	Error-reduction factor	$\frac{\text{Optimum switch distance}}{\text{Minimum Earth distance}}$
2011AG5	0.1	1.22	30.44	1.05
	1	1.22	27.09	1.05
	10	1.22	7.75	1.05
2012AP10	0.1	0.55	3.12	1.06
	1	0.59	5.63	1.14
	10	0.59	6.11	1.14
2004RQ252	0.1	0.60	4.80	1.04
	1	0.61	17.75	1.06
	10	0.61	13.51	1.06
2001AV43	0.1	0.34	N/A	N/A
	1	0.99	1.13	2.92
	10	1.21	2.51	3.57
99942 Apophis	0.1	0.04	N/A	N/A
	1	0.63	1.66	15.04
	10	0.57	2.99	14.11

Table 5.3: Summary of closest approaches.

Asteroid	Earth-asteroid minimum distance [au]	Moon-asteroid minimum distance [au]
2011AG5	7.2×10^{-3}	4.7×10^{-3}
2012AP10	3.2×10^{-3}	5.4×10^{-3}
2004RQ252	3.5×10^{-3}	1.3×10^{-3}
2001AV43	2.1×10^{-3}	1.7×10^{-3}
99942 Apophis	2.5×10^{-4}	6.5×10^{-4}

2001AV43, the results suggest that the initial orbit uncertainty could be too small to benefit from the switch, or that the linearization error of the Moon gravity during the flyby has a non-negligible importance. The closest approach distance of these two asteroids with the Earth is below 2.5×10^{-3} au (about the Earth-Moon distance), which could suggest that this is a limiting factor on the applicability of the primary body switch technique with the current formulation. To assess the frequency of such close Earth encounters, we searched the NEODyS database for the number of encounters with different maximum closest-approach distance. We carried out our query for encounters occurring at any epoch, and repeated the process for encounters only after the current epoch. Our search reveals 1784 close encounters in the future with a minimum nominal distance from the Earth smaller than $3\,R_{\mathrm{SoI}} \simeq 0.0185$ au. Among them, only 60 encounters occur closer than the Moon distance $a_{\leftmoon} = 0.00257$ au. The full result of our search is shown in Table 5.4.

Table 5.4: Statistics of Earth encounters after a search in the NEODyS database.

Maximum close-approach distance	Close encounters (in the future)	Close encounters (any epoch)
$3\,R_{\mathrm{SoI}} = 0.0185$ au	1784	5369
$2a_{\leftmoon} = 0.00514$ au	196	1046
$a_{\leftmoon} = 0.00257$ au	60	455

Finally, from the summary in Tables 5.2 and 5.3, a larger Earth-asteroid minimum distance seems to be correlated with a higher error-reduction factor. However, a more detailed study and a wider population of Earth-encountering asteroids are needed to understand this relation.

5.5 Conclusion

In this work, we extended the domain of validity of linear propagation in Dromo elements in the presence of planetary close encounters. We combined linear propagation in the heliocentric and geocentric frames with nonlinear transformations of the Dromo elements between the two. By using this approach, the linearization error of the third body gravitational force can be reduced when linearly propagating the orbit uncertainty.

We applied the method to a list of asteroids that have a close approach with the Earth before 2050, and with an Orbit Condition Code not greater than 1. We also scaled up and down by a factor of ten the standard deviations at the initial epoch to study how larger or smaller uncertainties affect the applicability of the method. We found that performing the primary body switch may improve the result of the linear propagation up to a factor of 30, and that in many cases a switch on very short arcs may drastically improve the orbit uncertainty prediction.

In future works, we will consider a broader set of asteroids, both real and simulated, to better understand the role of the switch distance. An alternative formulation for the geocentric arc, which could improve the accuracy of the method, is also under study.

Chapter 6

Orbit Determination using Dromo

6.1 Introduction

Orbit determination is the process of obtaining a trajectory statistically consistent with a set of observations. So far, we have assumed that the initial orbit and its associated uncertainty is available from traditional methods, and that no new observations are obtained. However, two questions arise. First, is it possible to update with new information the probability distribution function propagated with the Dromo formulation? Second, is it possible to calculate the initial pdf by processing directly the available observations using the Dromo formulation? In this chapter, we show how the Dromo formulation can accommodate observations of the orbital state to positively answer these questions.

Following the works of Tapley et al. [100] and Wiesel [110], the evolution of the unknown state $\boldsymbol{X}$ and and the equation of an observation $\boldsymbol{Y}_i$ are given by

$$\dot{\boldsymbol{X}} = \boldsymbol{F}(\boldsymbol{X}, \tau) \tag{6.1a}$$

$$\boldsymbol{Y}_i = \boldsymbol{G}(\boldsymbol{X}_i, \tau_i) + \boldsymbol{\epsilon}_i \tag{6.1b}$$

where the subindex $i = 1, \ldots, m$ corresponds to the epoch τ_i, and $\boldsymbol{\epsilon}$ is the random error of the observations. In general, $\boldsymbol{G}(\boldsymbol{X}_i, \tau_i)$ is a nonlinear function. The problem is how to calculate the best estimate of the state $\boldsymbol{X}_i^*$, also called nominal. If enough information with enough accuracy is available, the deviations between the real trajectory and its best

estimate will be small, that is,

$$\boldsymbol{x}(\tau) = \boldsymbol{X}(\tau) - \boldsymbol{X}^*(\tau), \tag{6.2a}$$

$$\boldsymbol{y}(\tau) = \boldsymbol{Y}(\tau) - \boldsymbol{Y}^*(\tau) = \boldsymbol{Y}(\tau) - G(\boldsymbol{X}^*(\tau), \tau), \tag{6.2b}$$

will be small quantities. Under this hypothesis, it is possible to linearize the equations of motion and the observation around the best estimate, and Eq. (6.1) can be rewritten for the state deviation $\boldsymbol{x}$ and the observation deviation $\boldsymbol{y}$ as

$$\dot{\boldsymbol{x}} = \boldsymbol{A}(\tau)\,\boldsymbol{x}(\tau), \tag{6.3a}$$

$$\boldsymbol{y}_i = \tilde{\boldsymbol{H}}_i \boldsymbol{X}_i + \boldsymbol{\epsilon}_i, \tag{6.3b}$$

with

$$\boldsymbol{A}(\tau) = \left[\frac{\partial \boldsymbol{F}(\tau)}{\partial \boldsymbol{X}}\right]^*, \tag{6.4a}$$

$$\tilde{\boldsymbol{H}} = \left[\frac{\partial \boldsymbol{G}}{\partial \boldsymbol{X}_i}\right]_i^*, \tag{6.4b}$$

and where the superscript $*$ means that the derivatives are to be evaluated on the nominal orbit. Manipulation of Eq. (6.3a) following the same procedure as in section 4.4 leads to the STM $\boldsymbol{\phi}(\tau, \tau_0)$. The STM solves Eq. (6.3a) for any initial condition:

$$\boldsymbol{x}(\tau) = \boldsymbol{\phi}(\tau, \tau_0)\,\boldsymbol{x}(\tau_0). \tag{6.5}$$

6.2 Observations

6.2.1 Range

The distance or range between the spacecraft and an instrument, usually Earth-based, is mathematically described as

$$\rho = \sqrt{\boldsymbol{\rho}^\top \boldsymbol{\rho}} \tag{6.6}$$

with

$$\boldsymbol{\rho} = \boldsymbol{r} - \boldsymbol{r}_I \tag{6.7}$$

where $\boldsymbol{r}_I(\tau)$ position vector of the instrument, which may depend on time. This is the case when the instrument is fixed on ground, because its coordinates in the inertial

frame depend on Earth's rotational state. The gradient matrix in Cartesian coordinates reads

$$\frac{\partial \rho}{\partial \boldsymbol{r}} = \frac{\boldsymbol{\rho}^\top}{\rho} \tag{6.8}$$

With this result, it is easy to express the gradient matrix with respect to the Dromo elements as

$$\frac{\partial \rho}{\partial \boldsymbol{q}} = \frac{\partial \rho}{\partial \boldsymbol{\rho}} \frac{\partial \boldsymbol{r}}{\partial \boldsymbol{q}} = \frac{\boldsymbol{\rho}^\top}{\rho} \begin{bmatrix} | & | & \cdots & | & | \\ \frac{\partial \boldsymbol{r}}{\partial q_1} & \frac{\partial \boldsymbol{r}}{\partial q_2} & \cdots & \frac{\partial \boldsymbol{r}}{\partial q_7} & \frac{\partial \boldsymbol{r}}{\partial \sigma} \\ | & | & \cdots & | & | \end{bmatrix} \tag{6.9}$$

where the derivatives of the position vector are given by Eqs. (D.8, D.9, D.11).

6.2.2 Range-Rate

The rate of change of the distance, usually called range-rate, is another quantity that is frequently measured. Mathematically,

$$\dot{\rho} = \frac{\boldsymbol{\rho}}{\rho} \dot{\boldsymbol{\rho}}. \tag{6.10}$$

While the instrument's coordinates are typically constant in the Earth-fixed reference frame, they will have a velocity in the inertial frame. Thus,

$$\dot{\boldsymbol{\rho}} = \boldsymbol{v} - \boldsymbol{v}_I. \tag{6.11}$$

The gradients in Cartesian coordinates read

$$\frac{\partial \dot{\rho}}{\partial \boldsymbol{r}} = \dot{\boldsymbol{\rho}}^\top \left(\frac{I_3}{\rho} - \frac{\boldsymbol{\rho}\,\boldsymbol{\rho}^\top}{\rho^3} \right), \qquad \frac{\partial \dot{\rho}}{\partial \boldsymbol{v}} = \frac{\boldsymbol{\rho}^\top}{\rho}. \tag{6.12}$$

This result allows one to calculate the gradients in Dromo elements as

$$\frac{\partial \dot{\rho}}{\partial \boldsymbol{q}} = \frac{\partial \dot{\rho}}{\partial \boldsymbol{x}} \frac{\partial \boldsymbol{x}}{\partial \boldsymbol{q}} = \begin{bmatrix} \frac{\partial \dot{\rho}}{\partial \boldsymbol{r}} & \frac{\partial \dot{\rho}}{\partial \boldsymbol{v}} \end{bmatrix} \begin{bmatrix} | & | & \cdots & | & | \\ \frac{\partial \boldsymbol{r}}{\partial q_1} & \frac{\partial \boldsymbol{r}}{\partial q_2} & \cdots & \frac{\partial \boldsymbol{r}}{\partial q_7} & \frac{\partial \boldsymbol{r}}{\partial \sigma} \\ \vdots & \vdots & \cdots & \vdots & \vdots \\ \frac{\partial \boldsymbol{v}}{\partial q_1} & \frac{\partial \boldsymbol{v}}{\partial q_2} & \cdots & \frac{\partial \boldsymbol{v}}{\partial q_7} & \frac{\partial \boldsymbol{v}}{\partial \sigma} \\ | & | & \cdots & | & | \end{bmatrix}. \tag{6.13}$$

As in the case of range measurements, the derivatives of the Cartesian coordinates with respect to the Dromo elements are given by Eqs. (D.8, D.9, D.11).

6.2.3 Optical navigation

Here we consider optical observations of celestial bodies or their centroids, or surface landmarks on those bodies [86]. In these observations, the observable quantity is the direction from a camera mounted on the spacecraft to the observed feature. We omit here techniques that exploit the relative size of the target celestial body in the sensor field of view to estimate the relative distance like the one presented in [26].

For convenience, we parametrize the observed direction in spherical coordinates with respect to the inertial frame. The azimuth and elevation angles, denoted by $\lambda \in (-\pi, \pi]$ and $\varphi \in [-\pi/2, \pi/2]$ respectively, read

$$\lambda = \operatorname{atan2}\left(y_t - y, z_t - z\right) \tag{6.14a}$$

$$\varphi = \arcsin \frac{z_r - z}{\|\boldsymbol{\rho}_t\|} \tag{6.14b}$$

where the t subindex stands for target, and with

$$\boldsymbol{\rho}_t = \boldsymbol{r}_t - \boldsymbol{r}. \tag{6.15}$$

The gradients of the spherical angles with respect to Cartesian coordinates can be easily calculated as

$$\frac{\partial \lambda}{\partial x} = 0 \tag{6.16a}$$

$$\frac{\partial \lambda}{\partial y} = -\frac{z_t - z}{\left(y_t - y\right)^2 + \left(z_t - z\right)^2} \tag{6.16b}$$

$$\frac{\partial \lambda}{\partial z} = \frac{y_t - y}{\left(y_t - y\right)^2 + \left(z_t - z\right)^2} \tag{6.16c}$$

$$\frac{\partial \lambda}{\partial \boldsymbol{v}} = \mathbf{0}^\top \tag{6.16d}$$

$$\frac{\partial \varphi}{\partial x} = \frac{(x_t - x)(z_t - z)}{\|\boldsymbol{\rho}_t\|^2 \sqrt{(x_t - x)^2 + (y_t - y)^2}} \tag{6.16e}$$

$$\frac{\partial \varphi}{\partial y} = \frac{(y_t - y)(z_t - z)}{\|\boldsymbol{\rho}_t\|^2 \sqrt{(x_t - x)^2 + (y_t - y)^2}} \tag{6.16f}$$

$$\frac{\partial \varphi}{\partial z} = -\frac{\sqrt{(x_t - x)^2 + (y_t - y)^2}}{\|\boldsymbol{\rho}_t\|^2} \tag{6.16g}$$

$$\frac{\partial \varphi}{\partial \boldsymbol{v}} = \mathbf{0}^\top \tag{6.16h}$$

(6.16i)

Note that with this parametrization of the unit sphere, the gradients of the angles are singular in the poles.

The gradient matrices in Dromo coordinates are constructed by applying the chain rule:

$$\frac{\partial \lambda}{\partial \boldsymbol{q}} = \frac{\partial \lambda}{\partial \boldsymbol{x}} \frac{\partial \boldsymbol{x}}{\partial \boldsymbol{q}}, \tag{6.17a}$$

$$\frac{\partial \varphi}{\partial \boldsymbol{q}} = \frac{\partial \varphi}{\partial \boldsymbol{x}} \frac{\partial \boldsymbol{x}}{\partial \boldsymbol{q}}, \tag{6.17b}$$

where the derivatives of the Cartesian coordinates with respect to the Dromo elements are given by Eqs. (D.8, D.9, D.11) as in the previous case.

6.3 Batch Estimation based on Least-Squares

Least-squares estimation is a powerful technique developed by Gauss in 1809. It is based on minimizing the sum of the squares of the residuals of the observations. To apply the least-squares method, we must convert all the observations and states to the same epoch τ_j. This is conveniently achieved via the STM. The state can be converted using Eq. (6.5), while the observations at the common epoch are given by

$$\boldsymbol{H}_i = \tilde{\boldsymbol{H}}_i \boldsymbol{\Phi}\left(\tau_i, \tau_j\right). \tag{6.18}$$

For the ease of notation, we will introduce the following definitions:

$$\begin{aligned} \boldsymbol{y} &= \begin{pmatrix} \boldsymbol{y}_1 \\ \vdots \\ \boldsymbol{y}_m \end{pmatrix}, \qquad \boldsymbol{H} = \begin{bmatrix} \boldsymbol{H}_1 \\ \vdots \\ \boldsymbol{H}_m \end{bmatrix} \\ \boldsymbol{\varepsilon} &= \begin{pmatrix} \boldsymbol{\varepsilon}_1 \\ \vdots \\ \boldsymbol{\varepsilon}_m \end{pmatrix}, \qquad \boldsymbol{W} = \begin{bmatrix} \boldsymbol{W}_1 & 0 & \dots & 0 \\ 0 & \boldsymbol{W}_2 & \dots & 0 \\ \vdots & \vdots & \ddots & \vdots \\ 0 & 0 & \dots & \boldsymbol{W}_m \end{bmatrix} \end{aligned} \tag{6.19}$$

where $\boldsymbol{W}_k$ are weighting matrices, usually picked as the inverse of the noise covariance matrices $\boldsymbol{R}_k$:

$$\boldsymbol{W}_k = \boldsymbol{R}_k^{-1}. \tag{6.20}$$

The least-squares estimation is based on minimizing the following objective func-

tion:

$$J\left(\boldsymbol{x}_j\right) = \frac{1}{2}\boldsymbol{\varepsilon}^\top \boldsymbol{W}\boldsymbol{\varepsilon}. \tag{6.21}$$

Equation (6.21) can be rewritten as a function of $\boldsymbol{x}_j$ with the help of Eq. (6.3b):

$$J\left(\boldsymbol{x}_j\right) = \frac{1}{2}\left(\boldsymbol{y} - \boldsymbol{H}\boldsymbol{x}_j\right)^\top \boldsymbol{W}\left(\boldsymbol{y} - \boldsymbol{H}\boldsymbol{x}_j\right). \tag{6.22}$$

A necessary condition of the $\hat{\boldsymbol{x}}_k$, the minimizer of the objective function, is derived from satisfying that the first derivative must be null at that point. This can be expressed as

$$\left(\boldsymbol{H}^\top \boldsymbol{W}\boldsymbol{H}\right)\hat{\boldsymbol{x}}_j = \boldsymbol{H}^\top \boldsymbol{H}\boldsymbol{y}. \tag{6.23}$$

The matrix $\boldsymbol{\mathcal{I}} = \left(\boldsymbol{H}^\top \boldsymbol{W}\boldsymbol{H}\right)$ on the left hand side is called *information matrix*. For the state to be observable, the information matrix must be full rank. If the information matrix is non-singular, then the following solution is obtained:

$$\boldsymbol{C}_j = \left(\boldsymbol{H}^\top \boldsymbol{W}\boldsymbol{H}\right)^{-1}, \tag{6.24a}$$

$$\hat{\boldsymbol{x}}_j = \boldsymbol{C}_j \boldsymbol{H}^\top \boldsymbol{W}\boldsymbol{y}. \tag{6.24b}$$

It can be proven that if $\boldsymbol{R}$ is constructed from the observations covariance, $\boldsymbol{C}_j$ is the best estimate of the covariance matrix [100, pp. 183–187].

Once Eq. (6.24) has been solved, the state and covariance matrix can be easily propagated in from time τ_j to time τ_k as

$$\bar{\boldsymbol{C}}_k = \boldsymbol{\Phi}\left(\tau_k, \tau_j\right) \boldsymbol{C}_j \boldsymbol{\Phi}^\top\left(\tau_k, \tau_j\right), \tag{6.25a}$$

$$\bar{\boldsymbol{x}}_k = \boldsymbol{\Phi}\left(\tau_k, \tau_j\right) \hat{\boldsymbol{x}}_j \tag{6.25b}$$

If after the filtering process the residuals of the observations are too high, a nonlinear version of the least-squares estimator is possible by updating the nominal trajectory and processing again the observations [100, pp. 194 – 199]. This iterative process can be employed until the filter converges and the residuals are below some tolerance.

6.3.1 A priori information

In many situations, *a priori* information about the state and covariance of the system is available. One possibility is to process again all the observations used to calculate the a priori state, adding the new information to them. This process can be greatly

time-consuming, and must be repeated every time new observations are obtained. To prevent this, it is possible to directly incorporate the results of a previous estimation into the least-squares formulation. Let $\bar{\boldsymbol{x}}_j$ be the a priori state, and $\bar{\boldsymbol{C}}_j$ be its associated covariance matrix, which can be considered as a weighing factor. When incorporating a priori information, Eq. (6.22) is modified as

$$J\left(\boldsymbol{x}_j\right) = \frac{1}{2}\left(\boldsymbol{y} - \boldsymbol{H}\boldsymbol{x}_j\right)^\top \boldsymbol{W}\left(\boldsymbol{y} - \boldsymbol{H}\boldsymbol{x}_j\right) + \frac{1}{2}\left(\bar{\boldsymbol{x}}_j - \boldsymbol{x}_j\right)^\top \bar{\boldsymbol{C}}_j^{-1}\left(\bar{\boldsymbol{x}}_j - \boldsymbol{x}_j\right), \tag{6.26}$$

which yields

$$\boldsymbol{C}_j = \left(\boldsymbol{H}^\top \boldsymbol{W}\boldsymbol{H} + \bar{\boldsymbol{C}}_j^{-1}\right)^{-1}, \tag{6.27a}$$

$$\hat{\boldsymbol{x}}_j = \boldsymbol{C}_j\left(\boldsymbol{H}^\top \boldsymbol{W}\boldsymbol{y} + \bar{\boldsymbol{C}}_j^{-1}\bar{\boldsymbol{x}}_j\right). \tag{6.27b}$$

6.3.2 Least-Squares Estimation in Dromo

Dromo uses an augmented state vector with constraints between its components, as explained in detail in Section 4.2. It was already proven that the covariance matrix in Dromo elements is rank-deficient by definition (see Section 4.1), and this has important consequences for batch estimation.

In the first place, it is not trivial how to incorporate a priori information in the estimator, as Eq. (6.27) requires to invert the covariance matrix. Second, the information matrix in Eq. (6.23) is always singular, and it cannot be inverted. This can be easily proven by constructing the matrix $\tilde{\boldsymbol{H}}$ by applying the chain rule using the dependence of $\boldsymbol{q}$ through the cartesian state $\boldsymbol{x}$.

These two issues are in fact related, and are caused by the implicit constraints of the Dromo variables. As it was explained in section D.2.4, a first constraint appears naturally by the unit norm of the quaternion elements, while a second constraint is introduced by fixing the value of β. Then, the unit vectors

$$\boldsymbol{u}_7 = \frac{1}{\sqrt{q_1^2 + q_2^2}}\left(-q_2, q_1, 0, 0, 0, 0, 0, 0\right)^\top, \tag{6.28a}$$

$$\boldsymbol{u}_8 = \left(0, 0, 0, q_4, q_5, q_6, q_7, 0\right)^\top \tag{6.28b}$$

will belong to the kernel of both the information and the covariance matrices. While the distribution in these directions cannot be observed, the additional information of the constraints allows us to compute the covariance matrix in Dromo elements. This

was discussed by Lefferts et al. when discussing the use of quaternions in spacecraft attitude [73].

The eigenvalues and eigenvectors problem for the Dromo information matrix is formulated as

$$\boldsymbol{\mathcal{I}}\,\boldsymbol{u} = \lambda \boldsymbol{u}. \tag{6.29}$$

Eight eigenvalues $\lambda_1 \geqslant \cdots \geqslant \lambda_8 \geqslant 0$ are obtained. Because of the two constraints, $\lambda_7 = \lambda_8 = 0$ will always be satisfied, and their corresponding eigenvectors can be chosen as in Eq. (6.28). The eigenvectors $\boldsymbol{u}_i$ can be arranged by columns into the matrix $\boldsymbol{U}$, diagonalizing the information matrix:

$$\boldsymbol{\mathcal{I}} = \boldsymbol{U}\boldsymbol{\Lambda}\boldsymbol{U}^\top, \quad \boldsymbol{\Lambda} = \begin{bmatrix} \lambda_1 & 0 & \dots & 0 & 0 & 0 \\ 0 & \lambda_2 & \dots & 0 & 0 & 0 \\ \vdots & \vdots & \ddots & 0 & 0 & 0 \\ 0 & 0 & \dots & \lambda_6 & 0 & 0 \\ 0 & 0 & \dots & 0 & 0 & 0 \\ 0 & 0 & \dots & 0 & 0 & 0 \end{bmatrix}, \quad \boldsymbol{U} = \begin{bmatrix} | & \dots & | \\ \boldsymbol{u}_1 & \dots & \boldsymbol{u}_8 \\ | & \dots & | \end{bmatrix}. \tag{6.30}$$

If the problem was observable, inversion of the information matrix would provide the covariance matrix. This is possible for the observable manifold spanned by the eigenvectors $\boldsymbol{u}_1, \dots, \boldsymbol{u}_6$. The inverse is not possible for the non-observable manifold spanned by $\boldsymbol{u}_7$ and $\boldsymbol{u}_8$, but in order to satisfy the constraints given by Eq. 6.28, the corresponding covariance eigenvalues must be zero. By writing the diagonal form of the covariance matrix as

$$\boldsymbol{C} = \boldsymbol{U}\boldsymbol{M}\boldsymbol{U}^\top, \quad \boldsymbol{M} = \begin{bmatrix} \mu_1 & 0 & \dots & 0 & 0 & 0 \\ 0 & \mu_2 & \dots & 0 & 0 & 0 \\ \vdots & \vdots & \ddots & 0 & 0 & 0 \\ 0 & 0 & \dots & \mu_6 & 0 & 0 \\ 0 & 0 & \dots & 0 & 0 & 0 \\ 0 & 0 & \dots & 0 & 0 & 0 \end{bmatrix}. \tag{6.31}$$

we can express the inverse as

$$\begin{cases} \mu_i = \frac{1}{\lambda_i} & \text{if } i = 1, \dots 6 \\ \mu_i = 0, & \text{if } i = 7, 8 \end{cases} \tag{6.32}$$

This is accomplished by employing the Moore-Penrose pseudo-inverse of the information matrix [19, p. 649], denoted by a † sign:

$$\boldsymbol{C} = \boldsymbol{\mathcal{I}}^\dagger, \qquad \boldsymbol{\mathcal{I}} = \boldsymbol{C}^\dagger. \tag{6.33}$$

Then, Eq. (6.27) can be rewritten as

$$\boldsymbol{C}_j = \left(\boldsymbol{H}^\top \boldsymbol{W} \boldsymbol{H} + \bar{\boldsymbol{C}}_j^\dagger\right)^\dagger, \tag{6.34a}$$

$$\hat{\boldsymbol{x}}_j = \boldsymbol{C}_j \left(\boldsymbol{H}^\top \boldsymbol{W} \boldsymbol{y} + \bar{\boldsymbol{C}}_j^\dagger \bar{\boldsymbol{x}}_j\right). \tag{6.34b}$$

Note that multiplying the covariance matrix by its pseudo-inverse does not result in an identity matrix:

$$\boldsymbol{C}_j \boldsymbol{C}_j^\dagger = \boldsymbol{U}\boldsymbol{M}\boldsymbol{U}^\top \boldsymbol{U}\boldsymbol{M}^\dagger \boldsymbol{U}^\top = \boldsymbol{U}\boldsymbol{M}\boldsymbol{M}^\dagger \boldsymbol{U}^\top, \tag{6.35}$$

which can be simplified since $\boldsymbol{M}\boldsymbol{M}^\dagger$ is a block diagonal matrix composed by a 6×6 identity matrix and a 2×2 null matrix:

$$\boldsymbol{C}_j \boldsymbol{C}_j^\dagger = \boldsymbol{U} \begin{bmatrix} \boldsymbol{I}_6 & \boldsymbol{0}_{6\times 2} \\ \boldsymbol{0}_{2\times 6} & \boldsymbol{0}_2 \end{bmatrix} \boldsymbol{U}^\top = \boldsymbol{I}_8 - \begin{bmatrix} | & | \\ \boldsymbol{u}_7 & \boldsymbol{u}_8 \\ | & | \end{bmatrix} \begin{bmatrix} | & | \\ \boldsymbol{u}_7 & \boldsymbol{u}_8 \\ | & | \end{bmatrix}^\top = \boldsymbol{I}_8 - \boldsymbol{u}_7 \boldsymbol{u}_7^\top - \boldsymbol{u}_8 \boldsymbol{u}_8^\top. \tag{6.36}$$

6.4 Sequential Estimation. Conventional Kalman Filter

Equation (6.27) usually requires inverting a matrix of dimension equal to the dimension of the state vector. When employing the Dromo formulation, the computational burden is further augmented because pseudo-inverse operations are involved (Eq. (6.34)). Thus, it is convenient to reformulate the filtering equations to avoid this situation, resulting in the so-called Kalman filter. Here we follow an approach similar to [100, pp. 199 – 201], adapting it to the constraints and rank-deficiency of the Dromo formulation.

Recalling Eq (6.25), an estimate $\hat{\boldsymbol{x}}_k$ and its associated covariance matrix $\boldsymbol{C}_k$ at time τ_k can be propagated to time τ_j as

$$\bar{\boldsymbol{C}}_j = \boldsymbol{\Phi}\left(\tau_j, \tau_k\right) \boldsymbol{C}_k \boldsymbol{\Phi}^\top\left(\tau_j, \tau_k\right), \tag{6.37a}$$

$$\bar{\boldsymbol{x}}_j = \boldsymbol{\Phi}\left(\tau_j, \tau_k\right) \hat{\boldsymbol{x}}_k. \tag{6.37b}$$

At the new time τ_j, we assume that an additional conservator is available:

$$\boldsymbol{y}_j = \tilde{\boldsymbol{H}}_j \boldsymbol{x}_j + \boldsymbol{\varepsilon}_j, \tag{6.38}$$

and the state and covariance matrix can be updated as:

$$\boldsymbol{C}_j = \left(\tilde{\boldsymbol{H}}_j^\top \boldsymbol{W}_j \tilde{\boldsymbol{H}}_j + \bar{\boldsymbol{C}}_j^\dagger\right)^\dagger, \tag{6.39a}$$

$$\hat{\boldsymbol{x}}_j = \boldsymbol{C}_j \left(\tilde{\boldsymbol{H}}_j^\top \boldsymbol{W}_j \boldsymbol{y}_j + \bar{\boldsymbol{C}}_j^\dagger \bar{\boldsymbol{x}}_j\right). \tag{6.39b}$$

Starting from Eq. (6.39a), and exploiting that the pseudo-inverse composed with itself provides the original matrix,

$$\boldsymbol{C}_j^{\dagger} = \tilde{\boldsymbol{H}}_j^{\top} \boldsymbol{W}_j \tilde{\boldsymbol{H}}_j + \bar{\boldsymbol{C}}_j^{\dagger}. \tag{6.40}$$

First, we premultiply Eq. (6.40) by $\boldsymbol{C}_j$ and postmultiply $\bar{\boldsymbol{C}}_j$

$$\boldsymbol{C}_j \boldsymbol{C}_j^{\dagger} \bar{\boldsymbol{C}}_j = \boldsymbol{C}_j \tilde{\boldsymbol{H}}_j^{\top} \boldsymbol{W}_j \tilde{\boldsymbol{H}}_j \bar{\boldsymbol{C}}_j + \boldsymbol{C}_j \bar{\boldsymbol{C}}_j^{\dagger} \bar{\boldsymbol{C}}_j. \tag{6.41}$$

According to Eq (6.36), the product $\boldsymbol{C}_j \boldsymbol{C}_j^{\dagger}$ is not an identity matrix. However, the left hand side can be simplified using the relation

$$\boldsymbol{C}_j \boldsymbol{C}_j^{\dagger} \bar{\boldsymbol{C}}_j = \left(\boldsymbol{I}_8 - \boldsymbol{U} \begin{bmatrix} \boldsymbol{0}_6 & \boldsymbol{0}_{6\times 2} \\ \boldsymbol{0}_{2\times 6} & \boldsymbol{I}_2 \end{bmatrix} \boldsymbol{U}^{\top} \right) \boldsymbol{U} \bar{\boldsymbol{M}} \boldsymbol{U}^{\top} = \bar{\boldsymbol{C}}_j, \tag{6.42}$$

and by using an equivalent relation on the right hand side, the expression can be simplified as:

$$\bar{\boldsymbol{C}}_j = \boldsymbol{C}_j \tilde{\boldsymbol{H}}_j^{\top} \boldsymbol{W}_j \tilde{\boldsymbol{H}}_j \bar{\boldsymbol{C}}_j + \boldsymbol{C}_j, \tag{6.43}$$

which provides the updated covariance matrix $\boldsymbol{C}_j$

$$\boldsymbol{C}_j = \bar{\boldsymbol{C}}_j - \boldsymbol{C}_j \tilde{\boldsymbol{H}}_j^{\top} \boldsymbol{W}_j \tilde{\boldsymbol{H}}_j \bar{\boldsymbol{C}}_j. \tag{6.44}$$

Further simplifications are possible. Post-multiplying Eq. (6.43) by $\tilde{\boldsymbol{H}}_j^{\top} \boldsymbol{W}_j$ leads to

$$\begin{aligned} \bar{\boldsymbol{C}}_j \tilde{\boldsymbol{H}}_j^{\top} \boldsymbol{W}_j =& \boldsymbol{C}_j \tilde{\boldsymbol{H}}_j^{\top} \boldsymbol{W}_j \left(\tilde{\boldsymbol{H}}_j \bar{\boldsymbol{C}}_j \tilde{\boldsymbol{H}}_j^{\top} \boldsymbol{W}_j + \boldsymbol{I} \right) \\ =& \boldsymbol{C}_j \tilde{\boldsymbol{H}}_j^{\top} \boldsymbol{W}_j \left(\tilde{\boldsymbol{H}}_j \bar{\boldsymbol{C}}_j \tilde{\boldsymbol{H}}_j^{\top} + \boldsymbol{W}_j^{-1} \right) \boldsymbol{W}_j. \end{aligned} \tag{6.45}$$

Solving for the term $\boldsymbol{C}_j \tilde{\boldsymbol{H}}_j^{\top} \boldsymbol{W}_j$, we obtain

$$\boldsymbol{C}_j \tilde{\boldsymbol{H}}_j^{\top} \boldsymbol{W}_j = \bar{\boldsymbol{C}}_j \tilde{\boldsymbol{H}}_j^{\top} \left(\tilde{\boldsymbol{H}}_j \bar{\boldsymbol{C}}_j \tilde{\boldsymbol{H}}_j^{\top} + \boldsymbol{W}_j^{-1} \right)^{-1}, \tag{6.46}$$

where the inverse in the right hand side does not face the problems that required using the pseudo-inverse for the Dromo formulation. We can then substitute this result into Eq. (6.44) to obtain the classical equation of the Kalman filter for the covariance update

$$\boldsymbol{C}_j = \bar{\boldsymbol{C}}_j - \bar{\boldsymbol{C}}_j \tilde{\boldsymbol{H}}_j^{\top} \left(\tilde{\boldsymbol{H}}_j \bar{\boldsymbol{C}}_j \tilde{\boldsymbol{H}}_j^{\top} + \boldsymbol{W}_j^{-1} \right)^{-1} \tilde{\boldsymbol{H}}_j \bar{\boldsymbol{C}}_j = \left(\boldsymbol{I}_8 - \boldsymbol{K}_j \tilde{\boldsymbol{H}}_j \right) \bar{\boldsymbol{C}}_j, \tag{6.47}$$

where $\boldsymbol{K}_j$ is the Kalman gain, given by

$$\boldsymbol{K}_j = \bar{\boldsymbol{C}}_j \tilde{\boldsymbol{H}}_j^\top \left(\tilde{\boldsymbol{H}}_j \bar{\boldsymbol{C}}_j \tilde{\boldsymbol{H}}_j^\top + \boldsymbol{W}_j^{-1} \right)^{-1}. \tag{6.48}$$

Here, one of the advantages of the Kalman filter with respect to a batch estimator becomes clear: we need to invert a matrix of dimension equal to the number of observations, instead of the size of the state vector.

The update of the state vector is performed with Eq. (6.39b). To prevent calculating the pseudo-inverse of the covariance matrix, we can rewrite the Kalman gain as a function of the updated covariance using Eqs (6.46, 6.48):

$$\boldsymbol{K}_j = \boldsymbol{C}_j \tilde{\boldsymbol{H}}_j^\top \boldsymbol{W}_j, \tag{6.49}$$

which yields

$$\hat{\boldsymbol{x}}_j = \boldsymbol{K}_j \boldsymbol{y}_j + \boldsymbol{C}_j \bar{\boldsymbol{C}}_j^\dagger \bar{\boldsymbol{x}}_j. \tag{6.50}$$

Substituting the updated covariance from Eq. (6.47) provides

$$\hat{\boldsymbol{x}}_j = \boldsymbol{K}_j \boldsymbol{y}_j + \left(\boldsymbol{I}_8 - \boldsymbol{K}_j \tilde{\boldsymbol{H}}_j \right) \bar{\boldsymbol{C}}_j \bar{\boldsymbol{C}}_j^\dagger \bar{\boldsymbol{x}}_j. \tag{6.51}$$

The product $\bar{\boldsymbol{C}}_j \bar{\boldsymbol{C}}_j^\dagger$ is given by Eq. (6.36), and the updated state becomes

$$\hat{\boldsymbol{x}}_j = \boldsymbol{K}_j \boldsymbol{y}_j + \left(\boldsymbol{I}_8 - \boldsymbol{K}_j \tilde{\boldsymbol{H}}_j \right) \left(\boldsymbol{I}_8 - \boldsymbol{u}_7 \boldsymbol{u}_7^\top - \boldsymbol{u}_8 \boldsymbol{u}_8^\top \right) \bar{\boldsymbol{x}}_j. \tag{6.52}$$

The difference between the classical Kalman filter formulae and Eq. (6.52) is the term associated to the outer product of $\boldsymbol{u}_7$ and $\boldsymbol{u}_8$. This additional term guarantees that the constraints of the Dromo formulation are satisfied.

6.5 Applications

6.5.1 Example in LEO

Orbital determination is key in the Low Earth Orbit region for satellites and space debris that revolve around the Earth in orbits with a relatively high density of objects. Examples of these are the Sun-Synchronous orbits whose inclination close to $100\,\text{deg}$ and the GEO region [66, pp. 14 – 15]. As the population of objects is expected to greatly increase in the future, both by new launches, mega-constellations and newly generated space debris, assuring frequent tracking can become a challenging task. Certain

space debris may additionally lay in orbits which makes them less easily observed by ground-based radars. In a scenario in which new information may be hard to come by, the increasing propagation time between observations makes the uncertainty region to grow and eventually lose Gaussianity in Cartesian coordinates. Here, the Dromo formulation may play an important role in the orbit determination of these objects, as the residual of the observation is expected to be smaller, leading to a better and faster convergence of the navigation filter.

As an example of orbit determination in LEO, we study the orbit uncertainty of a satellite that is able to communicate with several ground stations. We employ range and range-rate measurements to improve the best estimate of the orbit and its covariance matrix, assuming that the initial uncertainty follows a Gaussian in Cartesian coordinates. Furthermore, we assume that this initial Gaussian can be linearly converted into Dromo variables without loss of reality, and that the initial conditions of the reference orbit were drifted from the true orbit by an amount statistically admissible with the initial distribution.

The initial conditions for this simulations are given in Table 6.1, where the standard deviations are the 1–σ values of the pdf in the Cartesian space, and the simulation is performed for five hours.

Table 6.1: Initial conditions expressed expressed in the Earth-centered J2000 Equatorial frame. Position and velocity correspond to the true orbit.

Component	Value
Epoch	2018 June 01 23:11:09
x [km]	757.7
y [km]	5222.607
z [km]	4851.5
v_x [km/s]	2.21321
v_y [km/s]	4.68734
v_z [km/s]	-5.37130
Position standard deviation [km]	1
Velocity standard deviation [km/s]	10^{-5}

To generate the observations, the ground stations of Uchinoura Space Center, Goldstone and Malargüe are employed. Their locations are shown in Table 6.2. Figure 6.1 shows the elevation of the spacecraft as seen from each ground station. For simplicity,

we assume a perfectly spherical Earth. As can be seen in the ground track (Fig. 6.2), the ground stations were chosen to provide tracking at least once per orbit. When the elevation is greater than $10\,\text{deg}$, a pair of range and range-rate observations is planned every 20 seconds. Gaussian noise of standard deviations $\sigma_\rho = 10\,\text{m}$ and $\sigma_{\dot{\rho}} = 0.5\,\text{mm/s}$ is added to the range and range-rate measurements, respectively. These standard deviations are also employed as weights for the filtering process.

Table 6.2: Ground stations

Name	Latitude	Longitude
Uchinoura Space Center	31° 12′ 0″ S	131°4′48″ E
Goldstone	35° 25′ 36″ N	116° 53′ 24″ W
Malargüe	35° 46′ 34″ S	69° 23′ 54″ W

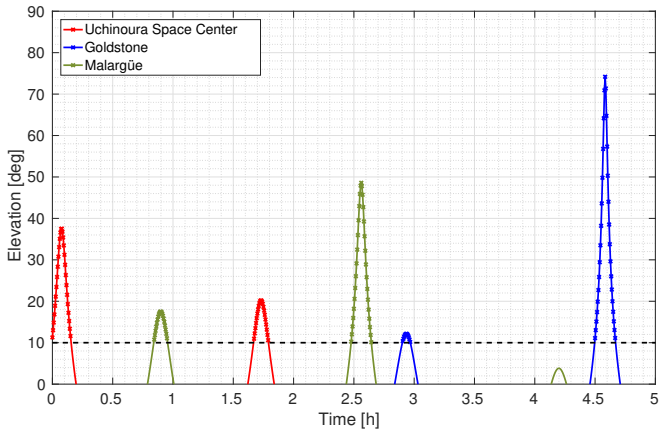

Figure 6.1: Elevation as seen from ground stations and observations.

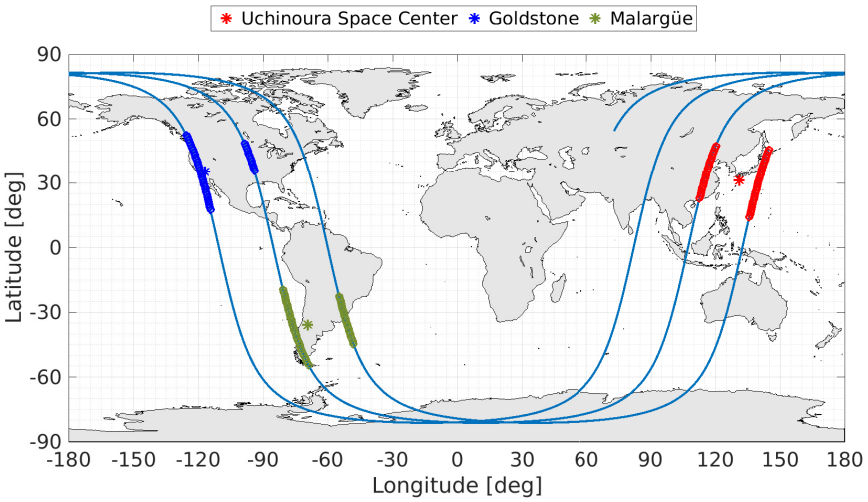

Figure 6.2: Ground track and observations. The ground track starts near Japan and moves east-wards.

The nonlinear version of the least-squares estimation algorithm using Dromo as used to process the range and range-rate measurements. After all the observations are processed in the first pass, the state deviation is used to update the reference orbit. Then, the process is repeated after the residuals of the observations are below the accuracy of the measurements. The a priori covariance matrix was chosen as that of the initial Gaussian distribution.

Figure 6.3 shows the residuals of the observations for 5 passes of the batch estimator, and the corresponding root mean square (RMS) error of the residuals is presented in Table 6.3 The residuals are distributed after the last pass of the filter as in Fig 6.4, and shows a reasonable agreement with the Gaussian distributions the observations were drawn from. Finally, the covariance envelope of Fig. 6.5 shows how the calculated reference is well within the 3–σ standard deviation of the true orbit.

Table 6.3: RMS error of the range and range-rate residuals after each pass of the Dromo least-squares algorithm.

Pass number	1	2	3	4
Range [m]	604.58	79.62	9.69	9.65
Range-rate [mm/s]	1822.69	426.87	5.49	0.49

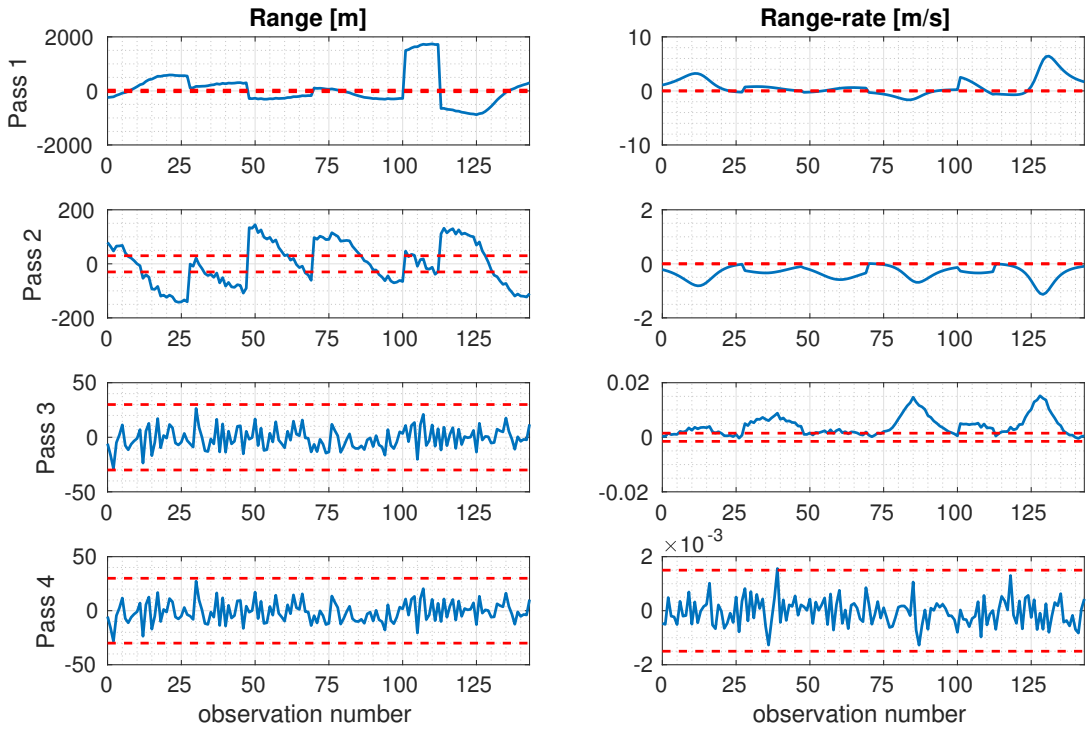

Figure 6.3: Range and range-rate residuals after each pass of the Dromo least-squares estimation algorithm.

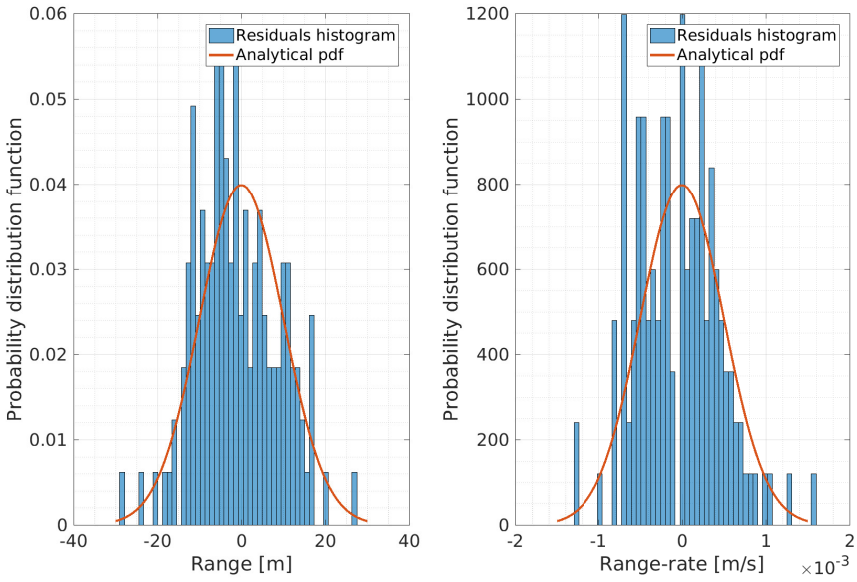

Figure 6.4: Distribution of range and range-rate residuals after the last pass of the Dromo least-squares estimation algorithm.

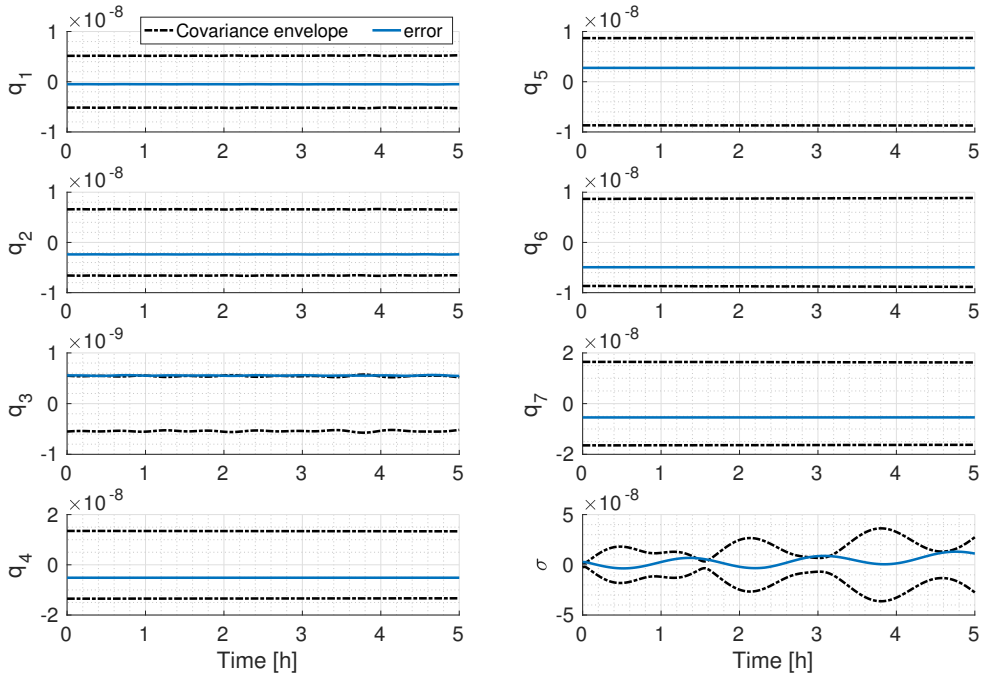

Figure 6.5: 3–σ Dromo covariance envelopes and error of the reference trajectory after the last pass of the Dromo least-squares estimation algorithm.

A classical least-squares algorithm using Cartesian coordinates was also employed for completeness, and its results are shown in Figs 6.6, 6.7 and 6.8, and in Table 6.4.

Table 6.4: RMS error of the range and range-rate residuals after each pass of the Cartesian least-squares algorithm.

Pass number	1	2	3	4
Range [m]	1316.55	32.42	9.65	9.65
Range-rate [mm/s]	2797.55	173.91	0.49	0.51

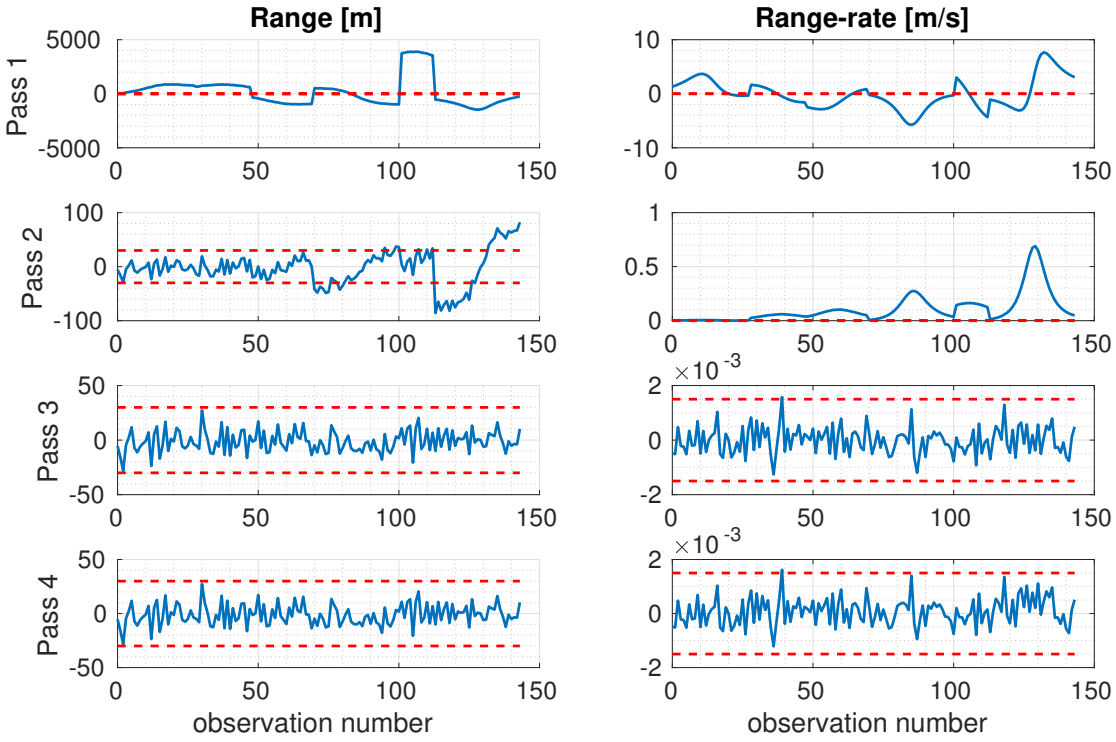

Figure 6.6: Range and range-rate residuals after each pass of the Cartesian least-squares estimation algorithm.

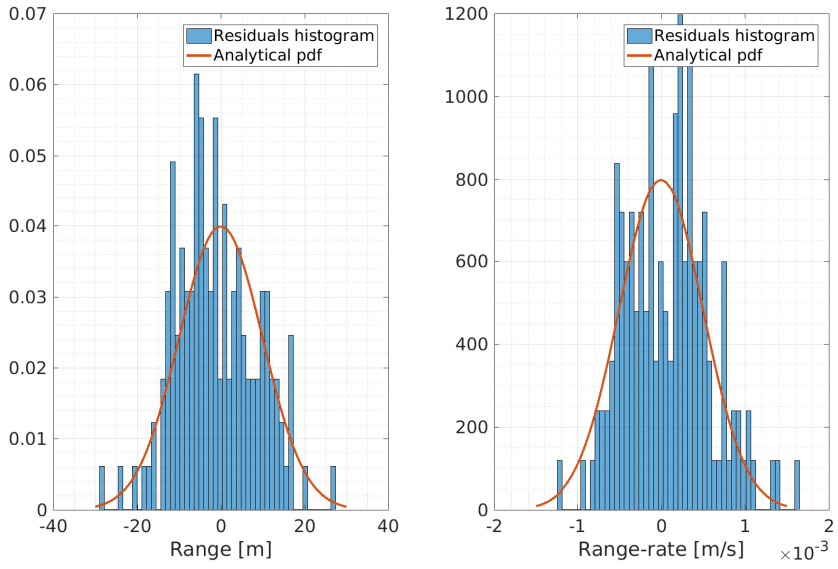

Figure 6.7: Distribution of range and range-rate residuals after the last pass of the Cartesian least-squares estimation algorithm.

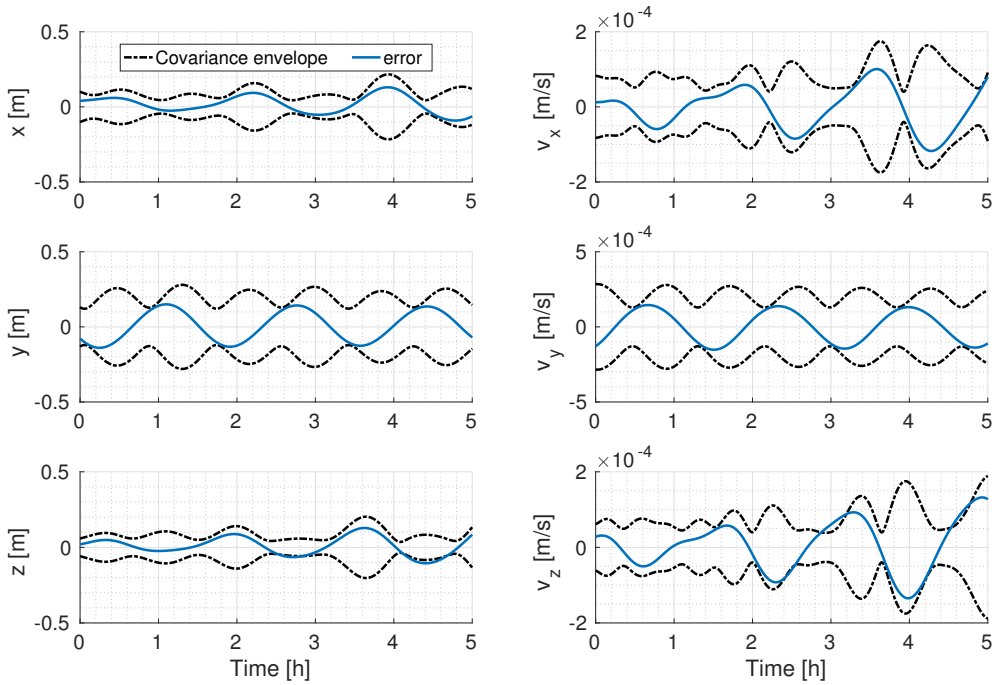

Figure 6.8: 3–σ Cartesian covariance envelopes and error of the reference trajectory after the last pass of the Cartesian least-squares estimation algorithm.

6.5.2 Application to Navigation of a Spacecraft in the Binary Asteroid System Didymos

The Didymos system is composed of two asteroid. The first of them is named *Didymos*, as the binary system. A small secondary, commonly called *Didymoon*, orbits around the center of mass of the binary system, which is well inside Didymos. This binary asteroid system is the target of the *Double Asteroid Redirection Test* (DART) mission, which seeks impacting on Didymoon in 2022 as a demonstration mission of asteroid orbit modification capabilities [24]. DART was part of a European-American joint mission called *Asteroid Impact and Deflection Assessment* (AIDA), but the European part *Asteroid Impact Mission* (AIM) failed to obtain funds and was canceled. AIM was to orbit the binary system to support DART operations [11], as well as possibly releasing small landers [22, 32, 102]. ESA is still considering a mission to the Didymos system called Hera to study the effect of DART, to be launched in 2023 [80]. Dell'Elce et al. [29] and Silva-Neto et al. [97] performed independent campaigns of simulations to assess the stability of the orbital environment in the Didymos system, concluding that most of the orbits

in the binary system are unstable and only a few are suitable for operations.

The current information of the characteristics of the Didymos system is limited, and the uncertainties are large. For the application presented in this section, we employ the values released by the European Space Agency[1], and collected in Table 6.5.

Table 6.5: Characteristics of the Didymos system

Parameter	Value
Diameter of Primary	$0.775\,\text{km}$
Diameter of Secondary	$0.163\,\text{km}$
Mass of Primary	$5.23 \times 10^{11}\,\text{kg}$
Mass of Secondary	$4.89 \times 10^{9}\,\text{kg}$
Distance between bodies	$1.18\,\text{km}$

While perturbations such as solar radiation pressure, non-spherical gravitational forces of Didymos and Didymoon and the gravitational of the Sun and the planets might cause an important influence in the motion of a spacecraft operating in the system, it is convenient to study the nominal trajectory in the context of the circular restricted three body problems. To this end, we will employ the semi-major axis of Didymoon as unit of length, and unit of time is chosen such that make the sum of the gravitational parameters of both asteroids equal to unity. For the Didymos-Didymoon system, $\mu \simeq 0.00926$. The distance from Didymoon to L1 and L2 is about 0.134 and 0.153, respectively, and L3 is about 1.004 from Didymos. For reference, the radius of the Sphere of Influence of Didymoon is about 0.154 times the semi-major axis of its orbit. Figure 6.9 shows the zero-velocity curves in the rotating frame for different values of the Jacobi constant up to 3.5, and the five Lagrange points are denoted by the red asterisks.

Orbiting a binary asteroid system is difficult. Most of the orbits are unstable and eventually escape the system or impact one of the bodies. This is exacerbated by forces not considered in the three body restricted problem, especially solar radiation pressure and the irregular gravitational field of the asteroids. For long-term operations, Dell'Elce et al. showed that only terminator and interior retrograde orbits are stable [29]. Other possibility is to safely deploy small landers from an actively controlled mothership that moves to a safe orbit after separation [22, 32, 102]. For a safe and robust landing of these

[1] `https://www.esa.int/Our_Activities/Space_Engineering_Technology/Asteroid_Impact_Mission/Didymos_facts_figures`, accessed on 2018 May 22

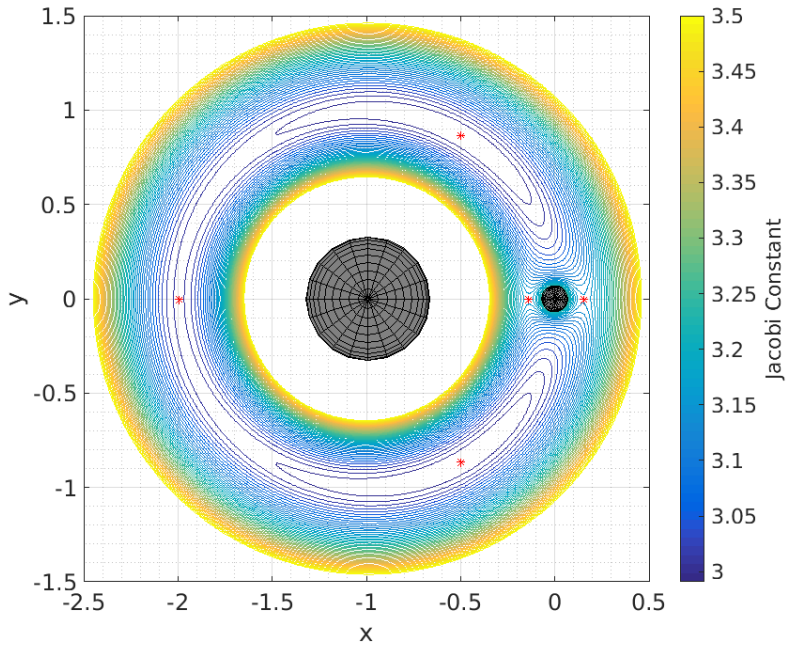

Figure 6.9: Didymos system. Lagrange points and zero-velocity curves in the synodic frame. The unit of length is the distance between the asteroids.

small payloads, it is convenient to exploit the zero-velocity curves of the three body problem to bound the possible motion under the influence of bouncing, navigation and deployment uncertainties. Following this approach, it is natural to start the deployment in the proximity of L1 or L2, as in these regions low energy trajectories can be trapped inside the zero-velocity curves.

Here, we focus on the trajectory up to the separation region close to the L2 point. The mothership starts its motion far from the asteroids, approaches the L2 point and perform a set of maneuvers to hover the secondary asteroid prior to deployment. One important factor in this mission scenario is the navigation error of this spacecraft. We explore in this example the applicability of the Dromo Formulation to the uncertainty propagation and orbit determination of a spacecraft performing this mission. For simplicity, we consider that the Didymos system is coplanar with the ecliptic, approximate the primary and the secondary bodies by perfect homogeneous spheres and neglect the solar radiation pressure effect. The gravitational effect of other bodies of the solar system will also be ignored. While more precise model could be employed, the effect on the orbit uncertainty will be small, since it is mainly affected by the gradient of the

forces, not by the perturbations themselves.

To construct the nominal orbit, we start from the final condition and propagate backwards in time, for a duration of 7 days. The final state is chosen such as that the osculating orbit with respect to the secondary Didymoon has zero eccentricity, 90 deg inclination and a semi-major axis equal to 0.25 in normalized units. We set the orbit plane such that the final position of the spacecraft is aligned with the Didymos–Didymoon line, on the L2 side of the secondary. This state places the spacecraft outside the Sphere of Influence of Didymoon, and backwards or forwards propagation further increases the distance to the secondary. Thus, we choose the primary Didymos as the reference body for the Dromo elements. The final and initial values of the state vector and the corresponding epochs are shown in Table 6.6. Figure 6.11(a) shows the components of the trajectory in the synodic frame (see Fig. 6.10 for the motion in the the x–y). At approximately -5.5 hours the spacecraft comes again close to Didymoon as can be seen in Fig. 6.11(b), but the close approach occurs when the spacecraft is out of the horizontal plane a distance about the Sphere of Influence of Didymoon.

Table 6.6: Final and initial values of the *backwards* propagation. The states are expressed in a Didymos-centered frame with axes parallel to the J2000 Ecliptic frame.

Component	Final values	Initial values
Epoch	2021 Jan 01 12:20	2020 Dec 25 12:20:00
X [-]	0.5831	2.9763
Y [-]	-1.1057	-0.6705
Z [-]	0	0.0671
V_x [-]	0.8845	0.3131
V_y [-]	0.4665	0.3889
V_z [-]	0.1934	0.0762

The spacecraft is assumed to employ optical navigation with respect to the primary of the system. For simplicity, we approximate the measurements of features on the surface of the asteroid by its centroid. We will study how often the spacecraft should make these observations and what accuracy should they have for a safe mission.

We assume an initial Gaussian distribution in Cartesian coordinates with 3–σ standard deviations equal to 100 m and 10^{-6} m/s for position and velocity, respectively. We want to compare the position standard deviation when choosing the 3–σ value of the angular measurements obtained by via of optical navigation as 1 deg and 0.1 deg.

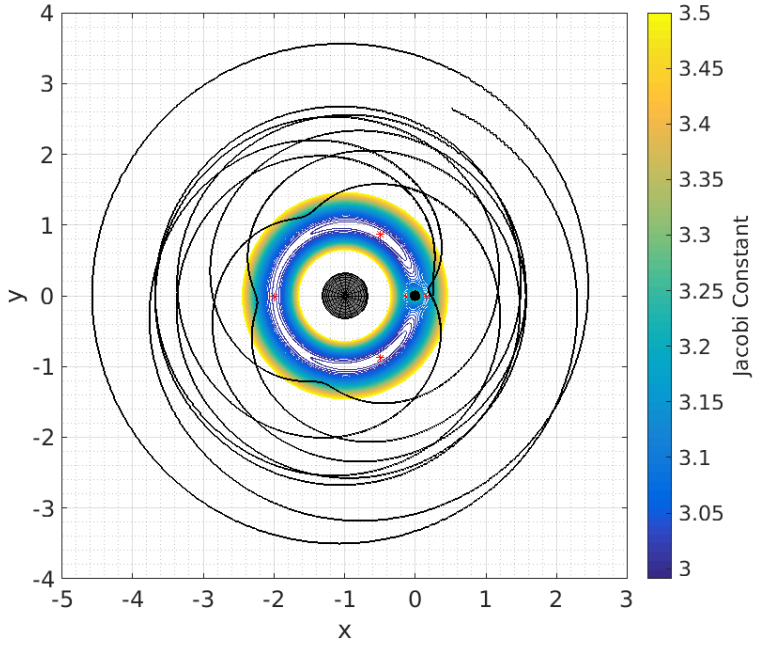

Figure 6.10: Seven days backwards propagation of the nominal trajectory.

We vary the observations interval from 0.1 to 84 hours, with a step of 0.05. Figure 6.12 shows the standard deviations associated to the maximum eigenvalue of the position covariance matrix for two epochs. The first one corresponds to the maximum value over time for fixed observations interval, while the second one is for the final epoch when the spacecraft is near L2 and the transfer phase finishes. The results for both values of the measurement accuracy are included, where the continuous lines represent the most precise set of measurements and the dash-dots lines are for less accurate observations. In both cases, a smooth trend is observed for shorter observations intervals, while for a decreasing number of measurements a rapidly varying behavior appears. The maximum value for the $\sigma_{\text{obs}} = \frac{1}{3}$ deg case crosses the 100 m threshold when the observations interval is greater than 0.5 hours, which might make it an unfeasible choice for this mission scenario as the close approach with the secondary between 1 and 2 days of propagation might strongly perturb the orbit of the spacecraft, or even cause a collision with Didymoon. This could be mitigated with several measurements per hour, by sensor fusion employing other observable quantity, or by choosing the more precise sensor for optical navigation. If the latest option is chosen, the $\sigma_{\text{obs}} = \frac{1}{3}$ deg set of observations can provide a small covariance

matrix: for 4 hour intervals $\simeq 40$ m at the final time, and below 1 m for the final epoch. Additionally, reducing the number of uniformly distributed observations does not impact dramatically the navigation accuracy.

Figure 6.13 shows the maximum standard deviations of the position as a function of time for different observations intervals. On the left, the results suggest that it is hard to obtain a value below 100 m at the close approach with the secondary Didymoon between 1 and 2 days. The results on the figure on the right suggest that a 3–σ accuracy of the optical navigation system of 0.1 deg should be enough for these purposes. Choosing the observations interval as 0.5 hours offers only small improvements over hourly measurements, but double computational burden. Selecting the observations interval as 3 or 6 hours could also be acceptable, depending on other requirements of the mission. The Dromo covariance envelopes are shown in Fig. 6.14.

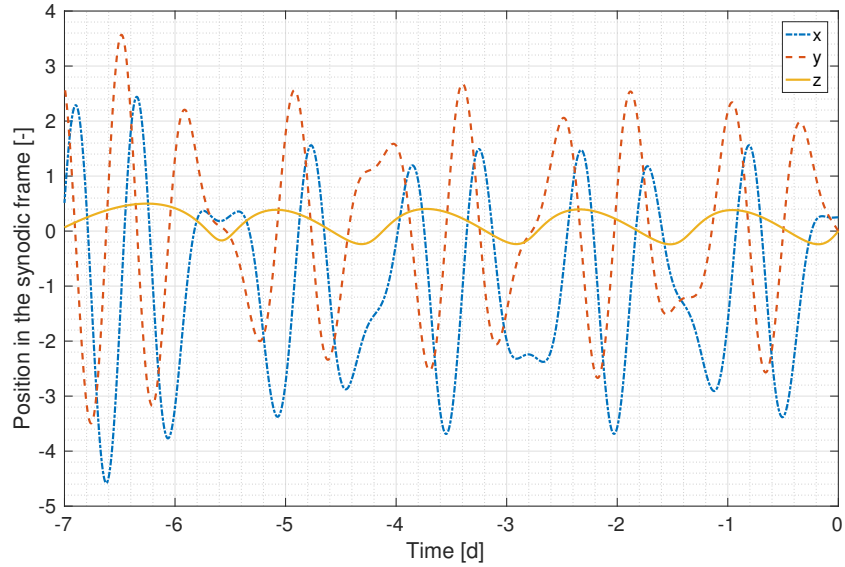

(a) Position components in the synodic frame.

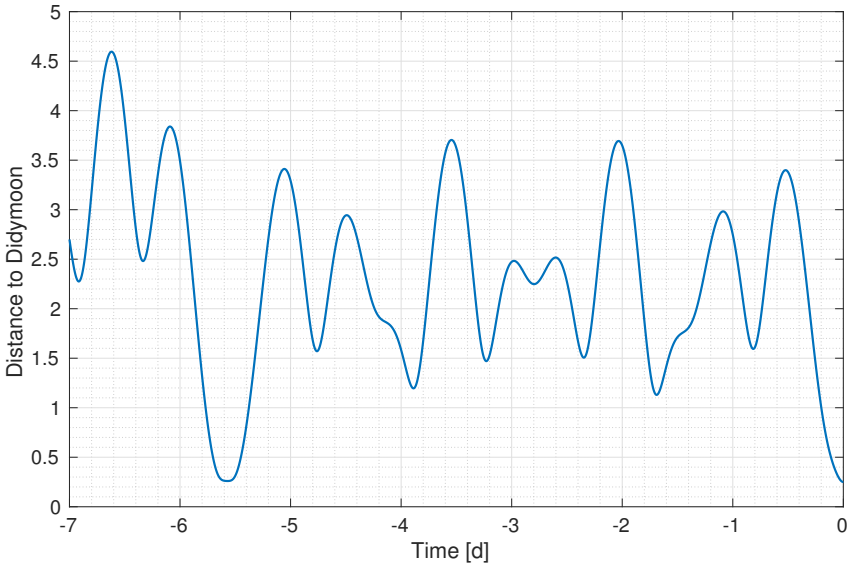

(b) Distance to Didymoon.

Figure 6.11: Seven days backwards propagation of the nominal trajectory

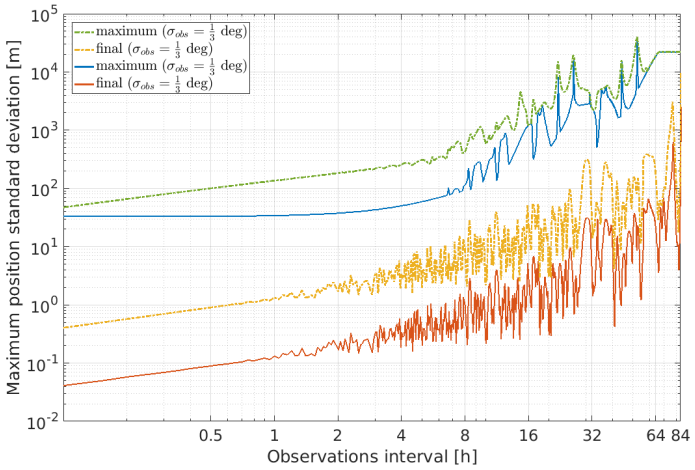

Figure 6.12: Maximum position standard deviation when changing the observations interval from 0.1 to 84 hours, with a step of 0.05. Values for the maximum value over time and for the final epoch.

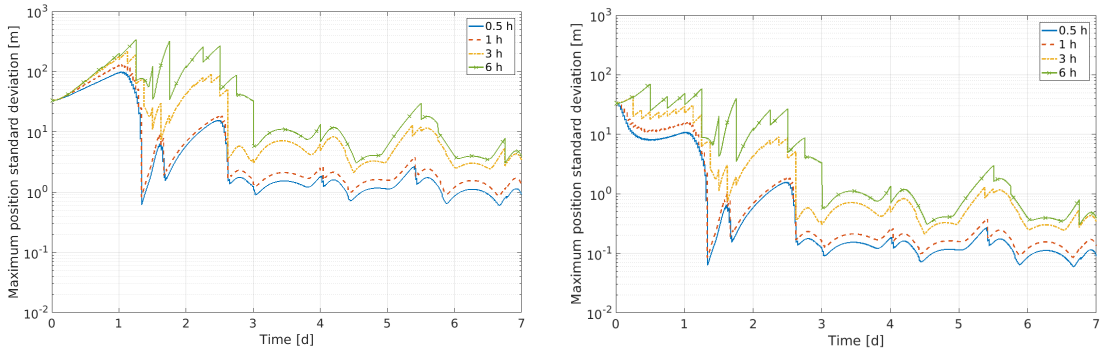

(a) $\sigma_{\text{obs}} = \frac{1}{3}$ deg.

(b) $\sigma_{\text{obs}} = \frac{0.1}{3}$ deg.

Figure 6.13: Maximum position standard deviation with observations taken at intervals of 0.5, 1, 3 and 6 hours.

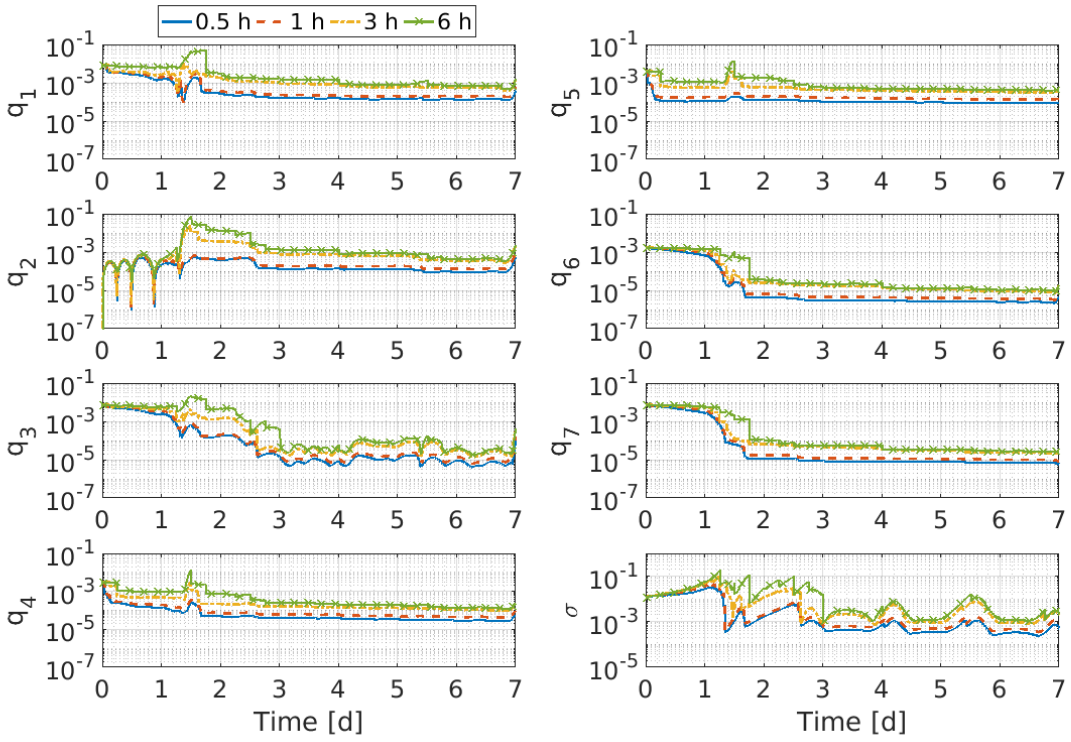

(a) $\sigma_{\text{obs}} = \frac{1}{3}$ deg.

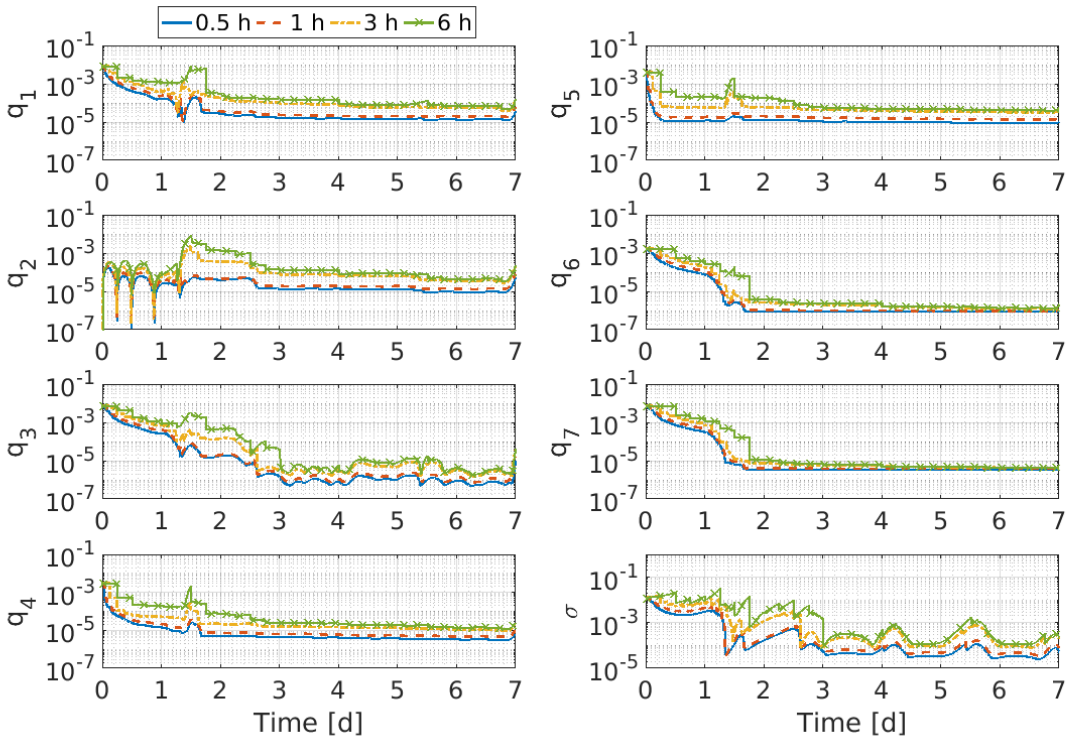

(b) $\sigma_{\text{obs}} = \frac{0.1}{3}$ deg.

Figure 6.14: Dromo Covariance envelopes for with observations taken at intervals of 0.5, 1, 3 and 6 hours.

6.6 Conclusions

In this chapter, the possibility of performing orbit determination with the Dromo formulation was explored, effectively updating the orbit uncertainty distribution. A batch least-squares estimation method and conventional Kalman Filter, a sequential algorithm, were presented, as well as the required formulae to compute the derivatives of the observable quantities in Dromo variables. A remarking result is that the constraints that affect the Dromo variables introduce correction terms in the filtering equations.

Examples in LEO and in the binary asteroid system Didymos were shown, demonstrating the feasibility of the Dromo formulation for navigation purposes when new information is available.

This page intentionally left blank.

Chapter 7

Conclusions

7.1 Concluding Remarks

In this thesis, the propagation of orbit uncertainty using alternate state representation was explored. Linear propagation is a fast and efficient technique for orbit uncertainty propagation, when applicable. In addition, linear propagation has the interesting property of conservation of Gaussianity, which has important advantages to analytically process the propagated uncertainty. However, the equations of motion are usually highly nonlinear. By using nonlinear transformations of the variables used to represent the state vector, the linearity of the motion can be improved, at the cost of solving nonlinear algebraic equations to convert between different representations. In this process, the nonlinearity of the differential equations that describe the motion is partially absorbed by these algebraic equations, being the latest easy to handle in general.

To investigate this phenomena, a campaign of numerical simulations was performed, considering several representations of the state vector and different orbits. It was observed the convenience of employing orbital elements for a more linear propagation. When employing an anomaly as a state variable, it was observed that in decreasing order of linearity, the best option was to choose mean anomaly, followed by eccentric anomaly, being the true anomaly the element with the least linear behavior. These differences vanish for circular orbits, as the three anomalies become equivalent. More over, choosing a time element (that is, a variable that is constant or proportional to the independent variable), or mean anomaly when the mean motion is also a state variable was found to be especially efficient. However, by choosing a state

variable following these results, one must sacrifice the generality of the formulation and particularize it according to the eccentricity of the orbit, and must solve Kepler's equation with its associated computational cost.

Then, using the idea of replacing the state representation, an analytical quadratic-order double-frequency state transition matrix in curvilinear coordinates was proposed for a fast analysis of the evolution of the orbit uncertainty for applications like space debris in LEO or GEO.

For a more precise result, the use of the Dromo formulation was proposed. Dromo is an orbit formulation that has shown excellent results in orbit propagation problems. In addition, it has several analytical advantages, like absorbing the $1/r^2$ term of the gravitational acceleration of the primary body in the variables and the decoupling between the in-plane the out-of-plane motion. In fact, it is specially easy to obtain the gradient matrices that, to the first order, govern the evolution of the orbit uncertainty distribution. This method was applied to several Near Earth Asteroids, and the applicability of the method was found to be limited only by close encounter with a planet. During this close encounters, the linearization error of the third body is no longer negligible, and the linearity of the motion may be lost.

For these cases, a primary body switch was proposed and successfully applied. A primary body switch consists in replacing the reference body of the Dromo variables by another body, the Earth in this application. By introducing geocentric propagation arcs, the orbit uncertainty propagation error was found to decrease up to a factor of 30.

Finally, the possibility of incorporating new information into the uncertainty distribution using the Dromo formulation was explored. A least-squares batch estimator and a sequential Kalman filter were proposed, and their differences with classical approaches were highlighted. The methods were applied to the orbit uncertainty of objects in LEO and to the navigation of a spacecraft in a binary asteroid system.

7.2 Future Work

In future works, there are several points that can be more deeply studied.

In the benchmark of state representations, a Dromo formulation employing a time element as state variable was found to be very effective. The convenience of employing such a formulation for an eccentricity regime, elliptic orbits for example, should be

more carefully evaluated and traded with the need of solving Kepler's Equation.

Moreover, the ease of obtaining the state transition matrix when employing Dromo elements naturally calls for the investigation of using Gaussian Mixture Models (GMM). In a GMM, the uncertainty distribution is modeled as a combination of Gaussian kernels, which are linearly propagated about their mean. This approach could allow for a more precise propagation of the orbit uncertainty.

Finally, and related to the previous point, the analytical expressions for the gradients of the equations of motion make this formulation a promising option for trajectory optimization. Combined to the availability of closed-form solutions for constant thrust in Dromo variables, its application for future deep space mission trajectory design should be further studied.

This page intentionally left blank.

Appendix A

Probability Distribution Function and Moments

A.1 One–Dimensional Random Variable

A.1.1 Parent Distribution

Given an unidimensional random variable X, its cumulative distribution function $g(x)$ is defined as

$$g(x) = P(X \leqslant x) = \int_{-\infty}^{x} p(x)\mathrm{d}x \tag{A.1}$$

where $p(x)$ is the probability distribution function (pdf), the derivative of $g(x)$. The pdf of an unidimensional Gaussian distribution, typically used in uncertainty modeling and propagation because of its analytical properties and because of the Center Limit Theorem, reads

$$p(x) = \frac{1}{\sqrt{2\pi}\sigma} \exp\left\{-\frac{1}{2}\left(\frac{x - \langle x \rangle}{\sigma}\right)^2\right\} \tag{A.2}$$

where $\langle x \rangle$ is the mean value and σ is the standard deviation of the random variable.

The estimation operator $\mathrm{E}[y(x)]$ allows to calculate quantities related to the distribution (see [28, pp. 170–182] or [110, pp. 14–16]):

$$\mathrm{E}\left[y(x)\right] \equiv \int_{-\infty}^{\infty} y(x)p(x)\mathrm{d}x. \tag{A.3}$$

The first order estimator or moment is simply the expected value of the random

variable

$$\mathrm{E}\left[x\right] = \langle x \rangle, \tag{A.4}$$

while the second order unbiased estimator corresponds to the variance

$$\mathrm{E}\left[\left(x - \langle x \rangle\right)^2\right] = \sigma^2. \tag{A.5}$$

We can totally define a Gaussian distribution with the two first moments, $\langle x \rangle$ and σ. Additionally, all the other odd-order moments are zero and the even-order moments are in general non-zero functions of the variance. For example, the fourth-order moment of a Gaussian is equal to $3\sigma^4$.

When studying the third and fourth order moments of a distribution, it is convenient to replace them by related quantities. Herein we introduce two quantities commonly used: the skewness and the excess kurtosis.

The skewness is defined as the standardized, unbiased moment of third order. It gives a measure of the asymmetry of the distribution, and is related to a disparity between the mean and the mode. For example, in the case of a unimodal distribution, positive skewness indicates that the right tail (that is, for large positive x) has more weight on the distribution. The coefficient of skewness γ_1 reads [28, pp. 183–184]

$$\gamma_1 = \mathrm{E}\left[\left(\frac{x - \langle x \rangle}{\sigma}\right)^3\right] = \frac{\mathrm{E}\left[\left(x - \langle x \rangle\right)^3\right]}{\sigma^3}. \tag{A.6}$$

The excess kurtosis is defined as the difference between the fourth-order standardized unbiased moments of the distribution itself and a Gaussian. The coefficient of excess kurtosis is [28, p. 184]

$$\gamma_2 = \frac{\mathrm{E}\left[\left(x - \langle x \rangle\right)^4\right]}{\sigma^4} - 3. \tag{A.7}$$

A positive excess kurtosis is usually associated with distributions that are tall and slim compared to a Gaussian. Conversely, negative excess kurtosis usually happens when the pdf is flatter and more widely distributed.

A.1.2 Sampling Distribution

We will follow Cramér [28] in this section. According to Cramér's notation, m_υ is a *consistent* estimator of order υ, and M_υ is an *unbiased* estimator of the same order. Here, consistent means that the estimator converges to the actual value for a large number of samples, and unbiased means that the estimator average value coincides with the actual average value. These two concepts are not equivalent, and one may occur without the other.

First, the sample mean $\langle x \rangle$ can be estimated as

$$\langle x \rangle = \frac{1}{n} \sum_{i=1}^{n} x_i. \tag{A.8}$$

Then, we introduce the υ-th order sample estimator as

$$m_\upsilon = \frac{1}{n} \sum_{i=1}^{n} \left(x_i - \langle x \rangle \right)^\upsilon , \tag{A.9}$$

which is in general biased. The simplest estimators we can build for the coefficients of skewness and excess kurtosis are

$$g_1 = \frac{m_3}{m_2^{3/2}}, \tag{A.10}$$

$$g_2 = \frac{m_4}{m_2^2} - 3 \tag{A.11}$$

but, unfortunately, they are biased too [28, pp. 342, 349]. We report in the following unbiased estimators up to the fourth order.

The unbiased sample variance follows the well known formula [28, p. 351]

$$M_2 = \frac{n}{n-1} m_2 = \frac{1}{n-1} \sum_{i=1}^{n} \left(x_i - \langle x \rangle \right)^2 . \tag{A.12}$$

Cramér provided unbiased estimators for the third and fourth order moments [28, pp. 351, 352]

$$M_3 = \frac{n^2}{(n-1)(n-2)} m_3 \tag{A.13}$$

$$M_4 = \frac{n\left[\left(n^2 - 2n + 3 \right) m_4 - 3 \left(2n - 3 \right) m_2^2 \right]}{(n-1)(n-2)(n-3)} \tag{A.14}$$

and using them, unbiased estimators for the skewness and excess kurtosis can be constructed as

$$\Gamma_1 = \frac{M_3}{M_2^{3/2}}, \tag{A.15}$$

$$\Gamma_2 = \frac{M_4}{M_2^4} - 3. \tag{A.16}$$

A.2 Multi–Dimensional Random Variable

The cumulative distribution function $g(\boldsymbol{x})$ and probability distribution function $p(\boldsymbol{x})$ (Eq. (A.1)) can be generalized to more than one dimension:

$$g(\boldsymbol{x}) = P(\boldsymbol{X} \leqslant \boldsymbol{x}) = \int_{-\infty}^{x_1} \dots \int_{-\infty}^{x_n} p(\boldsymbol{x}) \mathrm{d}\boldsymbol{x}, \tag{A.17}$$

with $\boldsymbol{X} \in \mathbb{R}^n$. To estimate moments of the distribution, the estimation operator can still be used

$$\mathrm{E}\left[y(\boldsymbol{x})\right] \equiv \int_{-\infty}^{\infty} \dots \int_{-\infty}^{\infty} y(\boldsymbol{x}) p(\boldsymbol{x}) \mathrm{d}\boldsymbol{x}. \tag{A.18}$$

The first order estimator becomes

$$\mathrm{E}\left[\boldsymbol{x}\right] = \langle \boldsymbol{x} \rangle, \tag{A.19}$$

and the second order unbiased estimator yields the covariance matrix $\boldsymbol{C}$:

$$\mathrm{E}\left[\left(\boldsymbol{x} - \langle \boldsymbol{x} \rangle\right) \left(\boldsymbol{x} - \langle \boldsymbol{x} \rangle\right)^\top \right] = \boldsymbol{C} = \begin{bmatrix} \sigma_1^2 & \sigma_1\sigma_2\rho_{12} & \dots & \sigma_1\sigma_n\rho_{1n} \\ \sigma_1\sigma_2\rho_{12} & \sigma_2^2 & \dots & \sigma_2\sigma_n\rho_{2n} \\ \vdots & \vdots & \ddots & \vdots \\ \sigma_1\sigma_n\rho_{1n} & \sigma_2\sigma_n\rho_{2n} & \dots & \sigma_n^2 \end{bmatrix}, \tag{A.20}$$

where ρ_{ij} is the correlation coefficient between the components i and j of the random variable $\boldsymbol{X} \in \mathbb{R}^n$. Note that $-1 \leqslant \rho_{ij} \leqslant 1$.

In the case of a multi-dimensional Gaussian distribution, the probability distribution function reads

$$p(\boldsymbol{x}) = \frac{1}{(2\pi)^{n/2}\sqrt{|\boldsymbol{C}|}} \exp\left\{ -\frac{1}{2} \left(\boldsymbol{x} - \langle \boldsymbol{x} \rangle\right)^\top \boldsymbol{C}^{-1} \left(\boldsymbol{x} - \langle \boldsymbol{x} \rangle\right) \right\}. \tag{A.21}$$

Finally, it is also possible to construct a multi-dimensional version of kurtosis and excess skewness. However, they will be third and fourth order tensors, respectively, and interpreting and analyzing exponentially growing number of components becomes challenging. Instead, when necessary we will use the one-dimensional equations for the marginal distributions, that is, considering one component of the multi-dimensional random variable at a time.

This page intentionally left blank.

Appendix B

Orbital Elements as a Function of the Curvilinear Coordinates

On the following, the expressions that provide the orbital elements of the Follower defined on the rotating frame as a function of its curvilinear coordinates are reported. The angular elements Ω, ω, ν and M_0 presented here must be converted to the interval $[0, 2\pi)$ in which they are usually defined.

The normalized semi-major axis a can be deduced from the vis-viva equation:

$$a = \frac{r}{2 - rv^2}, \tag{B.1}$$

where

$$r = \sqrt{(1+\rho)^2 + z^2}, \tag{B.2}$$

$$v = \sqrt{(1+\rho)^2 \left(1+\dot{\theta}\right)^2 + \dot{\rho}^2 + \dot{z}^2}. \tag{B.3}$$

The normalized mean motion n can be then easily computed as

$$n = \frac{1}{a^{3/2}}. \tag{B.4}$$

The normalized angular momentum vector $\boldsymbol{h}$ can be calculated as

$$\boldsymbol{h} = (h_\rho \cos\theta - h_\theta \sin\theta)\,\boldsymbol{i}' + (h_\rho \sin\theta + h_\theta \cos\theta)\,\boldsymbol{j}' + h_z \boldsymbol{k}' \tag{B.5}$$

with:

$$h_\rho = -\, z\,(1+\rho)\left(1+\dot{\theta}\right), \tag{B.6a}$$

$$h_\theta = z\dot{\rho} - (1+\rho)\,\dot{z}. \tag{B.6b}$$

$$h_z = (1+\rho)^2\left(1+\dot{\theta}\right). \tag{B.6c}$$

The eccentricity vector reads:

$$\boldsymbol{e} = (e_\rho \cos\theta - e_\theta \sin\theta)\,\boldsymbol{i}' + (e_\rho \sin\theta + e_\theta \cos\theta)\,\boldsymbol{j}' + e_z \boldsymbol{k}' \tag{B.7}$$

with:

$$e_\rho = (1+\rho)^3\left(1+\dot{\theta}\right)^2 - z\dot{z}\dot{\rho} + (1+\rho)\,\mathscr{g}^2 - \frac{1+\rho}{r}, \tag{B.8a}$$

$$e_\theta = -\,(1+\rho)\left(1+\dot{\theta}\right)\{(1+\rho)\,\dot{\rho} + z\dot{z}\}, \tag{B.8b}$$

$$e_z = z\dot{\rho}^2 - \dot{\rho}\dot{z}\,(1+\rho) + z\,(1+\rho)^2\left(1+\dot{\theta}\right)^2 - \frac{z}{r}, \tag{B.8c}$$

so that the eccentricity yields:

$$e = \sqrt{e_\rho^2 + e_\theta^2 + e_z^2}. \tag{B.9}$$

The relative inclination takes the form:

$$\cos i = \frac{h_z}{\sqrt{h_\rho^2 + h_\theta^2 + h_z^2}}. \tag{B.10}$$

The right ascension of the ascending node Ω, referred to an inertial frame parallel to $\mathcal{C}$ at $\tau = 0$, obeys

$$\sin\Omega = \frac{\boldsymbol{h}\cdot\boldsymbol{i}}{|\mathbf{h}|}, \qquad \cos\Omega = -\frac{\boldsymbol{h}\cdot\boldsymbol{j}}{|\mathbf{h}|} \tag{B.11}$$

The argument of periapsis ω satisfy

$$\sin\omega = \frac{h_\rho\,(e_z h_\rho - h_z e_\rho) + h_\theta\,(e_z h_\theta - h_z e_\theta)}{h e\sqrt{h_\rho^2 + h_\theta^2}}, \qquad \cos\omega = \frac{e_\theta h_\rho - e_\rho h_\theta}{e\sqrt{h_\rho^2 + h_\theta^2}}. \tag{B.12}$$

We calculate the true anomaly ν as

$$\nu = \phi - \omega. \tag{B.13}$$

where ϕ is argument of longitude, defined as

$$\sin\phi = \frac{z\left(h_\rho^2 + h_\theta^2\right) - (1+\rho)\, h_\rho h_z}{hr\sqrt{h_\rho^2 + h_\theta^2}}, \qquad \cos\phi = -\frac{(1+\rho)\, h_\theta}{r\sqrt{h_\rho^2 + h_\theta^2}}. \tag{B.14}$$

Finally, the mean anomaly at the initial epoch M_0 is computed as

$$M_0 = E_0 - e\sin E_0 \tag{B.15}$$

where E_0 is the initial eccentric anomaly:

$$E_0 = \nu_0 - 2\,\mathrm{atan}\left(\frac{e\sin\nu_0}{1+\sqrt{1-e^2}+e\cos\nu_0}\right). \tag{B.16}$$

This page intentionally left blank.

Appendix C

Melton´s Method

Melton [79] introduced a curvilinear coordinate system $\boldsymbol{c}_{\text{Melton}} = \left(\rho, \theta, z, \dot{\rho}, \dot{\theta}, \dot{z}\right)^{\top}$ to describe the motion of a Follower spacecraft with respect to the Chief's local vertical local horizontal frame $\langle x, y, z \rangle$ as

$$\rho = x, \tag{C.1a}$$

$$\theta = \frac{y}{r^*}, \tag{C.1b}$$

$$z, \tag{C.1c}$$

where r^* is the orbital radius of the Chief, which in the general case changes with time.

In these coordinates, the state transition matrix be expanded

$$\boldsymbol{\Phi}_{\text{Melton}} = {}_0^C\boldsymbol{\Phi} + e\,{}_1^C\boldsymbol{\Phi} + e^2\,{}_2^C\boldsymbol{\Phi} + \mathcal{O}\left(e^3\right), \tag{C.2}$$

where e is the eccentricity of the Chief's orbit.

The matrix with the first order terms ${}_0^C\boldsymbol{\Phi}$ reads

$${}_0^C\Phi = \begin{bmatrix} 4 - 3\cos n\tau & 0 & 0 & \frac{1}{n}\sin n\tau & \frac{2a}{n}(1 - \cos n\tau) & 0 \\ 6(-n\tau + \sin n\tau) & 1 & 0 & \frac{2}{an}(-1 + \cos n\tau) & -3\tau + \frac{4}{n}\sin n\tau & 0 \\ 0 & 0 & \cos n\tau & 0 & 0 & \frac{1}{n}\sin\tau \\ 3n\sin n\tau & 0 & 0 & \cos n\tau & 2a\sin n\tau & 0 \\ \frac{6n}{a}(-1 + \cos n\tau) & 0 & 0 & -\frac{2}{a}\sin n\tau & -3 + 4\cos n\tau & 0 \\ 0 & 0 & -n\sin n\tau & 0 & 0 & \cos n\tau \end{bmatrix}. \tag{C.3}$$

where a is the semi-major axis, and n is the mean motion of the Chief.

The non-zero terms of the corrections ${}_1^C\boldsymbol{\Phi}$ and ${}_2^C\boldsymbol{\Phi}$ are given by

$${}_1^C\Phi_{1,1} = -5\cos n(\tau - \tau_p) - 3\cos n(2\tau - \tau_p) + 13\cos n\tau_p - 5\cos n(\tau + \tau_p) - 6n\tau\sin n(\tau - \tau_p) \tag{C.4}$$

$$ {}_1^C\Phi_{1,4} = \frac{1}{n}\left(-3\sin n(\tau-\tau_p) + \sin n(2\tau-\tau_p) - 3\sin n\tau_p + \sin n(\tau+\tau_p)\right) \tag{C.5} $$

$$ {}_1^C\Phi_{1,5} = \frac{a}{2n}\left(\cos n(\tau-\tau_p) - 4\cos n(2\tau-\tau_p) + 4\cos n\tau_p - \cos n(\tau+\tau_p) - 6n\tau\sin n(\tau-\tau_p)\right) \tag{C.6} $$

$$ {}_1^C\Phi_{2,1} = -\frac{1}{2a}\left(24n\tau\cos n(\tau-\tau_p) + 30n\tau\cos n\tau_p - 4\sin n(\tau-\tau_p) - 15\sin n(2\tau-\tau_p) + \sin n\tau_p - 20\sin n(\tau+\tau_p)\right) \tag{C.7} $$

$$ {}_1^C\Phi_{2,4} = \frac{1}{2an}\left(-12\cos n(\tau-\tau_p) + 5\cos n(2\tau-\tau_p) + 3\cos n\tau_p + 4\cos n(\tau+\tau_p) + 6n\tau\sin n\tau_p\right) \tag{C.8} $$

$$ {}_1^C\Phi_{2,5} = \frac{1}{n}\left(-6n\tau\cos n(\tau-\tau_p) - 5\sin n(\tau-\tau_p) + 5\sin n(2\tau-\tau_p) - \sin n\tau_p + \sin n(\tau+\tau_p)\right) \tag{C.9} $$

$$ {}_1^C\Phi_{2,1} = -\frac{1}{2a}\left(24n\tau\cos n(\tau-\tau_p) + 30n\tau\cos n\tau_p - 4\sin n(\tau-\tau_p) - 15\sin n(2\tau-\tau_p) + \sin n\tau_p - 20\sin n(\tau+\tau_p)\right) \tag{C.10} $$

$$ {}_1^C\Phi_{2,4} = \frac{1}{2an}\left(-12\cos n(\tau-\tau_p) + 5\cos n(2\tau-\tau_p) + 3\cos n\tau_p + 4\cos n(\tau+\tau_p) + 6n\tau\sin n\tau_p\right) \tag{C.11} $$

$$ {}_1^C\Phi_{2,5} = \frac{1}{n}\left(-6n\tau\cos n(\tau-\tau_p) - 5\sin n(\tau-\tau_p) + 5\sin n(2\tau-\tau_p) - \sin n\tau_p + \sin n(\tau+\tau_p)\right) \tag{C.12} $$

$$ {}_1^C\Phi_{3,3} = \frac{1}{2}\cos n(2\tau-\tau_p) - \frac{3}{2}\cos n\tau_p + \cos n(\tau+\tau_p) \tag{C.13} $$

$$ {}_1^C\Phi_{3,6} = \frac{1}{2n}\left(-3\sin n(\tau-\tau_p) + \sin n(2\tau-\tau_p) - 3\sin n\tau_p + \sin n(\tau+\tau_p)\right) \tag{C.14} $$

$$ {}_1^C\Phi_{4,1} = -n\left(6n\tau\cos n(\tau-\tau_p) + \sin n(\tau-\tau_p) - 6\sin n(2\tau-\tau_p) - 5\sin n(\tau+\tau_p)\right) \tag{C.15} $$

$$ {}_1^C\Phi_{4,4} = -3\cos n(\tau-\tau_p) + 2\cos n(2\tau-\tau_p) + \cos n(\tau+\tau_p) \tag{C.16} $$

$$ {}_1^C\Phi_{4,5} = -\frac{a}{2}\left(6n\tau\cos n(\tau-\tau_p) + 7\sin n(\tau-\tau_p) - 8\sin n(2\tau-\tau_p) - \sin n(\tau+\tau_p)\right) \tag{C.17} $$

$$ {}_1^C\Phi_{5,1} = \frac{n}{a}\left(-10\cos n(\tau-\tau_p) + 15\cos n(2\tau-\tau_p) - 15\cos n\tau_p + 10\cos n(\tau+\tau_p) + 12n\tau\sin n(\tau-\tau_p)\right) \tag{C.18} $$

$$ {}_1^C\Phi_{5,4} = \left(6\sin n(\tau-\tau_p)) - 5\sin n(2\tau-\tau_p)) + 3\sin n\tau_p) - 2\sin n(\tau+\tau_p))\right)/a \tag{C.19} $$

$$ {}_1^C\Phi_{5,5} = -11\cos n(\tau-\tau_p) + 10\cos n(2\tau-\tau_p) + \cos n(\tau+\tau_p) + 6n\tau\sin n(\tau-\tau_p) \tag{C.20} $$

$$ {}_1^C\Phi_{6,3} = -n\left(\sin n(2\tau-\tau_p) + \sin n(\tau+\tau_p)\right) \tag{C.21} $$

$$ {}_1^C\Phi_{6,6} = \frac{1}{2}\left(-3\cos n(\tau-\tau_p) + 2\cos n(2\tau-\tau_p) + \cos n(\tau+\tau_p)\right) \tag{C.22} $$

$$
\begin{aligned}
{}^{C}_{2}\Phi_{1,1} = \frac{1}{8}\big(&40 - 40\cos 2n\tau - 40\cos n(\tau - 2\tau_p) - 27\cos n(3\tau - 2\tau_p) - 24\cos 2n(\tau - \tau_p) \\
&+ 152\cos 2n\tau_p - 61\cos n(\tau + 2\tau_p) - 60n\tau\sin n\tau - 60n\tau\sin n(\tau - 2\tau_p) - 48nt\sin 2n(\tau - \tau_p)\big)
\end{aligned}
\tag{C.23}
$$

$$
\begin{aligned}
{}^{C}_{2}\Phi_{1,4} = \frac{1}{8n}\big(&-12n\tau\cos n\tau + 12n\tau\cos n(\tau - 2\tau_p) - 4\sin n\tau + 8\sin 2n\tau + 9\sin n(3\tau - 2\tau_p) \\
&- 24\sin 2n(\tau - \tau_p) - 24\sin 2n\tau_p + 9\sin n(\tau + 2\tau_p)\big)
\end{aligned}
\tag{C.24}
$$

$$
\begin{aligned}
{}^{C}_{2}\Phi_{1,5} = \frac{a}{4n}\big(&-10 + 12\cos n\tau - 2\cos 2n\tau + 2\cos n(\tau - 2\tau_p) - 9\cos n(3\tau - 2\tau_p) \\
&+ 6\cos 2n(\tau - \tau_p) + 2\cos 2n\tau_p - \cos(n(\tau + 2\tau_p) - 12n\tau\sin 2n(\tau - \tau_p)\big)
\end{aligned}
\tag{C.25}
$$

$$
\begin{aligned}
{}^{C}_{2}\Phi_{2,1} = \frac{1}{4a}\big(&-12n\tau - 60n\tau\cos n\tau - 60n\tau\cos n(\tau - 2\tau_p) - 60n\tau\cos 2n(\tau - \tau_p) \\
&- 84n\tau\cos 2n\tau_p - 28\sin n\tau + 50\sin 2n\tau + 6\sin n(\tau - 2\tau_p) + 39\sin n(3\tau - 2\tau_p) \\
&+ 10\sin 2n(\tau - \tau_p) - 6\sin 2n\tau_p + 61\sin n(\tau + 2\tau_p)\big)
\end{aligned}
\tag{C.26}
$$

$$
\begin{aligned}
{}^{C}_{2}\Phi_{2,4} = \frac{1}{4an}\big(&-2 - 8\cos n\tau + 10\cos 2n\tau + 6\cos n(\tau - 2\tau_p) + 13\cos n(3\tau - 2\tau_p) \\
&- 30\cos 2n(\tau - \tau_p) + 2\cos 2n\tau_p + 9\cos n(\tau + 2\tau_p) + 12n\tau\sin n\tau \\
&- 12n\tau\sin n(\tau - 2\tau_p) + 12n\tau\sin 2n\tau_p\big)
\end{aligned}
\tag{C.27}
$$

$$
\begin{aligned}
{}^{C}_{2}\Phi_{2,5} = \frac{1}{4n}\big(&6n\tau - 30n\tau\cos 2n(\tau - \tau_p) - 16\sin n\tau + 5\sin 2n\tau + 26\sin n(3\tau - 2\tau_p) \\
&- 25\sin 2n(\tau - \tau_p) - sin(2n\tau_p + 2\sin n(\tau + 2\tau_p)\big)
\end{aligned}
\tag{C.28}
$$

$$
{}^{C}_{2}\Phi_{3,3} = \frac{1}{8}\big(-4\cos n\tau + 4\cos 2n\tau + 3\cos n(3\tau - 2\tau_p) - 12\cos 2n\tau_p + 9\cos n(\tau + 2\tau_p)\big)
\tag{C.29}
$$

$$
\begin{aligned}
{}^{C}_{2}\Phi_{3,6} = \frac{1}{8n}\big(&-4\sin n\tau + 2\sin 2n\tau + 3\sin n(3\tau - 2\tau_p) \\
&- 6\sin 2n(\tau - \tau_p) - 6\sin 2n\tau_p + 3\sin n(\tau + 2\tau_p)\big)
\end{aligned}
\tag{C.30}
$$

$$
\begin{aligned}
{}^{C}_{2}\Phi_{4,1} = \frac{n}{8}\big(&-60n\tau\cos n\tau - 60n\tau\cos n(\tau - 2\tau_p) - 96n\tau\cos 2n(\tau - \tau_p) - 60\sin n\tau + 80\sin 2n\tau \\
&- 20\sin n(\tau - 2\tau_p) + 81\sin n(3\tau - 2\tau_p) + 61\sin n(\tau + 2\tau_p)\big)
\end{aligned}
\tag{C.31}
$$

$$
\begin{aligned}
{}^{C}_{2}\Phi_{4,4} = \frac{1}{8}\big(&-16\cos n\tau + 16\cos 2n\tau + 12\cos n(\tau - 2\tau_p) + 27\cos n(3\tau - 2\tau_p) - 48\cos 2n(\tau - \tau_p) \\
&+ 9\cos n(\tau + 2\tau_p) + 12n\tau\sin n\tau - 12n\tau\sin n(\tau - 2\tau_p)\big)
\end{aligned}
\tag{C.32}
$$

$$\begin{aligned}{}^{C}_{2}\Phi_{4,5} = -\frac{a}{4}\big(&24n\tau\cos 2n(\tau-\tau_p) + 12\sin n\tau - 4\sin 2n\tau + 2\sin n(\tau-2\tau_p)\\ &- 27\sin n(3\tau-2\tau_p) + 24\sin 2n(\tau-\tau_p) - \sin\big(n(\tau+2\tau_p)\big)\big)\end{aligned} \tag{C.33}$$

$$\begin{aligned}{}^{C}_{2}\Phi_{5,1} = \frac{n}{4a}\big(&-12 - 88\cos n\tau + 100\cos 2n\tau - 54\cos n(\tau-2\tau_p) + 117\cos n(3\tau-2\tau_p)\\ &- 40\cos 2n(\tau-\tau_p) - 84\cos 2n\tau_p + 61\cos n(\tau+2\tau_p) + 60n\tau\sin n\tau\\ &+ 60n\tau\sin n(\tau-2\tau_p) + 120n\tau\sin 2n(\tau-\tau_p)\big)\end{aligned} \tag{C.34}$$

$$\begin{aligned}{}^{C}_{2}\Phi_{5,4} = \frac{1}{4a}\big(&12n\tau\cos n\tau - 12n\tau\cos n(\tau-2\tau_p) + 20\sin n\tau - 20\sin 2n\tau - 18\sin n(\tau-2\tau_p)\\ &- 39\sin n(3\tau-2\tau_p) + 60\sin 2n(\tau-\tau_p) + 12\sin 2n\tau_p - 9\sin n(\tau+2\tau_p)\big)\end{aligned} \tag{C.35}$$

$$\begin{aligned}{}^{C}_{2}\Phi_{5,5} = \frac{1}{2}\big(&3 - 8\cos n\tau + 5\cos 2n\tau + 39\cos n(3\tau-2\tau_p) - 40\cos 2n(\tau-\tau_p)\\ &+ \cos n(\tau+2\tau_p) + 30n\tau\sin 2n(\tau-\tau_p)\big)\end{aligned} \tag{C.36}$$

$${}^{C}_{2}\Phi_{6,3} = \frac{n}{8}\big(4\sin n\tau - 8\sin 2n\tau - 9\sin n(3\tau-2\tau_p) - 9\sin n(\tau+2\tau_p)\big) \tag{C.37}$$

$${}^{C}_{2}\Phi_{6,6} = \frac{1}{8}\big(-4\cos n\tau + 4\cos 2n\tau + 9\cos n(3\tau-2\tau_p) - 12\cos 2n(\tau-\tau_p) + 3\cos n(\tau+2\tau_p)\big) \tag{C.38}$$

In the equations above, τ_p corresponds to the time of periapsis passage of the Chief's orbit.

Appendix D

Relations of Dromo with Other Sets of Variables

D.1 Relations with Classical Orbital Elements

In this subsection, the relation between the Dromo state vector $\boldsymbol{q}$, and the classical orbital elements $\boldsymbol{\alpha e} = (a, e, i, \Omega, \omega, \nu)^\top$ is presented.

D.1.1 Dromo to Classical Orbital Elements Transformation

Once the Dromo elements have been calculated as a function of (real) time, it is convenient to obtain a more intuitive representation of the state. To this end, we employ the inverse of the transformation described by Eqs. (4.3, 4.4, 4.8) to express the classical orbital elements as a function of the Dromo elements:

$$a = \frac{1}{q_3^2 - q_1^2 - q_2^2}, \tag{D.1a}$$

$$e = \frac{1}{q_3}\sqrt{q_1^2 + q_2^2}, \tag{D.1b}$$

$$i = \cos^{-1}\left(-q_4^2 - q_5^2 + q_6^2 + q_7^2\right), \tag{D.1c}$$

$$\Omega = \operatorname{atan2}\left(q_5, q_4\right) + \operatorname{atan2}\left(q_6, q_7\right), \tag{D.1d}$$

$$\omega = \operatorname{atan2}\left(q_2, q_1\right) + \operatorname{atan2}\left(q_6, q_7\right) - \operatorname{atan2}\left(q_5, q_4\right), \tag{D.1e}$$

$$\nu = \sigma - \operatorname{atan2}\left(q_2, q_1\right). \tag{D.1f}$$

D.1.2 Dromo to Classical Orbital Elements Jacobian

After introducing the orbital element state vector $\boldsymbol{oe} = (a, e, i, \Omega, \omega, \nu)^\top$ and by taking into account Eqs. (D.1a – D.1f), one obtains the Jacobian matrix

$$\boldsymbol{J}_{\boldsymbol{q}\to\boldsymbol{oe}} = \frac{\partial \boldsymbol{oe}}{\partial \boldsymbol{q}} = \begin{bmatrix} \frac{2q_1}{\left(q_3^2-q_1^2-q_2^2\right)^2} & \frac{q_1}{q_3\sqrt{q_1^2+q_2^2}} & 0 & 0 & \frac{-q_2}{q_1^2+q_2^2} & \frac{q_2}{q_1^2+q_2^2} \\ \frac{2q_2}{\left(q_3^2-q_1^2-q_2^2\right)^2} & \frac{q_2}{q_3\sqrt{q_1^2+q_2^2}} & 0 & 0 & \frac{q_1}{q_1^2+q_2^2} & \frac{-q_1}{q_1^2+q_2^2} \\ \frac{-2}{\left(q_3^2-q_1^2-q_2^2\right)^2} & -\frac{\sqrt{q_1^2+q_2^2}}{q_3^2} & 0 & 0 & 0 & 0 \\ 0 & 0 & \frac{2q_4}{\sqrt{1-\left(q_4^2+q_5^2-q_6^2-q_7^2\right)^2}} & \frac{-q_5}{q_4^2+q_5^2} & \frac{q_5}{q_4^2+q_5^2} & 0 \\ 0 & 0 & \frac{2q_5}{\sqrt{1-\left(q_4^2+q_5^2-q_6^2-q_7^2\right)^2}} & \frac{q_4}{q_4^2+q_5^2} & \frac{-q_4}{q_4^2+q_5^2} & 0 \\ 0 & 0 & \frac{-2q_6}{\sqrt{1-\left(q_4^2+q_5^2-q_6^2-q_7^2\right)^2}} & \frac{q_7}{q_6^2+q_7^2} & \frac{q_7}{q_6^2+q_7^2} & 0 \\ 0 & 0 & \frac{-2q_7}{\sqrt{1-\left(q_4^2+q_5^2-q_6^2-q_7^2\right)^2}} & \frac{-q_6}{q_6^2+q_7^2} & \frac{-q_6}{q_6^2+q_7^2} & 0 \\ 0 & 0 & 0 & 0 & 0 & 1 \end{bmatrix}^\top . \tag{D.2}$$

Note that this Jacobian presents some singularities, which correspond to the singularities of the orbital elements used (i.e. $i = 0$, $e = 0$).

D.1.3 Classical Orbital Elements to Dromo Transformation

The classical orbital elements to Dromo transformation was introduced to define the Dromo elements in section 4.2.1. This mapping is governed by Eq. (4.3), Eq (4.4) and Eq. (4.8).

D.1.4 Classical Orbital Elements to Dromo Jacobian

Following the same approach as in section D.1.4, Eqs. (4.3, 4.4, 4.8) yield the Jacobian of the Dromo to orbital elements transformation:

$$\boldsymbol{J}_{\boldsymbol{\alpha e}\to\boldsymbol{q}} = \frac{\partial \boldsymbol{q}}{\partial \boldsymbol{\alpha e}} =$$

$$\begin{bmatrix}
\frac{-e\cos\beta}{2\sqrt{a^3(1-e^2)}} & \frac{\cos\beta}{\sqrt{a(1-e^2)^3}} & 0 & 0 & 0 & 0 \\
\frac{-e\sin\beta}{2\sqrt{a^3(1-e^2)}} & \frac{\sin\beta}{\sqrt{a(1-e^2)^3}} & 0 & 0 & 0 & 0 \\
\frac{-1}{2\sqrt{a^3(1-e^2)}} & \frac{e}{\sqrt{a(1-e^2)^3}} & 0 & 0 & 0 & 0 \\
0 & 0 & \frac{1}{2}\cos\frac{i}{2}\cos\frac{\Omega-\omega+\beta}{2} & -\frac{1}{2}\sin\frac{i}{2}\sin\frac{\Omega-\omega+\beta}{2} & \frac{1}{2}\sin\frac{i}{2}\sin\frac{\Omega-\omega+\beta}{2} & 0 \\
0 & 0 & \frac{1}{2}\cos\frac{i}{2}\sin\frac{\Omega-\omega+\beta}{2} & \frac{1}{2}\sin\frac{i}{2}\cos\frac{\Omega-\omega+\beta}{2} & -\frac{1}{2}\sin\frac{i}{2}\cos\frac{\Omega-\omega+\beta}{2} & 0 \\
0 & 0 & -\frac{1}{2}\sin\frac{i}{2}\sin\frac{\Omega+\omega-\beta}{2} & \frac{1}{2}\cos\frac{i}{2}\cos\frac{\Omega+\omega-\beta}{2} & \frac{1}{2}\cos\frac{i}{2}\cos\frac{\Omega+\omega-\beta}{2} & 0 \\
0 & 0 & -\frac{1}{2}\sin\frac{i}{2}\cos\frac{\Omega+\omega-\beta}{2} & -\frac{1}{2}\cos\frac{i}{2}\sin\frac{\Omega+\omega-\beta}{2} & -\frac{1}{2}\cos\frac{i}{2}\sin\frac{\Omega+\omega-\beta}{2} & 0 \\
0 & 0 & 0 & 0 & 0 & 1
\end{bmatrix}. \tag{D.3}$$

D.2 Relations with Cartesian Coordinates

D.2.1 Dromo to Cartesian Coordinates Transformation

It is also possible to express the inertial Cartesian position $\boldsymbol{r} = (x, y, z)^\top$ and velocity $\boldsymbol{v} = (v_x, v_y, v_z)^\top$ as a function of the Dromo elements. This relation can be written in compact form as

$$\boldsymbol{r} = \boldsymbol{R}\begin{pmatrix} r \\ 0 \\ 0 \end{pmatrix} = r\,\boldsymbol{P}\begin{pmatrix} \cos\sigma \\ \sin\sigma \\ 0 \end{pmatrix}, \tag{D.4}$$

$$\boldsymbol{v} = \boldsymbol{R}\begin{pmatrix} u \\ s \\ 0 \end{pmatrix} = \boldsymbol{P}\begin{pmatrix} -q_2 - q_3\sin\sigma \\ q_1 + q_3\cos\sigma \\ 0 \end{pmatrix}, \tag{D.5}$$

where the orbital radius r takes the expression

$$r = \frac{1}{q_3 s}. \tag{D.6}$$

D.2.2 Dromo to Cartesian Coordinates Jacobian

After denoting the Cartesian state vector by $\boldsymbol{x} = (x, y, z, v_x, v_y, v_z)^\top$ and taking into account Eqs. (D.4 – D.5), the Jacobian can be conveniently expressed as a set of column vectors:

$$\boldsymbol{J}_{\boldsymbol{q}\to\boldsymbol{x}} = \frac{\partial \boldsymbol{x}}{\partial \boldsymbol{q}} = \begin{bmatrix} | & | & \cdots & | & | \\ \frac{\partial \boldsymbol{r}}{\partial q_1} & \frac{\partial \boldsymbol{r}}{\partial q_2} & \cdots & \frac{\partial \boldsymbol{r}}{\partial q_7} & \frac{\partial \boldsymbol{r}}{\partial \sigma} \\ \vdots & \vdots & \cdots & \vdots & \vdots \\ \frac{\partial \boldsymbol{v}}{\partial q_1} & \frac{\partial \boldsymbol{v}}{\partial q_2} & \cdots & \frac{\partial \boldsymbol{v}}{\partial q_7} & \frac{\partial \boldsymbol{v}}{\partial \sigma} \\ | & | & \cdots & | & | \end{bmatrix}. \tag{D.7}$$

The derivatives with respect to the three first Dromo elements read:

$$\begin{aligned} \frac{\partial \boldsymbol{r}}{\partial q_1} &= -\frac{r}{s}\cos\sigma \boldsymbol{P}\begin{pmatrix}\cos\sigma\\ \sin\sigma\\ 0\end{pmatrix}, & \frac{\partial \boldsymbol{v}}{\partial q_1} &= \boldsymbol{P}\begin{pmatrix}0\\ 1\\ 0\end{pmatrix}, \\ \frac{\partial \boldsymbol{r}}{\partial q_2} &= -\frac{r}{s}\sin\sigma \boldsymbol{P}\begin{pmatrix}\cos\sigma\\ \sin\sigma\\ 0\end{pmatrix}, & \frac{\partial \boldsymbol{v}}{\partial q_2} &= \boldsymbol{P}\begin{pmatrix}-1\\ 0\\ 0\end{pmatrix}, \\ \frac{\partial \boldsymbol{r}}{\partial q_3} &= -r^2\left(s+q_3\right)\boldsymbol{P}\begin{pmatrix}\cos\sigma\\ \sin\sigma\\ 0\end{pmatrix}, & \frac{\partial \boldsymbol{v}}{\partial q_3} &= \boldsymbol{P}\begin{pmatrix}-\sin\sigma\\ \cos\sigma\\ 0\end{pmatrix}. \end{aligned} \tag{D.8}$$

The derivatives with respect to the Dromo elements that correspond to the quaternion components are:

$$\frac{\partial \boldsymbol{r}}{\partial q_j} = r\frac{\partial \boldsymbol{P}}{\partial q_j}\begin{pmatrix}\cos\sigma\\ \sin\sigma\\ 0\end{pmatrix}, \quad \frac{\partial \boldsymbol{v}}{\partial q_j} = \frac{\partial \boldsymbol{P}}{\partial q_j}\begin{pmatrix}-q_2 - q_3\sin\sigma\\ q_1 + q_3\cos\sigma\\ 0\end{pmatrix}, \tag{D.9}$$

for $j = 4, \ldots 7$. In the above expressions, the derivatives of the $\boldsymbol{P}$ matrix are given by:

$$\begin{aligned} \frac{\partial \boldsymbol{P}}{\partial q_4} &= 2\begin{bmatrix} q_4 & q_5 & q_6 \\ q_5 & -q_4 & -q_7 \\ q_6 & q_7 & -q_4 \end{bmatrix}, & \frac{\partial \boldsymbol{P}}{\partial q_5} &= 2\begin{bmatrix} -q_5 & q_4 & q_7 \\ q_4 & q_5 & q_5 \\ -q_7 & q_6 & -q_5 \end{bmatrix}, \\ \frac{\partial \boldsymbol{P}}{\partial q_6} &= 2\begin{bmatrix} -q_6 & -q_7 & q_4 \\ q_7 & -q_6 & q_5 \\ q_4 & q_5 & q_6 \end{bmatrix}, & \frac{\partial \boldsymbol{P}}{\partial q_7} &= 2\begin{bmatrix} q_7 & -q_6 & q_5 \\ q_6 & q_7 & -q_4 \\ -q_5 & q_4 & q_7 \end{bmatrix}. \end{aligned} \tag{D.10}$$

Finally, the derivatives with respect to the fictitious time σ can be written as

$$\frac{\partial \boldsymbol{r}}{\partial \sigma} = \frac{1}{q_3 s^2}\boldsymbol{P}\begin{pmatrix}-q_2 - q_3\sin\sigma\\ q_1 + q_3\cos\sigma\\ 0\end{pmatrix}, \quad \frac{\partial \boldsymbol{v}}{\partial \sigma} = -q_3\boldsymbol{P}\begin{pmatrix}\cos\sigma\\ \sin\sigma\\ 0\end{pmatrix}. \tag{D.11}$$

D.2.3 Cartesian Coordinates to Dromo Transformation

The inverse of the transformation given by Eqs. (D.4 – D.5) constitutes an alternative of Eqs. (D.1) for setting the initial values of the Dromo variables [8]:

$$q_1 = \left(\frac{h^2}{r} - 1\right)\cos\sigma_0 + h\,u\sin\sigma_0, \tag{D.12a}$$

$$q_2 = \left(\frac{h^2}{r} - 1\right)\sin\sigma_0 - h\,u\cos\sigma_0, \tag{D.12b}$$

$$q_3 = 1/h, \tag{D.12c}$$

$$q_4 = \frac{1}{4q_7}\left\{\left(\frac{h_x y - h_y x}{rh}\right)\cos\sigma_0 + \frac{z}{r}\sin\sigma_0 - \frac{h_y}{h}\right\}, \tag{D.12d}$$

$$q_5 = \frac{1}{4q_7}\left\{\left(\frac{h_x y - h_y x}{rh}\right)\sin\sigma_0 - \frac{z}{r}\cos\sigma_0 + \frac{h_x}{h}\right\}, \tag{D.12e}$$

$$q_6 = \frac{1}{4q_7}\left\{\left(-\frac{x}{r} - \frac{h_z x - h_x z}{rh}\right)\sin\sigma_0 + \left(\frac{y}{r} - \frac{h_y z - h_z y}{rh}\right)\cos\sigma_0\right\}, \tag{D.12f}$$

$$q_7 = \pm\frac{1}{2}\sqrt{1 + \frac{h_z}{h} + \left(\frac{x}{r} + \frac{h_z x - h_x z}{rh}\right)\cos\sigma_0 + \left(\frac{y}{r} - \frac{h_y z - h_z y}{rh}\right)\sin\sigma_0}, \tag{D.12g}$$

$$\sigma = \sigma_0 = \nu_0 + \beta = \operatorname{atan2}\left(h\,u, \frac{h^2}{r} - 1\right) + \beta, \tag{D.12h}$$

where the angular momentum vector and its components can be written as

$$\boldsymbol{h} = (h_x, h_y, h_z)^\top = \boldsymbol{r} \times \boldsymbol{v}, \qquad h = \sqrt{\boldsymbol{h}\cdot\boldsymbol{h}}, \tag{D.13}$$

and the radial velocity u reads

$$u = \frac{\boldsymbol{r}\cdot\boldsymbol{v}}{r}. \tag{D.14}$$

If $q_7 = 0$, the following expressions may be used:

$$q_4 = \frac{1}{2q_6}\frac{h_x}{h}, \tag{D.15a}$$

$$q_5 = \frac{1}{2q_6}\frac{h_y}{h}, \tag{D.15b}$$

$$q_6 = \pm\sqrt{\frac{1}{2}\left(1 + \frac{h_z}{h}\right)}. \tag{D.15c}$$

For the case of q_6 and q_7 being both zero, the inclination corresponds to 180 deg and the

quaternion is defined by

$$q_4 = \pm\sqrt{\frac{1}{2}\left(1 - \left(\frac{y}{r}\sin\sigma_0 + \frac{h_z x - h_x z}{hr}\cos\sigma_0\right)\right)}, \tag{D.16a}$$

$$q_5 = \frac{1}{2q_4}\left(\frac{x}{r}\sin\sigma_0 + \frac{h_y z - h_z y}{hr}\cos\sigma_0\right). \tag{D.16b}$$

Finally, if $q_4 = q_6 = q_7 = 0$, then $q_5 = \pm 1$.

D.2.4 Cartesian Coordinates to Dromo Jacobian

The Cartesian coordinates to Dromo Jacobian can be in principle calculated by differentiation of Eq. (D.12), taking into account the special cases that lead to $q_7 = 0$ (Equation (D.15)), $q_6 = q_7 = 0$ (Equation (D.16)) or $q_4 = q_6 = q_7 = 0$, $q_5 = \pm 1$.

However, a more interesting result can be obtained following the approach by Roa et al. [92]. It is based on inverting the Jacobian matrix of the inverse transformation given by Eq. (D.7). Unfortunately, the dimensions of the domain and image of the transformations are different and the Jacobian matrix cannot be inverted directly. Roa et al. proposed introducing two additional dummy variables to the Cartesian state to obtain an invertible Jacobian matrix. These two dummy variables are chosen following two constraints that naturally arise when increasing the dimension of the state vector from 6 to 8. The first one is the normalization constraint on the Dromo variables corresponding to the quaternion:

$$q_{4,\ldots 7}(\boldsymbol{q}) = q_4^2 + q_5^2 + q_6^2 + q_7^2 - 1 = 0. \tag{D.17}$$

Taking the gradient of the normalization constraint leads the first constraint

$$\frac{\partial q_{4,\ldots 7}}{\partial \boldsymbol{q}}\delta\boldsymbol{q} = \sum_{i=4}^{7} q_i\, \delta q_i = 0. \tag{D.18}$$

The second constraint is introduced by β, as incrementing its value by a constant only rotates the intermediate frame $\mathcal{P}$ around the orbital momentum direction. The new rotated intermediate frame is still one of the infinite Hansel ideal frames, and consequently a valid intermediate frame for the Dromo formulation. From Eqs (4.4a, 4.4b), β can be obtained as

$$\beta = \operatorname{atan2}\left(q_2,\ q_1\right), \tag{D.19}$$

which can be differentiated to obtain

$$\delta\beta = \frac{-q_2\delta q_1 + q_1\delta q_2}{q_1^2 + q_2^2}. \tag{D.20}$$

The second constraint is obtained by arbitrarily setting $\delta\beta = 0$.

By defining the extended Cartesian state $\tilde{\boldsymbol{x}} = (x, y, z, v_x, v_y, v_z, q_{4,\dots 7}, \beta)$, we can define the mapping $\tilde{\boldsymbol{x}} = \tilde{\boldsymbol{x}}(\boldsymbol{q})$, which is invertible except for isolated singularities ($q_3 = 0$ or $e = 0$). This means that it is possible to define

$$\boldsymbol{q} = \tilde{\boldsymbol{x}}^{-1}(\boldsymbol{q}(\tilde{\boldsymbol{x}})) \tag{D.21}$$

The (square) Jacobian matrix for the extended Cartesian state reads

$$\boldsymbol{J}_{\boldsymbol{q}\to\tilde{\boldsymbol{x}}} = \frac{\partial\tilde{\boldsymbol{x}}}{\partial\boldsymbol{q}} = \begin{bmatrix} \vdots & \vdots & \vdots & \vdots & \vdots & \vdots & \vdots & \vdots \\ \frac{\partial\boldsymbol{r}}{\partial q_1} & \frac{\partial\boldsymbol{r}}{\partial q_2} & \frac{\partial\boldsymbol{r}}{\partial q_3} & \frac{\partial\boldsymbol{r}}{\partial q_4} & \frac{\partial\boldsymbol{r}}{\partial q_5} & \frac{\partial\boldsymbol{r}}{\partial q_6} & \frac{\partial\boldsymbol{r}}{\partial q_7} & \frac{\partial\boldsymbol{r}}{\partial\sigma} \\ \vdots & \vdots & \vdots & \vdots & \vdots & \vdots & \vdots & \vdots \\ \frac{\partial\boldsymbol{v}}{\partial q_1} & \frac{\partial\boldsymbol{v}}{\partial q_2} & \frac{\partial\boldsymbol{v}}{\partial q_3} & \frac{\partial\boldsymbol{v}}{\partial q_4} & \frac{\partial\boldsymbol{v}}{\partial q_5} & \frac{\partial\boldsymbol{v}}{\partial q_6} & \frac{\partial\boldsymbol{v}}{\partial q_7} & \frac{\partial\boldsymbol{v}}{\partial\sigma} \\ \vdots & \vdots & \vdots & \vdots & \vdots & \vdots & \vdots & \vdots \\ 0 & 0 & 0 & q_4 & q_5 & q_6 & q_7 & 0 \\ \frac{-q_2}{q_1^2+q_2^2} & \frac{q_1}{q_1^2+q_2^2} & 0 & 0 & 0 & 0 & 0 & 0 \end{bmatrix}. \tag{D.22}$$

Which can be inverted to provide

$$\boldsymbol{J}_{\tilde{\boldsymbol{x}}\to\boldsymbol{q}} = \boldsymbol{J}_{\boldsymbol{q}\to\tilde{\boldsymbol{x}}}{}^{-1}. \tag{D.23}$$

D.3 Relations with Equinoctial Elements

The equinoctial elements $\boldsymbol{\varepsilon} = (a, P_1, P_2, Q_1, Q_2, l)^\top$ are a set of non-singular[1] orbital elements developed by Professor R. A. Broucke at the University of Texas at Austin [7, pp. 490-494]. They are conveniently defined from the orbital elements as

$$a, \tag{D.24a}$$

$$P_1 = e\sin(\Omega + \omega), \tag{D.24b}$$

$$P_2 = e\cos(\Omega + \omega), \tag{D.24c}$$

$$Q_1 = \tan\frac{i}{2}\sin\Omega, \tag{D.24d}$$

[1]Note that the equinoctial orbital elements still present singularities for $i = \pi$ and for degenerate rectilinear orbits, but these cases are usually of less practical importance.

$$Q_2 = \tan\frac{i}{2}\cos\Omega, \tag{D.24e}$$

$$\ell = \Omega + \omega + M, \tag{D.24f}$$

where l is the mean longitude and M is the mean anomaly, which is calculated using the Kepler's equation

$$M = E - e\sin E, \tag{D.25}$$

and the eccentric anomaly E is related to the true anomaly ν by [20]

$$E = \nu - 2\,\mathrm{atan}\left(\frac{e\sin\nu}{1+\sqrt{1-e^2}+e\cos\nu}\right). \tag{D.26}$$

The inverse equation of Eq. (D.24) is given by

$$a \tag{D.27a}$$

$$e = \sqrt{P_1^2 + P_2^2} \tag{D.27b}$$

$$i = 2\arctan\sqrt{Q_1^2 + Q_2^2} \tag{D.27c}$$

$$\Omega = \mathrm{atan2}\left(Q_1, Q_2\right) \tag{D.27d}$$

$$\omega = \mathrm{atan2}\left(P_1, P_2\right) - \mathrm{atan2}\left(Q_1, Q_2\right) \tag{D.27e}$$

$$\nu = \nu\left(P_1, P_2, Q_1, Q_2, l\right) \tag{D.27f}$$

where ν must be calculated by solving Kepler's Equation (Eq. (D.25)).

The equinoctial elements are especially important for the applications of chapters 4 and 5, as the orbital data used in the simulation is provided in these elements (see Appendix E for details).

D.3.1 Dromo to Equinoctial Elements Transformation

The first equinoctial element, the semi-major axis, can be expressed as a function of the Dromo variables as

$$a = \frac{1}{q_3^2 - q_1^2 - q_2^2} \tag{D.28}$$

After some algebra and with the help of a symbolic manipulator software, the second to fifth equinoctial elements are obtained:

$$P_1 = \frac{1}{q_3}\frac{q_2\left(q_7^2 - q_6^2\right) + 2q_1q_6q_7}{q_6^2 + q_7^2} \tag{D.29}$$

$$P_2 = \frac{1}{q_3}\frac{q_1\left(q_7^2 - q_6^2\right) - 2q_2q_6q_7}{q_6^2 + q_7^2} \tag{D.30}$$

$$Q_1 = \frac{q_4q_6 + q_5q_7}{q_6^2 + q_7^2} \tag{D.31}$$

$$Q_2 = \frac{q_4q_7 - q_5q_6}{q_6^2 + q_7^2} \tag{D.32}$$

The last element is more convoluted. First, using Dromo elements, the sum $\Omega + \omega$ reads:

$$\Omega + \omega = \operatorname{atan2}(q_2, q_1) + 2\operatorname{atan2}(q_6, q_7) \tag{D.33}$$

The mean motion M can be decomposed on the difference of the eccentric anomaly E and the $e\sin E$ term. These two terms are given by Eq. (4.50) and (4.48), respectively.

Combining the above terms, the mean longitude becomes

$$\begin{aligned}\ell =& \sigma - \beta - 2\operatorname{atan}\left(\frac{u}{s + \sqrt{q_3^2 - q_1^2 - q_2^2}}\right) - \frac{u}{s}\frac{\sqrt{q_3^2 - q_1^2 - q_2^2}}{q_3} + \\ &+ \operatorname{atan2}(q_2, q_1) + 2\operatorname{atan2}(q_6, q_7)\end{aligned} \tag{D.34}$$

D.3.2 Dromo to Equinoctial Elements Jacobian

The Jacobian for the Dromo to equinoctial elements transformation results in:

$$\boldsymbol{J}_{\boldsymbol{q}\to\boldsymbol{\varepsilon}} = \frac{\partial \boldsymbol{q}}{\partial \boldsymbol{\varepsilon}} =$$

$$\begin{bmatrix}
\frac{2q_1}{\left(q_3^2-q_1^2-q_2^2\right)^2} & \frac{2q_2}{\left(q_3^2-q_1^2-q_2^2\right)^2} & \frac{-2q_3}{\left(q_3^2-q_1^2-q_2^2\right)^2} & 0 & 0 & 0 & 0 & 0 \\
\frac{1}{q_3}\frac{2q_6q_7}{q_6^2+q_7^2} & -\frac{1}{q_3}\frac{q_6^2-q_7^2}{q_6^2+q_7^2} & 0 & 0 & 0 & \frac{\partial P_1}{\partial q_6} & \frac{\partial P_1}{\partial q_7} & 0 \\
-\frac{1}{q_3}\frac{q_6^2-q_7^2}{q_6^2+q_7^2} & -\frac{1}{q_3}\frac{2q_6q_7}{q_6^2+q_7^2} & 0 & 0 & 0 & \frac{\partial P_2}{\partial q_6} & \frac{\partial P_2}{\partial q_7} & 0 \\
0 & 0 & 0 & \frac{q_6}{q_6^2+q_7^2} & \frac{q_7}{q_6^2+q_7^2} & \frac{\partial Q_1}{\partial q_6} & \frac{\partial Q_1}{\partial q_7} & 0 \\
0 & 0 & 0 & \frac{q_7}{q_6^2+q_7^2} & -\frac{q_6}{q_6^2+q_7^2} & \frac{\partial Q_2}{\partial q_6} & \frac{\partial Q_2}{\partial q_7} & 0 \\
\frac{\partial \ell}{\partial q_1} & \frac{\partial \ell}{\partial q_2} & \frac{\partial \ell}{\partial q_3} & 0 & 0 & \frac{2q_7}{q_6^2+q_7^2} & -\frac{2q_6}{q_6^2+q_7^2} & \frac{\partial l}{\partial \sigma}
\end{bmatrix} \tag{D.35}$$

where

$$\frac{\partial P_1}{\partial q_6} = -\frac{1}{q_3}\frac{q_1\left(q_6^2 - q_7^2\right) + 2q_2q_6q_7}{\left(q_6^2 + q_7^2\right)^2}2q_7, \tag{D.36a}$$

$$\frac{\partial P_1}{\partial q_7} = \frac{1}{q_3}\frac{q_1\left(q_6^2-q_7^2\right)+2q_2q_6q_7}{\left(q_6^2+q_7^2\right)^2}2q_6, \tag{D.36b}$$

$$\frac{\partial P_2}{\partial q_6} = \frac{1}{q_3}\frac{q_2\left(q_6^2-q_7^2\right)-2q_1q_6q_7}{\left(q_6^2+q_7^2\right)^2}2q_7, \tag{D.36c}$$

$$\frac{\partial P_2}{\partial q_7} = -\frac{1}{q_3}\frac{q_2\left(q_6^2-q_7^2\right)-2q_1q_6q_7}{\left(q_6^2+q_7^2\right)^2}2q_6, \tag{D.36d}$$

$$\frac{\partial Q_1}{\partial q_6} = -\frac{q_4\left(q_6^2-q_7^2\right)+2q_5q_6q_7}{\left(q_6^2+q_7^2\right)^2}, \tag{D.36e}$$

$$\frac{\partial Q_1}{\partial q_7} = \frac{q_5\left(q_6^2-q_7^2\right)-2q_4q_6q_7}{\left(q_6^2+q_7^2\right)^2}, \tag{D.36f}$$

$$\frac{\partial Q_2}{\partial q_6} = \frac{q_5\left(q_6^2-q_7^2\right)-2q_4q_6q_7}{\left(q_6^2+q_7^2\right)^2}, \tag{D.36g}$$

$$\frac{\partial Q_2}{\partial q_7} = \frac{q_4\left(q_6^2-q_7^2\right)+2q_5q_6q_7}{\left(q_6^2+q_7^2\right)^2}, \tag{D.36h}$$

and

$$\begin{aligned}\frac{\partial \ell}{\partial q_1} =& -\frac{q_2}{q_1^2+q_2^2}-\frac{\sqrt{a}q_1u\cos E}{s\,e\,q_3}+\frac{\cos E\sin\sigma}{\sqrt{a}s\,e\,q_3}-\frac{2uq_1}{\sqrt{a}s^2e^2q_3^2}-\frac{u\cos\sigma}{\sqrt{a}s^2e^2q_3}\\ &+\frac{\sqrt{a}uq_1}{q_3s}+\frac{u\cos\sigma-s\sin\sigma}{\sqrt{a}q_3s^2},\end{aligned} \tag{D.37}$$

$$\begin{aligned}\frac{\partial \ell}{\partial q_2} =& \frac{q_1}{q_1^2+q_2^2}-\frac{\sqrt{a}q_2u\cos E}{s\,e\,q_3}-\frac{\cos E\cos\sigma}{\sqrt{a}s\,e\,q_3}-\frac{2uq_2}{\sqrt{a}s^2e^2q_3^2}-\frac{u\sin\sigma}{\sqrt{a}s^2e^2q_3}\\ &+\frac{\sqrt{a}uq_2}{q_3s}+\frac{u\sin\sigma+s\cos\sigma}{\sqrt{a}q_3s^2},\end{aligned} \tag{D.38}$$

$$\frac{\partial \ell}{\partial q_3} = \frac{\sqrt{1-e^2}}{s^2q_3}\left(\cos\sigma\left(q_1u-q_2s\right)+2q_3u+q_2q_3\cos\sigma+q_1q_2\right). \tag{D.39}$$

$$\frac{\partial \ell}{\partial \sigma} = \frac{\left(q_3^2-q_1^2-q_2^2\right)^{3/2}}{s^2q_3}. \tag{D.40}$$

D.3.3 Equinoctial Elements to Dromo Transformation

It is straightforward to obtain the third Dromo element:

$$q_3 = \frac{1}{h} = \sqrt{\frac{1}{a\left(1-P_1^2-P_2^2\right)}}. \tag{D.41}$$

The two first equinoctial elements also can be written without much difficulty as

$$q_1 = \frac{e}{h}\cos\beta = \sqrt{\frac{P_1^2 + P_2^2}{a\left(1 - P_1^2 - P_2^2\right)}}\cos\beta, \tag{D.42a}$$

$$q_2 = \frac{e}{h}\sin\beta = \sqrt{\frac{P_1^2 + P_2^2}{a\left(1 - P_1^2 - P_2^2\right)}}\sin\beta. \tag{D.42b}$$

Next, we introduce $\tilde{\omega} = \omega - \beta$, the angle from the $x_{\mathcal{I}}$ to the $x_{\mathcal{P}}$ axis.

In the first place, note that

$$\sin\frac{i}{2} = \sqrt{\frac{Q_1^2 + Q_2^2}{1 + Q_1^2 + Q_2^2}}, \tag{D.43a}$$

$$\cos\frac{i}{2} = \frac{1}{\sqrt{1 + Q_1^2 + Q_2^2}}. \tag{D.43b}$$

Additionally, to facilitate the calculation of q_4 and q_5, the following expressions are useful:

$$\cos\left(\frac{\Omega - \tilde{\omega}}{2}\right) = \cos\Omega\cos\left(\frac{\Omega + \tilde{\omega}}{2}\right) + \sin\Omega\sin\left(\frac{\Omega + \tilde{\omega}}{2}\right), \tag{D.44a}$$

$$\sin\left(\frac{\Omega - \tilde{\omega}}{2}\right) = \sin\Omega\cos\left(\frac{\Omega + \tilde{\omega}}{2}\right) - \cos\Omega\sin\left(\frac{\Omega + \tilde{\omega}}{2}\right). \tag{D.44b}$$

We can exploit Eq. (D.27d) and Eq. (D.27e) to express the trigonometric functions in the formulae above as

$$\sin\Omega = \frac{Q_1}{\sqrt{Q_1^2 + Q_2^2}} \tag{D.45a}$$

$$\cos\Omega = \frac{Q_2}{\sqrt{Q_1^2 + Q_2^2}} \tag{D.45b}$$

$$\sin\left(\frac{\Omega + \tilde{\omega}}{2}\right) = \sin\left(\frac{\operatorname{atan2}\left(P_1, P_2\right) - \beta}{2}\right) \tag{D.45c}$$

$$\cos\left(\frac{\Omega + \tilde{\omega}}{2}\right) = \cos\left(\frac{\operatorname{atan2}\left(P_1, P_2\right) - \beta}{2}\right) \tag{D.45d}$$

Combining the above results, the quaternion components are obtained

$$\begin{aligned} q_4 &= \sin\frac{i}{2}\cos\frac{\Omega - \tilde{\omega}}{2} = \\ &= \frac{1}{\sqrt{1 + Q_1^2 + Q_2^2}}\left(Q_2\cos\left(\frac{\operatorname{atan2}\left(P_1, P_2\right) - \beta}{2}\right) + Q_1\sin\left(\frac{\operatorname{atan2}\left(P_1, P_2\right) - \beta}{2}\right)\right) \end{aligned} \tag{D.46a}$$

$$q_5 = \sin\frac{i}{2}\sin\frac{\Omega-\tilde{\omega}}{2}$$
$$= \frac{1}{\sqrt{1+Q_1^2+Q_2^2}}\left(Q_1\cos\left(\frac{\operatorname{atan2}(P_1,P_2)-\beta}{2}\right) - Q_2\sin\left(\frac{\operatorname{atan2}(P_1,P_2)-\beta}{2}\right)\right) \tag{D.46b}$$

$$q_6 = \cos\frac{i}{2}\sin\frac{\Omega+\tilde{\omega}}{2} = \frac{1}{\sqrt{1+Q_1^2+Q_2^2}}\sin\left(\frac{\operatorname{atan2}(P_1,P_2)-\beta}{2}\right) \tag{D.46c}$$

$$q_7 = \cos\frac{i}{2}\cos\frac{\Omega+\tilde{\omega}}{2} = \frac{1}{\sqrt{1+Q_1^2+Q_2^2}}\cos\left(\frac{\operatorname{atan2}(P_1,P_2)-\beta}{2}\right) \tag{D.46d}$$

Finally, the initial value for the pseudo-anomaly is obtained after solving the modified Kepler's Equation in equinoctial coordinates:

$$E = \sigma - \beta - 2\operatorname{atan}\frac{\sqrt{P_1^2+P_2^2}\sin(\sigma-\beta)}{1+\sqrt{1-\left(\sqrt{P_1^2+P_2^2}\right)^2}+\sqrt{P_1^2+P_2^2}\cos(\sigma-\beta)}, \tag{D.47a}$$

$$\ell - \operatorname{atan2}(P_1,P_2) = E - \sqrt{P_1^2+P_2^2}\sin E. \tag{D.47b}$$

An alternative is to first calculate the eccentric anomaly using a standard Kepler's Equation solver, convert it to true anomaly, and finally obtain the initial value of σ. In any case, the initial value of β can be set to zero without any loss of generality.

Appendix E

NEODyS data

NEODyS is a web based service that provides information about all Near Earth Asteroids, including ephemerides and observational information, orbit uncertainty, future close approaches and other useful data like impact probability. NEODyS was created in 1999 at the Department of Mathematics of the University of Pisa, Italy. Nowadays, it is maintained by the University of Pisa and the SpaceDyS company, and economically supported by ESA. NEODyS directly processes astrometric data provided by the Minor Planet Center, and updates the predicted orbits and their uncertainty. An overview of NEODyS can be found in [25] and [12].

As noted in [12], the only other comparable service for Earth-impact monitoring is the American SENTRY system[1] maintained by the Jet Propulsion Laboratory (JPL). JPL also provides ephemeris and covariance information for Near Earth Asteroids and other minor bodies of the solar system in their Small-Body Database [2].

In the following pages, the NEODyS raw data used for all the simulations of the present dissertation are reported. The state vector (EQU) and its covariance matrix (COV) are expressed in equinoctial elements, employing the mean longitude as angular variable. All the elements are defined with respect to the mean ecliptic and equinox of J2000 reference frame, and the epoch is given as Modified Julian Date (MJD) in Terrestial Dynamical Time (TDT).

[1] `https://cneos.jpl.nasa.gov/sentry/`, Accessed on 2018 May 22
[2] `https://ssd.jpl.nasa.gov/sbdb.cgi`, Accessed on 2018 May 22

E.1 2000SG344

```
format  = 'OEF2.0'          ! file format
rectype = 'ML'              ! record type (1L/ML)
refsys  = ECLM J2000        ! default reference system
END_OF_HEADER
2000SG344
! Equinoctial elements: a, e*sin(LP), e*cos(LP), tan(i/2)*sin(LN), tan(i/2)*cos(LN), mean long.
 EQU    9.8285676439236425E-01    0.063139018864697   -0.017830918391328    -0.000224614467801    -0.000914937903828
       46.8358122160849
 MJD       51490.508335304 TDT
 MAG   24.788   0.150
! Non-grav parameters: model used, actual number in use, dimension
 LSP    0   0     6
! RMS     2.01984E-06    5.77370E-06    2.74613E-06    6.52276E-08    1.09378E-07    2.05218E-04
! EIG     4.76236E-09    9.01515E-09    7.64405E-08    7.90803E-08    3.33361E-07    7.59462E-06
! WEA     0.26571   -0.75988    0.36110    0.00198    0.01289    0.47056
 COV    4.079743672610729E-12  -1.166076037402100E-11   5.523885631879679E-12
 COV    3.026022973027605E-14   1.984814552553843E-13   4.120070104031324E-10
 COV    3.333565169521630E-11  -1.580306389162065E-11  -8.656919840223246E-14
 COV   -5.670248472984236E-13  -1.179275301839643E-09   7.541226074860318E-12
 COV    4.146839705884446E-14   2.665243963585391E-13   5.631144834569296E-10
 COV    4.254644050204784E-15   4.348633940776643E-15   3.092956608453093E-12
 COV    1.196363733130423E-14   1.988894139006423E-11   4.211439485192131E-08
 NOR    3.707460987091648E+16   1.404020130313298E+16  -5.350933391505376E+15
 NOR   -1.612658576295161E+14   2.220362475698557E+14   1.019018386731636E+14
 NOR    5.335225499378274E+15  -1.986674035062568E+15  -2.975348553172076E+14
 NOR    4.120637212969828E+14   3.843075453743004E+13   9.478747300222286E+14
 NOR   -4.312705605823994E+14   5.944954020117991E+14  -1.620504170390726E+13
 NOR    4.395732722920799E+15  -5.763081617323240E+15   1.411575274210380E+12
 NOR    8.008305839748438E+15  -1.941489527956386E+12   2.967324999808820E+11
```

E.2 2011AM37

```
format  = 'OEF2.0'          ! file format
rectype = 'ML'              ! record type (1L/ML)
refsys  = ECLM J2000        ! default reference system
END_OF_HEADER
2011AM37
! Equinoctial elements: a, e*sin(LP), e*cos(LP), tan(i/2)*sin(LN), tan(i/2)*cos(LN), mean long.
 EQU    1.1038918010272913E+00    0.131734645896958    0.075043640696685    -0.021859337322328    0.008615662281624
       100.5181102315087
 MJD       55575.062740815 TDT
 MAG   29.691   0.150
! Non-grav parameters: model used, actual number in use, dimension
 LSP    0   0     6
! RMS     4.26556E-04    3.81820E-04    2.13142E-04    4.95001E-05    2.01995E-05    3.43606E-02
! EIG     3.49145E-09    3.77176E-09    1.39077E-07    7.13694E-07    2.30587E-05    8.57402E-04
! WEA     0.49729    0.44515    0.24829    -0.05745    0.02347    -0.69932
 COV    1.819496993635343E-07   1.628673740084247E-07   9.063661744281500E-08
 COV   -2.094035885237365E-08   8.560593642929684E-09  -1.463968271123454E-05
 COV    1.457868630392961E-07   8.114201999464935E-08  -1.874824082328911E-08
 COV    7.664248239853916E-09  -1.310541968117600E-05   4.542961563524778E-08
 COV   -1.053684162222579E-08   4.302504382022841E-09  -7.320303134536399E-06
 COV    2.450261587850543E-09  -9.997676118243560E-10   1.695298246028275E-06
 COV    4.080210309852605E-10  -6.925537456132742E-07   1.180647525223728E-03
 NOR    3.146627938170614E+15  -7.186481520412913E+15  -9.231810888161546E+15
 NOR    3.251658833247517E+15   7.528511044756686E+15  -9.824651848122795E+13
 NOR    1.860345497280912E+16   2.763474852983175E+16  -3.490287220137036E+15
 NOR   -8.098255167020821E+15   2.889953229212129E+14   4.667580411999218E+16
 NOR    2.244627665236814E+15   5.145863089694378E+15   4.814762166435624E+14
 NOR    1.061019749632375E+16   2.458849826959601E+16   1.468205938659309E+13
 NOR    5.701732525943160E+16   3.350363370849934E+13   4.973517892233792E+12
```

E.3 2013HO

```
format  = 'OEF2.0'          ! file format
rectype = 'ML'              ! record type (1L/ML)
refsys  = ECLM J2000        ! default reference system
END_OF_HEADER
2013HO
! Equinoctial elements: a, e*sin(LP), e*cos(LP), tan(i/2)*sin(LN), tan(i/2)*cos(LN), mean long.
 EQU    1.0232233890992430E+00    0.028994063166331   -0.012644116201266    -0.033111190090623    -0.079436661604393
        205.00537994210 55
 MJD       56400.916880920 TDT
 MAG   25.679   0.150
! Non-grav parameters: model used, actual number in use, dimension
 LSP    0   0     6
! RMS     3.15931E-05    1.34652E-06    2.13852E-05    1.93406E-05    4.65032E-05    1.29584E-03
! EIG     5.13057E-09    5.98036E-09    6.89176E-08    7.91330E-07    1.93325E-06    6.70896E-05
! WEA     0.47075    0.01425   -0.31867   -0.28827   -0.69311   -0.33636
 COV    9.981220404509446E-10   2.944669245232316E-11  -6.754955340757331E-10
 COV   -6.107363458607172E-10  -1.468569008186696E-09  -4.077449221819273E-08
 COV    1.813115767088311E-12  -2.022456440099787E-11  -1.849818784438605E-11
 COV   -4.434069306209212E-11  -1.315210341508972E-09   4.573254411896619E-10
 COV    4.133908451407643E-10   9.939740517117441E-10   2.763362193315430E-08
 COV    3.740587064098304E-10   8.993927766717231E-10   2.500249673793733E-08
 COV    2.162544061738712E-09   6.010333701151700E-08   1.679200267392512E-06
 NOR    3.068207614040418E+15   2.776852841714432E+15   2.104602162595907E+15
 NOR   -6.936260292967826E+15   3.657300587011491E+15   1.441568862320295E+13
 NOR    2.557774469502500E+16  -9.869586768639242E+15  -7.613467035255562E+14
 NOR    6.282706961410154E+14   2.387277558210233E+14   7.456619475677726E+15
 NOR   -7.566751717054791E+15   3.873887575782390E+15  -1.053273932821742E+14
 NOR    1.778837432514690E+16  -9.225893638993336E+15   2.085883266784781E+13
 NOR    4.798871518229974E+15  -8.847353736977977E+12   2.276429216823781E+12
```

E.4 2016DJ

```
format  = 'OEF2.0'          ! file format
rectype = 'ML'              ! record type (1L/ML)
refsys  = ECLM J2000        ! default reference system
END_OF_HEADER
2016DJ
! Equinoctial elements: a, e*sin(LP), e*cos(LP), tan(i/2)*sin(LN), tan(i/2)*cos(LN), mean long.
 EQU  1.0231988694975496E+00  0.119159913646651  0.108495377809516  -0.014917174436943  0.034920616547363
      146.4782969220512
 MJD      57452.105958698 TDT
 MAG  25.652  0.150
! Non-grav parameters: model used, actual number in use, dimension
 LSP  0  0  6
! RMS   4.47804E-06  9.71574E-06  9.46227E-06  1.34897E-06  3.17717E-06  1.58888E-03
! EIG   8.01420E-09  8.90971E-09  5.08366E-08  1.74069E-07  3.85670E-07  3.13805E-05
! WEA   0.14249  0.30958  0.30140  -0.04296  0.10117  -0.88371
 COV   2.005284106826442E-11  4.346215454149933E-11  4.223378649529736E-11
 COV  -6.027532662755070E-12  1.419476182890737E-11  -7.104326186848901E-09
 COV   9.439566968725698E-11  9.183987352694578E-11  -1.309185530069565E-11
 COV   3.082983187015817E-11  -1.543558156750595E-08  8.953456364058501E-11
 COV  -1.275730911262965E-11  3.004542240693214E-11  -1.502729274768849E-08
 COV   1.819725272381100E-12  -4.285777966816858E-12  2.141866294592010E-09
 COV   1.009441652376883E-11  -5.044038159346785E-09  2.524540591840841E-06
 NOR   1.390566083632816E+14  4.223412686771727E+14  3.264771356827955E+14
 NOR  -2.648275856293538E+14  -2.492711057942669E+14  4.643595926858519E+12
 NOR   9.453993769416328E+15  4.757490233042424E+15  -8.967736690257752E+14
 NOR  -3.519727126967361E+14  8.736874613626517E+13  2.519339022924354E+15
 NOR  -6.936830844135491E+14  -4.317106833409945E+14  4.472935997280297E+13
 NOR   1.158524413804658E+16  4.775654197686226E+15  -1.064482205705382E+13
 NOR   2.228591586838438E+15  -5.022284600125611E+12  8.125068027603077E+11
```

E.5 (367789) 2011AG5

```
format  = 'OEF2.0'          ! file format
rectype = 'ML'              ! record type (1L/ML)
refsys  = ECLM J2000        ! default reference system
END_OF_HEADER
367789
! Equinoctial elements: a, e*sin(LP), e*cos(LP), tan(i/2)*sin(LN), tan(i/2)*cos(LN), mean long.
 EQU  1.4305693219850588E+00  -0.062358365157607  -0.385417317713688   0.022434681409097  -0.022998593128761
      333.4409698097048
 MJD      55894.708051299 TDT
 MAG  21.853  0.150
! Non-grav parameters: model used, actual number in use, dimension
 LSP  0  0  6
! RMS   3.53369E-08   6.27018E-08   3.48284E-08   5.45783E-08   3.24201E-08   5.74627E-06
! EIG   1.13325E-08   1.77191E-08   3.77510E-08   5.90593E-08   6.36220E-08   1.05253E-07
! WEA   0.25404   0.17583  -0.08546   0.00931  -0.00223  -0.94718
 COV   1.248693538115729E-15  -2.402550517134857E-16  -7.704066637066305E-16
 COV   3.281593592969466E-17  -1.855579759894068E-17  -1.496023668161782E-13
 COV   3.931517285227024E-15  -5.464760638375324E-17  -1.604848623886423E-16
 COV   2.548402944998297E-16  -7.954499482036419E-14   1.213019599159924E-15
 COV  -3.620768387140700E-17  -2.286898116606691E-17   3.856145636534673E-14
 COV   2.978786116989022E-15  -1.391065867816345E-15  -5.389934533112802E-15
 COV   1.051064177442225E-15   3.111763656544980E-15   3.301967141301515E-11
 NOR   5.674713118529383E+15   8.902461670994552E+14   2.863048720598804E+15
 NOR   1.516621817722036E+13  -1.059043985740981E+14   2.452396016384379E+13
 NOR   4.139874250397238E+14   4.362374851225258E+14  -4.024194003609715E+13
 NOR  -1.418321375483238E+14   4.528090339804182E+12   2.304492569413206E+15
 NOR   5.874871040060219E+13   3.910454002279043E+13   1.133717373139573E+13
 NOR   8.884447175347260E+14   1.187333376611016E+15  -6.370810202287504E+10
 NOR   2.558909715268078E+15  -9.145029352073711E+11   1.391399009918831E+11
```

E.6 2012AP10

```
format  = 'OEF2.0'          ! file format
rectype = 'ML'              ! record type (1L/ML)
refsys  = ECLM J2000        ! default reference system
END_OF_HEADER
2012AP10
! Equinoctial elements: a, e*sin(LP), e*cos(LP), tan(i/2)*sin(LN), tan(i/2)*cos(LN), mean long.
 EQU    8.8920636610553039E-01   -0.100482810605067    0.095943151462522     0.023352702043761    -0.004779774579820
        270.9470045736080
 MJD       56387.461106609 TDT
 MAG   26.472   0.150
! Non-grav parameters: model used, actual number in use, dimension
 LSP    0   0     6
! RMS     3.84316E-08    4.38773E-07    4.31774E-07    3.36307E-07    4.53650E-08    1.03307E-04
! EIG     1.29826E-09    6.33890E-09    8.71538E-08    1.21524E-07    2.67549E-07    1.91117E-06
! WEA     0.01679   -0.20197    0.20847    0.16089   -0.00102   -0.94318
 COV    1.476987322153907E-15 -1.498111205372421E-14  9.417238122553055E-15
 COV    1.064233414404498E-14  6.844413812312568E-17 -3.317899364653091E-12
 COV    1.925219091049900E-13 -1.264424974454006E-13 -1.345104275202012E-13
 COV   -9.701804106486453E-16  3.952147758109287E-11  1.864291328518284E-13
 COV    1.127190547284529E-13 -1.708097448563048E-15 -4.123209482726066E-11
 COV    1.131023164358840E-13 -4.949270218819794E-15 -3.150507600204035E-11
 COV    2.057982053084914E-15  1.675688735574932E-13  1.067235817503990E-08
 NOR    5.746830053577148E+17 -8.299826426373912E+15  8.698920861407877E+16
 NOR    1.615774933873040E+16  3.978477764445554E+16  5.925488451341829E+14
 NOR    9.978754941460872E+14 -1.402765234575811E+15  1.398017184494006E+15
 NOR    3.565075788561902E+15 -7.624107879411385E+12  1.326152185380957E+16
 NOR    2.249035181811618E+15  5.530977657759351E+15  9.002605705997875E+13
 NOR    3.662690178904087E+15  9.233262422835384E+15  1.920256376802269E+13
 NOR    2.377824552249132E+16  4.741864479712273E+13  6.162957240775663E+11
```

E.7 2004RQ252

```
format  = 'OEF2.0'          ! file format
rectype = 'ML'              ! record type (1L/ML)
refsys  = ECLM J2000        ! default reference system
END_OF_HEADER
2004RQ252
! Equinoctial elements: a, e*sin(LP), e*cos(LP), tan(i/2)*sin(LN), tan(i/2)*cos(LN), mean long.
 EQU  1.1256873311431759E+00   0.368409361590643   -0.122763270870089    0.029237030995799    0.061071945757693
      120.7997311650237
 MJD      53799.848967580 TDT
 MAG  22.498  0.150
! Non-grav parameters: model used, actual number in use, dimension
 LSP  0  0  6
! RMS    3.83718E-08   3.63373E-07   4.41336E-07   4.00024E-08   1.12546E-07   3.36580E-05
! EIG    1.68114E-09   1.65887E-08   2.57047E-08   4.31500E-08   6.51134E-08   8.24988E-07
! WEA    0.04644   0.43950   -0.53323   0.03609   -0.11357   0.71144
 COV   1.472393145705471E-15  1.391596674032341E-14 -1.686347009458753E-14
 COV   1.146240743737742E-15 -3.578929762015892E-15  1.287105946594909E-12
 COV   1.320402983980620E-13 -1.591556748512319E-13  1.079419945095033E-14
 COV  -3.381426670424776E-14  1.218919584005328E-11  1.947772734532339E-13
 COV  -1.362540884254477E-14  4.077549926417975E-14 -1.475400770297661E-11
 COV   1.600194885712685E-15 -1.882192509932251E-15  9.849199237899626E-13
 COV   1.266650543878842E-14 -3.142215219182533E-12  1.132860769928902E-09
 NOR   3.519061322944662E+17 -2.246744025995356E+16  1.171594400861245E+16
 NOR   5.656381876642594E+15 -1.616750098795358E+13 -1.045600951537356E+13
 NOR   2.673749919980166E+15 -6.397167290618110E+14 -6.502872040472540E+14
 NOR   6.886519358275277E+13 -1.081721711034579E+13  1.034936883893012E+15
 NOR   1.030829745273960E+15 -1.574818731694001E+14  5.717658802784176E+12
 NOR   3.125493813880074E+15 -6.217482865750536E+14  9.553651750279461E+12
 NOR   3.809814983607102E+14 -1.176307550113416E+12  1.920480999796538E+11
```

E.8 2001AV43

```
format  = 'OEF2.0'          ! file format
rectype = 'ML'              ! record type (1L/ML)
refsys  = ECLM J2000        ! default reference system
END_OF_HEADER
2001AV43
! Equinoctial elements: a, e*sin(LP), e*cos(LP), tan(i/2)*sin(LN), tan(i/2)*cos(LN), mean long.
 EQU    1.2770710799699776E+00    0.228599070669711    0.066529332853096     0.001267749937787     0.002061560694280
       149.9224260483016
 MJD       56214.603144821 TDT
 MAG   24.703   0.150
! Non-grav parameters: model used, actual number in use, dimension
 LSP    0   0     6
! RMS     5.75928E-10    2.78029E-08    5.50289E-08    1.67924E-08    1.67962E-08    5.73154E-06
! EIG     6.71635E-11    9.72760E-10    1.18643E-09    1.58670E-08    1.69528E-08    1.17605E-07
! WEA     0.00373   -0.23263    0.46742   -0.01561    0.06125   -0.85053
 COV    3.316935210329764E-19 -1.268517684871868E-17  2.405025133767687E-17
 COV   -2.988831565637742E-19  5.796443066211348E-18 -2.491580762103823E-15
 COV    7.730025184843727E-16 -1.492415105400574E-15  9.267690924343798E-17
 COV   -2.571060903972582E-16  1.564761055601290E-13  3.028184589796454E-15
 COV   -8.014287093710364E-17  3.661496227164082E-16 -3.151639274483198E-13
 COV    2.819832732877020E-16 -3.864309893348825E-19  1.027402069941270E-14
 COV    2.821113602779557E-16 -4.034149844410992E-14  3.285049857951552E-11
 NOR    2.003412502324968E+20  1.690477661400484E+18 -5.665642477818166E+19
 NOR    3.448028972225348E+18 -7.153766307258445E+18 -5.462758208761571E+17
 NOR    7.087651683593295E+17 -2.938631448426745E+17 -1.015831983268851E+17
 NOR    1.569959737356441E+17 -5.842553450611183E+15  1.684495229968939E+19
 NOR   -1.064069397732532E+18  2.153056159359812E+18  1.616879450629816E+17
 NOR    9.133928091687506E+16 -1.692861476250954E+17 -9.699627002634742E+15
 NOR    3.345439024811263E+17  1.982954932216948E+16  1.565027856388962E+15
```

E.9 (99942) Apophis

```
format  = 'OEF2.0'          ! file format
rectype = 'ML'              ! record type (1L/ML)
refsys  = ECLM J2000        ! default reference system
END_OF_HEADER
99942
! Equinoctial elements: a, e*sin(LP), e*cos(LP), tan(i/2)*sin(LN), tan(i/2)*cos(LN), mean long.
 EQU    9.2242562886554802E-01   -0.093156562272564    0.166975055470516    -0.012033463843986    -0.026474070069010
        40.7767973752541
 MJD       54957.268675100 TDT
 MAG   18.901   0.150
! Non-grav parameters: model used, actual number in use, dimension
 LSP    0   0     6
! RMS     1.30505E-10    5.36191E-09    6.34004E-09    9.12633E-09    7.13218E-09    9.03416E-07
! EIG     2.08590E-11    3.09855E-10    1.03140E-09    2.70568E-09    1.11407E-08    1.78646E-08
! WEA     0.00456   -0.28106   -0.33777    0.22018   -0.05014    0.86943
 COV    1.703144763435252E-20  -2.528616193250696E-19  -6.125233234486191E-19
 COV    9.511048527336443E-19  -7.013575977720047E-19   6.150950561086154E-17
 COV    2.875009528891401E-17   2.758662420668355E-17  -1.369287874100070E-17
 COV   -4.372658659561057E-18  -4.580215874343670E-15   4.019614105183713E-17
 COV   -3.307322945915814E-17   1.626891358344337E-17  -5.164313283851017E-15
 COV    8.328981296573713E-17  -5.811421170827577E-17   2.240116232937201E-15
 COV    5.086805502756089E-17   2.381873033641661E-16   8.161612396662175E-13
 NOR    2.293371656502339E+21  -4.328491873177247E+19  -6.414495527572917E+19
 NOR    2.259023675451635E+18   5.494709587701046E+19  -8.438666479348041E+17
 NOR    4.709079241575021E+18  -7.875265121109887E+17   2.291342676841818E+18
 NOR    2.594918960870082E+18   1.765956093438511E+16   3.825051504453857E+18
 NOR   -1.444369462403151E+18  -3.964836435761501E+18   2.973943793017867E+16
 NOR    1.544377516168374E+18   2.461025585973943E+18  -1.407876121317494E+15
 NOR    5.187366313203529E+18  -2.293503343114900E+16   3.626622063534528E+14
```

References

[1] Kyle Alfriend, Srinivas Rao Vadali, Pini Gurfil, Jonathan How, and Louis Breger. *Spacecraft formation flying: Dynamics, control and navigation*, volume 2. Butterworth-Heinemann, 2009. 36

[2] Samuel P. Altman. A unified state model of orbital trajectory and attitude dynamics. *Celestial mechanics*, 6(4):425–446, Dec 1972. doi: 10.1007/BF01227757. 66

[3] Samuel P. Altman. Velocity-space maps and transforms of tracking observations for orbital trajectory state analysis. *Celestial mechanics*, 11(4):405–428, Dec 1975. doi: 10.1007/BF01650281. 66, 69

[4] Davide Amato, Giulio Baù, and Claudio Bombardelli. Accurate orbit propagation in the presence of planetary close encounters. *Monthly Notices of the Royal Astronomical Society*, 470(2):2079–2099, 2017. doi: 10.1093/mnras/stx1254. 66, 97, 100

[5] R. Armellin, P. Di Lizia, F. Bernelli-Zazzera, and M. Berz. Asteroid close encounters characterization using differential algebra: the case of Apophis. *Celestial Mechanics and Dynamical Astronomy*, 107(4):451–470, 2010. doi: 10.1007/s10569-010-9283-5. 4

[6] Roberto Armellin and Pierluigi Di Lizia. Probabilistic initial orbit determination. In *Proceedings of the 26th AAS/AIAA Space Flight Mechanics Meeting held February 14–18, 2016, Napa, California, USA*, 2016. 4

[7] R.H. Battin. *An introduction to the mathematics and methods of astrodynamics*. AIAA, 1999. ISBN 1563473429. 18, 40, 69, 70, 78, 163

[8] G. Baù, C. Bombardelli, and J. Peláez. A new set of integrals of motion to propagate the perturbed two-body problem. *Celestial Mechanics and Dynamical Astronomy*, 116(1):53–78, 2013. doi: 10.1007/s10569-013-9475-x. 5, 19, 65, 161

[9] Giulio Baù and Claudio Bombardelli. Time elements for enhanced performance of the dromo orbit propagator. *The Astronomical Journal*, 148(3):43, 2014. doi: 10.1088/0004-6256/148/3/43. 5, 19, 65

[10] Giulio Baù, Claudio Bombardelli, Jesús Peláez, and Enrico Lorenzini. Non-singular orbital elements for special perturbations in the two-body problem. *Monthly Notices of the Royal Astronomical Society*, 454(3):2890–2908, 2015. doi: 10.1093/mnras/stv2106. 5, 20, 66

[11] Julie Bellerose, Shyamkumar Bhaskaran, and Steven Chesley. Aida: Measuring asteroid binary system parameters and dart-imparted deflection using the aim spacecraft. In *26th International symposium on Space Flight Dynamics, held together the 31st International Symposium on Space Technology and Science*, number ISTS-2017-d-148 / ISSFD-2017-148, Matsuyama, Japan, 2017. 128

[12] Fabrizio Bernardi. Neodys (and astdys and priority list) data provision. In *SSA-NEO Final Presentation Day*, November 2014. URL `https://indico.esa.int/indico/event/68/material/slides/1.pdf`. 169

[13] C Bombardelli. Analytical formulation of impulsive collision avoidance dynamics. *Celestial Mechanics and Dynamical Astronomy*, 118(2):99–114, 2013. doi: 10.1007/s10569-013-9526-32. 66

[14] C. Bombardelli and G. Baù. Accurate analytical approximation of asteroid deflection with constant tangential thrust. *Celestial Mechanics and Dynamical Astronomy*, pages 1–17, 2012. 66

[15] C Bombardelli, G Bau, and J Pelaez. Asymptotic Solution for the Two-Body Problem with Constant Tangential Thrust Acceleration. *Celestial Mechanics and Dynamical Astronomy*, 110(3):239–256, 2011. 66

[16] Claudio Bombardelli and Javier Hernando-Ayuso. Optimal impulsive collision avoidance in low earth orbit. *Journal of Guidance, Control, and Dynamics*, 38(2): 217–225, 2015. doi: 10.2514/1.G000742. 56, 66

[17] Claudio Bombardelli, Juan Luis Gonzalo, and Javier Roa. Approximate solutions of non-linear circular orbit relative motion in curvilinear coordinates. *Celestial Mechanics and Dynamical Astronomy*, 127(1):49–66, 2017. doi: 10.1007/s10569-016-9716-x. 6, 36, 39

[18] Claudio Bombardelli, Juan Luis Gonzalo, and Javier Roa. Approximate analytical solution of the multiple revolution lambert's targeting problem. *Journal of Guidance, Control, and Dynamics*, 41(3):792–801, January 2018. doi: 10.2514/1.G002887. 66

[19] Stephen P. Boyd and Lieven Vandenberghe. *Convex Optimization*. Cambridge university press, New York, 2004. ISBN 978-0521833783. 118

[20] R. Broucke and P. Cefola. A note on the relations between true and eccentric anomalies in the two-body problem. *Celestial mechanics*, 7(3):388–389, Apr 1973. doi: 10.1007/BF01227859. 78, 164

[21] Roger A Broucke and Paul J Cefola. On the equinoctial orbit elements. *Celestial Mechanics*, 5(3):303–310, 1972. 18

[22] Onur Celik and Joan Pau Sánchez. Opportunities for ballistic soft landing in binary asteroids. *Journal of Guidance, Control, and Dynamics*, 40(6):1390–1402, April 2017. doi: 10.2514/1.G002181. 128, 129

[23] F. K. Chan. *Spacecraft Collision Probability*. The Aerospace Press, El Segundo, California, 2008. ISBN 9781884989186. 2

[24] A.F. Cheng, J. Atchison, B. Kantsiper, A.S. Rivkin, A. Stickle, C. Reed, A. Galvez, I. Carnelli, P. Michel, and S. Ulamec. Asteroid impact and deflection assessment mission. *Acta Astronautica*, 115:262 – 269, 2015. doi: 10.1016/j.actaastro.2015.05.021. 128

[25] SR Chesley and A Milani. Neodys: an online information system for near-earth objects. In *Bulletin of the American Astronomical Society*, volume 31, page 1117, 1999. 169

[26] John A. Christian. Optical navigation using planetś centroid and apparent diam-

eter in image. *Journal of Guidance, Control, and Dynamics*, 38(2):192–204, December 2014. doi: 10.2514/1.G000872. 114

[27] Vincent T Coppola and Sergei Tanygin. Using bent ellipsoids to represent large position covariance in orbit propagation. *Journal of Guidance, Control, and Dynamics*, 38(9):1775–1784, 2015. doi: 10.2514/1.G001011. 5, 36

[28] Harald Cramér. *Mathematical Methods of Statistics*. Princeton University Press, Princeton, 1946. ISBN 0691005478. 99, 143, 144, 145

[29] L. Dell'Elce, N. Baresi, S.P. Naidu, L.A.M. Benner, and D.J. Scheeres. Numerical investigation of the dynamical environment of 65803 didymos. *Advances in Space Research*, 59(5):1304 – 1320, 2017. doi: 10.1016/j.asr.2016.12.018. 128, 129

[30] Amdre Deprit. Ideal elements for perturbed Keplerian motions. *Journal of Research of the National Bureau of Standards - B. Mathematical Sciences*, 79B(1 and 2), 1975. 66

[31] E. Fantino and S. Casotto. Methods of harmonic synthesis for global geopotential models and their first-, second- and third-order gradients. *Journal of Geodesy*, 83 (7):595–619, Jul 2009. doi: 10.1007/s00190-008-0275-0. 75

[32] Fabio Ferrari and Michèle Lavagna. Ballistic landing design on binary asteroids: The aim case study. *Advances in Space Research*, 2017. doi: 10.1016/j.asr.2017.11.033. 128, 129

[33] K. Fletcher. Space debris: The esa approach. 2017 . URL `https://download.esa.int/esoc/downloads/BR-336_Space_Debris_WEB.pdf`. 2

[34] Zachary Folcik, Arthur Lue, and Joshua Vatsky. Reconciling covariances with reliable orbital uncertainty. In *12th Advanced Maui Optical and Space Surveillance Technologies Conference*, September 13-16 2011. 5

[35] William M. Folkner, James G. Williams, Dale H Boggs, Ryan S. Park, and Petr Kuchynka. The planetary and lunar ephemerides DE430 and DE431. *Interplanetary Network Progress Report 42-196*, 196:1–81, 2014. 76

[36] Ricardo García-Pelayo and Javier Hernando-Ayuso. A series for the collision

probability in the short-encounter model. *Journal of Guidance, Control, and Dynamics*, 39(8):1908–1916, 2016. doi: 10.2514/1.G001754. 2

[37] David K. Geller and T. Alan Lovell. Angles-only initial relative orbit determination performance analysis using cylindrical coordinates. *The Journal of the Astronautical Sciences*, 64(1):72–96, 2017. doi: 10.1007/s40295-016-0095-z. 36

[38] Daniel Giza, Puneet Singla, and Moriba Jah. An approach for nonlinear uncertainty propagation: Application to orbital mechanics. In *AIAA Guidance, Navigation, and Control Conference*, number 2009-6082, Chicago, Illinois, 10-13 August 2009. doi: 10.2514/6.2009-6082. 4

[39] Juan Luis Gonzalo Gómez. *Propagation and Optimal Control of Space Trajectories Using Perturbation Methods*. Phd thesis, Escuela Técnica Superior de Ingenieros Aeronáuticos, Universidad politécnica de Madrid, 2017. 66

[40] Juan Luis Gonzalo Gomez and Claudio Bombardelli. Low-thrust trajectory optimization in dromo variables. In *AAS/AIAA Spaceflight Mechanics Meeting 2015. Advances in the Astronautical Sciences Series*, volume 155, pages 1803–1820. Univelt, 2015. 66

[41] Juan Luis Gonzalo and Claudio Bombardelli. Asymptotic solution for the two body problem with radial perturbing acceleration. In *Spaceflight Mechanics 2014*, pages 359–377, Santa Fe, 2014. American Astronautical Society. 66

[42] M. Hagenfeldt, J. L. Cano, L. F. Peñín, C. Bombardelli, J. Peláez, E. Luraschi, and A. Gálvez. Gnc design for asteroid orbit modification missions. In *AIAA Guidance, Navigation, and Control (GNC) Conference*, page 4547, Boston, MA, 2013. doi: 10.2514/6.2013-4547. 1

[43] Peter Andreas Hansen. *Auseinandersetzung einer zweckmässigen Methode zur Berechnung der absoluten Störungen der kleinen Planeten*, volume 4. 1859. 65

[44] Javier Hernando-Ayuso and Claudio Bombardelli. Orbit Uncertainty Propagation Using Dromo. In *AIAA/AAS Astrodynamics Specialist Conference*, number AIAA 2016-5632, 2016. doi: 10.2514/6.2016-5632. 6, 7, 9, 107

[45] Javier Hernando-Ayuso and Claudio Bombardelli. Advances in uncertainty propagation using curvilinear coordinates. In *26th Workshop on JAXA Astrodynamics and Flight Mechanics*, Sagamihara, Japan, 25 July 2016. 9

[46] Javier Hernando-Ayuso and Claudio Bombardelli. Orbit covariance propagation via quadratic-order state transition matrix in curvilinear coordinates. *Celestial Mechanics and Dynamical Astronomy*, 129(1):215–234, Sep 2017. doi: 10.1007/s10569-017-9773-9. 5, 7

[47] Javier Hernando-Ayuso and Claudio Bombardelli. Orbit uncertainty propagation around non-spherical bodies using the Dromo formulation. In *26th International symposium on Space Flight Dynamics, held together the 31st International Symposium on Space Technology and Science*, number 2017-d-071, Matsuyama, Japan, 3-9 June 2017. 6, 8, 71

[48] Javier Hernando-Ayuso, Claudio Bombardelli, and Giulio Baù. Uncertainty propagation in the N-body problem using dromo elements. In *2017 IAA Planetary Defense Conference*, number IAA-PDC-17-03-P21, Tokyo, Japan, 15-19 May 2017. 8

[49] Javier Hernando-Ayuso, Claudio Bombardelli, Giulio Baù, and Jun'ichiro Kawaguchi. Non-gaussianities in orbit uncertainty representation. In *27th Workshop on JAXA Astrodynamics and Flight Mechanics*, number 2017B_15, Sagamihara, Japan, July 2017. JAXA. 8

[50] Javier Hernando-Ayuso, Claudio Bombardelli, and Giulio Baù. Uncertainty propagation in the N-body problem using Dromo elements. *Acta Astronautica*, 2017 (in press). doi: 10.1016/j.actaastro.2017.12.030". 7

[51] Javier Herrera-Montojo, Hodei Urrutxua, and Jesús Peláez. An asymptotic solution for the main problem. In *AIAA/AAS Astrodynamics Specialist Conference*, number AIAA 2014-4155, San Diego, CA, 2014. AIAA. doi: 10.2514/6.2014-4155. 66

[52] Keric Hill, Kyle Alfriend, and Chris Sabol. Covariance-based uncorrelated track association. In *AIAA/AAS Astrodynamics Specialist Conference*, number AIAA 2008-7211, Honolulu, Hawaii, 18-21 August 2008. 5, 36

[53] Joshua T Horwood, Nathan D Aragon, and Aubrey B Poore. Gaussian sum filters for space surveillance: theory and simulations. *Journal of Guidance, Control, and Dynamics*, 34(6):1839–1851, November 2011. doi: 10.2514/1.53793. 19

[54] Ram Jakhu. Towards Long-term Sustainability of Space Activities: Overcoming the Challenge of Space Debris. Technical report, A/AC.105/C.1/2011/CRP.14. Committee on the Peaceful Uses of Outer Space. Available on line at http://www.oosa.unvienna.org, 03-02-2011. 2

[55] E.F.M. Jochim. The significance of the hansen ideal space frame. *Astronomische Nachrichten*, 333(8):774–783. doi: 10.1002/asna.201111711. 65

[56] Brandon A Jones, Alireza Doostan, and George H Born. Nonlinear propagation of orbit uncertainty using non-intrusive polynomial chaos. *Journal of Guidance, Control, and Dynamics*, 36(2):430–444, 2013. doi: 10.2514/1.57599. 4

[57] S. J. Julier and J. J. LaViola. On kalman filtering with nonlinear equality constraints. *IEEE Transactions on Signal Processing*, 55(6):2774–2784, June 2007. doi: 10.1109/TSP.2007.893949. 73

[58] Simon J Julier and Jeffrey K Uhlmann. A new extension of the kalman filter to nonlinear systems. In *The 11th International Symposium on Aerospace/Defence, Sensing, Simulation and Controls*, volume 3, pages 182–193. Orlando, FL, 1997. 4

[59] John L Junkins, Maruthi R Akella, and Kyle T Alfriend. Non-Gaussian error propagation in orbital mechanics. *The Journal of the Astronautical Sciences*, 44(4): 541–563, October-December 1996. 5, 35

[60] Jean A. Kéchichian. The streamlined and complete set of the nonsingular j2-perturbed dynamic and adjoint equations for trajectory optimization in terms of eccentric longitude. *The Journal of the Astronautical Sciences*, 55(3):325–348, Sep 2007. doi: 10.1007/BF03256528. 5, 22

[61] Jean A. Kéchichian. Inclusion of higher order harmonics in the modeling of optimal low-thrust orbit transfer. *The Journal of the Astronautical Sciences*, 56(1):41–70, Mar 2008. doi: 10.1007/BF03256541. 5, 22

[62] Jean A. Kéchichian. Analytic expansions of luni-solar gravity perturbations along rotating axes for trajectory optimization: Part 1: The dynamic system. *Acta Astronautica*, 68(11):1947 – 1963, 2011. doi: 10.1016/j.actaastro.2010.12.001. 5, 22

[63] Jean A. Kéchichian. Analytic expansions of luni-solar gravity perturbations along rotating axes for trajectory optimization—part 2: The multipliers system and simulations. *Acta Astronautica*, 68(11):1914 – 1930, 2011. doi: 10.1016/j.actaastro.2010.12.003. 5, 22

[64] Jean Albert Kechichian. Trajectory optimization using nonsingular orbital elements and true longitude. *Journal of Guidance, Control, and Dynamics*, 20(5):1003–1009, September 1997. doi: 10.2514/2.4147. 5, 22

[65] John T. Kent, Shambo Bhattacharjee, Islam I. Hussein, and Moriba Jah. Nonlinear filtering using directional statistics for the orbital tracking problem with perturbation effects. In *AIAA SciTech Forum*. American Institute of Aeronautics and Astronautics, 2018. doi: 10.2514/6.2018-0474. 72

[66] Heiner Klinkrad. *Space debris: models and risk analysis*. Springer, 2006. ISBN 978-3-540-37674-3. 2, 36, 121

[67] Holger Krag, Tim Flohrer, and Stijn Lemmens. Consideration of space debris mitigation requirements in the operation of leo missions. *SpaceOps Conference*, 2012. 2, 4

[68] Petr Kuchynka, Miguel Angel Martin Serrano, Mikel Catania, Xavier Marc, Dirk Kuijper, Vitali Braun, and Holger Krag. Sentinel-1A: Flight dynamics analysis of the august 2016 collision even. In *26th International Symposium on Space Flight Mechannics*, number ISTS-2017-d-028/ISSFD-2017-028, Matsuyama, Japan, June 2017. 2

[69] Christopher M Lane and Penina Axelrad. Formation design in eccentric orbits using linearized equations of relative motion. *Journal of Guidance, Control, and Dynamics*, 29(1):146–160, 2006. doi: 10.2514/1.13173. 5, 36

[70] Martin Lara. Note on the ideal frame formulation. *Celestial Mechanics and Dynamical Astronomy*, 129(1):137–151, Sep 2017. doi: 10.1007/s10569-017-9770-z. 66

[71] Byoung-Sun Lee, Yoola Hwang, Hae-Yeon Kim, and Bang-Yeop Kim. GEO satellite collision avoidance maneuver strategy against inclined GSO satellite. In *SpaceOps 2012 Conference*, Stockholm, Sweden, 11-15 June 2012. doi: 10.2514/6.2012-1294441. 2

[72] Sangjin Lee, Hao Lyu, and Inseok Hwang. Analytical Uncertainty Propagation for Satellite Relative Motion Along Elliptic Orbits. *Journal of Guidance, Control, and Dynamics*, 39(7):1593–1601, 2014. doi: 10.2514/1.G000258. 35

[73] Ern J Lefferts, F Landis Markley, and Malcolm D Shuster. Kalman filtering for spacecraft attitude estimation. *Journal of Guidance, Control, and Dynamics*, 5(5): 417–429, September 1982. doi: 10.2514/3.56190. 73, 118

[74] HG Lewis, Jonas Radtke, Alessandro Rossi, James Beck, Michael Oswald, Pamela Anderson, Benjamin Bastida Virgili, and Holger Krag. Sensitivity of the space debris environment to large constellations and small satellites. In *Proceedings: 7th European Conference on Space Debris, Darmstadt, Germany*, pages 18–21, 2017. 2

[75] J.-C. Liou. An active debris removal parametric study for leo environment remediation. *Advances in Space Research*, 47(11):1865 – 1876, 2011. doi: 10.1016/j.asr.2011.02.003. 2

[76] Kanti V Mardia and Peter E Jupp. *Directional statistics*. John Wiley & Sons, Baffins Lane, Chichester. West Sussex, PO19 1UD England, 2000. 72

[77] Peter S Maybeck. *Stochastic models, estimation, and control*, volume 141 of *Mathematics in Science and Engineering*. Academic press, New York, 1982. ISBN 012480701. 14

[78] Peter S Maybeck. *Stochastic models, estimation, and control Volume 2*, volume 141-2 of *Mathematics in Science and Engineering*. Academic press, New York, 1982. ISBN 012480702. 4, 15

[79] Robert G Melton. Time-explicit representation of relative motion between elliptical orbits. *Journal of Guidance, Control, and Dynamics*, 23(4):604–610, 2000. doi: 10.2514/2.4605. 5, 35, 47, 49, 153

[80] Patrick Michel. Triennial report 2015–2018 mear earth object working group. Technical report, IAU Near Earth Object Working Group, 2018. URL https://www.iau.org/static/science/scientific_bodies/working_groups/171/wg-neos-triennial-report-2015-2018.pdf. DIVISION F. 128

[81] Andrea Milani, Maria Eugenia Sansaturio, Giacomo Tommei, Oscar Arratia, and Steven R Chesley. Multiple solutions for asteroid orbits: computational procedure and applications. *Astronomy & Astrophysics*, 431(2):729–746, 2005. 5

[82] E. Mooij. Orbit-state model selection for solar-sailing mission optimization. In *Guidance, Navigation, and Control and Co-located Conferences*. American Institute of Aeronautics and Astronautics, August 2012. doi: 10.2514/6.2012-4588. 66

[83] Adam Morawiec. *Orientations and Rotations. Computations in Crystallographic Textures*. Springer Berlin Heidelberg, 2004. ISBN 9783642073861. doi: 10.1007/978-3-662-09156-2. 72

[84] Kraft Newman, Ryan Frigm, and David McKinley. It's Not a Big Sky After All: Justification for a Close Approach Prediction and Risk Assessment Process. *Advances in the Astronautical Sciences*, 135(2):1113–1132, 2009. AAS 09-369. AAS/AIAA Astrodynamics Specialist Conference; Pittsburgh, PA; USA. 2

[85] ESA Space Debris Office. Esa's annual space environment report. Technical Report GEN-DB-LOG-00208-OPS-GR, ESA, 27 April 2017. Produced with the DISCOS Database. 2, 3

[86] William M Owen Jr. Methods of optical navigation. In *AAS/AIAA Space Flight Mechanics Meeting*, number 2011-215, 2011. 114

[87] M Palacios and C Calvo. Ideal frames and regularization in numerical orbit computation. *Journal of the Astronautical Sciences*, 44(1):63–77, 1996. 66

[88] Ryan S Park and Daniel J Scheeres. Nonlinear mapping of Gaussian statistics: theory and applications to spacecraft trajectory design. *Journal of guidance, Control, and Dynamics*, 29(6):1367–1375, 2006. doi: 10.2514/1.2017. 4

[89] Jesús Peláez, José Manuel Hedo, and Pedro Rodríguez de Andrés. A special perturbation method in orbital dynamics. *Celestial Mechanics and Dynamical Astronomy*, 97(2):131–150, 2007. doi: 10.1007/s10569-006-9056-3. 5, 19, 65, 68

[90] J. R. Raol and N. K. Sinha. On the orbit determination problem. *IEEE Transactions on Aerospace and Electronic Systems*, AES-21(3):274–291, May 1985. doi: 10.1109/TAES.1985.310558. 66

[91] J. Roa, M. Sanjurjo-Rivo, and J. Peláez. Singularities in dromo formulation. analysis of deep flybys. *Advances in Space Research*, 56(3):569 – 581, 2015. doi: 10.1016/j.asr.2015.03.019. Advances in Asteroid and Space Debris Science and Technology - Part 1. 66

[92] Javier Roa and Jesús Peláez. Frozen-anomaly transformation for the elliptic rendezvous problem. *Celestial Mechanics and Dynamical Astronomy*, 121(1):61–81, 2015. doi: 10.1007/s10569-014-9585-0. 19, 66, 67, 162

[93] Javier Roa and Jesús Peláez. Orbit propagation in minkowskian geometry. *Celestial Mechanics and Dynamical Astronomy*, 123(1):13–43, Sep 2015. doi: 10.1007/s10569-015-9627-2. 5, 66

[94] Javier Roa and Jesús Peláez. The theory of asynchronous relative motion i: time transformations and nonlinear corrections. *Celestial Mechanics and Dynamical Astronomy*, 127(3):301–330, Mar 2017. doi: 10.1007/s10569-016-9728-6. 6, 66, 67

[95] Javier Roa Vicens and Jesús Peláez Álvarez. Efficient trajectory propagation for orbit determination problems. In *AAS/AIAA Astrodynamics Specialist Conference*, number AAS-15-730, Vail, Colorado, USA, August 2015. Univelt. 5, 6, 66

[96] C. Sabol, T. Sukut, K. Hill, K. T. Alfriend, B. Wright, Y. Li, and P. Schumacher. Linearized orbit covariance generation and propagation analysis via simple monte carlo simulations. In *AAS 10-134, AAS/AIAA Space Flight Mechanics Conference*, pages 14–17, San Diego, CA, February, 2010. 5

[97] José B. Silva Neto, Diogo M. Sanchez, and Antonio F. Prado. Co-orbital orbits around the asteroid 65803 didymos (1996 gt). In *AIAA SciTech Forum*. American Institute of Aeronautics and Astronautics, January 2018. doi: 10.2514/6.2018-0719. 128

[98] Simon, J.-L., Francou, G., Fienga, A., and Manche, H. New analytical planetary theories VSOP2013 and TOP2013. *Astronomy & Astrophysics*, 557:A49, 2013. doi: 10.1051/0004-6361/201321843. 76

[99] Eduard Stiefel and Gerhard Scheifele. *Linear and regular celestial mechanics*. Springer-Verlag, 1971. 19

[100] Byron Tapley, Bob Schutz, and George H Born. *Statistical orbit determination*. Elsevier Academic Press, 200 Wheeler Road, Burlington, MA 01803, USA, 2004. ISBN 0-12-683630-2. 3, 111, 116, 119

[101] Chiara Tardioli, Martin Kubicek, Massimiliano Vasile, Edmondo Minisci, and Annalisa Riccardi. Comparison of non-intrusive approaches to uncertainty propagation in orbital mechanics. Number AAS 15-545, pages 3979–3992, San Diego, California, 2015. American Astronautical Society. 4

[102] Simon Tardivel. Optimization of the ballistic deployment to the secondary of a binary asteroid. *Journal of Guidance, Control, and Dynamics*, 39(12):2790–2798, December 2016. doi: 10.2514/1.G000593. 128, 129

[103] H. Urrutxua, M. Sanjurjo-Rivo, and J. Peláez. Dromo propagator revisited. *Celestial Mechanics and Dynamical Astronomy*, 124(1):1–31, 2015. doi: 10.1007/s10569-015-9647-y. 5, 19, 65, 68, 70

[104] Hodei Urrutxua, David Morante, Manuel Sanjurjo-Rivo, and Jesús Peláez. Dromo formulation for planar motions: solution to the tsien problem. *Celestial Mechanics and Dynamical Astronomy*, 122(2):143–168, Jun 2015. doi: 10.1007/s10569-015-9613-8. 65

[105] M. Valli, R. Armellin, P. Di Lizia, and M. R. Lavagna. Nonlinear mapping of uncertainties in celestial mechanics. *Journal of Guidance, Control, and Dynamics*, 36 (1):48–63, January 2013. doi: 10.2514/1.58068. 4

[106] V. Vittaldev, E. Mooij, and M. C. Naeije. Unified state model theory and application in astrodynamics. *Celestial Mechanics and Dynamical Astronomy*, 112(3): 253–282, Mar 2012. doi: 10.1007/s10569-011-9396-5. 66

[107] Vivek Vittaldev, Ryan P Russell, and Richard Linares. Spacecraft uncertainty propagation using gaussian mixture models and polynomial chaos expansions. *Journal of Guidance, Control, and Dynamics*, 39(12):2615–2626, December 2016. doi: 10.2514/1.G001571. 4

[108] Lorraine M. Weis. Uncertainty in ks space with arbitrary forces. In *AIAA SciTech Forum*. American Institute of Aeronautics and Astronautics, January 2018. doi: 10.2514/6.2018-0728. 5

[109] R. M. Weisman, M. Majji, and K. T. Alfriend. Analytic characterization of measurement uncertainty and initial orbit determination on orbital element representations. *Celestial Mechanics and Dynamical Astronomy*, 118(2):165–195, Feb 2014. doi: 10.1007/s10569-013-9529-0. 5, 17

[110] W. E. Wiesel. *Modern orbit determination*. Aphelion Press, 2652 Yalonda Ct. Beavercreek, Ohio, 45434 USA, second edition edition, 2010. ISBN 9781453611982. 3, 111, 143

[111] K. Yamanaka and F. Ankersen. New State Transition Matrix for Relative Motion on an Arbitrary Elliptical Orbit. *Journal of guidance, control and dynamics*, 25(1): 60–66, 2002. doi: 10.2514/2.4875. 35

This page intentionally left blank.